A platform for the optimisation of metabolic pathways for glycosylation to achieve a narrow and targeted glycoform distribution

Philip M Jędrzejewski

Department of Chemical Engineering and Engineering Technology

Imperial College London

August, 2015

A thesis submitted to Imperial College London in partial fulfilment of the requirements of the degree of

Doctor of Philosophy and Diploma of Imperial College

Abstract

Glycoproteins make up the bulk of biologically-derived medicines, and are taking up an ever increasing share of the prescription pharmaceuticals market. As opposed to small molecule drugs, glycoproteins are large complex molecules with heterogeneity arising from a multitude of glycan moieties. Glycans are complex post-translation modifications, which result from a number of enzymatic reactions in the ER and Golgi collectively known as glycosylation and play an important role in pharmacokinetics such as drug safety, efficacy and half-life. It is known that the availability of the nucleotide sugar donors (NSDs), which are the co-substrates to the enzymatic glycosylation reactions of the Golgi, can be affected by a number of process conditions such as nutrient availability, as well as the addition of precursor molecules to the culture medium. Consequently, feeding strategies of nucleotide and nucleotide sugar precursors have been explored to exert control over the glycoform. In this work, a mathematical model platform is presented to quantify the impact of nutrient availability and feeding strategies on the glycosylation process with the aim to enable the design of feeding strategies to optimise the product glycoform.

A modelling platform was developed and trained to link the extracellular environment, through the availability of intracellular metabolites in the cytoplasm and the Golgi apparatus, to the glycosylation of the conserved glycan site of the IgG heavy chain. The model platform comprises four parts, which are interlinked through dynamic fluxes and metabolite concentrations: A modified cell growth model based on Monod kinetics capturing cell culture dynamics and the impact of various hexose and nucleotide precursor additions to the cell culture media; A semi-structured purine and pyrimidine synthesis network describing the intracellular concentrations of nucleotide triphosphates, which are the co-substrates of NSD synthesis; A structured and mechanistic representation of the NSD synthesis pathway; The del Val et al. model describing the N-linked glycosylation process of the conserved glycan structure of the IgG antibody heavy chain.

An initial proof-of-concept model framework was able to reproduce hybridoma batch cell growth dynamics, extracellular nutrient availability, dynamic intracellular NSD and nucleotide concentrations, product titer and the antibody product glycoform. Refinement of the original model framework and further training was achieved through a two-step CHO cell-based experimental process. In a first set of experiments the cells' dynamic response to mannose and guanosine feeding was observed. The data allowed a model extension to fed-batch operation as well as inclusion of additional control and inhibitory mechanisms in the *in silico* representation of the nucleotide and NSD *de novo* synthesis networks. A second set of experiments probed the dynamic impact of galactose and uridine feeding strategies on antibody product galactosylation. The effects were dynamic perturbations with respect to cell culture dynamics, nucleotide and NSD synthesis as well as the antibody product glycoform. This formed a basis for further model refinement and to provided a calibrated operating space with respect to galactose and uridine additions to cell culture media. The calibrated model platform was able to produce an optimal dynamic feeding strategy *in silico* with a predicted increase in galactosylation of 46.9% through pulse feeding of galactose and uridine on even days of culture. This framework is a first step towards a platform for the *in silico* optimisation of bioprocess conditions with respect to product quality and safety in line with the Quality by Design (QbD) paradigm.

Acknowledgements

I would like to thank my supervisors; Dr Cleo Kontoravdi, for all the support I received, project guidance and providing an ever stimulation working environment and, Dr Karen M Polizzi, for all her patience, support and the many fruitful discussion.

Thank you Dr Ioscani Jiménez del Val for providing the hybridoma data and guidance throughout my project. I would like to acknowledge MedImmune for their help in analysing the glycan samples. Many thanks to Dr Sergei Kucherenko for the help with the Global Sensitivity Analysis. I thank all the past and present students of the Bio-Systems Engineering group especially Dr Sarantos Kyriakopoulos, Dr Ioanna Z Stefani, Dr Oleksiy Klymenko and the past and present members of the Polizzi lab. I extend my full gratitude to the EPSRC and CPSE for the generous financial support.

I will be forever grateful to Si Nga Sou for her love, kindness and helping hand in the lab. Lastly, I would like to thank my parents for being there for me during times of doubt and the giving me that support that brought me this far.

Declaration

The copyright of this thesis rests with the author and is made available under a Creative Commons Attribution Non-Commercial No Derivatives licence. Researchers are free to copy, distribute or transmit the thesis on the condition that they attribute it, that they do not use it for commercial purposes and that they do not alter, transform or build upon it. For any reuse or redistribution, researchers must make clear to others the licence terms of this work

I hereby certify that all material in this thesis which is not my own work has been properly acknowledged.

Philip M. Jedrzejewski
London, UK
Monday 10th August 2015

Reproduced Material

Disclaimer of Copyright (Chapter 1)

The work presented in chapter 1 takes text passages and images from "Jedrzejewski, P. M., Jimenez del Val I., Polizzi, K. M. and Kontoravdi C. (2013). Applying quality by design to glycoprotein therapeutics: experimental and computational efforts of process control, *Pharmaceutical Bioprocessing*, **1**(1), 51-69. The work was published with Future Science Ltd, who remains the owners of the copyright. Permission was granted to re-use the material as part of this thesis (Jedrzejewski et al., 2013, Jedrzejewski et al., 2014a).

Disclaimer of Copyright (Chapter 3)

The work presented in chapter 3 takes text passages and images from "Jedrzejewski, P. M., Jimenez del Val I., Constantinou, A., Dell, A., Haslam, S. M., Polizzi, K. M. and Kontoravdi C. (2014). Towards Controlling the Glycoform: A Model Framework Linking Extracellular Metabolites to Antibody Glycosylation, *Int. J. Mol. Sci*, **15**(3), 4492-4522. The work was published with MDPI, where the authors' copyright was not transferred and the author retains copyright and the right to re-use material without obtaining permission .

Nomenclature

$[i]_{feed}$	Feed concentration of species i (*mM*)
$[i]_{ext}$	Extracellular concentration of species i (*mM*)
$[i]_{flux}$	Flux of species I to/from the extracellular environment (*mM / h*)
$[i]_{IC}$	Intracellular concentration of species i (*mM*)
F_{feed}	Flow of Feed C into culture (*L / h*)
F_{in}	Flow of supplementation into culture (*L / h*)
f_{inh}	Growth inhibiting factor
f_{lim}	Nutrient growth limiting factor
F_{out}	Flow of sampling out of culture (*L / h*)
$K_{c,i}$	Competitive inhibitory constant of species i (*mM*)
k_d	Cell death (h^{-1})
$K_{d,i}$	Death dissociation constant of species i (*mM*)
$k_{d,max}$	Maximum cell death (h^{-1})
$K_{I,i}$	Inhibitory dissociation constant of species i (*mM*)
$K_{M,i}$	Dissociation constant of species i (*mM*)
m_i	Maintenance coefficient of species i (*mmol / (cell h)*)
$M_{r,i}$	Molecular weight species i (*kg / kmol*)
$n_{r,i}$	Exponential coefficient of reaction r for species i
q_i	Cellular species consumption/production (*mmol / (cell h)*)
s_i	Synthesis rate of species i (*mmol / (cell h)*)
V	Cell culture volume (*L*)
$v_{max,i}$	Maximum turnover rate of reaction i (*mM / h*)
X_d	Dead cell density (cell / *L*)
X_t	Total cell density (cell / *L*)
X_V	Viable cell density (cell / *L*)
$Y_{i/j}$	Yield of species i from species j
$Y_{Xv/i}$	Growth yield from species i (cell / *mol*)
M	Cell growth (h^{-1})
μ_{max}	Maximum cell growth (h^{-1})

Table of Contents

Declaration....iv

Reproduced Material....v

List of Figures....xi

List of Tables....xix

Introduction....1

Chapter 1 Literature Review....6

1.1. The Glycosylation Process....6

1.2. The Role of Glycosylation in Biology....11

1.3. Biopharmaceuticals in Industry....14

1.4. Glycosylation and Post Translational Modifications in Industry....16

1.5. Biopharmaceutical Glycoproteins....18

1.5.1. Interferon - β....18

1.5.2. Erythropoietin....20

1.5.3. Monoclonal antibodies (mAbs)....21

1.6. Controlling the glycoform....29

1.6.1. Glycan Engineering....29

1.6.2. Feeding Strategies....31

1.7. Modelling of Biological Systems....39

1.8. Modelling Hierarchy and Development....40

1.9. Computational Modelling of Glycosylation....44

1.10. Conclusions of Introduction and Literature Review....49

Chapter 2 Experimental Materials and Method 52
2.1. Cell Culture 52
2.2. Antibody Quantification, Extracellular Nutrients and Metabolite Monitoring 53
2.3. Intracellular Metabolite, Nucleotide and Nucleotide Sugar Extraction 54
2.4. Glycan Purification and Analysis 55
Chapter 3 Model development 56
3.1. Model structure 57
3.2. Cell culture dynamics 58
3.3. Nucleotide model 61
3.4. Nucleotide Sugar Donor model 64
3.4.1. Enzyme mechanisms 67
3.4.2. Parameter Estimation 76
3.4.3. Non-NSD Species 79
3.5. N-linked Glycosylation model 80
3.6. Model Training, Results and Discussion 81
3.7. Conclusions 86
Chapter 4 Mannose and Guanosine Feeding 90
4.1. Cell dynamics and extracellular environment 92
4.2. Intracellular metabolites 97
4.3. Intracellular Nucleotide Sugar Donors 102
4.4. Product glycoform 106
4.5. Conclusions and Further work 107
Chapter 5 Model Translation and Expansion 112
5.1. Cell culture dynamics 113

5.2. Nucleotide model 120
5.2.1. Purine synthesis 121
5.2.2. Pyrimidine synthesis 123
5.3. Nucleotide Sugar Donor model 124
5.4. Model Training, Results and Discussion 126
5.4.1. Cell culture dynamics output 127
5.4.2. Nucleotide model output 134
5.4.3. Nucleotide sugar donor model output 137
5.5. Conclusions 142
Chapter 6 Galactose and Uridine Feeding 146
6.1. Cell dynamics and extracellular environment 149
6.2. Intracellular metabolites 156
6.3. Intracellular Nucleotide Sugar Donors 161
6.4. Product glycoform 166
6.5. Conclusions and Further work 170
Chapter 7 Model refinement and *in silico* optimisation 176
7.1. Cell culture dynamics model 177
7.2. Nucleotide synthesis model 181
7.2.1. Purine synthesis 182
7.2.2. Pyrimidine synthesis 183
7.3. Nucleotide sugar donor model 184
7.4. N-linked glycosylation model 187
7.5. *In silico* feeding strategy optimisation 187
7.6. Model Training, Results and Discussion 188
7.6.1. Cell culture dynamics model output 189

7.6.2. Nucleotide synthesis model output 201
7.6.3. Nucleotide sugar donor model output 208
7.6.4. Glycan model output 216
7.7. *In silico* feeding strategy optimisation 223
7.8. Conclusion 227
Chapter 8 Final Conclusions and Future Work 231
8.1. Project summary 231
8.2. Overall thesis achievements 233
8.2.1. Experimental achievements 233
8.2.2. Computational achievements 234
1.1. Future work and application 236
Bibliography 241

List of Figures

EMA approved biologically-derived drugs.. 1

Figure 1.1 Schematic of the N-linked glycosylation assembly 7

Figure 1.2 Examples of glycan structure diversity.. 9

Figure 1.3 Schematic of an IgG mAb with glycan structures in the CH2 domain 22

Figure 1.4 Schematic of antibody mediated activity. 23

Figure 1.5 Glycan moieties found in the Fc region of mAbs 25

Figure 1.6 Metabolic pathway of NSD de novo synthesis. 33

Figure 3.1 Structure of the model platform 56

Figure 3.2 Schematic of the model framework depicting the interaction of the cell culture dynamics model with the remaining parts of the framework. 58

Figure 3.3 Schematic of the model framework depicting the interaction of the nucleotide model with the remaining parts of the framework. 61

Figure 3.4 Simplified purine and pyrimidine synthesis network 62

Figure 3.5 Position of the NSD synthesis model within the model framework 64

Figure 3.6 Reaction network of the de novo NSD synthesis pathway 65

Figure 3.7 Single substrate Michaelis-Menten kinetics 67

Figure 3.8 Random order bi-bi kinetics 68

Figure 3.9 Ordered bi-bi kinetics 69

Figure 3.10 Ping-pong bi-bi kinetics 70

Figure 3.11 Ping-pong ter-ter kinetics 71

Figure 3.12 Hexokinase reaction scheme 72

Figure 3.13 Visual representation of the GSA output. 79

Figure 3.14 Schematic of the glycan model within the model framework 80

Figure 3.15 Experimental data against generated fits from the dynamic Monod growth model 82

Figure 3.16 Experimental data compared with generated fits from the nucleotide model 83

Figure 3.17 Experimental data compared with generated fits from the NSD model 84

Figure 3.18 Simulated and experimentally distributions of the product glycoform. 85

Figure 4.1 Viable cell density 94

Figure 4.2 Total cell density 94

Figure 4.3 Antibody titer 94

Figure 4.4 Comparison of specific mAb productivity 94

Figure 4.5 Extracellular guanosine 95

Figure 4.6 Extracellular mannose 95

Figure 4.7 Extracellular glucose 96

Figure 4.8 Extracellular lactate 96

Figure 4.9 Extracellular glutamate 97

Figure 4.10 Extracellular glutamine 97

Figure 4.11 Extracellular ammonia 97

Figure 4.12 Intracellular glucose 99

Figure 4.13 Intracellular mannose 99

Figure 4.14 Intracellular glutamine 99

Figure 4.15 Intracellular GTP 100

Figure 4.16 Intracellular ATP 101

Figure 4.17 Intracellular ADP 101

Figure 4.18 Intracellular AMP 101

Figure 4.19 Intracellular CTP 102

Figure 4.20 Intracellular UTP 102

Figure 4.21 Intracellular GDP-Fuc 103

Figure 4.22 Intracellular GDP-Man 103

Figure 4.23 Intracellular UDP-GlcNAc 104

Figure 4.24 Intracellular UDP-GalNAc 104

Figure 4.25 Intracellular UDP-Gal 105

Figure 4.26 Intracellular UDP-Glc 105

Figure 4.27 Intracellular CMP-Neu5Ac 105

Figure 4.28 Antibody product Fc region glycoform on day 7 of culture 107

Figure 4.29 Antibody product Fc region glycoform on final culture day. 107

Figure 5.1 Schematic of the model framework. 113

Figure 5.2 a schematic of the nucleotide model 120

Figure 5.3 a semi structured reaction network of the de novo purine synthesis. 121

Figure 5.4 simplified reaction network of the *de novo* pyrimidine synthesis 123

Figure 5.5 The reaction network of the de novo nucleotide sugar donor synthesis pathway,. 125

Figures 5.6a-c Experimental and computational outputs of viable cell density 127

Figure 5.7a-c Experimental data and computational outputs of dead cell density 127

Figure 5.8a-c Experimental data and computational outputs of antibody titer. 128

Figures 5.9a-c Experimental data and computational outputs of extracellular glucose. 129

Figures 5.10a-c Experimental data (markers) and computational outputs (lines) of extracellular mannose for the High G and Low G culture with respect to time. 130

Figures 5.11a-c Experimental data (markers) and computational outputs (lines) of extracellular lactate for the control, High G and Low G culture with respect to time. 130

Figures 5.12a-c Experimental data (markers) and computational outputs (lines) of extracellular glutamate for the control, High G and Low G culture with respect to time. ... 131

Figure 5.13a-c Experimental data (markers) and computational outputs (lines) of extracellular glutamine for the control, High G and Low G culture. 131

Figures 5.14a-cExperimental data (markers) and computational outputs (lines) of extracellular ammonia for the control, High G and Low G culture with respect to time. 132

Figures 5.15a-bExperimental data (markers) and computational outputs (lines) of extracellular guanosine for the control, High G and Low G culture with respect to time. ...133

Figures 5.16a-c Experimental data (markers) and computational outputs (lines) of extracellular asparagine for the control, High G and Low G culture with respect to time...133

Figures 5.17a-c Experimental data (markers) and computational outputs (lines) of intracellular ATP for the control, High G and Low G culture with respect to time.....134

Figures 5.18a-c Experimental data (markers) and computational outputs (lines) of intracellular ADP for the control, High G and Low G culture with respect to time.....135

Figures 5.19a-c Experimental data (markers) and computational outputs (lines) of intracellular AMP for the control, High G and Low G culture with respect to time. 135

Figures 5.20a-c Experimental data (markers) and computational outputs (lines) of intracellular GTP for the control, High G and Low G culture with respect to time.....136

Figures 5.21a-c Experimental data (markers) and computational outputs (lines) of intracellular UTP for the control, High G and Low G culture with respect to time.....137

Figures 5.22a-c Experimental data (markers) and computational outputs (lines) of intracellular CTP for the control, High G and Low G culture with respect to time. 137

Figures 5.23a-c Experimental data (markers) and computational outputs (lines) of intracellular GDP-Fuc for the control, High G and Low G culture with respect to time. 139

Figures 5.24a-c Experimental data (markers) and computational outputs (lines) of intracellular GDP-Man for the control, High G and Low G culture with respect to time.....139

Figures 5.25a-c Figures 5.26a-c Experimental data (markers) and computational outputs (lines) of intracellular UDP-Glc for the control, High G and Low G culture with respect to time.....140

Figures 5.27a-c Experimental data (markers) and computational outputs (lines) of intracellular UDP-Gal for the control, High G and Low G culture with respect to time.....140

Figures 5.28a-c Experimental data (markers) and computational outputs (lines) of intracellular UDP-GlcNAc for the control, High G and Low G culture with respect to time. 141

Figures 5.29a-c Experimental data (markers) and computational outputs (lines) of intracellular UDP-GalNAc for the control, High G and Low G culture with respect to time. 141

Figures 5.30a-c Experimental data (markers) and computational outputs (lines) of intracellular CMP-Neu5Ac for the control, High G and Low G culture with respect to time. 142

Figure 6.1 Viable cell density with respect to culture time 150

Figure 6.2 Dead cell density with respect to culture time 150

Figure 6.3 Integral viable cell concentration (IVCC). 150

Figure 6.4 Antibody titer with respect to cell culture tim 151

Figure 6.5 Final day Antibody titer for all experimental conditions. 151

Figure 6.6 Specific mAb productivity in the post feeding interval from day 4 to day 8 151

Figure 6.7 Specific mAb productivity in the post feeding interval from day 4 the respective final days of culture 151

Figure 6.8 Extracellular uridine with respect to culture time. 152

Figure 6.9 Extracellular galactose for control, 10G5U, 10G20U and 10G conditions with respect to culture time 153

Figure 6.10 Extracellular galactoe for the 50G5U condition with respect to culture time 153

Figure 6.11 Extracellular glucose for all conditions with respect to culture time 154

Figure 6.12 Extracellular lactate for all conditions with respect to culture time 154

Figure 6.13 Extracellular glutamate for all conditions with respect to culture time 155

Figure 6.14 Extracellular glutamine for all conditions with respect to culture time 155

Figure 6.15 Extracellular ammonia for all conditions with respect to culture time 155

Figure 6.16 Intracellular galactose for all conditions with respect to culture time 157

Figure 6.17 Intracellular glucose for the control, 50G5U and 10G with respect to culture time. 157

Figure 6.18 Intracellular glucose for the 10G5U and 10G20U with respect to culture time 157

Figure 6.19 Intracellular uridine for all conditions with respect to culture time. 158

Figure 6.20 Intracellular UTP for all conditions with respect to culture time 159

Figure 6.21 Intracellular CTP for all conditions with respect to culture time 159

Figure 6.22 Intracellular ATP for all conditions with respect to culture time 160

Figure 6.23 Intracellular ADP for all conditions with respect to culture time. 160

Figure 6.24 Intracellular uridine AMP for all conditions with respect to culture time. 160

Figure 6.25 Intracellular GTP for all conditions with respect to culture time 161

Figure 6.26 Intracellular UDP-Gal for all conditions with respect to culture time.....163

Figure 6.27 Intracellular UDP-Glc for all conditions with respect to culture time.....163

Figure 6.28 Intracellular UDP-GlcNAc for all conditions with respect to culture time.....164

Figure 6.29 Intracellular UDP-GalNAc for all conditions with respect to culture time.....164

Figure 6.30 Intracellular CMP-Neu5Ac for all conditions with respect to culture time.....165

Figure 6.31 Intracellular GDP-Fuc for all conditions with respect to culture time.....166

Figure 6.32 Intracellular GDP-Man for all conditions with respect to culture time.....166

Figure 6.33 Distribution of glycan structures on day 7 of culture for all conditions 167

Figure 6.34 Distribution of glycan structures on final day of culture for all conditions.....168

Figure 6.35 Average number of galactose molecules per product glycan structure for all conditions for culture days 7, 9, 11 and 12. 169

Figure 6.36 Normalised galactosylation per product glycan for all conditions for each respective final culture day 169

Figure 7.1 Schematic of the model framework depicting the interaction of the cell culture dynamics model with the remaining parts of the framework.....177

Figure 7.2 a schematic of the nucleotide model and its dependence within the mathematical model platform.....181

Figure 7.3 A semi structured reaction network of the de novo purine synthesis. Reaction steps 182

Figure 7.4 simplified reaction network of the de novo pyrimidine synthesis network. The inhibition mechanisms are indicated by dashed lines.....183

Figure 7.5 a schematic of the NSD model and its dependence within the mathematical model platform.....184

Figure 7.6 The reaction network of the de novo nucleotide sugar donor synthesis pathway 186

Figure 7.7 a schematic of the glycan model and its dependence within the mathematical model platform.....187

Figure 7.8a-e Experimental data (markers) and computational outputs (lines) of viable cell density for all culture conditions with respect to time. 189

Figures 7.9a-e Experimental data (markers) and computational outputs (lines) of dead cell for all culture conditions with respect to time.....191

Figures 7.10a-e Experimental data (markers) and computational outputs (lines) of antibody titer for all culture conditions with respect to time. 192

Figures 7.11a-d Experimental data (markers) and computational outputs (lines) of extracellular glucose for all culture conditions with respect to time. 193

Figures 7.12a-d Experimental data (markers) and computational outputs (lines) of extracellular for all galactose fed culture conditions 10G5U, 50G5U, 10G20U and 10G with respect to time 194

Figures 7.13a-e Experimental data (markers) and computational outputs (lines) of extracellular lactate for all culture conditions with respect to time. 195

Figures 7.14a-e Experimental data (markers) and computational outputs (lines) of extracellular glutamate for all culture conditions with respect to time. 196

Figures 7.15a-e Experimental data (markers) and computational outputs (lines) of extracellular glutamine for all culture conditions with respect to time. 197

Figures 7.16a-e Experimental data (markers) and computational outputs (lines) of extracellular ammonia for all culture conditions culture with respect to time. 198

Figures 7.17a-c Experimental data (markers) and computational outputs (lines) of extracellular uridine for the uridine fed culture conditions 10G5U, 50G5U and 10G20U with respect to time 199

Figures 7.18a-e Experimental data (markers) and computational outputs (lines) of extracellular asparagine for all culture conditions with respect to time. 200

Figures 7.19a-e Experimental data (markers) and computational outputs (lines) of intracellular ATP for all culture conditions with respect to time. 202

Figures 7.20a-e Experimental data (markers) and computational outputs (lines) of intracellular ADP for all culture conditions with respect to time. 203

Figures 7.21a-e Experimental data (markers) and computational outputs (lines) of intracellular AMP for all culture conditions with respect to time. 204

Figures 7.22a-e Experimental data (markers) and computational outputs (lines) of intracellular GTP for all culture conditions with respect to time 205

Figures 7.23a-e e Experimental data (markers) and computational outputs (lines) of intracellular UTP for all culture conditions with respect to time. 206

Figures 7.24a-e Experimental data (markers) and computational outputs (lines) of intracellular CTP for all culture conditions with respect to time. 207

Figures 7.25a-e Experimental data (markers) and computational outputs (lines) of intracellular UDP-Gal for all culture conditions with respect to time. 209

Figures 7.26a-e Experimental data (markers) and computational outputs (lines) of intracellular UDP-Glc for all culture conditions with respect to time. 210

Figures 7.27a-e Experimental data (markers) and computational outputs (lines) of intracellular UDP-GalNAc for all culture conditions with respect to time. 211

Figures 7.28a-e Experimental data (markers) and computational outputs (lines) of intracellular UDP-GlcNAc for all culture conditions with respect to time. 212

Figures 7.29a-e Experimental data (markers) and computational outputs (lines) of intracellular GDP-Fuc for all culture conditions with respect to time. 213

Figures 7.30a-e Experimental data (markers) and computational outputs (lines) of intracellular GDP-Man for all culture conditions with respect to time. 214

Figures 7.31a-e Experimental data (markers) and computational outputs (lines) of intracellular CMP-Neu5Ac for all culture conditions with respect to time. 215

Figures 7.32a-e Experimental data (markers) and computational outputs (lines) of G1F glycan abundance with respect to culture time. 217

Figures 7.33a-e Experimental data (markers) and computational outputs (lines) of G2F glycan abundance with respect to culture time. 218

Figures 7.34a-e Experimental data (markers) and computational outputs (lines) of G2 glycan abundance with respect to culture time 219

Figures 7.35a-e Experimental data (markers) and computational outputs (lines) of G0 glycan abundance with respect to culture time 221

Figures 7.36a-e Experimental data (markers) and computational outputs (lines) of G0F glycan abundance with respect to culture time. 222

Figures 7.37a-e Experimental data (markers) and computational outputs (lines) of Man5 glycan abundance. 223

Figure 7.38 optimised galactose feed additions, in total culture volume 225

Figure 7.39 optimised uridine feed additions, in total culture volume 225

Figure 7.40 Comparison of galactosylation, as defined by expression 7.15 225

Figure 7.41 viable cell density as predicted for the optimal feed condition. 226

Figure 7.42 intracellular UDP-Gal concentrations as predicted for the optimal feed condition. 226

Figure 8.1 A graphic representation of the thesis chronology 231

List of Tables

Table 1.1 Table of glycosyltransferases (Krambeck and Betenbaugh, 2005)....8
Table 3.1 Frequency of sugar species occurrence in glycans of mature human B-cells. 75
Table 3.2 Non-nucleotide sugar species and their intracellular concentrations. 80
Table 5.1 Frequency of sugar species occurrence in glycans of CHO cells (Stanley, 2010). ..126
Table 6.1 Relative increase of UTP with respect to the control on day 5 of the culture....159
Table 6.2 Relative increase of CTP with respect to the control on day 5 of the culture 159
Table A.1 Summary of all reaction mechanisms of the NSD model....266
Table A.2 Numerical GSA outputs for UDP-GlcNAc and UDP-GalNAc....268
Table A.3 Numerical GSA outputs for GDP-Fuc and GDP-Man....269
Table A.4 Numerical GSA outputs for UDP-Gal and UDP-Glc....270
Table A.5 Numerical GSA outputs for CMP-Neu5Ac. 271
Table A.6 Estimated NSD model parameter values in chapter 3....272
Table A.7 Estimated cell dynamics model parameter values in chapter 3 273
Table A.8 Estimated N-linked glycan model parameters in chapter 3....273
Table A.9 Estimated nucleotide model parameter values in chapter 3....274
Table A,10 Estimated parameters of the cell culture dynamics model in chapter 5....275
Table A.11 Estimated parameters of the nucleotide synthesis model in chapter 5 276
Table 12 Estimated parameters of the NSD synthesis model in chapter 5 277
Table A.13 Estimated parameters of the cell culture dynamics model in chapter 7....278
Table A.14 Estimated parameters of the nucleotide synthesis model in chapter 7 279
Table A.15 Estimated parameters of the NSD synthesis model in chapter 7 280
Table A.16 Estimated parameters of the glycan model in chapter 7 281

Introduction

A biopharmaceutical, or biologic, is defined as a medicinal drug produced, extracted or semi-synthesised using biological means. It can be a macromolecule, cellular component or cells used as a pharmaceutical. The largest group of biopharmaceuticals currently approved by the European Medical Agency (EMA) are products derived from biological systems using recombinant DNA (rDNA). These products of rDNA technology application are made up of glycoproteins, proteins and recombinant vaccines, where glycoproteins present the largest group with 67 out of 126 EMA licensed drugs (figure I.1). Glycoproteins are complex entities comprising a protein as well as an oligosaccharide component, more commonly referred to as a glycan. Biopharmaceuticals and especially glycoproteins represent a growing sector of the pharmaceutical market and consequently of the pharmaceutical industry. The approval of the first rDNA product humulin, a human insulin product, in 1982 was a medical milestone that displaced animal derived insulin with a product that was indistinguishable from pancreatic human insulin (Junod, 2007). The result was a safer product of known and controlled efficacy, which paved the path for the ongoing revolution of biopharmaceuticals within the medical industry.

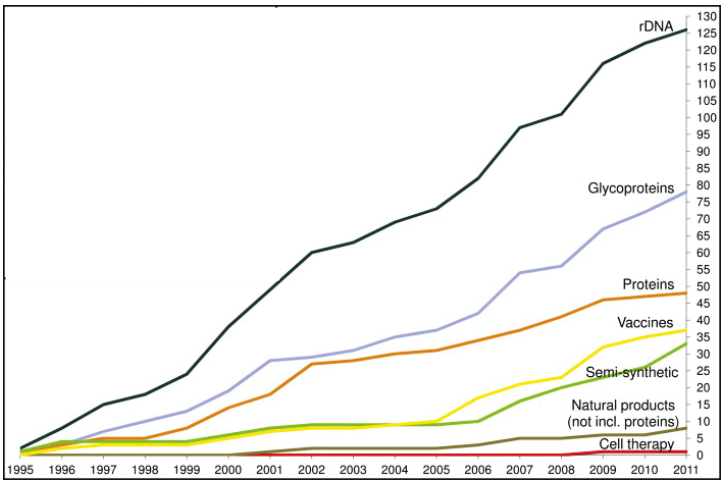


Figure I.1 The graph was modified from Kyriakopoulos and Kontoravdi. Depicted is the cumulative number of EMA approved biologically-derived drug, where the recombinant DNA technology (rDNA) drug products are the summation of 67 glycoprotein drugs, 46 protein drugs and 13 recombinant vaccine drugs. (Kyriakopoulos and Kontoravdi, 2013).

The growth of the market for biotech products has steadily outperformed the growth of the total pharmaceuticals market over the past years, in the United States (Gatyas, 2011, EvaluatePharma, 2014). Monoclonal antibodies (mAbs), which are also glycoproteins, are the highest selling biologics class and an upward trend of sales figures is still observed (Aggarwal, 2011). As opposed to small drug molecules, biopharmaceuticals are heterogeneous and complex macromolecules of high-molecular weight. A well-defined glycoprotein product may have consistent protein backbones but still a multitude of glycan structures, collectively referred to as the glycoform, with a distribution of more than a hundred detectable isoforms (Balaquer and Neususs, 2006). The glycoform can have a strong impact on the product efficacy, safety, half-life and specificity of a biotherapeutic (del Val et al., 2010). Fucose-deficient glycan structures, for example, are known to increase target receptor affinity resulting in up to 50-fold increased antibody-dependent cellular toxicity (ADCC), a desired mode of action of many biotherapeutics (Shields et al., 2002). Consequently, the product glycoform and the underlying process of glycosylation play an important role in the production of biotherapeutics.

On a biological level the process of glycosylation is a post-translational modification taking place in eukaryotic cells and to a lesser and different extent also in prokaryotic cells (Dell et al., 2010). The resulting glycan structures and their collective profile, i.e. the glycoform, are not encoded and determined by the host cell line but instead by the location at which the covalent bond with the polypeptide is formed as well as the cells' environment. The theoretical number of different glycan structures in humans is above 20,000 although, in practice the number of structures of significant abundance is much smaller in biotherapeutics (Krambeck and Betenbaugh, 2005). The number of theoretical glycan structures of mAbs in particular is smaller due to spatial constraints in the antibody Fc region with fewer than 10 different glycan structures of significant abundance found in many mAb therapeutics (del Val et al., 2011). In this context mAbs are not only an industrially relevant glycoprotein but also offer a good platform for first efforts of steering and control of the glycoform.

A number of non-DNA encoded posttranslational modifications (PTMs), including acetylation, disulfide bond formation, glycosylation, and phosphorylation amongst others,

are found in biotherapeutics. However, of these glycosylation represents the most widespread and most complex modification found in biopharmaceutical and natural proteins (Walsh and Jefferis, 2006). N-linked glycosylation occurs in 40% of all approved therapeutic proteins, including eight of the top ten selling biologics in 2010 (EvaluatePharma, 2011b, Walsh, 2010). From the above discussion it becomes clear that glycosylation becomes an important product characteristic for many biotherapeutics that must be controlled in order to maintain safety and efficacy of products. Changes to the manufacturing process can have a large impact on glycosylation and hence, the product quality attributes. This means that any changes made at any stage of the manufacturing process can only get introduced if the product is not altered and such must be demonstrated by the manufacturer in order to gain FDA approval (Schiestl et al., 2011).

The quality by design (QbD) paradigm, a conceptual framework in which end-product quality is built into the design process, presents a generic manufacturing approach that promises a streamlined approval process of biopharmaceuticals (ICH, 2009, del Val et al., 2010, Rathore and Winkle, 2009). The QbD process is information-driven, where all available knowledge of the drug product is used to define an acceptable range of manufacturing conditions in order to ensure product safety and efficacy. In this context manufacturers are required to identify the product CQAs and the process inputs affecting these to arrive at the quality target product profile (QTPP). An appropriate manufacturing process and process control strategy is then selected to achieve the QTPP and maintain these within their predefined limits. While the QbD paradigm has been widely adopted in various manufacturing industries, the complexity of the biopharmaceutical manufacturing process provides difficulties in the implementation of the paradigm. As a result most biotherapeutic manufacturing takes places under the traditional retroactive Quality by Testing approach. QbD places emphasis on upfront experimentation and the Design of Experiment (DoE) in process design to understand the effect of possible multidimensional interactions of parameters on the final biotherapeutic quality (Rathore et al., 2007). The upfront experimentation under the QbD paradigm provides scientific understanding of the underlying processes in product manufacture and seeks to characters the parameters affecting the product CQAs to establish a design space and control strategy.

In order to capture the impact of processing and unit operations in a biomanufacturing facility on critical quality attributes such as glycosylation, a modelling framework is key (Inc, 2011). In this context DoE can produce data to aid the development of mathematical models that can be used to guide and improve process development. A model framework can provide a cost effective and fast *in silico* way of process development within the QbD paradigm, which can prove to be a beneficial tool for both manufacturers and regulatory bodies. In the context of glycosylation an *in silico* model with the ability to steer and guide the glycoform could provide a valuable platform for process development in glycoprotein manufacture, production of safe and comparable biosimilars and guide the development of bio-betters. In a growing biopharmaceutical market, with many regulatory difficulties arising from product heterogeneity, an effective computational tool that is able to steer and control the glycoform would reduce development and production costs. However, ultimately the successful model would provide better, safer and more affordable healthcare to patients. The work presented in this thesis seeks to address this issue by means of a modelling platform that bridges the gap from the extracellular environment via the cell's metabolites to the mAb product's glycoform.

The literature review of this thesis starts by outlining the current knowledge of the glycosylation process; its underlying process, the role it plays in biology, the factors impacting it and its role in the biopharmaceutical industry. Emphasis is placed on metabolic means of controlling the glycosylation process and past approaches of targeted manipulation of the glycoform with an in depth review of feeding strategies seeking to impact the availability of nucleotide sugar donors, the co-substrates of the glycosylation process. The effects and roles of various glycan structures *in vivo* with respect to biotherapeutics are discussed and highlighted in glycoproteins of industrial relevance. The second part of the literature review under chapter 1.7 presents the current achievements within the dynamic field of computational systems biology. Strategies towards the development of biological models are highlighted and the differences in model structures discussed. Particularly important with respect to this work are the developments in the modelling of metabolic systems and the glycosylation process. The outcome of the literature review is to highlight the current knowledge of glycosylation and relevant computational efforts within systems biology with the aim of demonstrating the place and value of this

thesis within this field of research. Chapter 2 discusses the materials and method used in the experimental part of the work. The development of the model framework is shown in chapter 3. The first proof-of-concept modular framework is based on previously obtained murine hybridoma cell data from a batch process as well as literature data for the *in silico* reconstruction of the nucleotide sugar donor synthesis metabolic network. The subsequent experimental work of chapter 4 aims to perturb the synthesis of the nucleotide sugar donor species GDP-Fuc and GDP-Man in a fed-batch system utilising Chinese Hamster Ovary cells (CHO). Cell cultures were supplemented with guanosine and mannose and the effects observed on cell culture dynamics, the intracellular metabolites and the mAb glycoform are used as a stepping stone towards the modelling efforts of chapter 5. Here, the modelling platform of chapter 3 is developed further and translated to a CHO system, fed-batch process operation and the platform is enriched based on experimental observations. Subsequent experimental work presented in chapter 6 uses additions of manganese, galactose and uridine to perturb the nucleotide sugar donor concentrations further with the aim of maximising antibody galactosylation. The rich data set gives insights into the limits of a feasible operating space with respect to cell proliferation and product quality, which is used to train the modelling platform further in chapter 7. The calibrated model is used to find an optimal feeding strategy and thus, create a computationally optimised feeding strategy for maximal product galactosylation. The overall outcomes of the work presented here are summarised and discussed in chapter 8 as well as limitations and scope for further improvement deliberated.

Chapter 1

Literature Review

1.1. The Glycosylation Process

To gain understanding of the complexity and the various parameters affecting the glycosylation process, this literature review aims at firstly discussing the underlying process of glycosylation. Glycosylation is the most complex of post-translational modifications (PTM) and must by definition occur during or after protein biosynthesis. Glycans are split into groups of O-linked and N-linked glycans, referring to the nature of the covalent bond formed with the protein backbone. O-linked glycosylation is a PTM where an N-acetylglucosamine (GlcNAc) monosaccharide residue is attached to a serine or threonine amino acid. While N-linked glycosylation is induced by specific tri-peptide sequences no specific amino acid consensus sequence has been identified to induce O-linked glycosylation. Further glycosyltransferase catalysed reaction steps extend the glycan moiety further and give rise to large numbers of complex structures. Unlike its N-linked counterpart, the O-linked glycosylation is thought to be initiated in the Golgi apparatus by direct enzymatic attachment of a GlcNAc residue to the fully folded protein (Van den Steen et al., 1998). While no sequence has been identified to induce O-linked glycan formation, regions of high serine, threonine and proline proportions have shown higher occurrence of this PTM (Van den Steen et al., 1998). O-linked glycosylation currently receives little attention in industry as few relevant serum proteins exhibit this particular PTM. EPO is an exception to this and is discussed further in chapter 1.5.2. Apart from IgA1 (Allen et al., 1995), which is currently of little or no relevance to biopharmaceuticals, most classes of mAbs such as IgG are not known to be O-glycosylated (Hirayama et al., 1998, Leibiger et al., 1999). Other than the example of the industrially relevant glycoprotein EPO with an O-

linked glycan moiety (shown and discussed in chapter 1.5.3), this review will not focus further on this glycan type due to the emphasis on pharmaceutically relevant N-linked glycoproteins.

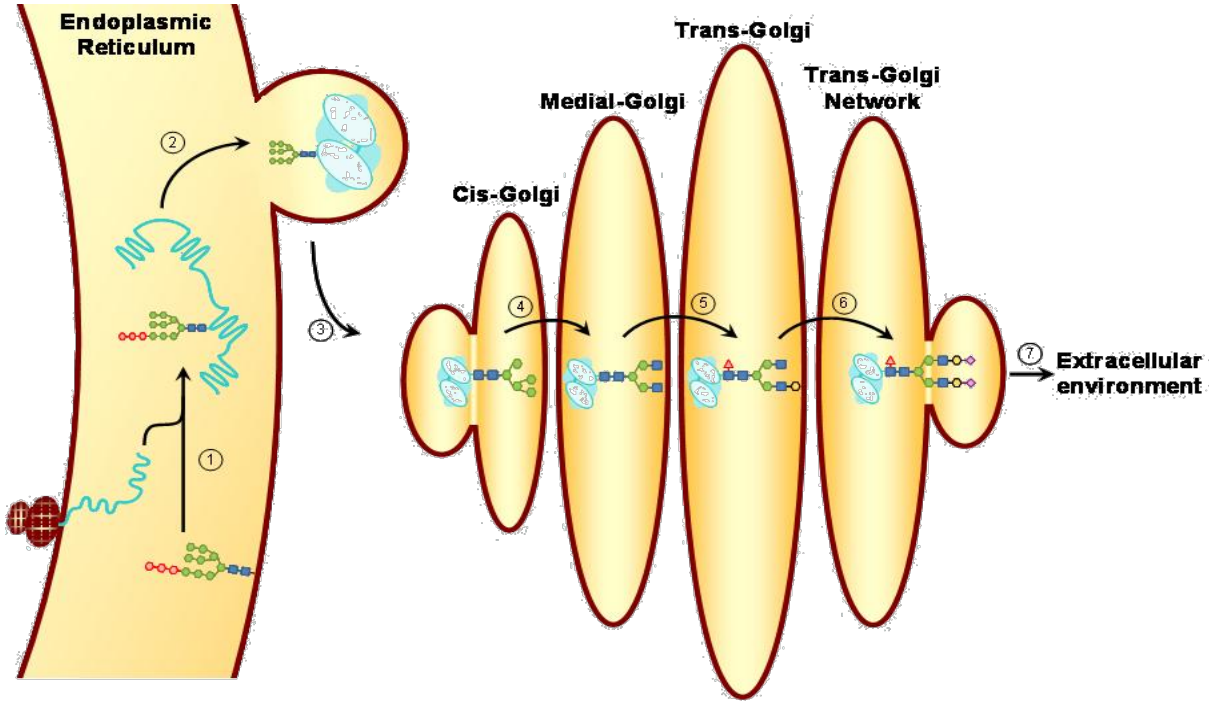


Figure 1.1 Schematic of the N-linked glycosylation assembly. Steps 1 & 2 represent the attachment of the lipid bound oligosaccharide precursor to the protein backbone. Step 3 represents the transport of the glycoprotein to the Golgi Apparatus where a series of enzymatic trimming and elongation steps (steps 4-6) take place before the glycoprotein is secreted into the extracellular environment as shown in step 7 (del Val et al., 2010).

N-linked glycans have received a lot of attention in an industrial context due to their occurrence in many industrially relevant biopharmaceuticals such as antibodies, hormones or growth factors. Potential N-linked glycosylation sites can be identified based on their specific tripeptide sequence of Asn-X-Thr or Asn-X-Ser, where X is any amino acid other than proline. A statistical analysis by Petrescu et al. has revealed that 65% of all reported potential glycan sites were occupied. It was further revealed that a split in tripeptide sequence of 70% and 30% of Asn-X-Thr and Asn-X-Ser was observed, respectively (Petrescu et al., 2004). The synthesis of the lipid linked oligosaccharide precursor structure and its attachment to the protein backbone occurs in the endoplasmic reticulum (ER) of the cell as shown in figure 1.1. The oligosaccharide precursor is synthesised while attached to a membrane bound lipid dolichol phosphate, which is integrated in the ER membrane.

Initially two GlcNAc molecules are attached to the dolichol phosphate on the outer ER membrane facing the cell cytoplasm and are translocated towards the inner ER lumen upon the addition of five mannose molecules. In the ER lumen further mannose and glucose molecules are added to give rise to a homogeneous structure containing 2 molecules of GlcNAc, 9 of mannose and 3 of glucose (figure 1.2 first structure). This precursor structure is then attached co-translationally to the protein backbone by means of an N-glycosidic bond to an asparagine residue. Due to the co-translational attachment, the secondary and tertiary structure around a glycan site have little effect on site occupancy however, a statistical analysis can give an insight into the N-glycan sites that have been selected and retained during evolution (Petrescu et al., 2004). The three glucose molecules are then removed stepwise by a number of enzymatic reactions, which is described in greater detail in section 1.2 of this review.

Table 1.1 Selection of relevant enzymes found in the Golgi apparatus. It has to be noted that the presence of a specific glycosyltransferase is cell line dependent (Krambeck and Betenbaugh, 2005).

Abbreviations	EC No.	Name
ManI	3.2.1.113	Mannosyl-oligosaccharide 1,2-α-mannosidase
ManII	3.2.1.114	Mannosyl-oligosaccharide 1,3-1,6-α-mannosidase
FucT	2.4.1.68	Glycoprotein 6-α-L-fucosyltransferase
GnTI	2.4.1.101	α-1,3-mannosyl-glycoprotein 2-β-*N*-acetylglucosaminyltransferase
GnTII	2.4.1.143	α-1,6-mannosyl-glycoprotein 2-β-*N*-acetylglucosaminyltransferase
GnTIII	2.4.1.144	α-1,4-mannosyl-glycoprotein 4-β-*N*-acetylglucosaminyltransferase
GnTIV	2.4.1.145	α-1,3-mannosyl-glycoprotein 4-β-*N*-acetylglucosaminyltransferase
GnTV	2.4.1.155	α-1,6-mannosyl-glycoprotein 6-β-*N*-acetylglucosaminyltransferase
GnTE	2.4.1.149	*N*-acetyllactosaminide β-1,3-*N*-acetylglucosaminyltransferase
GalT	2.4.1.38	β-*N*-acetylglucosaminylglycopeptide β-1,4-galactosyltransferase
SiaT	2.4.99.6	*N*-acetyllactosaminide α-2,3-sialyltransferase

As the glycoprotein leaves the ER it is transported to the Golgi apparatus, where the glycan is sequentially trimmed by the enzymes ManI (EC 3.2.1.113) to form an oligosaccharide formed of 5 Man and 3 GlcNAc monosaccharides. After completion of the sequential modification of the glycan structures, further processing by the highly specialised glycosyltransferases takes place. A list of these enzymes, bound to the membrane of the Golgi is shown in table 1.1. This list has been taken from the computational work of Krambeck and Bettenbaugh and only shows a limited overview of the highly diverse glycosyltransfereases enzyme family, where the enzymes themselves vary depending on the

cell line and organism (Krambeck and Betenbaugh, 2005). The glycosyltransferases elongate the core glycan through attachment of GlcNAc, galactose (Gal), fucose (Fuc) and different sialic acids. The conformation of the arising bond is specific to the glycosyltransferase in question and is also highly specific to its substrate resulting in a multitude of configurations. For example, the glucosaminetransferase GnTIII will only add a GlcNAc to the central Man of the glycan structure in a 1-β-4 bond conformation after which no further addition of GlcNAc to the central Man oligosaccharides is possible (Ihara et al., 2002). An example of this is shown in figure 1.2 (third structure). The addition of this bisecting GlcNAc fixes the number of branches of the glycan, i.e. its antennarity. The glycan antennarity is determined by the number of GlcNAc saccharides bound to the Man core saccharides, excluding any bisecting GlcNAc moieties, and allows further elongation of the glycan. Another example of a glycosyltransferase is SiaT, which can catalyse the 2-α-3 addition of sialic acid to a galactose molecule, however only in the case where galactose itself is previously linked by 1-β-4 bond conformation to the remaining moiety (Jones et al., 2012). The sialylation step catalysed by the SiaT enzyme terminates the elongation process. However, this is only restricted to the sialylated antenna and enzymatic processing of the other branches of the glycan is still possible. Depending on the host cell line and spatial configuration, SiaT will compete with a number of glycosyltransferases that may either lead to different bond

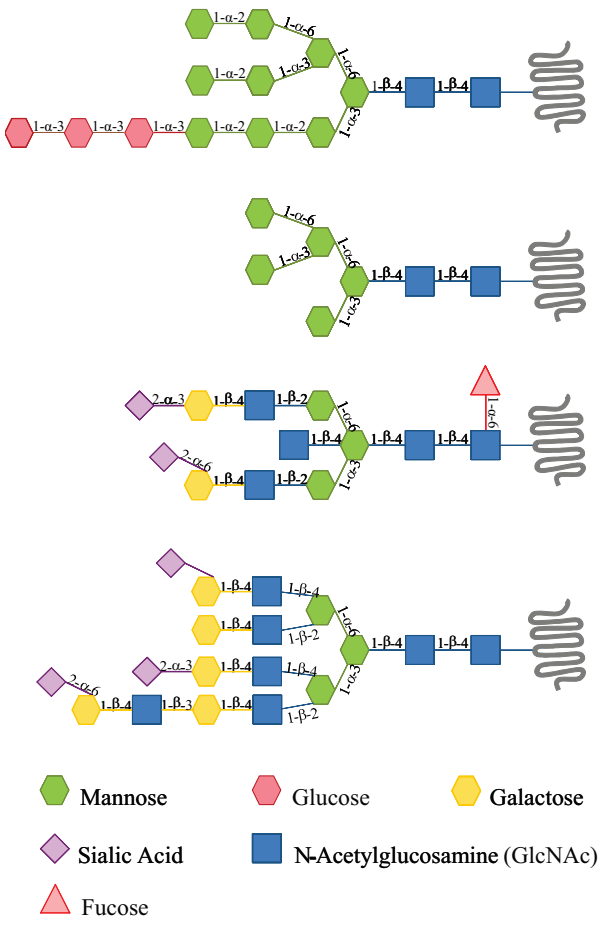


Figure 1.2 Examples of glycan structure diversity. The homogeneous glycan precursor with three glucose molecules (first). An underprocessed high mannose structure (second). A fully sialylated bi-antennary structure with core fucosylation and a bi-secting GlcNAc (third). Both the 2-α-3 and 2-α-6 covalent bond configuration of sialic acid attachement are shown. Lastly, a tetra-antennary structure with a lactosamine repeat and terminal sialiation and a lactosamine repeat on the lowest branch (fourth).

conformation, repeating lactosamine (figure 1.2 bottom branch of the fourth structure) units or a terminating galactose.

The above illustrates the large number of potential parallel reaction steps and the complexity of the reaction network. The branching of the reaction steps in the glycosylation process leads to a multitude of terminal structures in addition to a larger number of intermediate products that are readily secreted from the Golgi. Based on the enzymes shown in Table 1 only, and known constraints of enzyme activity, Krambeck and Betenbaugh (Krambeck and Betenbaugh, 2005) predicted the number of possible glycan structures as 7,565 structurally and conformationally different oligosaccharides. This has been extended with respect to human glycosyltransferases and enzyme-substrate interaction rules to include over 20,000 potential glycan structures in subsequent work (Krambeck et al., 2009). Classification of glycan moieties can occur according to the degree of processing into high mannose, hybrid and complex structures. Hybrid refers to partially under-processed structures, where remaining mannose molecules prevent the extension of the structure beyond a single additional branch (example given in figure 1.2 second structure). A number of other characteristics are also used for glycan classification, such as antennarity, sialylation and fucosylation amongst others.

The above reactions take place in the Golgi apparatus, where the mode of Golgi transport and thus, the transport of glycoproteins, is still under debate. Work carried out by Matsuura-Tokita et al. (Matsuura-Tokita et al., 2006) as well as by Losev et al. (Losev et al., 2006) seems to point towards a cisternal maturation model rather than a vesicular transport mode. Under the cisternal maturation hypothesis a single compartment evolves and matures with time and thus, passes through all the stages of the Golgi. The vesicular transport mode on the other hand hypothesises a maturation process, where glycoproteins are transported by vesicles between Golgi sacs until maturation is reached. Regardless of the Golgi model, literature values for glycoprotein residence time vary widely and values of 5 to 15 minutes, 10 minutes and 40 minutes have been reported, during which the protein is exposed to the full panel of modifying enzymes (Helenius and Aebi, 2001, Karrenbauer et al., 1990, Hirschberg et al., 1998). The compartments or stages of the Golgi are named in the order in which glycoproteins pass through the organelle, as cis-Golgi, medial-Golgi, trans-Golgi and

trans-Golgi network (TGN). Snapshot concentrations of a number of glycosyltransferases at various stages of the Golgi have been taken by Rabouille et al. (Rabouille et al., 1995) who have shown enzyme concentrations to vary significantly and hence, glycosylation reaction steps can be assigned to specific locations of the Golgi apparatus. The concentration of ManII, catalysing trimming reactions of Man molecules from the glycan moiety, was shown to be highest in the medial-Golgi and tail off towards the TGN. GalT and SiaT, responsible for antennae elongation and termination, were distributed towards the later stages of the apparatus i.e. the trans-Golgi and TGN. The overlapping distribution of the enzymes and associated reaction steps shows the importance of the transport of newly folded glycoproteins through this organelle in order to achieve controlled glycosylation.

The described enzymatic reactions need a glycan acceptor as well as a specific nucleotide sugar donor (NSD) co-substrate. Nucleotide sugars are activated monosaccharides and must be transported from the cytoplasm across the Golgi membrane in to the Golgi lumen. The transporters in question are complex membrane antiports exchanging nucleotide sugars for spent nucleotides. Studies on NSD transporters have shown a closely co-localised distribution to corresponding glycosyltransferases such as the CMP-sialic acid NSD transporter and the corresponding enzyme SiaT (Ishida et al., 1999, Yoshioka et al., 1997, Zhao et al., 2006). The results suggest a distributed transport protein that will allow for high transport of enzyme NSD substrates according to substrate consuming enzyme distribution. It has to be noted that all of the above enzymes as well as the antiports are membrane bound proteins although exceptions of soluble glycosyltransferases have been proven to exist in human cells (Cho and Cummings, 1997).

1.2. The Role of Glycosylation in Biology

In 2001, when the human genome was fully sequenced, it was found that it contains fewer genes than expected. However, it was speculated that this was compensated for by the diversity found at the level of protein architecture, structure, transcription as well as posttranslational modifications of which glycosylation is the most complex (Venter et al., 2001). Glycan moieties have a very diverse number of roles in biological systems and as such

only a relevant few can be discussed in the context of this review. The order of the topics discussed is arranged in accordance to the stage in glycan synthesis and processing in a cell. Starting with the co-translational attachment of glycan structures it was suggested by Petrescu et al. (Petrescu et al., 2004) that glycan structures act as nucleation sites for the folding of remote aromatic parts in an amino acid sequence, which has been supported by the finding that glycans promote folding based on glycan and protein hydrophobic interactions (Nishimura et al., 1998, Jitsuhara et al., 2002). An additional co-translational function of glycans has been suggested to be that of indicating landmarks for changes in secondary protein structure and thus increase folding efficiency (Petrescu et al., 2004). Through statistical analysis it has also been suggested that glycans have a marked preference for hydrophobic amino acid sequences and thus, covering and stabilising hydrophobic patches on protein surfaces (Toyoda et al., 2002). This may also explain why 44.2% of all glycan structures are found in convex or flat regions of a protein surface (Petrescu et al., 2004). Although glycans play an important role in local as well as global folding of proteins, it has to be pointed out that they are usually not essential in order to maintain the overall structure once folded (Helenius, 1994, Imperiali and O'Connor, 1999, Olden et al., 1982), as illustrated by IFN-β (see section 3.2.1.).

The oligosaccharide precursor with its three glucose units enables the glycoprotein to enter the Calnexin-Calreticulin cycle upon enzymatic removal of one glucose saccharide each by Glucosidase I and Glucosidase II. If the glycosylation site is within the first 50 amino acids the interaction with calnexin and calreticulin may start co-translationally (Molinari and Helenius, 2000). While calnexin is membrane bound and calreticulin is soluble both molecules are lectins found within the ER that assist the folding process of glycoproteins. The vital role of the N-linked glycan moiety in this particular cycle is that of a quality assurance marker. The lectins interact with the monoglucosylated glycan moiety, which can last from a few minutes to several hours, depending on the folding rate. During this interaction the glycoprotein is exposed to a further protein ERp57, which forms a complex with calnexin and calreticulin. ERp57 is a co-factor that provides assistance for the formation of disulfide bonds during the folding process (Huppa and Ploegh, 1998). As glycoproteins enter the Calnexin-Calreticulin cycle they also become protected against premature degradation during the folding process and although the rate of folding is generally

decreased through entering the cycle, the efficiency becomes much improved. To release the glycoprotein from calnexin and calreticulin the third and single remaining glucose of the glycan moiety is removed by Glucosidase II. The folded protein is now able to leave the ER and enter the Golgi unless detected by a glucosyltransferase (GT) that detects unfolded proteins and reglucosylates the N-linked glycan. The GT acts as a folding sensor in the cycle and ensures that glycoproteins re-enter the Calnexin-Calreticulin cycle until folded, oligomerised or degraded (Helenius and Aebi, 2004). This regulatory mechanism is only limited to the ER, while the Golgi has no system for controlling the fidelity of its biosynthetic processes, which means that defective glycan moieties are readily exported (Elbein, 1991, Stanley, 1984).

Once exported from the ER, glycans can take up a very wide range of functions depending on the glycoprotein location and the extent of glycan processing in the Golgi. An example where the function of a glycoprotein depends very heavily on its glycan moieties are LAMP-1 and LAMP-2, which are membrane proteins with up to 20 N-linked glycans each (Cha et al., 1990, Granger et al., 1990). Through this extremely high number of glycan moieties a close to continuous carbohydrate coat over the luminal surface of the lysosomal membrane is formed and thus, protects the LAMP proteins against proteolytic degradation. Another major function of protein-linked glycans is to provide additional recognition epitopes for protein receptors (Drickamer and Taylor, 1993, Lis and Sharon, 1998). The mere presence of the glycans at specific locations of the protein can alter physiological behavior by changing solubility or stability, protection from proteolysis or aggregation or masking any antigenic sites (Dwek, 1996, Rudd et al., 1999, Wormald and Dwek, 1999). Examples of these will be given and discussed in chapter 1.5 as well as other more specific effector functions of glycan moieties in biotherapeutics.

1.3. Biopharmaceuticals in Industry

Today biopharmaceuticals, including bioengineered vaccines as well as recombinant proteins, constitute 22% of the pharmaceutical market with a total sales volume of $152bn as of 2013 (EvaluatePharma, 2014). The market share of biotech products within the top 100 selling pharmaceutical products in the word is already 45% as of 2013 but is expected to increase further to 52% by 2020. The growth of the market for biotech products has steadily outperformed the growth of the total pharmaceuticals market over the past years, in the United States (Gatyas, 2011, EvaluatePharma, 2014). Monoclonal antibodies (mAbs), which are also glycoproteins, are the highest selling biologics class and an upward trend of sales figures is still observed (Aggarwal, 2011). The high sales figures of the pharmaceuticals industry are threatened by the patent expirations of many blockbuster drugs between 2014 and 2020, with a total $259bn of sales at risk, many of which are biopharmaceuticals. The "patent cliff" is expected to lead to plummeting in sales of original biotechnology products due to replacement by generic products (Harrison, 2011). One commonly pursued strategy to extend the product life cycle and maintain income is through reformulation and to improve product properties.

With the patent cliff comes opportunity in the form of biosimilars or bio-betters. While the first describes generic products that come off patent protection, the latter describes engineered off-patent drugs with enhanced drug efficacy, half-life or other product properties. All of the former represent product characteristics that are influenced by critical quality attributes (cQAs). Critical quality attributes are defined by the International Conference of Harmonisation as a "physical, chemical, biological or microbiological property or characteristic that should be within an appropriate limit, range or distribution to ensure the desired product quality" (Harmonisation, 2009). For example take an antibody with a desired bioactivity by means of binding to the FcγRIII receptor leading to the desired mode of action through antibody-dependent cellular toxicity (ADCC). Fucose-deficient glycan structures in the antibody Fc region are known to increase receptor affinity and increase ADCC up to 50-fold (Shields et al., 2002). This means fucosylation, or the lack there

of i.e. fucose-deficiency, becomes a cQA and engineering the off-patent product accordingly leads to the development of an enhanced bio-better product.

As opposed to small drug molecules biopharmaceuticals are heterogeneous and complex macromolecules of high-molecular weight. A well-defined product may have consistent protein backbones but still a glycoform distribution of more than a hundred detectable isoforms (Balaquer and Neususs, 2006). Biosimilars are usually produced from different cell clones and under different conditions and as a consequence differences in glycosylation and other microvarations will arise (Beck et al., 2012). Even a well-defined product can show heterogeneity due to the nature of the biological production platform and the complexity of the production system can lead to batch-to-batch variation as well as to deviations from innovator products (Combe et al., 2005). Consequently, it still remains a challenge to demonstrate similarity of biosimilars to the original innovator biopharmaceuticals. The first licensed biosimilar product to reach the market was a generic erythropoietin (EPO) version, which presented a much more affordable alternative to the innovator product. However, biosimilars of EPO have shown differences in structure, stability, concentration and activity (Schellekens, 2009). The physicochemical heterogeneity presents a challenge in the substitution of innovator products for the cheaper generic versions and therefore, it has to be performed with caution as to not compromise patient safety (Brinks et al., 2011a). As a result the emergence of biosimilars presents a new challenge to regulatory authorities when assessing the resemblance of the pharmacokinetics of the innovator products and subsequent drug licensing (Schellekens, 2009). This in turns leads to softer erosions of biological products and much reduced impact of the feared patent cliff (EvaluatePharma, 2014).

Biobetters, on the other hand are not copies of innovator products and are therefore not considered generics. While they are linked to existing and licensed products, they are altered to improve various product characteristics such as efficacy, safety or manufacturing attributes. This can be achieved by means of point substitutions of amino acids, which has led to much improved *in vivo* half-life in the Fc region of therapeutic antibodies (Zalevsky et al., 2010). Other strategies have been concerned with the engineering of the glycan structures of therapeutic antibodies. While these sugar structures only make up 2-3% of the molecules

mass, they have shown to have a large impact on pharmacokinetics. A glyco-engineered version of the licensed monoclonal antibody (mAb) Trastuzumab® demonstrated higher cytotoxicity activity for cancer cells (Beck et al., 2012). Engineering of the glycoform comes with its own set of challenges with respect to product development and licensing.

1.4. Glycosylation and Post Translational Modifications in Industry

The majority of currently approved biopharmaceutical, bear some form of PTM (Walsh and Jefferis, 2006). Additionally, the current wave of "follow-on" biotech products re-emphasise the importance of PTMs, which are critical quality attributes in the production of therapeutic proteins with significant effect on product safety, efficacy and immunogenicity (Schellekens, 2004a). In a biological system there is a wide range of PTMs, which however play only a minor role or none at all in terms of most biopharmaceuticals. The most industrially relevant biological PTMs besides glycosylation are γ-carboxylation, deamidation, glycation, hydroxylation and sulfation of therapeutics (Walsh and Jefferis, 2006, Merkler, 1994). However, it is glycosylation that has the greatest effect on protein function, structure and manufacturability (Kornfeld and Kornfeld, 1985, Spellman, 1990). As a consequence this review will focus on the topic of glycosylation, only. The presence of glycan structures in biopharmaceutical is of paramount importance *in vivo* due to the resulting effects on pharmacokinetics, bioactivity, secretion, clearance, solubility, receptor recognition and antigenicity (Takeuchi et al., 1988, Narhi et al., 1991, Wasley et al., 1991, Storring, 1992). As a result it is essential for a biopharmaceutical to ensure a consistent glycosylation profile between batches (Restelli and Butler, 2002), which includes macroheterogeneity i.e. site occupancy of glycans as well as microheterogeneity i.e. the structure and conformation of glycan moieties. This is a particular problem with respect to biosimilars, as discussed below.

In order to launch a generic upon patent expiration in either the United States, Europe or Japan, the regulatory framework foresees that the drug needs to show identical

physiochemical properties and as the innovator's original drug and bioequivalence in a limited crossover clinical study in volunteers (Schellekens, 2004b). As a result of this development and licensing costs as well as development time of generics is much decreased, which allows generics to be brought onto the market at a discounted price. This in turn leads to a decrease in price for the original medicine. This route however is much more difficult to follow for biosimilars, since even the same amino acid sequence and culture conditions can lead to a biopharmaceutical that is substantially different in its pharmacokinetics precisely because of post-translational modifications. One of the greatest challenges with respect to the production of biosimilar products is to establish a process where the glycoform of the biosimilar is comparable to that of the original biopharmaceutical, which in practice is not achieved (Endo, 2009). As a result the pharmaceuticals are similars, rather than exact copies. A study of two original erythropoietin products and two approved biosimilar products showed that although quality of biosimilars is high, major differences in potency were found in all four products (Brinks et al., 2011b). The same study found also that product potency for the two original products differed significantly to what was stated on the label and as such, direct substitution of biopharmaceutical products can only be performed cautiously and with monitoring of patients. This raises the need to constantly monitor product quality in order to avoid immunogenic factors. Despite the highlighted differences in post-translational modifications, extrapolation of the original erythropoietin drug indication is allowed, with respect to biosimilars, which have not been tested for these specific indications (Jelkmann, 2012). All of the above raise the need to gain further understanding and control over biopharmaceutical production with respect to the post translational modifications such as glycosylation.

A very different but no less important role of glycans in the development and manufacture of biotech products is that of diseases markers and by extension as targets in a patient's body. The glycosylation mechanism in the Golgi is highly complex and involves a large number of enzymes, as discussed in chapter 1.1, and as a result it is highly sensitive to changes in the biochemical environment, which are reviewed in chapter 1.6. It does not come as a surprise that changes in the glycoform distribution have been associated with a number of autoimmune inflammatory diseases (Parekh et al., 1985, Ito et al., 1993, J. Gu et al., 1994). As an example, patients suffering from anti-neutrophil cytoplasmic antibodies

(ANCA) associated vasculitis have marked deficiency of galactosylation in Fc glycan structures of polyclonal IgG, which is associated with profound inflammation (Holland et al., 2002). It is not understood whether this aggravates or initiates autoimmune disease. Changes in glycoform distribution have also been observed as a result of cancer. Most eukaryotic cells have surfaces covered with glycan moieties, which at the onset of cancer or an inflammatory episode will show a distinct change in glycoform (Meezan et al., 1969, Turner, 1992). Those changes can be a result of under- or representation of naturally-occurring glycans as well as glycans normally restricted to embryonic tissue (Dube and Bertozzi, 2005). This offers significant scope for development of new drugs or anti-cancer vaccines that could recruit the body's immune system to target cancer cells based on altered glycosylation. Analysis of blood serum glycoproteins offers a non-invasive method of disease prognosis and monitoring. While much progress has been made in high-throughput characterisation of the serum glycoform, the analysis of data remains a major bottleneck requiring solutions in bioinformatics (Campbell et al., 2008, Campbell et al., 2015).

1.5. Biopharmaceutical Glycoproteins

As seen from the above, many facets of glycosylation are of industrial importance with large scope for new developments in drug therapy as well as diagnostics. However, this review focuses on the development of biotherapeutics. A selection of three such glycoprotein therapeutics of industrial relevance is shown below with a more in-depth discussion of the associated glycan moieties and their impact with respect to each product.

1.5.1. Interferon - β

Interferon-β (IFN-β) is a naturally occurring glycoprotein of 166 amino acids that is produced in the human body in response to viral infections or other biologics (Sen and Lengyel, 1992). Human IFN-β contains a conserved Asn-80 glycan attachment site and as a biopharmaceutical it is marketed for the treatment of multiple sclerosis. Currently there are three IFN-β products marketed under the names of AVONEX®, Rebif® and Betaseron® with sales volumes of $2.518bn, $2.214bn and $1.600bn, respectively, placing AVONEX® and

Rebif® into the top 50 selling pharmaceutical products in the world (EvaluatePharma, 2011a, EvaluatePharma, 2012).

An investigation into the glycan structures that were cleaved from the protein backbone of IFN-β showed a limited distribution where 95% of all structures were biantennary and fully sialylated (Conradt et al., 1987). No tetraantennary structures were detected although structures were found that may have been of triantennary nature. The distribution and no indication of expansive lactosamine motives, a repetition of the GlcNAc-Gal motif, would indicate a steric hindrance around the glycan moiety. This means reduced accessibility by the glycosyltransferases during the glycosylation process, which limits the glycoform distribution. This points towards the hypothesis of contact between the glycan and the protein backbone leading towards the formation of hydrogen bonds with the two nearby alpha helixes of IFN-β (Runkel et al., 1998).

The licensed drugs AVONEX® (IFN-β-1a) and Rebif® are produced in CHO cells and are therefore fully glycosylated products while Betaseron® (IFN-β-1b) is produced in *E. coli* resulting in an aglycosylated pharmaceutical (Taniguchi et al., 1980). AVONEX® and Betaseron® were compared side-by-side in order to study the effect of glycosylation on various physical properties of IFN-β. First and foremost it was found that the glycosylated therapeutic had a 10-fold increase in anti-viral assay activity as compared to the aglycosylated *E. coli* product (Runkel et al., 1998). After deglycosylation of AVONEX® using enzymatic digestion (PNGase F) the proteins started to aggregate and eventually precipitate due to formation of disulfide bridges between single molecules (Sola and Griebenow, 2009). Even when stabilised in buffered solution, a lower solubility was observed due to the newly exposed uncharged and hydrophobic amino acids that were initially shielded by the glycan structure of AVONEX® (Runkel et al., 1998). Interestingly the *E. coli* produced IFN-β only formed soluble aggregates rather than a precipitate. This is believed to be a result of a cysteine-17 to serine mutation, which is not only more hydrophilic, but also stops the formation of disulfide bridges, which lead to precipitation of the protein. Further investigation showed that even when enzymatically deglycosylated, AVONEX® still showed increased heat stability (7°C higher T_m) and anti-viral assay activity (3-fold larger) as compared to Betaseron®, which leads to the conclusion that the glycan structure plays an

important role in the folding of the protein. Furthermore it has been shown that the glycan moiety of IFN-β can offer protection from proteolysis by Gelatinase B, while aminoterminal residues were removed from any deglycosylated form of IFN-β (Opdenakker et al., 2006).

1.5.2. Erythropoietin

Erythropoietin (EPO) is a glycoprotein hormone that binds to the receptors of red blood cell precursors in the bone marrow. This leads to their survival, proliferation and differentiation and thus, increases the red blood cell count (Dandrea et al., 1989, Lodish et al., 1995, Constantinescu et al., 1999). EPO is used in the treatment of anaemia associated with a number of disease states such as chronic renal failure, cancer and HIV infection (Winearls et al., 1986, Eschbach et al., 1989, Markham and Bryson, 1995, Cazzola et al., 1997). A large variety of EPO products have gained approval by the FDA of which Epogen®/Procrit®/Eprex®, an epoetin alpha, as well as Aranesp®, a darbepoetin alpha, are the highest selling erythropoietin products with worldwide sales volumes of $4.963bn and $2.930bn as of 2010, respectively (EvaluatePharma, 2011a).

EPO consists of a single polypeptide chain of 165 amino acids (Lai et al., 1986) with four total glycan attachment sites. At positions 24, 38 and 83 N-linked carbon moieties can be found while the carbohydrate chain at position 126 is an O-linked glycan structure (Browne et al., 1986, Egrie et al., 1986). The four glycan moieties have been estimated to contribute approximately 40% to the total molecular mass of EPO and probably cover much of the surface of the molecule (Egrie and Browne, 2001). This is further supported by an analysis of the glycan moieties, which revealed predominantly fucosylated tetra-antennary complex type glycan chains at the N-linked glycosylation sites (Sasaki et al., 1988) and as such suggest surface exposure and no spatial constraints. The glycan structures have been shown to play an important role in biological activity. For example, it is known that higher glycan antennarity leads to an increase in EPO's *in vivo* activity (Misaizu et al., 1995). Furthermore, Delorme at al. have demonstrated that all three N-linked glycan structures are necessary for biological activity *in vivo* while the O-linked glycan structure does not appear to be required for *in vivo* activity (Delorme et al., 1992). For recombinant human EPO it has

been shown that the N-linked glycan moieties are required for product secretion by the cell as well as ensuring solubility (Dube et al., 1988, Delorme et al., 1992).

Egrie et al. demonstrated that plasma clearance of EPO was regulated by sialic acid containing carbohydrates (Egrie et al., 1993, Egrie and Browne, 2001), where an increase in sialic acid moieties was shown to increase glycoprotein half-life and would also explain why higher antennarity was linked to increased plasma half-life. An investigation into EPO glycan structures and biological activity showed that desialylated structures showed an increased *in vitro* activity but a much reduced *in vivo* activity, which is a consequence of increased EPO clearance by asialoglycoprotein receptors in the liver (Fukuda et al., 1989, Spivak and Hogans, 1989). In order to increase protein half-life, increase drug efficacy and thus, decrease dosing rates in patients, a glyco-engineered darbepoetin was created (Egrie and Browne, 2001). Darbepoetin features an additional two N-linked glycosylation sites by changing five amino acid residues through site-directed mutagenesis. The resulting biopharmaceutical commercially marketed as Aranesp® showed a three-fold lower plasma clearance rate and resulting increased *in vivo* potency over epoetin with three N-linked glycan sites, only (Egrie et al., 2003). The introduction of Aranesp® marked the first licensing of a bio-better product.

1.5.3. Monoclonal antibodies (mAbs)

The experimental work presented in this thesis was carried out using monoclonal antibody (mAb)-producing cell lines. As a result of this and their prevalence as biotherapeutics, these molecules are discussed to a larger extent. Monoclonal antibodies are the highest selling biotechnology products and made up five of the top ten selling pharmaceutical products worldwide, as of 2013 (EvaluatePharma, 2014). The five mAbs Humira®, Remicade®, Rituxan®, Avastin® and Herceptin® have a combined sales volume of $40.197bn, where Humira® has the highest sales volume at $11.014bn (EvaluatePharma, 2014). With over 30 FDA approved mAbs (Reichert, 2012) for treatment of cancer, auto-immune diseases and inflammatory diseases the field of application is very broad, although limited by high treatment costs. With a total of 205 reported antibodies under trial (Rekhert

and Wenger, 2008) and approval success rates of 9.0% and 17.5% for humanized and human antibodies respectively (Nelson et al., 2010), the total number of approved antibody therapeutics is expected to increase significantly in the foreseeable future. Additionally there is an increased focus on the development of antibody fragments for various diseases and conditions (Nelson and Reichert, 2009).

The concept of a "magic bullet" that would go straight to the intended cell-structural target, yet remain harmless in healthy tissue, was introduced in the late 19th century by Paul Ehrlich (Strebhardt and Ullrich, 2008). A key strategy for realising Ehrlich's vision of these magic bullets was enabled through the development of hybridoma cells by Köhler and Milstein's discovery of the hybridoma technology, which enabled the production of monoclonal antibodies of predefined specificity (Kohler and Milstein, 1975). The first hybridoma cell lines were produced by the fusion of mouse spleen cells with myeloma tumour cells. The result is an immortalised cell line able to produce a single type of antibody, i.e. a monoclonal antibody.

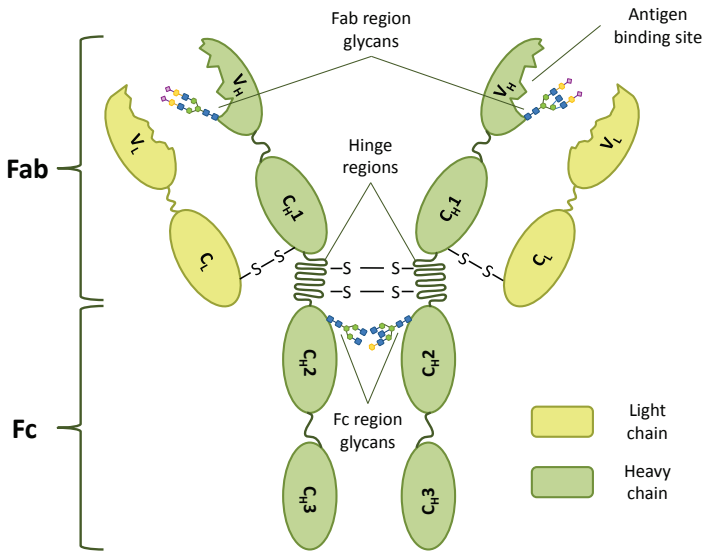


Figure 1.3 Schematic of an IgG mAb with glycan structures in the CH2 domain

Antibodies are generally described as symmetric structures composed of two identical heavy- and two identical light-chains (figure 1.3). Antibodies, also known as immunoglobulins, can be split into five different classes based on the type of heavy chain,

where IgA, IgG, IgE, IgG and IgM antibody types can be distinguished. Light chains are also classified into Kappa and Lambda types, where two identical light chains are covalently bound through disulfide bridges to two identical heavy chains forming together a Y shaped structure. Both the heavy and light chains contain a 110 amino acid length hypervariable segment also referred to as complementary determining regions (CDR). While the CDR is the antigen binding site, located in the Fab region and responsible for antigen binding, the constant Fc region is responsible for secondary effects such as activating the complementary cascade or binding to Fc receptors. 80% of all antibodies found in the blood plasma are of the IgG class (with a molecular weight of approximately 150kDa) and as of today only IgG type mAb products have been licensed as biopharmaceutical. As a consequence this report will only discuss the biological mechanisms of this antibody subclass, which are discussed below.

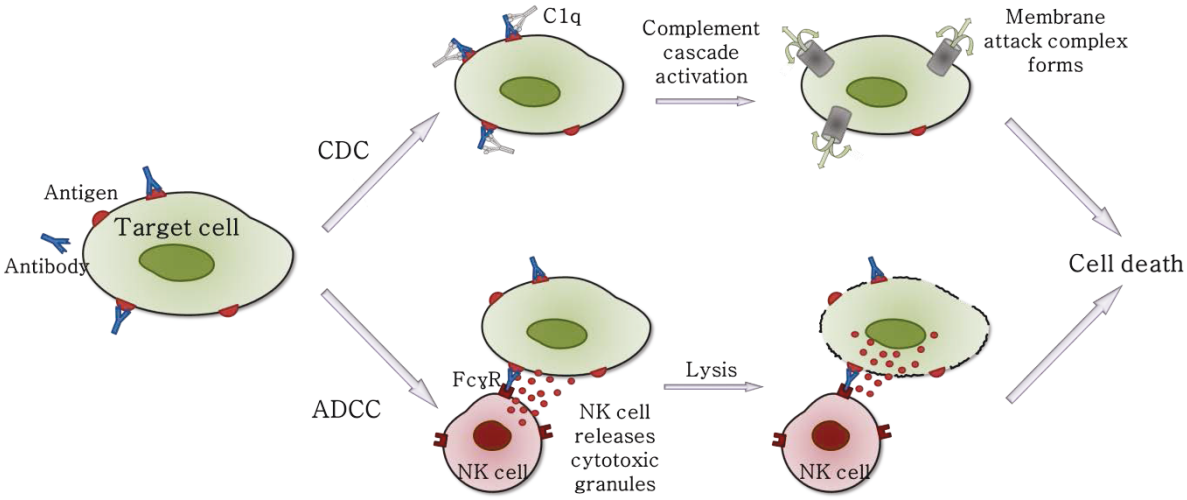


Figure 1.4 Schematic of antibody mediated activity. The top two images (top mechanism) depict the ADCC mechanism, while the bottom two images (bottom mechanism) depict the CDC mechanism.

Complement-dependent cellular cytotoxicity (CDC): In this mechanism the antibody binds with high specificity through its CDR to a target cell such as a pathogen. The hosts' own C1 protein is recruited and binds to the glycosylated Fc region of the antibody triggering the complementary cascade. The cascade mechanism results in the formation of complement membrane attack complex consisting of a number of protein subunits. This in

turn leads to the disruption of the phospholipid bilayer of the target cell and therefore, leading to cell lysis and death (figure 1.4 top mechanism).

Antibody-dependent cellular-mediated toxicity (ADCC): In this mechanism an antibody binds to an infected or cancerous cell depending on its CDR specificity and thus, recruits natural killer cell and neutrophil binding. As the CDR binds to the target cell the glycosylated Fc region of the antibody is exposed such that FcγRIII receptors on the natural killer and the FcγRII-A receptors of the neutrophils are enabled to bind to the attached antibody. This causes the release of cytokines and cytotoxic granules, which trigger apoptosis known as programmed cell death and thus, removing the antibody labelled cell (figure 1.4 bottom mechanism).

The biological *in vivo* mechanisms that are triggered by antibodies are highly dependent on the glycan moiety at the Asn297 position. In order to plan for quality at the design stage under the QbD paradigm, the mAb mechanism of biological action must be pre-defined according to the disease to treated. As a consequence the carbohydrate moiety, which exerts major control over the biological mechanism used, must become a critical quality attribute in the early construction of the mAb. Due to steric hindrance at the Asn297 position the structures found at this site are limited to mostly complex bi-antennary structure with or without core Fuc structures. Representations of the most abundant structures found in the Fc region are depicted in figure 1.5. As discussed in chapter 1.1 the glycosylation pattern depends on the glycosyltransferases expressed in the host cell line. Murine cells express GnTIII (2.4.1.144) and are consequently able to produce glycans with bi-secting GlcNAc residues (figure 1.2 third structure) in mAbs. Chinese Hamster Ovary (CHO) and Baby Hamster Kidney (BHK) cell lines on the other hand naturally lack GnTIII (Butler, 2006) and thus, are not able to attach GlcNAc residues to the central Man molecule in a 1-β-4 conformation (figure 1.5).

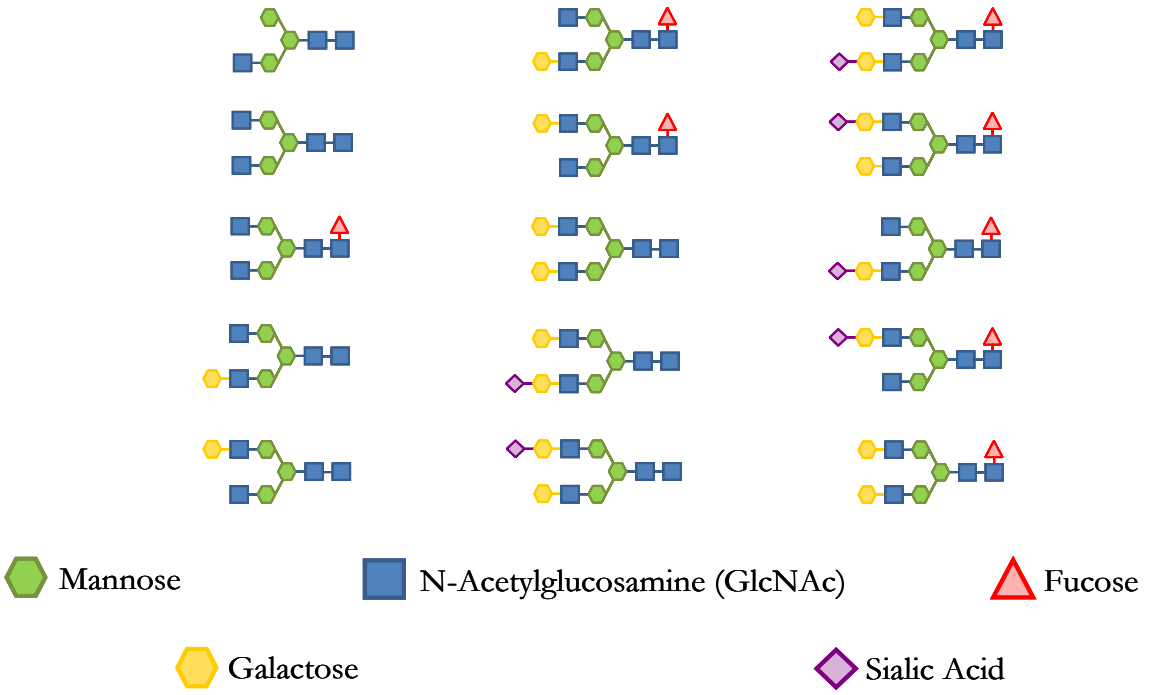


Figure 1.5 showing a number of common glycan moieties found in the Fc region of mAbs (del Val et al., 2011).

1.5.3.1. Structural-functional relationships of monoclonal antibody glycans

A large number of studies have been carried out on the effector functions of specific glycan structures with reference to the biological activity of mAbs and will be discussed in order of glycan complexity from least processed to the most complex structures typically found in the antibody Fc region.

Goetze et al. have conducted a plasma clearance study of different therapeutic IgGs in humans (Goetze et al., 2011). The results suggested that under-processed Man structures of five mannose molecules (Man5) have an increased plasma clearance rate. The conclusion reached was that high mannose structures will have a significant negative impact on drug efficacy and should therefore be considered an important CQA for therapeutic antibodies. Furthermore, Man5 glycoforms have shown deficiency in complement activation, reduced affinity for certain Fc receptors as well as reduced *in vivo* half-life in mouse studies (Wright

and Morrison, 1998, Wright et al., 2000). However, recent studies have shown that high mannose structures enhance ADCC and maybe therefore, be desirable depending on the desired mode of action (Yu et al., 2012).

N-acetylglucosamine is found as part of the core glycan structure but also determines glycan antennarity, which in case of Fc glycan moieties is limited to two, due to spatial constraints. However, based on host cell line, the GnTIII catalysed addition of an additional bisecting GlcNAc can have significant effects on receptor binding but also on further glycan processing in the Golgi. GnTIII can introduce a bisecting GlcNAc to any non-galactosylated complex or hybrid glycan but the resulting GlcNAc cannot be extended further by GalT (EC 2.4.1.38), the glycosyltransferase responsible for the addition of galactose structures to GlcNAc molecules (Umana and Bailey, 1997). Davies et al. transfected CHO cells with the rat GnTIII gene resulting in antibodies containing 48% to 71% bisecting GlcNAc residues (Davies et al., 2001). The same group found that the resulting antibodies had higher affinity for the FcγRIII receptor and as a result could induce ADCC at 10- to 20-fold lower antibody concentrations than the antibody featuring the non-bisected glycoform. However, Shinkawa et al. suggested that the above increase in ADCC was not a direct result of bisecting GlcNAc but rather the absence of core fucosylation of the antibody glycan moiety (Shinkawa et al., 2003). Core fucosylation refers to the addition of a fucose molecule to the GlcNAc molecule nearest to the protein backbone (figure 1.2 third structure). The fucosylation argument was based on the finding that Fuc addition is blocked by GalT as well as GnTIII activity (Umana and Bailey, 1997). This was further confirmed by a number of research groups leading to the finding that the absence of core fucose can increase ADCC up to 50-fold (Shields et al., 2002, Matsumiya et al., 2007). This finding has been translated into the development of third generation mAbs, which are currently undergoing many promising clinical trials (Friess T, 2008). While this is well established, further studies into the effect of bisecting structures present in antibody glycan moieties have shown that bisecting GlcNAc does in fact lead to increased ADCC although to a lesser extent than originally suggested by the research of Davies et al. (Zou et al., 2011). While the bisecting GlcNAc has a significant effect on receptor affinity, exposed terminal GlcNAc residues in glycoproteins are known to reduce *in vivo* half-life through binding to the mannose receptor. However, this effect has not been

observed in antibodies due to reduced accessibility of the glycan moiety at the Asn297 position (Jones et al., 2007).

Galactose terminating structures in the Fc region of antibodies are known to be the most abundant terminating saccharides at the Asn297 position of human polyclonal antibodies. They have a substantial effect on affinity towards the C1q and a removal results in a decrease in complement lysis activity (Hodoniczky et al., 2005). However the enzymatic removal of terminating galactose of carbon moieties did not impair the antibodies ability to induce ADCC (Boyd et al., 1995). The enzymatic addition of a galactose residue to the processed glycan structure results in the moiety no longer being a substrate for the remaining GnTs or ManII glycosyltransferase and thus, it prevents additional antennarity or mannose trimming, resulting in the formation of hybrid structures (Schachter, 1986). Lastly, there are α-1,3 linked galactose to galactose terminating bonds. Although there are no reports of their presence in the Fc region of antibodies, they have been observed in the variable Fab region of antibodies, where they have led to immunogenic responses.

Sialic acid structures may well be the most complex and diverse of monosaccharides found attached to glycan moieties. 18 kinds of sialyltransferases have been isolated from different animal species as well as over 50 different types of sialic acid to modulate the structure and function of sialic acid bearing glycoproteins (Angata and Varki, 2002). However, only a small proportion of human IgG is naturally sialylated (Parekh et al., 1985), which can be directly related to the spatial constraints in the C_H2 domain of an IgG antibody (Raju et al., 2001). Still crucial physiological functions of sialic acid bearing glycan structures of antibodies have been identified and described. Sialic acid can be found in either a 2,3- or 2,6-linkage to the penultimate galactose of a glycan moiety in human IgG (Takahashi et al., 1987). However, Anthony et al. found that intravenous immunoglobulin (IVIG) that conferred anti-inflammatory activity displayed a preferential 2,6-linkage (Anthony et al., 2008). A further analysis showed an abrogation of anti-inflammatory activity after removal of IgG containing a 2,6-linked sialic acid as part of the Fc glycan moiety. Similarly 10-fold enrichment of these IgG molecules in IVIG induced the same anti-inflammatory response at 10-fold reduced doses. In contrast, IgG with 2,3-linked sialic acid terminating glycan structures failed to induce anti-inflammatory response even at 4-fold higher doses thus,

demonstrating the specificity of *in vivo* bioactivity not only to structural but also conformational changes in glycan moieties. Still both conformations of terminating sialic acid molecules are known to lead to decreased ADCC activity due to reduced binding to FcγIIIa receptors on NK cells (Scallon et al., 2007, Kaneko et al., 2006).

In addition to glycan structures in the Fc region of human antibodies, it has been estimated that between 20-30% of human antibodies also carry a glycan structure in the variable region (Fab), where the glycosylation site can be found on both the heavy as well as the light chain (Youings et al., 1996, Abel, 1968). Although the role of variable region carbohydrate is not clear, it is suggested that carbohydrate moieties may influence antigen affinity, specificity, antibody solubility, *in vivo* half-life and stability, thus, limiting aggregation (Coloma et al., 1999, Holland et al., 2006, Huang et al., 2006). The work by Huang et al. showed that while 99% of the Fc glycan moieties, of the antibody used in the study, could be accounted for by G2F, G2FS1 and G2FS2 structures. The glycoform of the Fab region showed a selection of 15 different structures, which could only account for 89% of the total glycoform with significant amounts of tri- as well as tetraanetennary structures (Huang et al., 2006). This shows a larger degree of glycan processing of the Fab region structures. However, another study found that the glycoform of the variable region is largely dependent on the glycan position within the antibody amino acid sequence due to changing accessibility (Wright et al., 1991). With respect to the Huang et al. study, it has to be mentioned that significant amounts of α-1,3 linked Gal residues were found. The latter residues are not only known to terminate antenna elongation similar to sialic acid (Fukuda and Hindsgaul, 2000) but are also known to induce anaphylaxis in humans as they are non-native structures and linkages (Chung et al., 2008). As discussed in chapter 1.1 the glycoform is highly dependent on the host cell line. The α-1,3 linked Gal residues are a prominent example, which are commonly known to arise in murine cells such as NSO or SP2/0. However, the corresponding galactosyltransferase has recently been found to be present in CHO, with a number of CHO cell clones also expressing the enzyme (Bosques et al., 2011). The immunogenic α-1,3 linked Gal residues have received medical and industrial attention through the case of the biopharmaceutical mAb Cetuximab®, which is administered as a cancer biopharmaceutical for the treatment of patients with metastatic colorectal cancer (Qian et al., 2007). This biopharmaceutical has been reported to induce anaphylaxis in

patients due to the host production of IgE antibodies specifically targeting the murine double galactose motif (Chung et al., 2008). A study conducted by Galili et al. has shown that up to 1% of all circulating human IgG is directed against the alpha Gal motif (Galili et al., 1993). It may therefore not be surprising that a third of all subjects showed a reaction upon administration of Cetuximab®, which was directly linked to the moiety at position Asn88 of the heavy chain in the Fab region.

1.6. Controlling the glycoform

From the above discussion relating glycan moieties of IFN-β, EPO and both the antibodies Fc as well as the Fab region to *in vivo* function, it becomes apparent that exerting control over the glycoform of a biopharmaceutical is highly desirable. It is known that many process conditions will affect the glycoform. CO_2 is one example, which leads to increased osmolality and can limit growth, antibody production and lastly also affect the glycoform (Takuma et al., 2007). Similarly ammonia and the associated changes in pH are known to impact glycosylation negatively (Yang and Butler, 2000). Culture modes, growth phase and temperature among other factors also have significant effects on the glycoform of biotherapeutics. The various environmental factors have been extensively summarised and discussed by del Val et al. and will not be expanded on further as part of this review (del Val et al., 2010). This review will instead discuss metabolic and genetic manipulation of the glycoform.

1.6.1. Glycan Engineering

Overexpression or deletion of glycosyltransferases is one strategy that has been pursued in order to influence and eventually control the glycoform of a given biopharmaceutical. Umaña and Bailey in 1997 were the first researchers to propose the overexpression of glycosyltransferases to control the glycoform in a biopharmaceutical context (Umana and Bailey, 1997). The study was based on an *in silico* model to assess the impact of various enzyme concentrations on final glycan products and thus, creating a first model to predict *in vivo* glycan microheterogeneity, which is discussed further in chapter 1.9

of this review. In 1999, a subsequent experimental implementation of the findings involved the tetracycline-regulated overexpression of GnTIII and GnTV. These glycosyltransferases are responsible for the transfer of bisecting GlcNAc and the addition of GlcNAc to the α-6-mannose arm of biantennary or tri-antennary complex oligosaccharides, respectively, resulting in increased antennarity (Umana et al., 1999). However, a correlation between overexpression and cell growth inhibition was established. These results showed an upper biological limit for the overexpression of glycosyltransferases. This represents a poor strategy in an industrial context, as overexpressing cell lines would be eliminated during the selection process due to their reduced growth. In the same year, Weikert et al. reported the successful overexpression of 2-α-3-sialyltransferase as well as 1-β-4-galactosyltransferase in Chinese Hamster Ovary (CHO) cells (Weikert et al., 1999). In this work cell lines producing Tissue plasminogen activator (TNK-tPa) and tissue necrosis factor receptor – IgG1 fusion protein (TNFR-IgG) were transfected to overexpress both of the glycosyltransferases. An analysis of the glycoform showed more than 90% of glycan antennae in TNK-tPa to be capped with sialic acid residues, representing an increase from an initial 77%. Similarly the content of fully sialylated biantennary glycan moieties in TNFR-IgG increased from 7% to 68%, while the content of GlcNAc terminating antennae decreased sharply. It has to be noted at this point that the TNFR-IgG was found to have three occupied glycan sites in the Fab region and the numbers given represent a combined value of three Fab and one Fc glycan moiety per combined light and heavy chain (Raju et al., 2001). A similar degree of sialylation would therefore not be expected in an IgG molecule with Fc glycosylation, only. A combined experimental and computational approach was also used by McDonald et al. to control the antennarity of glycans. The work found the galactosyltransferase isoform 4 (GalT4 EC 2.4.1.38) to strongly impact antennarity through competition with GnTIV (EC 2.4.1.145) and GnTV (EC 2.4.1.155), both of which facilitate the addition of GlcNAc residues in the Golgi (McDonald et al., 2014).

1.6.2. Feeding Strategies

The previously described approaches aimed at steering the reactions in the Golgi through changes in enzyme concentrations, yet the rate of reaction can also be manipulated through changes in substrate concentration. As stated earlier, the substrates of the glycosyltransferase reactions are the glycan moiety as well as nucleotide sugars. The nucleotide sugar donors (NSDs) of relevance to therapeutic glycoproteins are as follows:

- Uridine diphosphate N-acetylglucosamine (UDP-GlcNAc) is the GlcNAc sugar donor and co-substrate to the various GnT enzymes leading to increased antennarity and additions of bisecting GlcNAc residues. GlcNAc is also found as part of the glycan precursor structure, where it forms a covalent bond with the protein backbone.

- Uridine diphosphate galactose (UDP-Gal) is the sugar donor and co-substrate to GalT and is consumed in the addition of galactose to GlcNAc residues.

- Guanosine diphosphate fucose (GDP-Fuc) is the substrate to the fucosylation reaction catalyzed by FucT, where fucose is added onto the GlcNAc residue forming the covalent bond with the protein backbone.

- N-Acetylneuraminic acid (CMP-Neu5Ac) and N-Glycolylneuraminic acid (CMP-Neu5Gc) are donors to the sialylation reaction catalyzed by the various forms of SiaT and leading to termination of antennae elongation. CMP-Neu5Gc is particularly abundant in murine cell lines and to a smaller extent also in CHO cells. Its presence is unfavourable in a therapeutic context as it is believed to be oncofetal and potentially immunogenic (Lavecchio et al., 1995, Sanai et al., 1988).

- Lastly uridine diphosphate N-acetylgalactosamine (UDP-GalNAc) is mostly used in O-linked glycosylation but has been observed as a building block of N-linked glycans, when murine cell lines were employed. However, it has been associated with glycans of larger complexity outside the antibody Fc region, only (Huang et al., 2006).

The metabolic pathways and biosynthesis of sugars in mammalian cells are well known and are graphically represented in figure 1.6, including all NSD species transported into the Golgi. Expanding on this, the concept of feeding strategies is based on the hypothesis that addition of specific metabolic intermediates or precursors of the nucleotide sugar biosynthesis to culture media will drive metabolic flux towards the desired nucleotide-sugar. This will eventually influence the glycoform through an increased availability of the NSD co-substrate and the resulting increase of rates of desired glycosylation reactions (Hills et al., 2001). In the context of metabolic control via NSDs their composition has to be highlighted at this stage. NSDs comprise a sugar as well as a nucleotide. The metabolic network of sugar and NSD *de* novo synthesis is shown in figure 1.6. In the reactions leading up to the synthesis of NSD species, nucleotide triphosphate structures are an important co-substrate to the reactions catalysed by nucleotidyltransferases. There are four nucleotides involved in this context, namely adenine triphosphate (ATP), cytidine triphosphate (CTP), guanosine triphosphate (GTP) and uridine triphosphate (UTP). In the NSD synthesis reaction one, or depending on the species sometimes two, phosphate groups are cleaved from the nucleotide triphosphate and replaced by the monosaccharide. Nucleotides are grouped into pyrimidines (CTP and UTP) and purines (ATP and GTP) and form also the building blocks of DNA and RNA intracellularly. The *de novo* synthesis occurs via nucleosides, the direct dephosphorylated nucleotide precursors, which represent a point of attack for the implementation of feeding strategies in addition to various saccharide additions. This chapter seeks to summarise a number of efforts undertaken to steer NSD availability and ultimately glycosylation through various feeding strategies.

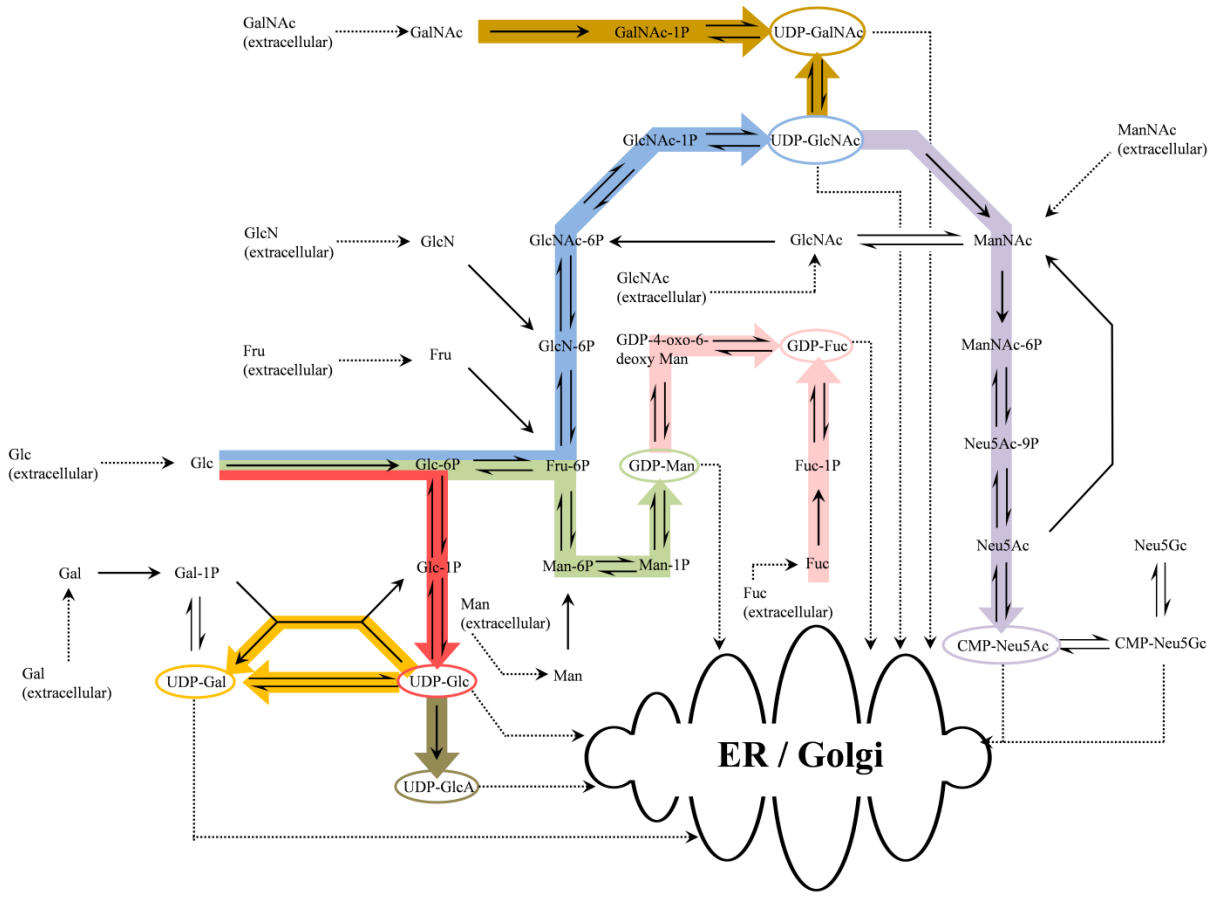


Figure 1.6 a graphical representation of the metabolic pathways of glycosylation-related nucleotide sugars as well as their transport into the Golgi.

Gawlitzek et al. were the first to investigate the effect of 10mM glucosamine feeding, which is known to be a metabolic precursor to UDP-GlcNAc and UDP-GalNAc (Gawlitzek et al., 1998). Measurements taken of intracellular UDP-HexNAc (UDP-GlcNAc and UDP-GalNAc) concentrations showed a three-fold increase in UDP-HexNAc levels in BHK cells and an increase in glycan antennarity was observed in the absence of steric hindrance. Grammatikos et al. took the investigation a step further by increasing the glucosamine feed to 12.5mM and also adding 2mM of uridine, the precursor of the nucleotide UTP in order to prevent depletion. The results showed a 26-fold increase in UDP-HexNAc levels in BHK cells, but surprisingly a slightly smaller increase in antennarity than in the previous study (Grammatikos et al., 1998). Baker et al. extended this study further by comparing the impact of glucosamine (10 mM) and uridine (2 mM) feeding on murine NS0 as well as CHO nucleotide sugar pools and the resulting glycoform (Baker et al., 2001). The UDP-HexNAc

levels in this study were elevated 18- and 60-fold in NS0 and CHO cells, respectively. The CMP-Sialic acid and UDP-Hex are metabolically linked as metabolic substrates of UDP-HexNAc and UTP, respectively. As a result an increase in their concentrations was also observed, although to a lesser extent. However, the feeding proved to inhibit cell growth and reduce proteins yields by 45% and 29% in NS0 and CHO cells, respectively.

Wong et al. extended the experimental work to include feeding of galactose, glucosamine, N-acetylmannosamine (ManNAc) as well as the nucleosides uridine and cytidine (Wong et al., 2010b). Again, a decrease in cell growth was observed as a result of glucosamine feeding. It was argued that the reduced growth was an effect of UTP entrapment as UDP-HexNAc and thus, depletion of the nucleotide. However, the addition of uridine, the precursor to UTP, did not mitigate the reduction in cell growth. Alternatively, Valley et al. speculated this to be the result of altered O-glycosylation of cytoplasmic proteins (Valley et al., 1999). As part of the same investigation the effect of 20 mM ManNAc feeding on sialic acid pools was measured. Sialic acids are produced from UDP-GlcNAc, which is subject to a negative feedback control loop. The addition of ManNAc bypasses the controlled reaction step from UDP-GlcNAc to ManNAc and consequently the feeding strategy results in greater accumulation of sialic acids. A 30- and 12-fold increase in sialic acid levels was observed for NS0 and CHO, respectively. While this strategy did not inhibit cell growth, the ManNAc supplementation did also not lead to significantly increased sialylation of glycan moieties. This phenomenon was explained by the limitation of CMP-NeuAc/CMP-NeuGc transport into the Golgi by inhibition through UDP-HexNAc, which has previously been reported by Pels Rijcken et al. (Rijcken et al., 1995). Again this has been confirmed and extended further by Wong et al. who included an addition of cytidine (10 mM) with the result of a 120-fold increase in CMP-SA levels with no significant improvement in sialylation (Wong et al., 2010b). The addition of galactose to the culture media with as well as without uridine was able to increase the availability of UDP-Gal, uridine nucleotides and cytidine nucleotides (Wong et al., 2010b). However, no conclusion was drawn with respect to the impact on the product glycoform. The authors of the study concluded that while each combination of sugar with and without nucleotide medium supplementation can have a limited effect on glycosylation, a combination of supplements

can increase overall nucleotide sugar concentrations more significantly. This would lead to increased glycosylation flux and therefore, more complete glycosylation.

Another approach towards increasing sialic acid pools has been taken by Jones et al. who substituted ManNAc for its acetylated form Ac4ManNAc (Jones et al., 2004). Despite being very efficient at supporting sialic acid production and yielding 100- to 900-fold increases in intracellular sialic acid levels the presence of Ac4ManNAc has been identified to reduce cell growth rate. Furthermore, as previously discussed an increase in sialic acid pools alone is insufficient to increase sialylation significantly. Wong et al. have found the transporter facilitating the transport of CMP-sialic acid across the Golgi membrane to be a bottleneck in CHO cells (Wong et al., 2006). An overexpression of the transporter was able to increase the sialylation of INF-β by up to 16%. However, a study conducted by Liu et al. suggests that galactosylation is a further limiting factor of sialylation in high producing GS-CHO cell lines. Galactosylated glycans are the substrates to the sialylation reaction in the Golgi. Consequently, a galactose feeding strategy was employed and sialylation was increased by 20% in an Fc-fusion protein through addition of 40 mM galactose to culture media (Liu et al., 2015).

In a different strategy, a metabolic flux analysis in CHO cells was carried out by Burleigh et al. to investigate the effects of glutamine concentration in batch and continuous culture (Burleigh et al., 2011). Glutamine plays a crucial role in the metabolic synthesis of nucleotide sugars as it provides the amino group for the conversion of fructose-6-phosphate to glucosamine-6-phosphate (Fru-6P and GlcN-6P, respectively and shown in figure 1.6), which is necessary for the synthesis of GlcNAc and thus, forms the corner-stone for further *in vivo* processing. Not surprisingly, it was shown that no glutamine supplementation during batch culture led to overall decreased sialylation, fucosylation and antennarity of glycans, while cell product secretion only decreased by a small amount. Although glutamine is synthesized in low quantities by CHO cells, lack of supplementation slows initial growth and glucose uptake by CHO cells, as shown in the Burleigh et al. study. In continuous culture however, no difference in growth rate was observed when no glutamine was supplemented, although a decreased UDP-GlcNAc pool was noted as well as a decrease in glucose consumption. Again the effects of this were overall decreased glycan antennarity,

sialylation and fucosylation. However, one of the key findings of the study was that the presence of varying glutamine concentrations can lead cells into multiple steady states under otherwise unchanged culture conditions, which may guide cells into key metabolic states that could improve the attributes of biopharmaceutical.

The above discussed the effects of feeding strategies on fully exposed glycan moieties with no steric hindrance. Hills et al. investigated the effect of feeding strategies specifically for a monoclonal IgG antibody with Fc glycosylation produced in murine NS0 cells (Hills et al., 2001). The glycoform of control samples showed predominantly fucosylated biantennary structures varying in β-1,4 linked galactose content with no detectable amount of sialylation. The α-1,6 mannose arm was preferably glycosylated compared with the α-1,3 mannose arm, where a ratio of 4:1 was observed. The galactose content decreased through culture time from 0.3 mol galactose per complex glycan to 0.2 mol after 168h of culture time, which has been argued to be not only an effect of varying glycosylation with respect to changes in nutrient availability but also due to extracellular digestion of N-glycans as cells start to lyse. In order to increase galactosylation of glycan moieties, cells were supplemented with 10mM galactose to increase UDP-Hex (UDP-Gal and UDP-Glc) levels. Interestingly no overall increase in UDP-Hex levels was observed, but instead the fraction of UDP-Gal shifted from 20% up to 94% of total UDP-Hex. The lack of increase in total UDP-Hex concentration has been argued to be due to the UDP-HexNAc "sink", where the uridine nucleotides were trapped. The effect on β-1,4 galactosylation was minor with an increase of only 6%. As part of the same study, glucosamine at 10 mM concentration was supplemented to the culture medium causing a 17-fold increase in cellular UDP-HexNAc content and a 63% reduction in mean UDP-Hex levels. A 56% reduction in galactosylation was observed. Finally the effect of ManNAc supplementation to the culture medium at 20 mM concentration was investigated yet, no signs of sialylation were observed despite a 13-fold increase in cellular CMP-sialic acid content. This result is not surprising as sialylation is limited by enzyme accessibility at Asn297 position rather than CMP-sialic aicd levels.

Grainger and James expanded on the above studies further by devising a strategy to optimise antibody Fc region galactosylation (Grainger and James, 2013). In this study the authors supplemented a number of CHO cell lines with varying amounts of galactose,

uridine and manganese in the culture media to increase IgG glycosylation. It was found that manganese alone was able to induce an "on/off" switch mechanism at concentrations as low as 1 μM due to its role as co-factor of β-1,4 galactosyltransferase (Witsell et al., 1990). However, no further effects on galactosylation were noticed at higher concentrations and thus, providing little means of control beyond the threshold. Maximal galactosylation was observed as a synergistic result of galactose and uridine supplementation in addition to manganese. Varying results were achieved for different CHO cell lines with a maximum galactose increase of up to 100% as compared to the control cultures. Cell cultures were supplemented with varying amounts of galactose, uridine and manganese and the resulting effects on terminal integral viable cell concentration (IVCC), antibody product titer and product galactosylation, measured. The data was used in a statistical modelling approach to produce a response surface model. In this approach the relationship of uridine and galactose supplementation on IVCC and also independently on product galactosylation were calculated. The results showed that it was theoretically possible to predict and improve the degree of product galactosylation with minimal impact on cell growth. However, the results show that the nature of modelling approach as well as the variability of CHO cell lines requires a cell line by cell line approach towards the optimisation of product galactosylation.

Even before the above investigation Tachibana et al. examined the effect of feeding strategies and the resulting Fab region glycosylation on antibody affinity (Tachibana et al., 1997). The initial finding showed that when 20 mM glucose was substituted for 20 mM glucosamine antibody affinity increased despite 40% lower antibody productivity. Interestingly, addition of 0.5 mM glucose to the 20 mM glucosamine yielded the highest, although marginally increased, antibody production from a range of glucose and glucosamine concentrations. Antibody light chain structures secreted in a range of glucose, glucosamine and combined monosaccharide media were analyzed through electrophoresis where populations of 27, 28, 29 and 32kDa were observed. 32kDa chains were mainly observed with high glucose and/or GlcNAc concentrations and were attributed to tri- or tetraantennary glycan attachments, while 29kDa light chains were believed to show complex asialylated biantennary glycan moieties with bisecting GlcNAc structures. The study showed that the light chains of 29kDa displayed greatest antigen affinity and were produced where GlcNAc was supplemented to the culture medium. Unfortunately, no further data

was gathered about the glycoforms obtained but this still demonstrates the potential of optimizing the monosaccharide composition of media with respect to antibody efficacy.

Heterogeneity of glycan structures is classified into micro- and macroheterogeneity. The former describes heterogeneity with respect to glycan structures, while the latter refers to heterogeneity with respect to the occupation of glycan sites on the protein backbone. The above discussed the effects of feeding strategies on microheterogeneity however, the effect of feeding on macroheterogeneity has also been studied. Macroheterogeneity can be affected by folding rate as it has been demonstrated that folding and glycosylation do in fact compete with each other to a limited extent in the endoplasmic reticulum (Holst et al., 1996). Interferon-γ has been identified by Kochanowski et al. to be of interest in the study of changes in glycosylation macroheterogeneity and its metabolic control (Kochanowski et al., 2008). This glycoprotein has two glycosylation sites with varied occupancy and as such three possible heterogeneous glycoforms of non-glycosylated, mono-glycosylated and doubly-glycosylated structures where each configuration has been reported to be secreted by CHO cells (Xie et al., 1997). Hayter et al. have previously found that nutrient limitation, as well as changes in pH caused by changes in ammonia concentration can lead to a reduction in IFN-γ glycosylation (Hayter et al., 1993, Borys et al., 1994). The Kochanowski et al. study found a maximum proportion of 70% of doubly glycosylated IFN-γ, which showed decline as early as the late stage of the exponential growth phase. The reduction was not accredited to limitations in glucose or glutamine but a limitation in UTP was found, which led to reduced UDP-Glc concentrations in one of the media employed. UDP-Glc is required for the synthesis of the dolichol bound glycan precursor molecule in the ER (figure 1.2 first structure). Additionally a buildup in ammonia concentration was detected at the late exponential phase, which is known to affect IFN-γ glycosylation. However, more pronounced changes were observed with respect to Adenylate Energy Charge (AEC) levels at later stages of the cell culture. The AEC, an indicator of the metabolic and physiological status of a cell is defined as (ATP + 0.5ADP)/(AMP + ADP + ATP) and is approximately 0.9 in exponentially growing cells (Kochanowski et al., 2006). The author came to the conclusion that a strong relationship between doubly-glycosylated IFN-γ and the cell's metabolic energy level exist. This was further supported by fed-batch experiments where dynamic feeding maintained AEC levels and the doubly-glycosylated interferon content remained

steady. Although only investigated with IFN-γ, this trend should prove applicable to other glycoproteins as well.

1.7. Modelling of Biological Systems

The second part of the literature review aims to discuss the modelling of biological systems. The motivation behind the creation of computational models is "to be able to bring measure of order to our experience and observations, as well as making *specific* predictions about *certain aspects* of the world we experience" (Bailey, 1998). This statement and its phrasing already imply the current limits of accurate model representation with respect to the rich complexity found in many biological systems. In this context it is crucial to define the model, its application and the problem to be solved to arrive at a successful model. In 1998 Bailey argued that while much progress has been made in biology and biological sciences, mathematical modeling and analysis in biochemical engineering has not been keeping pace (Bailey, 1998). Bailey argued, that much like the introduction of mathematical research into chemical engineering has revolutionized the field in the 1960's, modeling of biological systems has progressed a lot through borrowing research principles from process systems engineering (Kiparissides et al., 2011). In 1998, Bailey stated that "[…] mathematical biology receives so little respect from biological scientists […]". However, in the year 2015 hardly the same can be said, which goes to show the exciting explosion of mathematical modelling in biological sciences and the progress that has been made since the former statement was made. This section aims to discuss this progress as well as addressing the current shortcomings of mathematical modelling of biological systems in the context of biotherapeutics.

As discussed in section 1.3, the QbD paradigm is heavily reliant on the ability to understand and eventually predict the effects of changes to the process on the final product. It is not only changes in process conditions and culture media but also changes in production processes and between sequential unit operations in a biomanufacturing facility that will affect cQAs. As the majority of biotech products are produced in batch processes, batch-to-batch consistency needs to be maintained and controlled. This leads to a highly

prolonged time for the product to move through the supply chain (cash-to-cash cycle). This cycle in the biotechnology industry has been estimated to take 3 times longer than in any other industry such that 90% of the cash-to-cash cycle for a single batch of biotech products is comprised of quality release times. To facilitate quantitative understanding and accurately capture and control the manufacturing process, a modelling framework is key (Group, 2011a). In addition, a suitable model framework can help guide genetic engineering or feeding strategies, and ultimately form the basis for the rational design of manufacturing conditions.

1.8. Modelling Hierarchy and Development

Firstly the different types of model structures have to be distinguished before further discussion. The choice of an appropriate model type is guided by the definition of the model aim, its subsequent use and tradeoffs in structural complexity. In this the distinction between structured vs. unstructured models is a general case as well as a good starting point to illustrate different model types and complexity that the decision will entail. A structured model attempts to describe processes on an intracellular level, where a cell's biomass is compartmentalised by physical separation based on biological knowledge, such as the nucleus or Golgi apparatus etc. (Sidoli et al., 2004). A first, although simple, structured model for hybridoma cells was developed as early as 1989 in order to describe cell growth and mAb production with the aim to optimise cell viability (Batt and Kompala, 1989). An unstructured model, on the other hand, views the cell biomass as a "black-box" and does not take into account the inner cell structure. The result is a decrease in complexity as well as computational power required and thus, unstructured models have been proposed to be appropriate for applications in control, optimisation and process development in the production process of biopharmaceuticals (Kontoravdi et al., 2010). The most prominent example of such an unstructured blackbox model is the modelling of cell growth using Monod kinetics, which is a successful and well-established approach in the context of biotechnological modelling. The advantage is that only a limited number of essential and growth-determining metabolites are required need to be monitored.

Classifications can also be made into deterministic models where cellular processes do not vary and full homogeneity is assumed with respect to variables such as space. A stochastic model will describe randomness of biological processes, caused by low molecule counts where the assumption of homogeneity breaks down. Furthermore, modeling approaches can be classified as segregated or unsegregated, where the heterogeneity of cell cultures is taken into account. This means that sub-populations of different properties exist, such as cell populations in different stages of the cell cycle. This raises the need for the development of computationally demanding population balances as opposed or in addition to single cell kernels. In the latter case only single cells are studied, consequently treating cells homogeneously, rather than splitting them into populations or their subsets. Single cell models aiming to describe cellular metabolism will be composed of four interrelated components of transport, primary metabolism, product synthesis and cell growth & death (Sidoli et al., 2004). However, this does not require model modularity and can be solved as a unified set of equations. Population balance (PB) models, on the other hand, require expressions for the transition rate between each cell cycle phase, cell growth & death and lastly a partition function. The transition and hence, the model, can depend on cell characteristics such as single cell mass or cell maturity, giving rise to mass- or age-structured PB models, respectively (Mantzaris et al., 2001). These factors lead to population-wide processes of large complexity in mammalian systems and present an added difficulty in the development of biologically accurate mathematical modelling tools. While most models follow a PB model or a single cell kernel model only, Sidoli et al. carried out an investigation into coupling single cell kernels (SCK). The consolidation of both approach was achieved by the introduction of homogeneous sub-populations coupled with a population balance type transition between the different states (Sidoli et al., 2006). In a hierarchical approach, a bioreactor environment was split into a medium and a population component. The population was divided further into two lumped sub-populations of cells in different stages of their cell-cycle and subsequently different cell biology. The cells were compartmentalised into mitochondria and cytoplasm. The SCK described cell growth and death as well as single cell mass, where the cell number of a population is distributed in the space of cell mass and thus, provides the transition link from single cell to PB. However, the result was a model with partially compromised accuracy and over 700 parameters requiring a reduction in the

number of parameters and further parameter estimation. Due to model complexity this becomes a computationally expensive task, as well as requiring a rich set of experimental data for model training and validation.

A further distinction between models has to be made as to their kinetic or stoichiometric nature. A kinetic model requires the setup of a number of differential algebraic equations, which are readily solved in the time domain to study the dynamic behavior of a biological system. Kinetic models allow the inclusion of mechanistic knowledge of enzyme kinetics and the incorporation of regulation based on species concentrations, which are also mostly easily determinable in an experimental context. However, a rich set of parameters is often required and systems run the risk of becoming overparameterised. Rich databases of kinetic data and metabolic systems are available such as the Braunschweig enzyme database (BRENDA: http://www.brenda-enzymes.org) and the Kyoto encyclopedia of genes and genomes (KEGG: http://www.genome.jp/kegg/). Yet kinetic data is often a function of environmental conditions and reliability can be limited, while experimental determination of large numbers of kinetic parameters can prove to be an overwhelming task. A stoichiometric model, on the other hand, will arise from flux balance equations based on metabolic reaction stoichiometry of a biological network. While traditional stoichiometric models were solved under steady state, recent efforts have focused on relaxing this condition and creating dynamic flux analysis approaches (Antoniewicz, 2013). The advantage of stoichiometric models is that competing reactions can be readily simulated. However, experimental flux measurements are difficult and flux analysis model approaches tend to include more reactions than measurable compounds, resulting in underdetermined systems (Chen et al., 2012a).

The building of mathematical models of biological systems can generally be split into a "bottom-up" and "top-down" approach. In the bottom-up approach all existing mechanistic knowledge of a system is used to model a system from its fundamental details to form a larger system once put together. In a system of pre-existing mechanistic knowledge, the fundamental building blocks of the bottom-up approach model are readily testable by means of experimentation. However, in a less well-defined system, the complexity can be overwhelming, leading to difficulties in model reliability and rational design of experiments.

Creating a model from individual building blocks can also lead to missing of interactions and regulatory mechanisms on the systems level (Kholodenko et al., 2002). On the other hand the top-down approach may offer a more intuitive path towards the development of model structures, especially where pre-existing knowledge of the system is sparse. In this approach a system's input-output relations are examined to find a "lumped behavior". As more knowledge emerges, through experimentation or otherwise, more details are added to the model structure to give a truer representation of the system studied. This approach can lead to a fully mechanistic representation of a biological system, when initial assumptions and simplifications are progressively eliminated by implementation of emerging knowledge into the model structure (Hildebrandt et al., 2008).

With all the above approaches of the mathematical representation of biological systems, a rational selection and model design process becomes necessary. Kiparissides et al. proposed a solution to this problem by means of a closed loop approach, for the development of model structures with an ultimate application in biotechnological scenarios, where the steps are as follows (Kiparissides et al., 2011):

- Initial model development – The model aim is defined to allow for an appropriate choice of model type. Within these boundaries the model equations are established based on pre-existing biological knowledge.

- Parameter identifiability test – Testing for the number of identifiable parameters based on model inputs and allowing for changes in model structure if an adequate number of parameters cannot be defined.

- Model analysis – Identify the crucial parameters of the system with respect to model outputs, which can be achieved by means of a sensitivity analysis.

- Optimal experimental design – Design and tailor experiments to minimise uncertainty of crucial parameters and allow for a reliable estimation. Experiments need to be designed such, that maximal knowledge of crucial parameters can be obtained by experimental

means. In this context specific dynamic perturbations or limiting/saturating experimental conditions are sought out.

- Range of validity – The model is tested against a set of independent data of varying environmental conditions thus, creating a window of validation for the model, the model's effective operating space.

- Model based optimisation/automation – The model is applied to optimise inputs within the window of validation or used as a tool of process control.

The failure of progression along the outlined pathway was suggested to be solved by means of an iterative process, until satisfactory results are achieved. The above approach provides a general framework for the development of computational models of biological systems. Within the QbD paradigm, the above strategy offers a path towards the development of powerful tool for the control and optimisation of CQAs, such as glycosylation. However, the complexity encountered in the glycosylation process meant that iterations along multiple generations of model representation have taken place to date. The next section discusses the evolution of computational glycosylation models.

1.9. Computational Modelling of Glycosylation

Early mathematical models of the glycosylation process focused on single aspects of the biochemistry. This was a result of the combination of the biological complexity discussed in section 1.1, ever new emergence of knowledge regarding the mechanics of glycosylation and computational limitations. A first such model explored the role of diffusion in glycosylation and its impact on the level of sialylation (Monica et al., 1997). The model was constructed assuming an isotropic compartment with respect to both substrate and enzyme concentration. This effort concluded that diffusion is not a rate-limiting factor for sialyltransferase-catalysed reactions, indicating that the bottleneck in sialylation lies elsewhere. This was an important finding with respect to future computational work, as stochastic effects could be excluded thereby, significantly reducing model complexity.

Other work investigated macroheterogeneity of glycoproteins (Shelikoff et al., 1996) by focusing on the attachment of the glycan precursor to nascent protein in the endoplasmic reticulum (ER). Site occupancy becomes relevant for complex glycoproteins such as EPO and IFN-γ (chapter 1.5). The authors built a flexible mathematical framework based on available theoretical knowledge and a set of simplifying assumptions. Protein synthesis rate, oligosaccharyldolichol availability, the mRNA elongation rate and the competition of glycan attachment with the protein folding rate were taken into account in the model design. The study suggests that the competition between glycosylation and the folding rate may result in an optimal folding rate at which maximal site occupancy is reached. While the model was not validated against experimental data, it provides a powerful tool towards designing rational future experimentation towards better understanding of the glycosylation process.

The first computational model of glycan microheterogeneity was produced by Umana and Bailey (UB) with the aim of guiding cell line engineering of glycosyltransferases (Umana and Bailey, 1997). In order to limit the number of parameters, the effort focused on the 33 species which comprise the early central reaction network of the glycosylation process thus, reducing computational complexity. This includes both mannosidases and GnTs I to V with model termination upon the addition of the first galactose residue by GalT. The concentrations of glycan species were made into a function of total enzyme concentrations and their localisation, the kinetic constants of the reactions and the space-time yield of the glycoprotein. The Golgi apparatus was approximated as four continuously stirred tank reactors (CSTRs) in series (the cis-, medial, trans-Golgi cisternae and the trans-Golgi network each as separate reactors), which biologically equates to the vesicular transport model. The focus of the study was the manipulation of glycosyltransferase GnTIII, which catalyses the transfer of a bi-secting GlcNAc to an agalactosylated glycan. This in turn prevents further processing by other GnTs and thus, caps antennarity. Using the model, the authors examined the effect of overexpression of GnTIII *in silico*, which confirmed their prediction that antennarity was reduced and hybrid glycan content increased. This study provided an important first insight into the power of mathematical modelling as an approach towards glycan engineering. However, the subsequent experiments found high levels of overexpressed glycosyltransferase to be toxic to the cells (Umana et al., 1999). This provided upper limits for successful glycosyltransferase strategies as well as highlighting the need for

a more global approach towards the modelling of glycosylation where macroscopic cell culture effects are also taken into account.

To obtain further detailed information on microheterogeneity, the UB reaction network was extended to include more glycosyltransferases, increasing the number of potential structures from 33 to 7,565 arising from 22,871 reactions (Krambeck and Betenbaugh, 2005). This allowed for the modelling of structures that were core fucosylated, galactosylated and sialylated. As in the work of Umana and Bailey, Michaelis-Menten kinetic equations were used. Where available, kinetic parameters from the UB model were used and missing values were obtained from literature. However, the reaction rate expressions were extended by Krambeck and Betenbaugh (KB) to include literature values of dissociation constants for the NSD co-substrates, while UB assumed full saturation with respect to NSDs. The concentrations of NSDs in the Golgi were estimated based on cytoplasm concentrations found in literature and were assumed to be constant with respect to culture time. Enzyme concentrations were estimated based on experimental data from a study of glycan heterogeneity in recombinant human thrombopoietin with 6 potential N-linked glycan sites (Inoue et al., 1999). Krambeck and Betenbaugh argued for the estimation of enzyme concentrations over other kinetic parameters as various enzyme concentrations are known to vary significantly between cell lines as well as culture conditions. The resulting model was able to reproduce the experimental data for the averaged glycoform of the various thrombopoietin glycan sites, representing a major advance in the field of computational glycosylation. However, the simplification of reaction kinetics and other assumptions targeted at reducing model complexity reduce confidence in the quantitative predictive abilities of the model. Nonetheless the model provides a powerful tool towards guiding experimentations of glycan control to identify and estimate crucial model parameters, where intuitive design of experiment becomes nearly impossible due to the complexity of the glycosylation process.

Krambeck et al. extended the model further in a follow up study, where the model was tailored to analyse glycoforms from mass spectrometric data of human monocyte N-glycans (Krambeck et al., 2009). Mass spectrometry is based on mass to charge ratio of species only and will therefore not be able to distinguish between different structures of same molecular

mass. The updated KB model (KB2) attempts to resolve the issue by predicting all glycan structures that may be contained in a single mass spectrometric data peak to enable screening for glycan disease markers in humans. The model was extended by addition of further glycosylation enzymes to makeup a total of 19 glycosyltransferases and subsequently enzyme activities were adjusted to match normal and malignant human monocyte N-glycan mass spectra obtained from experimental data. Through application of limiting conditions based on prior glycosylation knowledge, glycans of probable negligible abundance can be dropped resulting in a total of 10,000 – 20,000 structures. The model gives valuable insight into changes in enzyme activity as a result of different diseases states and enables a more reliable screening of patients for associated glycan biomarkers. However, the model application is limited with respect to the development and production of biotherapeutics, as factors beyond Golgi enzyme activity are not considered in greater detail. A suitable model requires large specificity with respect to specific glycan sites as well as taking into account the impact of process conditions and unit operations.

Parallel work by Hossler et al., focused on improving the predictive capability of microheterogeneity models by varying reaction-related variables and incorporating bi-substrate reaction kinetic mechanisms into the mathematical description (Hossler et al., 2007). Previous models assumed the vesicular transport regime and modelled this as four CSTRs in series, one for each of the Golgi compartments (chapter 1.1). Hossler et al. tested the hypothesis of Golgi maturation vs. vesicular transport by means of an *in silico* study of the glycosylation process. In an idealised case Golgi maturation can be mathematically described as a single plug flow reactor (PFR) with varying enzyme concentrations. However, due to experimental constraints of *in vivo* qualitative as well as quantitative data of enzyme distributions and concentrations in the Golgi is sparse. Hossler circumvented this problem by employing four PFRs, each with constant enzyme concentrations to approximate changes in the enzyme concentration along the length of the Golgi apparatus. The results generally showed less deviation from the experimental data than those obtained with the CSTR-based model, particularly with respect to the ability to predict underprocessed structures. It was further shown that modifications of the enzyme concentrations for the PFR based model could lead to the most targeted glycoform and thus, demonstrating enzyme localisation to be a very potent approach in glycan engineering. The work by Hossler et al. presents a

valuable contribution in both the debate of the Golgi maturation model, as well as leading towards a more robust model structure of the Golgi with greater predictive capability towards the *in silico* representation of the glycosylation process.

The work by Jimenez del Val et al. (JdV) aimed at accurately modelling the glycoform of the IgG Fc region (Jimenez del Val et al., 2011). By limiting the number of structures to the Fc region, the JdV model was able to mechanistically describe the kinetic expressions of each individual glycosyltransferase reaction step based on available knowledge of the bi-substrate reactions. The JdV model expanded on the findings of the Hossler, where cisternal maturation was assumed. In the JdV model, the Golgi apparatus was modelled as a single ideal PFR (no axial dispersion) of constant diameter, constant flow with no mass transfer limitations as well as recycling of NSDs along the biological reactor. In order to account for the spatial variation of glycosyltransferases along each of the cisternae of the Golgi, this work assumed a normal distribution of the enzymes along the axial length of the Golgi. The enzyme spatial distributions were approximated by an optimization-based method, where the unknowns of the three parameter normal functions were found by solving the minimum amount of total enzyme necessary to achieve terminal oligosaccharide processing, including 50% sialylation. A similar treatment was used to find the distribution of NSD transport proteins, where concentrations were estimated such that NSD consumption by glycosyltransferase reaction was met by NSD transport rates. In a case study the computational results of the Krambeck and Bettenbaugh, Hossler *et al.* and Jimenez del Val *et al.* models were compared with experimental data for commercial vials of two licensed monoclonal antibodies (Nakano et al., 2009). All three models were capable of reproducing experimental findings and identifying the most abundant species. However, the greatest accuracy was achieved by the most mechanistically accurate JdV model. The model proved also a powerful tool for the *in silico* study of gene silencing strategies towards controlling the glycoform. Although, as with previous modelling efforts, this model does not account for changes in the cell culture environment or offers any insight into metabolic feeding strategies, that are known to impact the product glycoform and which may be used as a means of control.

Ohadi et al. present the latest development in the field of computational glycobiology with an attempt at linking the extracellular environment to the final product glycoform (Ohadi et al., 2013). The model was split into three parts describing cell culture dynamics as a function of glucose and glutamine in a batch process, a NSD model based on the same two metabolites and finally a glycosylation model. The novel aspect of the work involved the inclusion of a NSD model based on a semi-structured metabolic network with lumped reactions assuming CSTR behaviour of the cytosol. Reaction mechanisms were modelled as simple Michaelis-Menten kinetics of one or two substrates species of random order. No control mechanisms were considered and consumption due to biomass production was modelled as first order dissociation kinetics. Only a select few NSDs were modelled and no experimental or computational results are shown, thus not allowing for the assessment of the approach's effectiveness. The glycosylation process was modelled based on the 4 PFR cisternal maturation assumption, as proposed by Hossler. The approach employed by Kaveh et al., where the extracellular environment is taken into account when computing the glycoform is an important step towards a full picture of the glycosylation process. However, no outputs beyond cell density, glucose, glutamine and a partial glycoform are presented and consequently rendering an assessment of the outcomes of the strategy not feasible.

1.10. Conclusions of Introduction and Literature Review

Chapter 1.3 aims to highlight the importance of biotechnological products and the expanding nature of the market with a particular focus on monoclonal antibodies. However, the nature of biotechnological products is complex and the manufacturability of biopharmaceuticals remains challenging. With the passing of the patent cliff many new opportunities for biotherapeutic follow-on products such as biosimilars and bio-betters arise. This represents a new chapter in drug regulation and brings its own set of hurdles to balance patient safety, product efficacy and speed of approval. The implementation of a Quality by Design approach in the biotherapeutics industry hopes to address all the above concerns as well as reducing costs of product and process development for the

manufacturers. The glycosylation of biotherapeutics proves particularly difficult with respect to product manufacture as well as the implementation of the QbD paradigm. But glycosylation also represents a promising post-translational modification with room for improvement of product efficacy, safety, half-life and specificity.

This literature review presents the many factors that affect micro- and macroheterogeneity of glycan moieties as well as its control through feeding strategies and expression levels of glycosyltransferases amongst other environmental factors. However, while strategies for glycan engineering start to emerge, most studies were of an exploratory nature with respect to changes in the glycoform. The complex nature of the glycosylation process and the many environmental factors affecting it make an intuitive approach towards the design of experiments and the manufacturing process of biotherapeutics very challenging. To rationally capture the impact of various glycan engineering approaches in a manufacturing context process and unit operation, a modelling framework is required. Computational glycobiology has been able to advance considerably, to the point, where the full set of reactions involved in the glycosylation process have been mapped and quantitative predictions of the glycoform made. However, the predictive capability is currently limited to the glycosylation process in the Golgi and no verified framework includes the extracellular environment or captures the impact of feeding strategies.

The author shows the development of a model framework that would capture the impact of saccharide and nucleotide precursor supplementation, glycosyltransferase expression and the enzymes of the NSD metabolic network. A successful framework allows the steering, targeting and control of the glycoform. Furthermore, it is proposed to study the glycoform of a monoclonal antibody, due to its application in the biotherapeutics industry as well as its limited glycoform, reducing computational complexity as well as allowing the use of the mechanistic del Val model (del Val et al., 2011). The Kiparissides approach for the development of computational models of biological systems provides an excellent guidance for the rational development of a computational platform, which was readily applied to the work presented as part of this thesis. Consequently, the author produced the following deliverables in this thesis:

- Development of a flexible proof of concept mathematical model framework of antibody glycosylation relating the product extracellular environment to the glycoform. The framework captures cell culture dynamics, availability of nucleotides and NSDs as well as the mAb product secretion rate and its glycoform.

- Validation and training of the model structure using experimental data for all the above.

- Extension of the model framework to industrially relevant CHO cell lines and a fed-batch unit operation.

- Design of a dynamic set of experiments to probe and perturb any parts of the biological system deemed of importance to the modelling framework to ensure greater confidence and robustness in model training.

- Validation of the improved model framework against a set of experiments and demonstrate its application by means of a case study optimisation strategy relevant to the glycoform of industrially applicable biotherapeutics.

A framework addressing all the above is a tool enabling integration of process-level information about the macro environment and intracellular systems to the glycomic profile. The framework requires a degree of flexibility in order to extend its application to other production platforms of the highly diverse manufacturing environment of biotherapeutics in the future. This framework is a first step towards a platform for the *in silico* optimisation of bioprocess conditions with respect to product quality and safety in line with the Quality by Design (QbD) paradigm.

Chapter 2

Experimental Materials and Method

2.1. **Cell Culture**

A Chinese hamster ovary CHO-T cell line (MedImmune, Cambridge, UK) producing IgG antibody was used in this study. The cells were maintained in suspension cultures in CD-CHO medium (Life Technologies, Paisley, UK) at 36.5 °C and 5% CO_2 on an orbital shaking platform rotating at 150 rpm. Subcultures were performed every three days and new cultures were seeded in fresh medium at 3×10^5 viable cells / mL. 50 μM methionine sulfoximine (MSX) was supplemented during the first two passages only. Experiments were seeded at 2×10^5 viable cells/mL in 500 mL vented Erlenmeyer flasks with a working volume of 100 mL. Cell concentration was determined using a Neubauer ruling haemocytometer and viability was estimated by the trypan blue dye exclusion method using light microscopy. Each condition was repeated in duplicates with the exception of control flasks, where triplicates were examined. All cultures were supplemented with 10% v / v CD EfficientFeedC™ C AGT™ Nutrient supplement (Life Technologies, Paisley, UK) on all even culture days starting on day 2 of culture. Experiments presented in chapter 4 were supplemented with varying amounts of D-(+)-mannose and guanosine (both Sigma-Aldrich, Dorset, UK) on day 5 of culture. Experiments presented in chapter 6 were supplemented with 1 μM manganese(II) chloride solution at seeding as well as varying amounts of D-(+)-galactose (10 mM to 50 mM in total culture volume) and uridine (5 mM to 20 mM in total culture volume) (all Sigma-Aldrich, Dorset, UK) on days 4 and 8 of culture.

2.2. Antibody Quantification, Extracellular Nutrients and Metabolite Monitoring

Secreted antibody concentrations in the supernatant were determined using the BLItz® system (Pall ForteBio, Portsmouth, UK) and the Dip and Read™ Protein A (ProA) Biosensors (Pall ForteBio, Portsmouth, UK). The Dip and Read™ tips are coated with Protein A, which displays high affinity for the Fc region of human IgG and allows for its direct measurement. 4 µL of cell culture were used for antibody titer measurements. Extracellular glucose, glutamine, glutamate, ammonia and lactate concentrations were measured using the BioProfile 400 (Nova Biomedical, Runcorn, UK). The BioProfile system analysis is based on a combined enzymatic and amperometric method for species quantification. Galactose concentrations were determined using the Amplex® Red Galactose/Galactose Oxidase Assay kit (Life Technologies, Paisley, UK). In this enzymatic assay the hexose species is oxidised to produce H_2O_2 and eventually resorufin, which is directly quantifiable using monochromatic absorbance readings at 560 nm. Mannose concentrations were determined using the D-Mannose/D-Fructose/D-Glucose Assay kit (Megazyme, Bray, Ireland). In this assay kit the hexoses are firstly phosphorylated by hexokinase and in a second step a glucose dehydrogenase produces NADPH, which is directly quantifiable using monochromatic absorbance readings at 340 nm. Subsequently phosphoglucose isomerase is added to convert Fru-6-P to Glc-6-P, which then produces NADPH. Lastly, phosphomannose isomerase is added to convert Man-6-P to Fru-6-P, which will eventually produce another quantifiable increase in NADPH. Uridine and guanosine concentrations were measured using a high-performance anion-exchange chromatography (HPAEC) method as optimised and described by del Val et al. (del Val et al., 2013).

2.3. Intracellular Metabolite, Nucleotide and Nucleotide Sugar Extraction

Cell culture samples containing 2 × 10^6 viable cells were centrifuged at 800 rpm. In a washing step the resulting cell pellet was resuspended in 2 mL of ice cold 0.9% w / v sodium chloride and then immediately centrifuged at 800 rpm to remove supernatant residues. The cell pellet was resuspended in 400 µL of ice cold 50% v / v aqueous acetonitrile (Sigma-Aldrich, Gillingham, UK). The solution was incubated on ice for 10 minutes before centrifugation (4 °C, 10,000× g, 5 min). The nucleotide and nucleotide sugar containing supernatant was dried using a SpeedVac (Savant Inc.Laboratory, MI) and resuspended in 150 µL water. The final supernatant sample was filtered through a 0.22 µm syringe filter and stored at -80 °C prior to analysis. Intracellular hexose concentrations were measured using the Amplex® Red Galactose/Galactose Oxidase Assay kit (Life Technologies, Paisley, UK) for galactose the D-Mannose/D-Fructose/D-Glucose Assay kit (Megazyme, Bray, Ireland) for mannose and the Amplex® Red Glucose/Glucose Oxidase Assay kit (Life Technologies, Paisley, UK) for intracellular glucose concentrations. Glutamine concentrations were determined Glutamine EnzyChrom™ Assay Kit (Universal Biologicals, Cambridge, UK). The assay kit is based on the hydrolysis of glutamine to glutamate, which is quantifiable using monochromatic absorbance readings at 565 nm.

An optimized high-performance anion-exchange chromatography (HPAEC) method as described by del Val et al. was used for nucleotide sugar and nucleotide quantification. HPAEC elutions were performed with gradients of 1.5 M sodium acetate solution (Sigma-Aldrich, Gillingham, UK) in 3 mM potassium hydroxide (Sigma-Aldrich, Gillingham, UK) with a maximum ion concentration of 1 M sodium acetate using a CarboPac PA1 column (Dionex, Bannockburn, IL, USA). A modified method was used for the quantification of GDP-Fuc and GDP-Man to prevent species co-elution with intracellular tryptophan. Elutions were performed with gradients of 1.5 M sodium acetate solution in 3 mM potassium hydroxide. Elutions of the sodium acetate solution were carried out using the following

gradients: $t_{0\ min}$ = 20%, $t_{1\ min}$ = 66%, $t_{6\ min}$ = 66%, $t_{23\ min}$ = 20%, $t_{30\ min}$ = 20%. Detection was performed at 262.1 nm.

2.4. Glycan Purification and Analysis

Secreted antibody was purified from cell culture supernatant with a Protein A IgG Purification Kit (Thermo Scientific, Horsham, UK) and concentrated using Vivaspin® 2 ultracentrifugation spin columns 50kDa (Generon, Maidenhead, UK). Further glycan processing and glycan quantification was kindly performed by MedImmune (Cambridge, UK). The workflow involved the denaturation of purified and concentrated IgG samples, PNGase digestion and glycan labeling. Separation/quantification was performed using the LabChip® platform (PerkinElmer, Seer Green, UK) based on capillary electrophoresis.

Chapter 3

Model development

In this chapter a modelling framework was developed to provide a link from the extracellular environment to the antibody product glycoform via an array of metabolites. The model comprises four interlinked modules: 1) A modified Monod kinetics model describing cell growth dynamics and nutrient uptake, 2) a semi-structured nucleotide model capturing dynamic changes in intracellular nucleotide concentrations, 3) a fully structured and mechanistic model of dynamic intracellular nucleotide sugar donor (NSD) concentrations, 4) a dynamic model of antibody glycosylation at the conserved Asn297 position of IgG antibodies as developed by del Val et al. (Jimenez del Val et al., 2011). Both the nucleotide as well as the nucleotide sugar donor models presented here are a novel contribution, however the main point of focus is on the development of the nucleotide sugar donor model. The *in silico* reconstruction of the *de novo* synthesis of NSD sugars was achieved by representing each of the 34 species as individual material balances, which were connected by a total of 60 metabolic reactions expressed as saturation type kinetics. The model has been trained in its entirety using in house experimental data

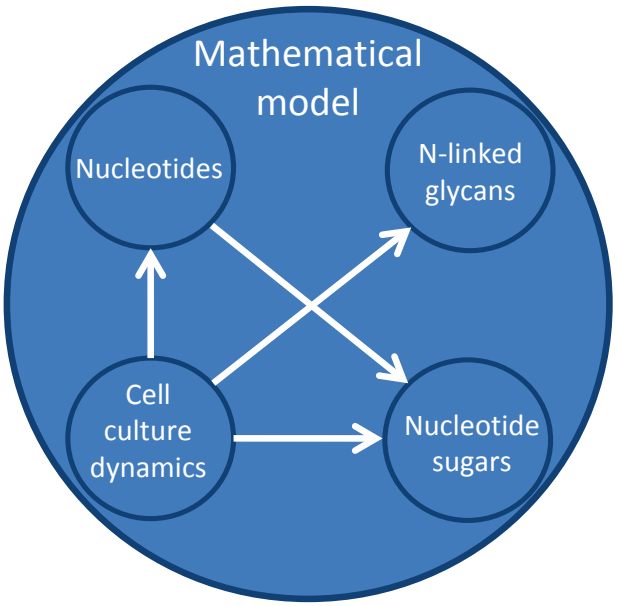


Figure 3.1 Structure of the model platform, where each module is represented as a circle. The arrows indicate the direct interdependencies of the respective modules. [Reproduced with permission]

obtained from a murine hybridoma cell line. Model training refers to parameter estimation based on experimental data for an *in silico* reproduction using the gPROMS model building environment.

3.1. Model structure

As shown in Figure 3.1 the model platform consists of four modules that are linked through either molecular species flux or species concentrations. A modular platform allows operation across the multiple levels of organisation in a biological system that are involved in the glycosylation process. While a cell culture dynamics model describes the processes on a macroscopic level, the molecular processes on the microscopic level within the cells are described by the other three modules of the platform.

As previously discussed in section 1.6, critical quality attributes, such as glycosylation, are not only affected by process conditions but also by changes in the production process and bioreactor operation (Group, 2011b). The modular nature of the model structure allows for single modules to be exchanged, reflecting production changes such as changes in cell line or operation mode, without having to alter the structure of the entire model platform. Thus, it is possible to simulate different feeding regimes or switching from a fed-batch to a continuous operation mode through corresponding changes to the structure of the cell culture dynamics model only. Lastly, the modular approaches allows not only for future module updates but also for the building on previous modelling achievements, such as Monod kinetics models, as well as previous efforts at recreating the glycosylation process *in silico* (Ljunggren and Haggstrom, 1994, Jimenez del Val et al., 2011, Glacken et al., 1989, Detremblay et al., 1992).

3.2. Cell culture dynamics

The cell culture dynamics model accounts for the interactions of the cells with their extracellular environment and the resulting cell growth, death, nutrient utilisation as well as fluxes into the intracellular environment (figure 3.2). Ultimately the cell culture dynamics indicates the cells' response to changes in the environment such as the feeding of hexoses and nucleotide precursors to drive the product glycoform. A single kernel model was chosen in the context of this work, as a population balance model or a population balance hybrid model structure adds multiple layers of additional complexity due to a much increased parameter space, which in turn would require further estimation and/or experimentation to avoid potential overparameterisation. A population balance model offers clear advantages when considering cell cycle heterogeneity or stochasticity. However, this is outside the scope of this work and population balance type model structures were not considered further. To eliminate further areas of complexity, an unstructured model for cell growth has been used as part of this study, which is a successful and well-established approach in the context of biotechnological modelling. The advantage is that only a limited number of essential metabolites are required to be monitored, and due to all the above the use of structured or semi-structured cell growth models is unwarranted.

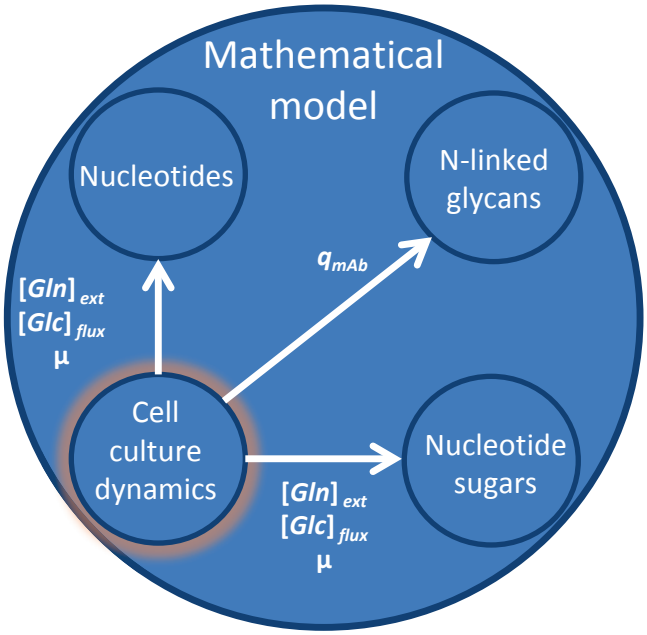


Figure 3.2 Schematic of the model framework depicting the interaction of the cell culture dynamics model with the remaining parts of the framework.

The model presented here is built on Monod kinetics, which have been modified to account for non-ideal behaviour of cell cultures and is based on the extracellular

concentrations of glucose and glutamine. Homogeneity with respect to species and cell concentrations was assumed at all times. The viable cell density (X_V in cells/L) is a function of growth rate (μ in h^{-1}), death rate (k_d in h^{-1}) and the flow out of the reactor (F_{out} in L/h):

$$\frac{dVX_V}{dt} = \mu V X_V - k_d V X_V - F_{out} X_V \quad 3.1$$

The growth rate is a function of the concentrations of extracellular glucose ($[Glc]_{ext}$ in mM) and glutamine ($[Gln]_{ext}$ in mM), as well as the saturation coefficients for glucose ($K_{M,glc}$ in mM) and glutamine ($K_{M,gln}$) all in units of mM and the maximum growth rate μ_{max} (h^{-1}).

$$\mu = \mu_{max}\left(\frac{[Glc]_{ext}}{K_{M,glc} + [Glc]_{ext}}\right)\left(\frac{[Gln]_{ext}}{K_{M,gln} + [Gln]_{ext}}\right) \quad 3.2$$

The death rate is an inverse Monod function of the glucose and glutamine availability, the maximum death rates for glucose ($k_{d,max,glc}$ in h^{-1}) and glutamine ($k_{d,max,gln}$ in h^{-1}), the species depletion coefficients for glucose ($K_{M,gln}$ in mM) and glutamine ($K_{M,gln}$ in mM).

$$k_d = k_{d,max,glc}\left(\frac{K_{d,glc}}{K_{d,glc} + [Glc_{ext}]}\right) + k_{d,max,gln}\left(\frac{K_{d,gln}}{K_{d,gln} + [Gln_{ext}]}\right) \quad 3.3$$

The metabolism of glucose and glutamine were represented by the following equations:

$$\frac{dV[Glc_{ext}]}{dt} = -q_{glc}VX_V - F_{in}[Glc_{feed}] - F_{out}[Glc_{ext}] \quad 3.4$$

$$\frac{dV[Gln_{ext}]}{dt} = -q_{gln}VX_V - F_{in}[Gln_{feed}] - F_{out}[Gln_{ext}] \quad 3.5$$

In the above, q_{glc} and q_{gln} (mmol/(h cell)) denote the specific glucose and glutamine cell uptake rate, respectively, and are defined by the equations shown below:

$$q_{glc} = \left(\frac{\mu}{Y_{Xv/glc}}\right) + m_{glc} \quad 3.6$$

$$q_{gln} = \left(\frac{\mu}{Y_{Xv/gln}}\right) + m_{gln} \quad 3.7$$

$Y_{Xv/glc}$ and $Y_{Xv/gln}$ (cell/mmol) denote the biomass yield coefficient for glucose and glutamine, respectively. The m_{glc} and m_{gln} (mmol/(h cell)) terms are the maintenance coefficients for glucose and glutamine, respectively. Lastly the product term and the specific productivity terms are represented by the following:

$$\frac{dV[mAb]}{dt} = q_{mAb}VX_V - F_{out}[mAb] \quad 3.8$$

$$q_{mAb} = {}^{Y_{mAb}}/_{Y_{Xv}} \qquad 3.9$$

The antibody material balance features a cell density dependent production term as well as accounting for product loss in the outlet. The production rate (q_{mAb} in mg/(cell h)) was assumed to be a constant and equals to a constant antibody yield coefficient ($Y_{mAb/Xv}$ in mg/(cell h)). Consequently, antibody production rate is not dependent on cell growth rate and a function of cell density, only.

3.3. Nucleotide model

A novel nucleotide model was created based on a simplified purine and pyrimidine synthesis network. The presented model is a much simplified semi-structured attempt at capturing the nucleotide *de novo* synthesis, where glucose and glutamine act as the carbon and nitrogen source, respectively (Xie and Wang, 1994) (figure 3.3). While asparagine, aspartate, glutamate and glycine also play a role in nucleotide synthesis they have not been included in this model due to lack of experimental data and to reduce both experimental and computational complexity. Furthermore, no self-regulating control mechanisms i.e. inhibition terms of any kind have been included at this stage, as this required further

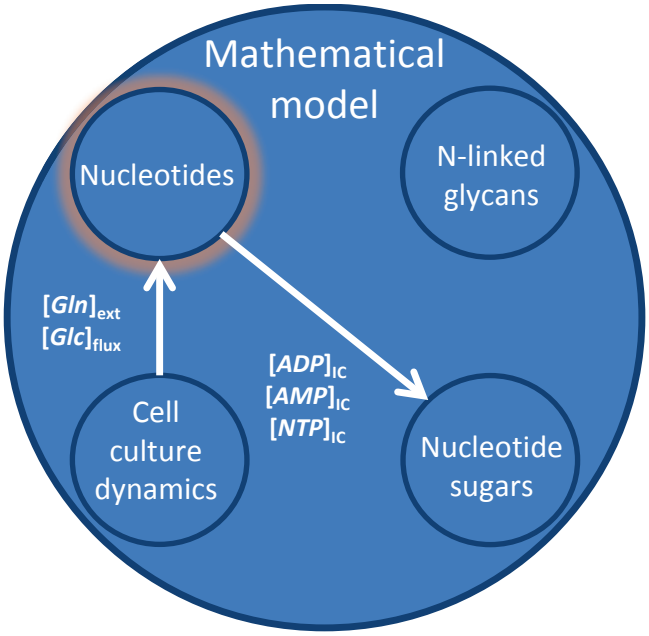


Figure 3.3 Schematic of the model framework depicting the interaction of the nucleotide model with the remaining parts of the framework.

experimental probing of the metabolic network. The model outputs are the concentration of the six nucleotide species, which in turn are an input to the NSD model.

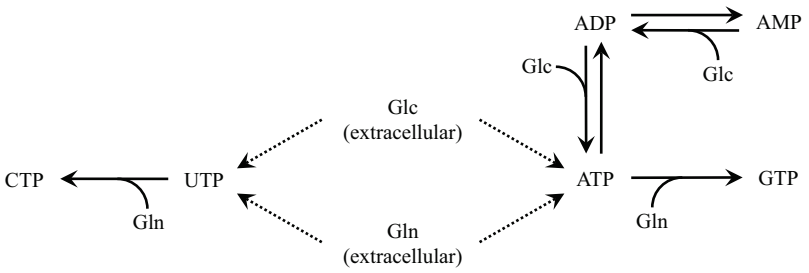


Figure 3.4 A simplified reaction network of the de novo synthesis of purine and pyrimidine species. Source: Jedrzejewski et al. 2014. [Used with permission]

The resulting network contains six mass balances (equation 1.10), one each for adenine diphosphate (ADP), adenine monophosphate (AMP), adenine triphosphate (ATP), cytosine triphosphate (CTP), guanosine triphosphate (GTP) and uridine triphosphate (UTP), connected by a network of eight reactions based on Michaelis-Menten kinetics as displayed in figure 3.4. All glucose and glutamine co-substrate terms are based on extracellular concentrations of the two species. The reactions of ATP to ADP and ADP to AMP are the following:

$$\frac{d[Nuc]_{IC}}{dt} = \sum r_{producing} - \sum r_{consuming} - Cell\ consumption \qquad 3.10$$

$$r = k\left(\frac{[Nuc]_{IC}}{K_{M,nuc} + [Nuc]_{IC}}\right) \qquad 3.11$$

The synthesis of CTP and GTP are represented by the following equation:

$$r = k\left(\frac{[Nuc]_{IC}}{K_{M,nuc} + [Nuc]_{IC}}\right)\left(\frac{[Gln]_{ext}}{K_{M,gln} + [Gln]_{ext}}\right) \qquad 3.12$$

The reaction of AMP to ADP and ADP to ATP are of the following form:

$$r = k\left(\frac{[Nuc]_{IC}}{K_{M,nuc} + [Nuc]_{IC}}\right)\left(\frac{[Glc]_{ext}}{K_{M,glc} + [Glc]_{ext}}\right) \quad 3.13$$

Lastly, the synthesis of ATP and UTP are represented by the following:

$$r = k\left(\frac{[Gln]_{ext}}{K_{M,gln} + [Gln]_{ext}}\right)\left(\frac{[Glc]_{ext}}{K_{M,glc} + [Glc]_{ext}}\right) \quad 3.14$$

Extracellular glucose and glutamine are the sole inlets into the nucleotide model, however, the model is constrained through outlet fluxes. There are a total of four flux-constrained outlets, one each for AMP, CTP, GTP and UTP. For the outlets, it was assumed that each species is consumed in the formation of NSDs for host cell glycoproteins as well as antibody production, DNA synthesis and RNA synthesis. The latter two were taken to be dependent on growth rate and are described by the following equation:

$$F_{out,nuc} = \left(\frac{[Nuc]_{IC}}{K_{TP,nuc} + [Nuc]_{IC}}\right)\frac{\mu}{V_{cell}}\left(\frac{DNA_{f,nuc}m_{DNA}}{Mr_{DNA}} + \frac{RNA_{f,nuc}m_{RNA}}{Mr_{RNA}}\right) \quad 3.15$$

The molecular mass for each DNA monomer (Mr_{DNA} in kg/kmol) and RNA monomer (Mr_{RNA} in kg/kmol) as well as the fraction of each nucleotide in DNA ($DNA_{f,nuc}$ no units) and RNA ($RNA_{f,nuc}$ no units) was based on the data used by Nolan and Lee (Nolan and Lee, 2011). The mass of DNA (m_{DNA} in kg/kmol) and RNA (m_{RNA} in kg/kmol) were taken as 7.05 pg/cell and 28.55 pg/cell, respectively (Bonarius et al., 1996).

3.4. Nucleotide Sugar Donor model

The main focus of this Chapter is on a bottom-up modelling approach for the *in silico* reconstruction of the nucleotide sugar donor (NSD) synthesis metabolic network. This approach implies that the system is constructed from its individual components to give rise to a complex model, which translates to describing all known reactions in full dynamic detail to represent the NSD model. The NSD model is a function of the glucose and glutamine inlet fluxes from the cell growth model as well as of the nucleotide concentrations from the nucleotide model. The outputs of the model are the concentrations of the NSD species and their transport rates into the ER and Golgi. The bottom-up reconstruction of the NSD metabolic network is based on the murine metabolic network as depicted in the Kyoto Encyclopedia of Genes and Genomes (Genomes)) and individual enzyme data as found on BRENDA (BRENDA, 2015). In total, the network includes 34 sugar and nucleotide sugar species, each represented as a separate mass balance (equation 3.16) connected through a network of 35 reaction steps as shown in figure 3.6. The rate of each enzymatic reaction is represented by a single equation and is used to predict the dynamic behavior of the metabolic network with respect to the system inputs, *i.e.*, hexoses and nucleotides.

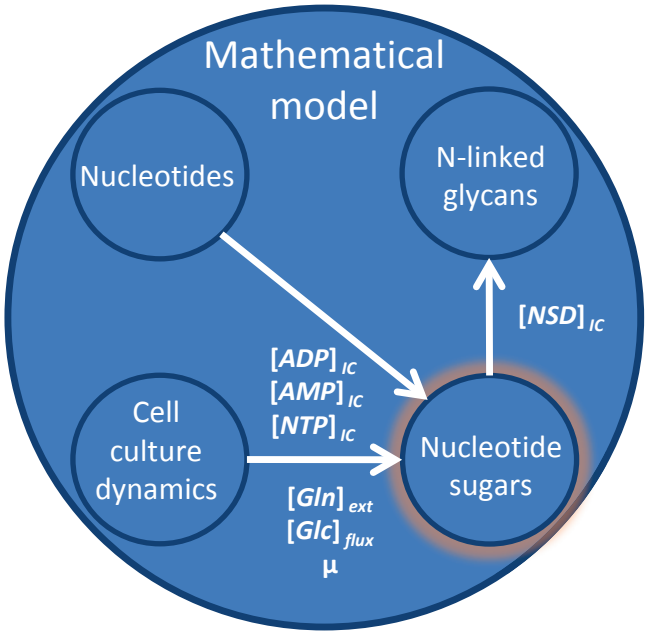


Figure 3.5 a schematic of the NSD model and its dependence within the mathematical model platform.

$$\frac{d[i_{IC}]}{dt} = \sum r_{producing} - \sum r_{consuming} + Transport_{from\ EC} - Transport_{to\ Golgi} \qquad 3.16$$

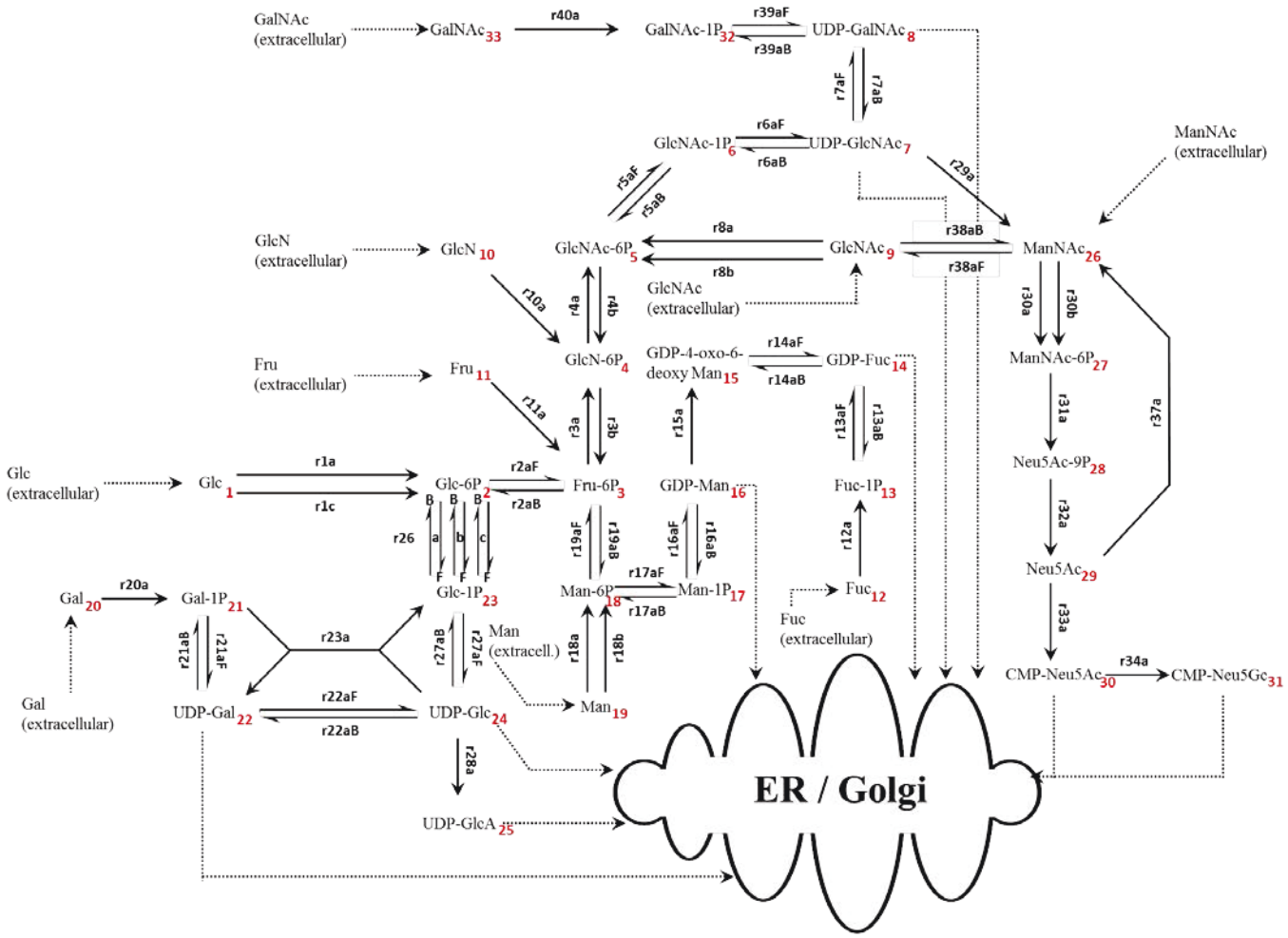


Figure 3.6 The reaction network of the de novo nucleotide sugar donor synthesis pathway, as modelled. Each species is represented as a separate mass balance and the arrows indicate the reaction steps and directions of reaction. [Used with permission]

Individual rate expressions are based on enzyme mechanisms and kinetics found in the literature, and are summarised in Appendix A together with dissociation constants (K_m), turnover rates (k_{cat}), inhibitory terms (K_i), enzyme activity and any Hill coefficients. Rate equations are based on Michaelis-Menten kinetics, accounting for reported reaction mechanisms and inhibitory compounds and the Hill equation is used where data indicating deviation from Michaelis-Menten kinetics (*i.e.*, independent binding) was available. Murine (*Mus musculus*) enzyme data was used where available and when lacking, preference in data was based on most recent common ancestors, as described in the molecular tree of mammals of the placental orders (Springer et al., 2004). While the dissociation constant (K_m) is an

intrinsic parameter, V_{max} is not, and is a function of the turnover rate constant, k_{cat}, and the initial enzyme concentration used in a particular experimental condition [E_0]. The following assumptions were made for the derivation of the rate of reaction expressions:

- Equilibrium is rapidly reached for all intermediate reactants
- Rate-limiting steps are irreversible
- Where water is required for catalysis, full enzyme saturation is assumed due to the aqueous environment of the cytoplasm
- Where more than one substrate is required for catalysis, a random order of substrate binding is assumed, unless reported otherwise
- Rapid dissociation of reaction products from enzyme
- Michaelis-Menten kinetics are assumed to hold true, unless reported otherwise
- All enzyme and transport protein concentrations throughout the network are constant
- No stochastic behavior of any species or enzymes involved in the reaction pathway
- No compartmentalisation of any reaction steps within the network
- Enzyme inhibition is assumed to be reversible

In total the mechanisms split into 20 single substrate uni-uni reactions, seven random order bi-bi, 14 ordered bi-bi, 17 Ping-Pong bi-bi and one Ping-Pong ter-ter. The model equations for the most simple uninhibited reaction case and the single specific ter-ter mechanism equations are shown below. A and B denote substrate concentrations, k_{cat} turnover rate, E_0 initial enzyme concentrations, and I denotes inhibitor concentrations. Each individual reaction and its corresponding mechanism are also listed in Appendix A. The equations for each type of kinetic mechanism are shown below.

3.4.1. Enzyme mechanisms

Based on the listed assumptions the following reaction scheme for single substrate Michaelis-Menten kinetics was set up:

3.4.1.1. Single substrate Michaelis-Menten rate equation

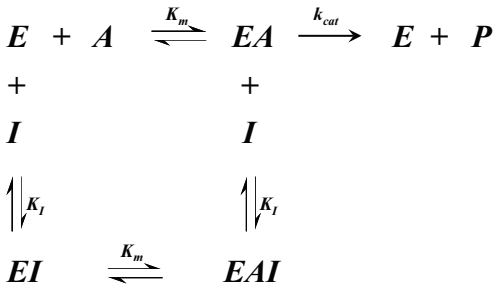


Figure 3.7 Single substrate Michaelis-Menten kinetics with competitive inhibition of species A by I. [Used with permission]

Based on this reaction scheme and the previously described assumptions, the following rate of reaction equations were derived including inhibitory enzyme kinetics for competitive and non-competitive inhibition:

Equation 3.17 Rate of reaction for Single substrate Michaelis-Menten kinetics

$$v = \frac{d[P]}{dt} = \frac{k_{cat}[E_0][A]}{K_m + [A]}$$

Equation 3.18 Rate of reaction for Single substrate Michaelis-Menten kinetics with competitive inhibition of species A

$$v = \frac{d[P]}{dt} = \frac{k_{cat}[E_0][A]}{K_m\left(1 + \sum_{i=1}^{NI}\frac{[I_i]}{K_{I,i}}\right) + [A]}$$

Equation 3.19 Rate of reaction for Single substrate Michaelis-Menten kinetics with non-competitive inhibition

$$v = \frac{d[P]}{dt} = \frac{k_{cat}[E_0][A]}{(K_m + [A])\left(1 + \frac{[I]}{K_I}\right)}$$

3.4.1.2. Random Order Bi-Bi Kinetics

Based on the previous assumptions the following reaction scheme for random order bi-bi kinetics was set up:

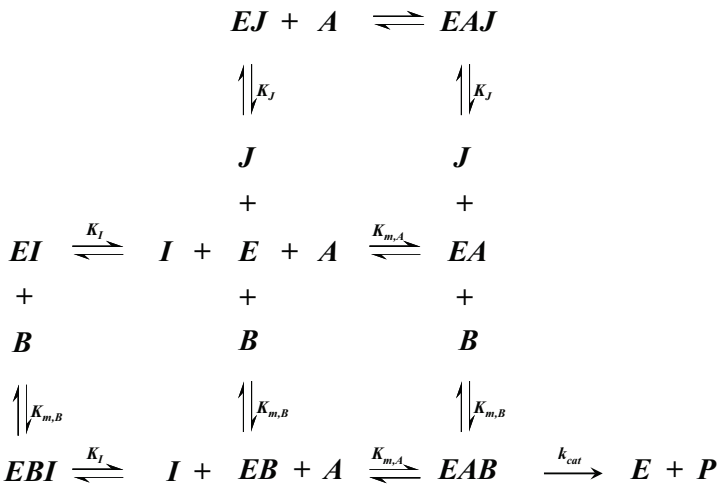


Figure 3.8 Random order bi-bi kinetics and competitive inhibition of species A by I and species B competing with J. [Used with permission]

Based on this reaction scheme and the previously described assumptions, the following rate of reaction equations were derived including inhibitory enzyme kinetics for competitive and non-competitive inhibition:

Equation 3.20 Rate of reaction for random order bi-bi kinetics

$$v = \frac{d[P]}{dt} = \frac{k_{cat}\,[E_0][A][B]}{K_{m,A}\,K_{m,B} + K_{m,A}[B] + K_{m,B}[A] + [A][B]}$$

Equation 3.21 Rate of reaction for random order bi-bi kinetics with competitive inhibition of species A and B

$$v = \frac{d[P]}{dt} = \frac{k_{cat}\,[E_0][A][B]}{K_{m,A}\,K_{m,B}\left(1 + \sum_{i=1}^{NI}\frac{[I_i]}{K_{I,i}} + \sum_{j=1}^{NJ}\frac{[J_j]}{K_{J,j}}\right) + K_{m,A}[B]\left(1 + \sum_{i=1}^{NI}\frac{[I_i]}{K_{I,i}}\right) + K_{m,B}[A]\left(1 + \sum_{j=1}^{NJ}\frac{[J_j]}{K_{J,j}}\right) + [A][B]}$$

Equation 3.22 Rate of reaction for random order bi-bi kinetics with non-competitive inhibition

$$v = \frac{d[P]}{dt} = \frac{k_{cat}\,[E_0][A][B]}{(K_{m,A}\,K_{m,B} + K_{m,A}[B] + K_{m,B}[A] + [A][B])\left(1 + \frac{[I]}{K_I}\right)}$$

3.4.1.3. Ordered Bi-Bi Kinetics

Based on the previous assumptions the following reaction scheme for ordered bi-bi kinetics was set up:

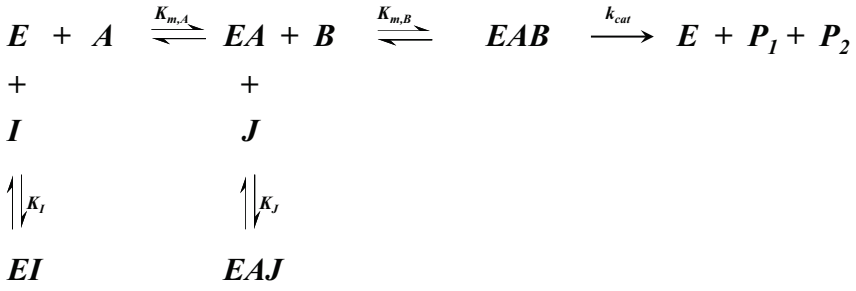


Figure 3.9 Ordered bi-bi kinetics with competitive inhibition of species A through I and species B competing with J. [Used with permission]

Based on this reaction scheme and the previously described assumptions, the following rate of reaction equations were derived including inhibitory enzyme kinetics for competitive and non-competitive inhibition:

Equation 3.23 Rate of reaction for ordered bi-bi kinetics

$$v = \frac{d[P]}{dt} = \frac{k_{cat}\,[E_0][A][B]}{K_{m,A}\,K_{m,B} + K_{m,B}[A] + [A][B]}$$

Equation 3.24 Rate of reaction for ordered bi-bi kinetics with competitive inhibition of species A and B

$$v = \frac{d[P]}{dt} = \frac{k_{cat}\,[E_0][A][B]}{K_{m,A}\,K_{m,B}\left(1 + \sum_{i=1}^{NI}\frac{[I_i]}{K_{I,i}}\right) + K_{m,B}[A]\left(1 + \sum_{j=1}^{NJ}\frac{[J_j]}{K_{J,i}}\right) + [A][B]}$$

Equation 3.25 Rate of reaction for ordered bi-bi kinetics with non-competitive inhibition

$$v = \frac{d[P]}{dt} = \frac{k_{cat}\,[E_0][A][B]}{(K_{m,A}\,K_{m,B} + K_{m,B}[A] + [A][B])\left(1 + \frac{[I]}{K_I}\right)}$$

3.4.1.4. Ping-Pong Bi-Bi Kinetics

Based on the previous assumptions the following reaction scheme for ping-pong bi-bi kinetics was set up:

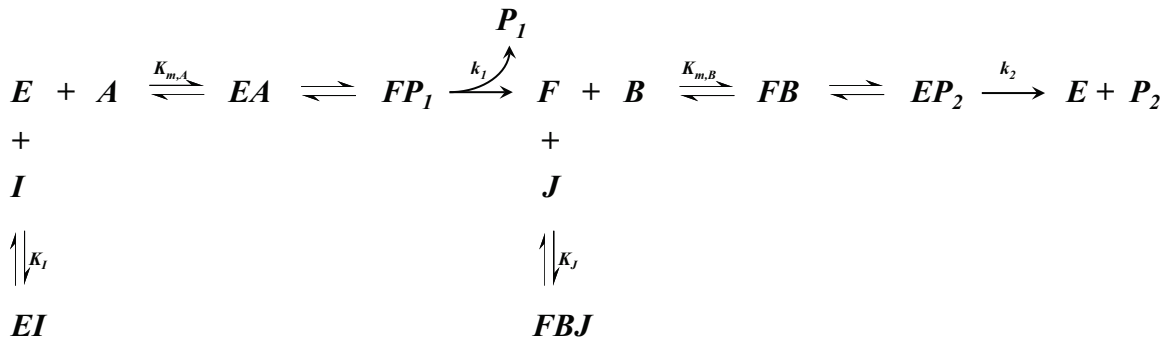


Figure 3.10 Ping-pong bi-bi kinetics with competitive inhibition of species A by I and species B competing with J. [Used with permission]

Based on this reaction scheme and the previously described assumptions, the following rate of reaction equations were derived including inhibitory enzyme kinetics for competitive and non-competitive inhibition:

Equation 3.26 Rate of reaction for ping-pong bi-bi kinetics

$$v = \frac{d[P]}{dt} = \frac{k_{cat}[E_0][A][B]}{K_{m,A}[B] + K_{m,B}[A] + [A][B]}$$

Equation 3.27 Rate of reaction for ping-pong bi-bi kinetics with competitive inhibition of species A and B

$$v = \frac{d[P]}{dt} = \frac{k_{cat}[E_0][A][B]}{K_{m,A}[B]\left(1 + \sum_{i=1}^{NI}\frac{[I_i]}{K_{I,i}}\right) + K_{m,B}[A]\left(1 + \sum_{j=1}^{NJ}\frac{[J_j]}{K_{J,j}}\right) + [A][B]}$$

Equation 3.28 Rate of reaction for ping-pong bi-bi kinetics with non-competitive inhibition

$$v = \frac{d[P]}{dt} = \frac{k_{cat}[E_0][A][B]}{(K_{m,A}[B] + K_{m,B}[A] + [A][B])\left(1 + \frac{[I]}{K_I}\right)}$$

3.4.1.5. Ping-Pong Ter-Ter Kinetics

Based on the previous assumptions the following reaction scheme for ping-pong ter-ter kinetics was set up:

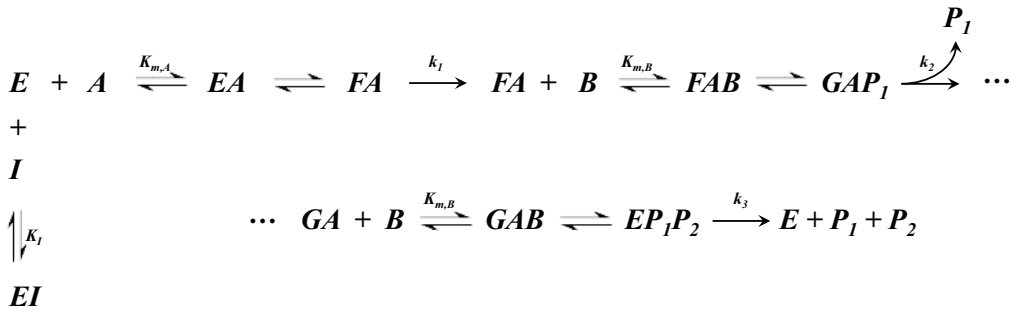


Figure 3.11 Ping-pong ter-ter kinetics with competitive inhibition of species A by I. [Used with permission]

Based on this reaction scheme and the previously described assumptions, the following rate of reaction equations were derived including inhibitory enzyme kinetics for competitive and non-competitive inhibition:

Equation 3.29 Rate of reaction for ping-pong ter-ter kinetics with competitive inhibition of species A

$$v = \frac{d[P]}{dt} = \frac{k_{cat}\,[E_0][A][B]^2}{2K_{m,A}\,K_{m,B}\,[B] + 2K_{m,B}\,[A][B] + K_{m,A}\,[B]^2\left(1 + \frac{[I]}{K_I}\right) + (K_{m,B})^2[A] + [A][B]^2}$$

3.4.1.6. Hexokinase Rate of Reaction Expression

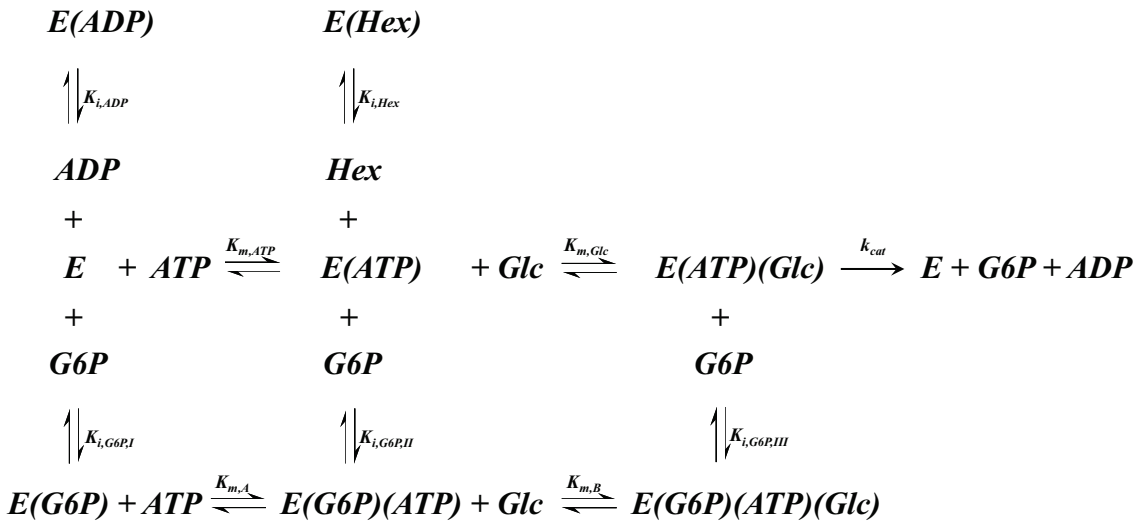


Figure 3.12 Hexokinase reaction scheme with competitive inhibition of ATP by ADP, Glucose competing with other hexose species and un-competitive inhibition through Glucose-6P. [Used with permission]

The rate of reaction for Hexokinase cannot be described by any of the previously described rate expressions. This is due to its competitive inhibition of ADP with ATP, competition between various hexose sugar substrates (namely glucose, glucosamine, fructose and mannose) and un-competitive inhibition by glucose-6-phosphate (Easterby and Qadri, 1982). Based on previous assumptions, a reaction scheme for the catalysis of glucose to glucose-6-phosphate can be represented as depicted in figure 3.12. Based on this reaction scheme and the previously described assumptions, the following rate of reaction equations were derived:

Equation 3.30 Rate of reaction for hexokinase based on the above reaction scheme

$$v = \frac{d[P]}{dt} = \frac{k_{cat}[E_0][ATP][Glc]}{K_{m,ATP}K_{m,Glc}\left(1+\frac{[ADP]}{K_{i,ADP}}+\frac{[G6P]}{K_{i,G6P,I}}\right)+[ATP]K_{m,Glc}\left(1+\frac{[G6P]}{K_{i,G6P,I}}+\frac{[G6P]}{K_{i,G6P,II}}+\sum\frac{[Hex_i]}{K_{i,Hex}}\right)+[ATP][Glc]\left(1+\frac{[G6P]}{K_{i,G6P,I}}+\frac{[G6P]}{K_{i,G6P,II}}+\frac{[G6P]}{K_{i,G6P,III}}\right)}$$

3.4.1.7. Hill Coefficients

The Hill equation is used to yield thermodynamic information about homotropic reactions and is a measure of cooperativity of the binding reaction. A value of 1 for n indicates non-cooperative behaviour and thus simple Michaelis-Menten kinetics, while values of less than 1 indicate negatively cooperative behaviour and values greater than 1 indicate positive cooperativity. Hill coefficients were obtained from literature for a number of reactions within the NSD metabolic network and are indicated in Appendix A. Fractional occupation (θ no units) of an enzyme species for a single substrate reaction is described by Equation (15), where S denotes substrate concentration.

Equation 3.31 Hill equation describing the fractional occupation of an enzyme by its substrate

$$\theta = \frac{[S]^n}{K_m + [S]^n}$$

3.4.1.8. Glycolysis

The rate of the glycolysis reaction has been described by Chen *et al.* and is given by Equation 16, where both the dissociation constant for Fructose-6-phosphate and the Hill coefficient, are a function of fructose-2,6-bisphosphate (Chen et al., 2012b).

Equation 3.32 The rate of Fructose-6-P removal to glycolysis

$$v = \frac{d[P]}{dt} = \frac{k_{cat}[E_0]}{\left[1 + \left(\frac{K_{m,F6P}}{[F6P]}\right)^n\right]\left(1 + \frac{K_{m\_ATP}}{[ATP]}\right)}$$

The reactions of the NSD network include five reactions with allosteric regulation, six species with cooperative binding behavior and a total of 76 competitive, non-competitive and un-competitive inhibitory terms. For the case of enzyme activation through allosteric regulation, the initial enzyme concentration term was replaced as shown below.

Equation 3.33 Enzyme concentration with Allosteric activation

$$[E_0] = \frac{[E_0][A_{activator}]}{K_{A,A} + [A_{activator}]}$$

Additionally, there are nine transport rate equations, each accounting for the transport of a specific nucleotide sugar species out of the model, *i.e.*, from the cytoplasm into the Golgi or ER. The transport equations contain a Michaelis-Menten kinetics term including the transport protein dissociation constants, as summarized by del Val *et al.* (del Val et al., 2011), and a second term reflecting the theoretical nucleotide sugar consumption rate. An exception to this was the CMP-Neu5Ac transporter, which is known to be competitively inhibited by UDP-HexNAc species and hence, an inhibitory term has been included in the transport protein dissociation constant to reflect this (Rijcken et al., 1995).

Equation 3.34 General NSD transport rate equation from the cytoplasm to the Golgi or ER

$$NSD\ transport\ rate = \left(\frac{[NSD]_{IC}}{K_{TP,\,NSD} + [NSD]_{IC}}\right)\left[\left(\frac{\mu}{V_{cell}} N_{gly,cell} N_{NSD,gly}\right) + \left(N_{gly,mab}\, N_{NSD,mAb} F_{mAb}\right)\right]$$

The NSD consumption rate contains terms for the host cell glycan structures and the antibody product. The first term of the summation describes the rate of glycan addition to host cell protein and is a function of cell growth. The glycan distribution on host cell proteins is assumed to be constant throughout the culture. Based on a protein weight of 33.7 µg/10^5 cells as reported by Bonarius *et al.* (Bonarius et al., 1996) and an averaged computed amino acid monomer molecular weight of 127 µg/µmol (Nolan and Lee, 2011), an amino acid concentration per cell was found. Multiplying the cellular amino acid concentration with an *O*-linked glycan frequency of 0.00371 glycans per amino and an *N*-linked glycan frequency of 0.00400 glycans per amino acid for 64.9% of glycosylated host cell proteins (Apweiler et al., 1999), an *O*-linked and *N*-linked glycan concentration of 1.41 × 10^{-8} µmol/cell and 1.31 × 10^{-8} µmol/cell, respectively, was calculated for each glycan species. This in turn gives a total number of glycans per cell of 2.72 × 10^{-8} µmol/cell ($N_{glyc,cell}$). Furthermore, mass spectrometry data of the human mature B-cell glycoform was used to find the average compositions of *O*-linked and *N*-linked glycan structures based on the relative abundance of each species. The findings for each sugar species are summarized in

Table 3.1. Thus, the system becomes constrained through the nine calculated outlet fluxes required to maintain cell growth. The glucose flux towards glycolysis is a function of the enzyme concentration (E_{glyc}) for the reaction step from fructose 6-phosphate to fructose 1,6-bisphosphate and thus, is allowed to vary as part of the parameter estimation as well as with the concentration of its substrate fructose 6-phosphate. The kinetic data and reaction mechanism were obtained from Chen *et al.* (Chen et al., 2012b). This step is assumed to be irreversible and acts as the main outlet flux from the NSD network. The NSD flux towards antibody production is based on the antibody production rate from the cell growth model and the experimentally determined glycoform of the HFN7.1 monoclonal antibody.

Table 3.1 Frequency of sugar species occurrence in glycans of mature human B-cells.

Glycan type	GlcNAc	GalNAc	Man	Gal	Neu5Ac	Fuc
N-linked glycan	2.896	0	5.813	0.759	0.516	0.332
O-linked glycan	0.156	1	0	1.156	1.543	0
Glycan average ($N_{NSD,glyc}$)	1.579	0.481	3.018	0.950	1.010	0.173

While enzyme concentration levels of the nucleotide sugar metabolic network have been predicted to change based on transcriptomic analysis (Wong et al., 2010a), they were held constant as part of this study due to lack of dynamic proteomic data. An initial enzyme concentration value was obtained based on an average hybridoma cell protein dry weight fraction and an averaged cell volume as reported by Frame *et al.* (Frame and Hu, 1990) and Lee *et al.* (Lee and Lee, 2000). The average enzyme purification, to obtain a pure sample for a specific enzyme from the NSD metabolic pathway, was found to be 1000-fold with an average molecular mass of 61kDa based on the obtained literature values. Based on the above purification data each enzyme makes up 0.1% of total cell protein resulting in an average molar enzyme concentration of 3.9 μM, which was used as an initial value for all subsequent parameter estimations.

Glycolysis and the pentose phosphate pathway account for the majority of glucose and other hexose feed consumption in mammalian cells. The first three species of the nucleotide sugar network, namely glucose, glucose-6-phosphate and fructose-6-phosphate are substrates for both glycolysis and nucleotide sugar synthesis. The NSD model input is that of the total glucose consumption by the cells and, hence, the fraction consumed by glycolysis

needs to be accounted for, where fructose-6-phosphate branches off from NSD metabolism to glycolysis. This has been addressed by inclusion of the appropriate glycolysis equation as described in 3.4.1.8.

Studies by Fujita *et al.* on phosphomannose isomerase deficient mice suggested that the mannose salvage pathway is in fact substantial (Fujita et al., 2008). As a result the cleaved mannose from the glycan core structure is fed back into the metabolic pathway as part of the mathematical model. The amount of salvaged mannose per *N*-linked glycan is obtained through the difference of the original glycan precursor structure featuring nine mannose molecules and the final average mannose count per glycan of the host cell protein or antibody product. This also applies to UDP-Glc, where the glucose molecules added to the glycan precursor are salvaged as intracellular glucose. It was assumed that four UDP-Glc molecules are consumed per glycan in the Calnexin and Calreticulin cycle.

Including reverse and parallel reactions as well as the nine transport rates, a total of 69 distinct reactions is simulated as part of the bottom-up approach model. In addition, there are nine non-NSD species held at constant concentration and intracellular glutamine, which due to lack of experimental data has been assumed to follow intracellular glucose concentrations. While initial concentrations for nucleotide sugar species have been experimentally determined, no data was available for any intermediate species. The initial concentrations of the remaining 27 species have been estimated at steady state using the mathematical model such that the initial conditions for the seven experimentally measurable nucleotide sugars are met.

3.4.2. Parameter Estimation

Sensitivity analysis is a powerful tool, which can be used in model development for identifying and ranking the impact of input parameters variation with respect to model outputs. Knowledge about the relationship of model inputs with respect to outputs can offer a valuable insight into complex models and thus, allow for improved design of experiments (Kontoravdi et al., 2010) or, as presented in this study, to allow for more targeted parameter

estimation and parameter space reduction during model training. The method employed in this study is the Sobol global sensitivity analysis (GSA) method, which provides quantitative results and incorporates the entire range of parameter values. With this method, all input parameters are varied simultaneously, accounting for non-linearities and capturing parameter interaction effects. In this study total effect Sobol Sensitivity Indices have been computed, which are based on the ANOVA decomposition as extensively discussed in literature (Sobol, 2001, Kontoravdi et al., 2005, Kiparissides et al., 2009).

The Sobol GSA was applied to the bottom-up model with a total of 46 input parameters to be examined. The 46 parameters included the enzyme concentrations and any other parameters for which no numerical values were available in literature. The GSA has been performed on the parameters as initially estimated, as opposed to values obtained from literature. The first parameter estimation was carried out to ensure that the predicted NSD concentrations were within a physiological range as well as to prevent species accumulation, thus defining a physiologically-relevant range for parameter values. A GSA performed on parameter values far removed from their physiological range carries no significance, as the parameter contribution to the output could be artificially small or large. Once the relevant nominal value set had been identified, the GSA range was set at 25-400% of these nominal values in the case of the NSD network. The values are based on experimentally observed changes in mRNA transcription levels of N-glycosylation related genes during fed-batch culture of CHO cells (Wong et al., 2010a). The parameter set includes 30 enzyme concentrations, eight dissociation constants, seven turnover rates and one Hill coefficient. The enzyme concentration governing the outlet rate towards glycolysis has been excluded from the GSA as it accounts for between 95.8% and 97.6% of total glucose flux into the cell at any given time. Those values are in agreement with Chen *et al.*, who calculated the fraction of glucose, going towards the nucleotide sugar metabolic network to be 3.52% for CHO cells (Chen et al., 2012b) based on previous experimental work by Goudar *et al.* (Goudar et al., 2010). This parameter is known to be important and was expected to dwarf others, as was confirmed by a preliminary GSA study. The remaining 46 parameters created a very large parameter space and thus, a very large sample set was required in order to map the model behavior accurately resulting in computationally very expensive calculations. In order to reduce calculation times, a metamodel was created using SobolHDMR v2.0, a general

purpose metamodeling software. The program is based on a number of Random Sampling-High Dimensional Model Representation (RS-HDMR) methods. The original RS-HDMR method is presented by Li *et al.* (Li et al., 2002, Li et al., 2006) and Li and Rabitz (Li and Rabitz, 2006) while the improved techniques have also been extensively described (Feil et al., 2009, Zuniga et al., 2013). All of the implemented techniques use Quasi-Monte Carlo sampling based on Sobol sequences. Supplied with "black-box" data of input parameter values with a sample set of 131,072 (2^{17}) and corresponding model outputs, a metamodel was created upon which the GSA was performed, thus greatly reducing computational cost.

The GSA was performed on the parameters with respect to the seven outputs of the NSD model, which are the intracellular NSD concentrations. The GSA was performed for the outputs at time points 20 h, 40 h, 60 h, 80 h and 120 h corresponding to early-exponential, mid-exponential, late-exponential, stationary and decline growth phases, respectively. Indices greater than 0.036, the lowest experimental error in NSD concentration measurements, have been deemed significant and are marked in red in figure 3.13 (numerical values in Appendix B). As indicated by one or more red spaces in a vertical columns in the figure, the results indicate that 22 of the 46 analysed parameters are, in fact, significant. The results suggest that UDP-GlcNAc and UDP-GalNAc as well as GDP-Man, UDP-Gal and UDP-Glc share a group of input parameters by which they are affected. CMP-Neu5Ac and GDP-Fuc lying at outer extreme points of the network are each affected most by distinct parameter sets. The results also suggest that the significance of most parameters does not change with time but rather with respect to NSD output species. In all subsequent parameter estimations only 22 of the original 46 parameters were estimated and the remainder left at their nominal values. This allowed for a more targeted parameter estimation, which reduces computational costs and increase parameter confidence, while reducing chances of overparameterisation.

Since many parameters were shown not to have significant impact on model outputs, this presents scope for a formal model reduction to tackle the aforementioned difficulties. All estimated parameters are summarised in Appendix C. While extensive quantitative proteomic (Geiger et al., 2013, Baycin-Hizal et al., 2012) as well as transcriptomic (Xu et al., 2011) maps for mammalian species are beginning to appear, there is no data available for

absolute enzyme concentrations within the NSD metabolic network. Additionally, the uncertainty in turnover rate data makes a comparison of estimated enzyme concentrations with literature data not feasible at this point.

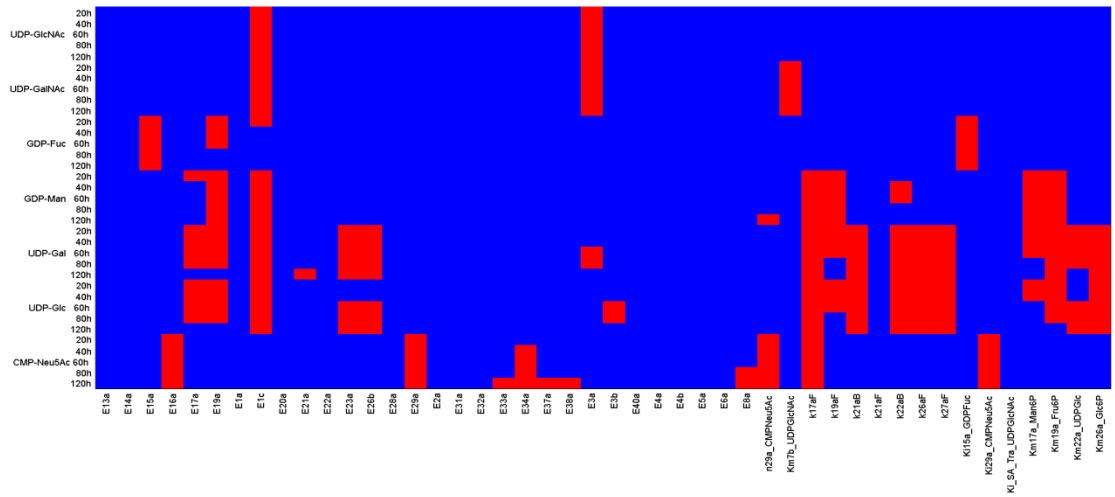


Figure 3.13 Visual representation of the GSA output (S_{Tot}) of input parameters (x-axis) against NSD outputs at different time points in cell culture time (y-axis). Red fields indicate an indice greater than 0.036.

3.4.3. Non-NSD Species

Table 3.2 Non-nucleotide sugar species and their intracellular concentrations.

Intracellular species	Intracellular conc. (mM)	Source tissue
Acetyl Coenzyme A (**ACoA**)	0.029	Rat liver
Coenzyme A (**CoA**)	0.13	Rat liver
Glucose-1,6-biphosphate (**Glc16PP**)	0.014	Mouse liver
Nicotinamide adenine dinucleotide (**NAD**)	0.76	Rat liver
Nictotinamide adenine dinucleotide phosphate (**NADP**)	0.067	Rat liver
Nictotinamide adenine dinucleotide phosphate, reduced (**NADPH**)	0.30	Rat liver
Phosphoenolypyruvic acid (**PEP**)	0.11	Mouse liver
Inorganic phosphate (**PPi**)	3.37	Rat liver
Pyruvate (**Pyr**)	0.18	Mouse liver

In addition to the 34 sugars and nucleotide sugars of the NSD *de novo* synthesis network, the nucleotides and glutamine there are nine additional intracellular species, which play a role in the catalysis of the NSD metabolic network as co-substrates, activators and inhibitors. Intracellular data of these species concentrations was obtained from literature as reported by Williamson *et al.* and is listed in Table 3.2 (J.T., 1974). Fortunately all reactions involving the listed species did not feature parameters that contribute significantly to NSD species output, as determined by the GSA. This suggests that none of these reaction steps were rate-limiting and by extension none of the nine additional intracellular species had any significant impact on NSD outputs. As a result of this all concentrations are assumed to remain constant throughout the investigation.

3.5. N-linked Glycosylation model

The fourth part of the model framework describes the glycosylation process of a monoclonal antibody product in the Golgi apparatus. The model has been developed and described previously by del Val et al. (del Val et al., 2011). The model is a function of the antibody production rate as described by the cell culture dynamics model and the availability of NSD species as described by its corresponding module. The Golgi apparatus is modelled as a dynamic plug flow reactor (PFR) and hence,

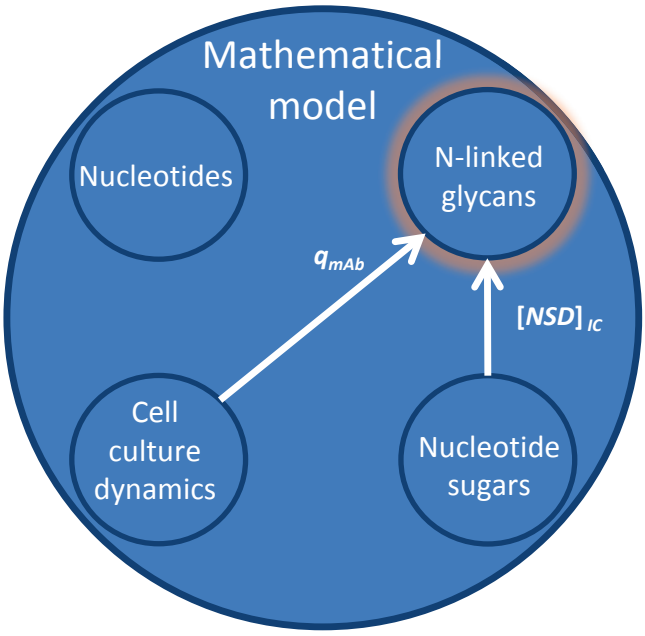


Figure 3.14 a schematic of the glycan model and its dependence within the mathematical model platform

assumes Golgi maturation as discussed in chapter 1.1. This model was chosen over other previous modelling efforts due to its specificity to antibody glycosylation and highest predictive accuracy. The result is a dynamic product glycoform and thus, the final output of the modelling framework. It was assumed that transport of NSD species into the Golgi is not limiting. This allows for the transport rate expressions of the del Val model to be bypassed and the glycosyltransferase rate expressions to become a function of the cytosolic NSD concentrations, as opposed to those of the Golgi lumen. This allows for the mathematical model structure to be reduced from a complex system of partial differential system (PDEs) to a simpler system of ordinary differential equations (ODEs). Consequently, computational costs are reduced and thus, model running time significantly reduced. Furthermore, no experimental data was collected of intra-Golgi NSD and nucleotide concentrations due to experimental limitations. Consequently, to arrive at intra-Golgi concentrations would require an additional set of assumptions to make up for lack of data and hence, little added benefit is perceived in compartmentalisation of *in silico* NSD concentrations, with respect to this work.

3.6. Model Training, Results and Discussion

This first proof of concept model was trained using in house hybridoma data. The main emphasis of the training was to demonstrate the model framework's ability to reproduce experimentally derived data. Successful training gives confidence in the platform structure and justifies further model development based on the framework outlined in this chapter.

The dynamic Monod kinetics growth model was able to describe the consumption of glucose and glutamine as well as cell growth and cell death (figure 3.15). Interestingly, the model equation describing mAb production was a function of cell density only, but was still able to describe mAb titer well, indicating that mAb productivity was independent of the specific cell growth rate, which has been reported previously for hybridoma cell culture systems (Ozturk and Palsson, 1991).

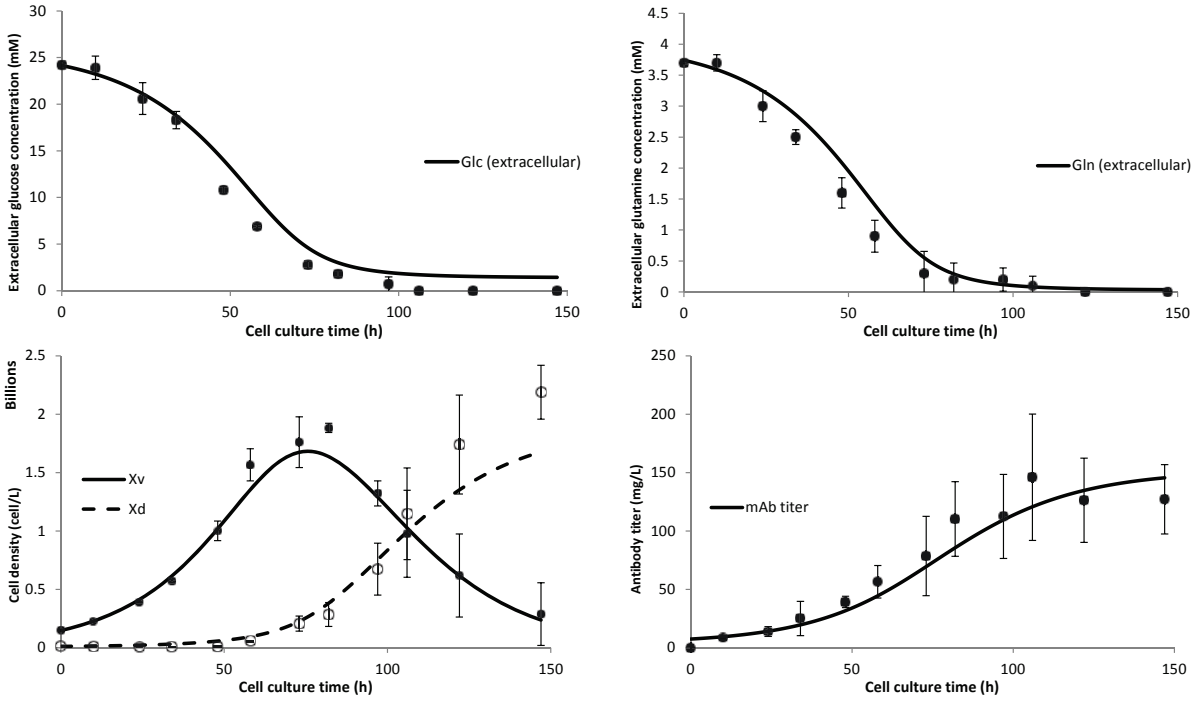


Figure 3.15 Experimental data compared with generated fits from the dynamic Monod growth model. Fits for extracellular glucose concentration (top left), extracellular glutamine concentration (top right), viable and dead cell density (bottom left) and antibody titer. [Reproduced with permission]

Figure 3.16 depicts the fits of the simple nucleotide model as compared with the experimentally determined intracellular nucleotide concentrations. The model based on the reduced network was able to produce fits that are within the experimental error range for most data points. Some oscillatory behaviour can be observed, most notably with the GTP output. This effect is most likely due to the assumption that the flux of nucleotides out of the system is a function of growth only. This may create a mismatch between species synthesis and consumption, which may become much more prominent in a simplified network representation, where no control mechanisms, such as various types of inhibitions are considered. To improve upon this fit would require an extensive analysis of the intracellular fluxes of the nucleotides involved and thus, decoupling the outlet flux from the cell growth term or inclusion of the cell regulatory mechanisms by means of inhibitory terms.

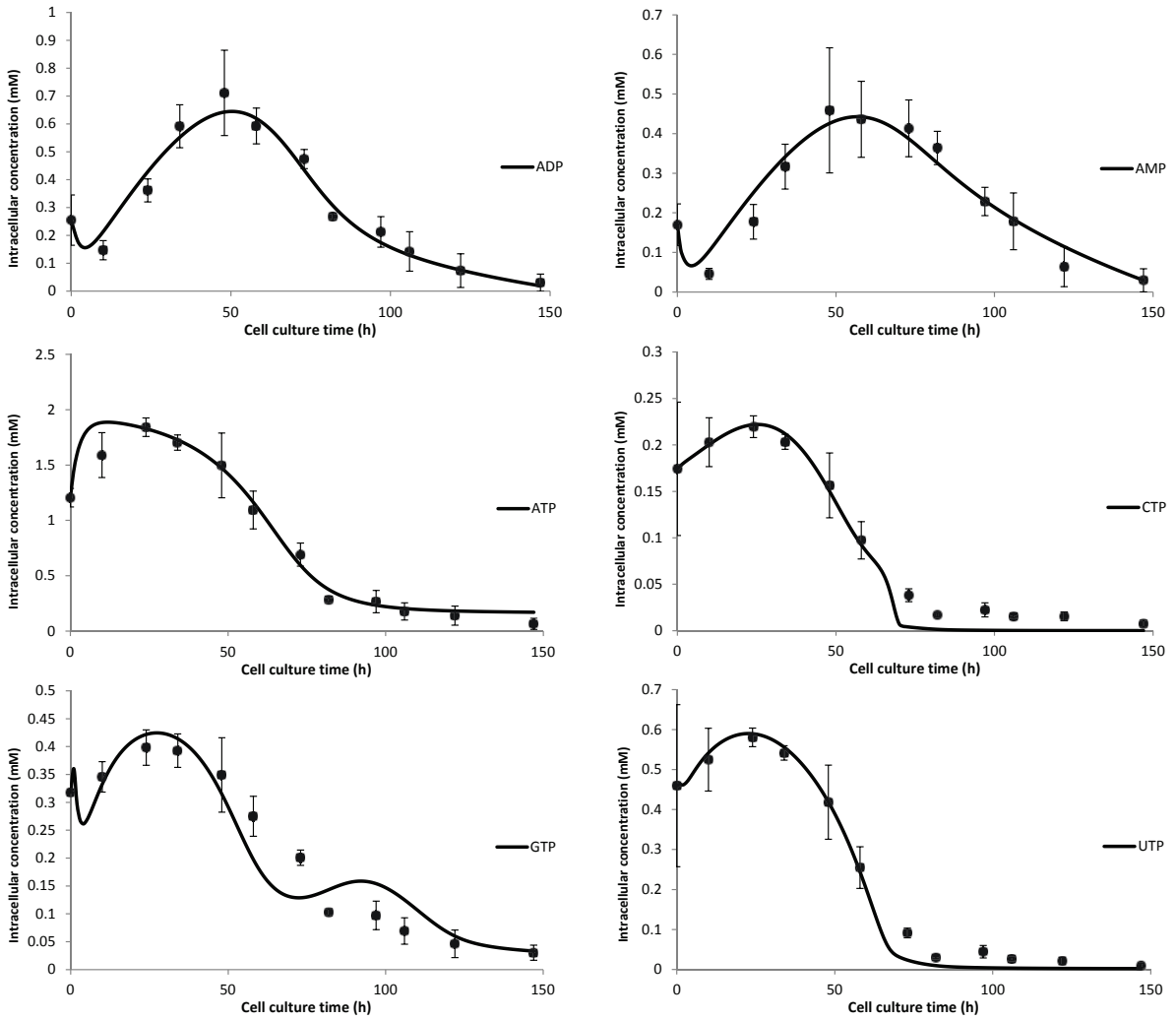


Figure 3.16 Experimental data compared with generated fits from the nucleotide model. Fits for intracellular ADP concentration (top left), intracellular AMP concentration (top right), intracellular ATP concentration (center left), intracellular CTP concentration (center right), intracellular GTP concentration (bottom left) and intracellular UTP concentration (bottom right). [Reproduced with permission]

The main focus of this chapter is the mechanistic bottom-up nucleotide sugar synthesis model, which was able to produce satisfactory fits for all species other than GDP-Fuc (figure 3.17) and the late culture stage UDP-Gal concentrations. The difficulties in estimating GDP-Fuc concentrations stem from its comparatively low intracellular concentration and, thus, the relatively large uncertainty in its measurements (including concentrations below the detection limit for some time points). Additionally, due to the lack of dynamic GDP-Man data, estimations of dissociation constants and enzyme concentrations of the reaction steps leading up to GDP-Fuc do not restrict the parameter space sufficiently to arrive at a satisfying result. Like the nucleotide model, the NSD outlet fluxes are a function of the cell

growth rate. The size of the metabolic network and the various intra-network interactions pose an additional challenge to the estimation of parameters as well as the design of experiments to improve parameter fit. The under-prediction of UDP-Gal concentrations during the late culture stage may be a result of the depletion in extracellular glucose, which in turn led to depletion of intracellular glucose. Due to the proximity and connection by means of reversible reactions of UDP-Gal to the glycolysis outlet, a combined depletion resulting from glycolysis as well as species consumption may have taken place.

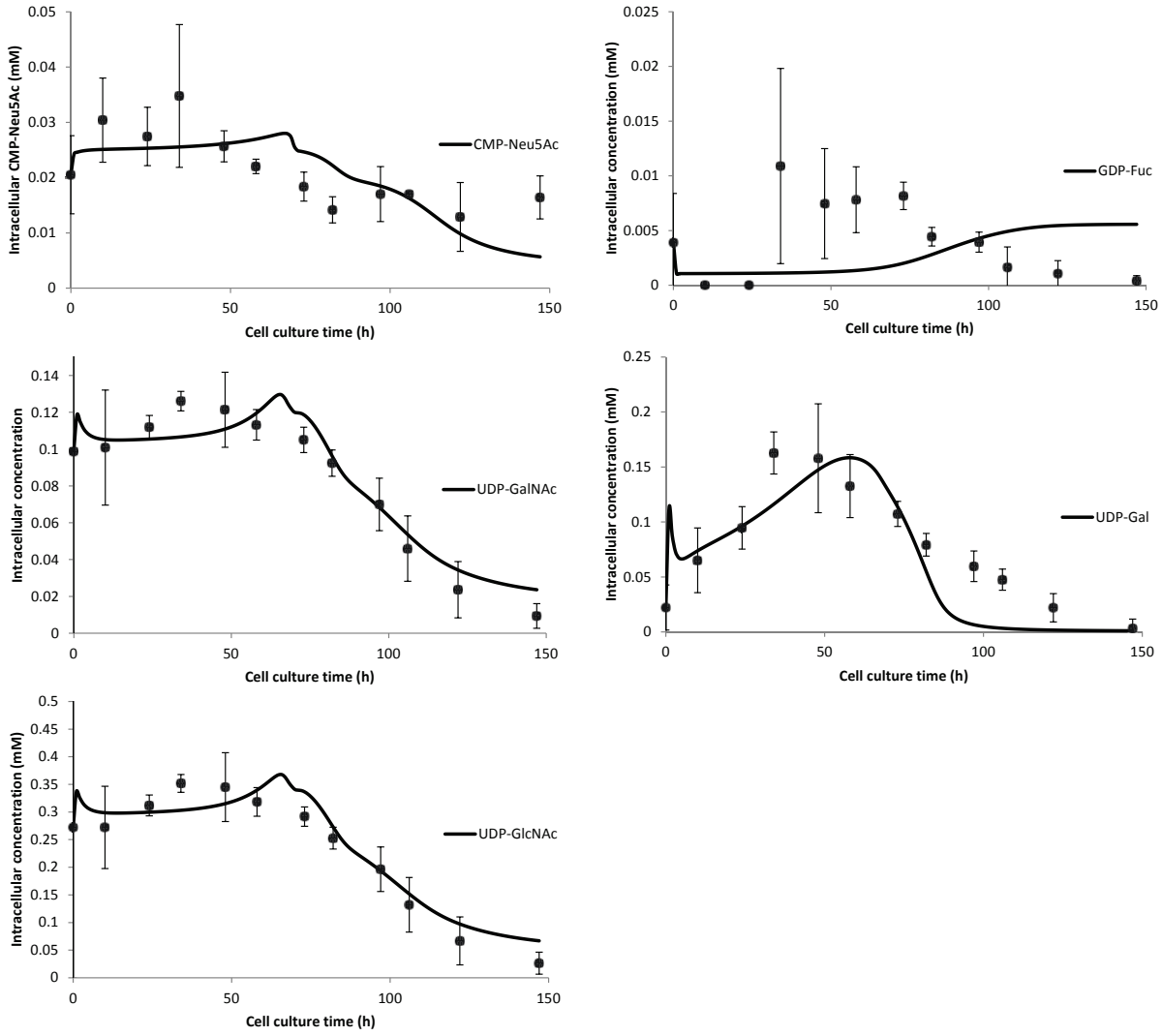


Figure 3.17 Experimental data compared with generated fits from the mechanistic bottom-up approach nucleotide sugar synthesis model. Fits for intracellular CMP-Neu5AC concentration (top left), intracellular GDP-Fuc concentration (top right), intracellular UDP-GalNAc concentration (center left), intracellular UDP-Gal concentration (center right) and intracellular UDP-GlcNAc concentration (bottom left). [Reproduced with permission]

The output from the nucleotide sugar donor model, *i.e.*, the NSD concentrations, were fed into a model describing the cumulative *N*-linked glycosylation of the antibody Fc region in order to estimate the resulting glycan distribution on the product. The results compare well with the measured data for product glycosylation, as shown in figure 3.18. The glycan data for time points 48 h and 72 h of the cell culture corresponding to exponential and stationary growth phases, respectively, are shown compared to the model simulation results. The glycan distribution is estimated by the model with fair accuracy, where the largest deviation of the computational output is 16% of the experimentally determined value. The deviations observed suggest that the experimentally observed changes during this period may not be due to changes in nucleotide sugar concentration alone, but possibly also caused by variations in the levels of glycosyltransferases, whose expression level has been previously reported to change during culture in response to changes in nutrient availability (Wong et al., 2010a). Changes in mAb Golgi flux appear as an unlikely cause as the models suggest a constant recombinant protein flux through the Golgi however, the growth dependent NSD flux for the host cell protein production may play a role. A further indication that the degree of galactosylation is not a strong function of UDP-Gal during the given time period is a low Km value of 0.0024 mM for the UDP-Gal Golgi transporter (Milla et al., 1992). This is well below the measured and estimated UDP-Gal concentrations and indicates near saturation of the transport protein until later stages of the cell culture.

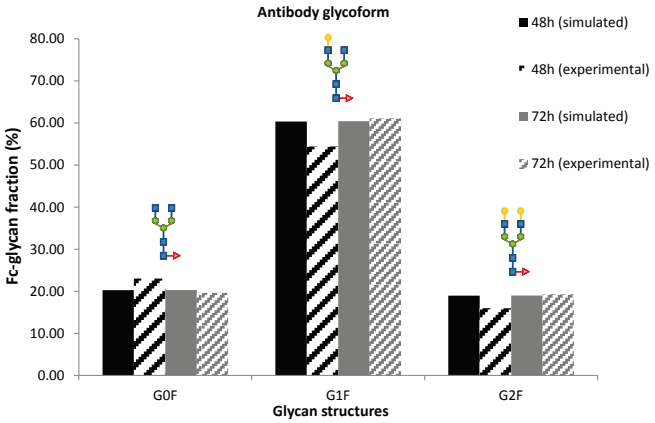


Figure 3.18 Simulated and experimentally determined distribution of the cumulative N-linked glycoform of the antibody Fc region for two time points during cell culture.

3.7. Conclusions

The holistic modelling framework presented is a first step towards quantifying the impact of extracellular nutrient concentrations on the glycoform of biotherapeutics through capturing changes in the nucleotide and nucleotide sugar metabolism. When trained with experimental hybridoma data the platform was able to reproduce cell dynamics and nutrient consumption throughout the culture time. However, the model is limited to batch cultures of hybridoma cell lines. This provides a strong starting point for further expansion to cell lines more relevant in the context of the production of biotherapeutics and cell culture regimes. Further experimentation and model training with Chinese hamster ovary cells (CHO) cell lines can address all the above and lead to a more relevant modelling platform for *in silico* optimisation of the glycosylation process in the context of biotherapeutics. More specifically a more industrially relevant glutamine synthetase (GS) CHO cell line presents an excellent choice for subsequent experimental and computational work. The GS technology enables cells to produce glutamine, which removes glutamine limitations that have been observed with the hybridoma cell line, as part of this work. However, regarding NSD metabolism this may also influence UDP-HexNAc production, where the GSA has indicated that the glutamine dependent reaction step (r3a in figure 3.6) has a significant impact on UDP-HexNAc model outputs. The decrease in UDP-HexNAc species in the late stages of cell culture may be a result of the glutamine depletion. Lastly, GS CHO cell lines can be grown in serum free cell culture media such that fully chemically defined media can be employed. This is particularly important with respect to subsequent feeding strategies, which can be used as a means to steer the cell culture. An extension of the experimental and modelling efforts to fed-batch culture is another compelling step. Fed-batch cultures are not only more industrially relevant but also prolong cell culture life, increase cell density and enable studying cell behaviour during the stationary phase, where total recombinant protein production is at its highest. With this operation mode nutrient limitations, such as that of glucose, can be delayed or avoided and thus, produce data that enables a better understanding of cell behaviour for a more complete probing and training of subsequent modelling efforts. A fed-batch operation regime also enables the study of accumulating metabolic by-products such as lactate and ammonia, which are known to inhibit cell growth.

In the case of ammonia detrimental effects can extend to the product glycoform, where high concentrations have been linked to a reduction in glycan complexity and thus, raising the need for observation and potentially control (Yang and Butler, 2000, Borys et al., 1994).

The performance of the novel intracellular nucleotide *de novo* synthesis model has been within the experimental error with respect to most species. While these are satisfactory results they are anticipated to only hold true under conditions where clear limitations of glucose and glutamine can be observed. An expansion of the modelling platform to a fed-batch platform is expected to remove these constraints and expose further dependencies, most notably those of glutamine and by extension glutamate as well as asparagine, who are known to play a role in the *de novo* synthesis of nucleotide sugars. Inclusion of glutamate and asparagine in the modelling platform would increase model robustness and accuracy. Further robustness can be added by inclusion of intracellular control mechanisms regulating nucleotide synthesis. These are most likely inhibitory mechanisms that not only regulate synthesis across the system but also prevent accumulation. Targeted experimental perturbations of the system by means of precursor additions provide a powerful tool to address these issues.

The model outputs for the intracellular NSD concentrations show promising results with respect to most species. The largest deviation can clearly be observed for the GDP-Fuc fit, where the computational and experimental results are in the same concentration range but the trends appear to be opposing. A probing of this branch of the *de novo* synthesis network is required, as there was not only a poor GDP-Fuc fit but also no experimental data available for GDP-Man due to its low concentration and analytical limitations. An effective perturbation of this branch of the network needs to be specific and sufficiently large to be easily and accurately quantified. In section 1.6.2 targeted nucleotide feeding strategies have been discussed and while none had been aimed at GDP-Fuc and GDP-Man a similar approach can be employed, where guanosine, the nucleotide precursor to guanosine triphosphate, can be supplied in the culture media. This approach should have a dual impact as it is expected to perturb both the intracellular nucleotide and the NSD network. This would give information about the speed and extend of response on GTP synthesis as well as its limitations due to cellular regulatory mechanisms of the nucleotide synthesis

pathway and also demonstrate the dependency of GDP-Fuc and GDP-Man on intracellular GTP. To further increase chances of a substantial response in the concentrations of both NSD species, additions of mannose can be made in order to achieve a synergetic effect, as has been reported for uridine and glucosamine with respect to UDP-HexNAc species (Grammatikos et al., 1998, Wong et al., 2010b). While both NSDs are not direct intermediates of the pathway linking intracellular mannose to glycolysis, the increased flux may translate to the metabolic offshoot branch, where both species are synthesised as shown in figure 3.6. A pulse addition of both supplements introduced during mid-exponential cell growth may yield the best results as no cell growth limiting factors should exist at this point and thus, allow solely for the observation of the effect of the two species on cell culture behaviour and *de novo* NSD synthesis.

The model also shows limitations with respect to the outputs for UDP-Gal towards late culture stages where glucose starts to become limiting. Studying UDP-Gal under glucose limiting condition may lead to richer data under this regime and hence, better fits at the late culture stage. However, the case of glucose depletion during a fed-batch operation in a biopharmaceutical environment appears rather unlikely, as it is known to impact glycan quality negatively to the extent of a near complete loss of glycan moieties in the antibody Fc region during periods of glucose depletion (Seo et al., 2014). As a result of this a further investigation into the impact of glucose depletion on NSD concentrations and associated metabolic changes is not warranted at this stage.

While the glycoform model outputs still leave room for improvement, a propagation of the computational limitations cannot be excluded at this point. This is underscored by previous work, where the model has been able to recreate the glycoforms of a range of antibody products (del Val et al., 2011) and thus, further training of the NSD model is expected to improve the final output of the modelling platform as well. Overall the results give confidence in the model platform and its structure and suggest a strong starting point for further improvement of the modelling framework. An immediate improvement should be achievable in a two-step approach of experimental work, where guanosine and mannose are fed to a GS CHO cell culture and a subsequent computational effort to capture the experimental observation and increase model robustness.

Portner and Schafer put forward that regardless of cultivation mode, cell growth will follow the same kinetics, although different cultivation modes will have differing suitability for the measurement of specific process conditions (Portner and Schafer, 1996). While batch cultures will give reliable date data on growth rate, additional fed-batch culture measurements can be employed to gain reliable data on nutrient utilization at low concentration. A further analysis showed that most modeling approaches will choose one or two growth limiting substrates, which preferably can be measured on-line. While previous data from batch-culture was available, fed-batch cultures at prolonged growth and high cell densities maximized the data output on utilization of nutrients at close to depletion.

Chapter 4

Mannose and Guanosine Feeding

In this chapter experimental fed-batch data obtained from a guanosine and mannose feeding experiment is presented. The experimental work was crucial, as further model training and extension based on experimental data allowed for improvements in model accuracy and relevance of the modelling platform with respect to biotherapeutic production. The outcome of chapter 3 highlighted the need to extend the experimental and computational efforts to GS-CHO fed-batch culture with a wider range of monitored metabolic species in the cell culture media and a targeted probing of the NSD metabolic network. Working with a glutamine synthetase cell line, where the cells are able to produce glutamine from glutamate and ammonia, made the inclusion of these metabolites in the measurement an obvious choice. Furthermore, lactate data became crucial during an extended fed-batch culture period due to its detrimental effect on cell growth at elevated concentrations as well as its potential partial substitution for glucose as a carbon source. Lastly and most importantly with respect to the novelty of this work, the design of a feeding strategy was required to improve the accuracy of the NSD model, which had particular shortcomings with respect to GDP-Fuc and GDP-Man metabolism. The latter, which is a precursor to the *de novo* synthesis of GDP-Fuc, was not observed in the previous hybridoma data. This was partly an analytical issue with the chromatography separation method due to co-elution of Tryptophan, as well as a problem of very low intracellular GDP-Man levels. GDP-Man is only involved in the formation of the glycan precursor and not in any of the subsequent modifications in the Golgi, however, intracellular concentration data would help to constrain the parameter space of the reactions leading up to GDP-Fuc via GDP-Man and should allow for improved model accuracy and robustness for both species.

Guanosine supplementation to mammalian cell culture, at concentrations as low as 100µM, is known to significantly increase intracellular GTP concentrations (Hines et al., 2010). Addition of this nucleotide precursor is expected to have a dual impact, as it will not only perturb *de novo* GTP synthesis but is also expected to affect the concentrations of GDP-Fuc and GDP-Man. The resulting data would offer valuable input for both the nucleotide as well as the NSD model. Previous work on phosphomannomutase (PMM)-deficient and phosphomannose isomerase (PMI)-deficient human fibroblast cells also suggests that mannose supplementation can increase GDP-Man pools (Rush et al., 2000). PMM catalyses the reversible conversion of mannose-6-phosphate to mannose-1-phosphate and PMI catalyses the reversible conversion of fructose-6-phosphate to mannose-6-phosphate labelled as reactions r17 and r19 on figure 3.6, respectively. The same study suggests that mannose feeding alone does not lead to an increase in GDP-Man in the experimental setup with control cells. However, feeding experiments with analogous aims of targeted increase in NSD species report a synergetic effect of nucleotide and sugar precursor additions with respect to intracellular NSD concentrations in recombinant mammalian cell culture systems (Wong et al., 2010b, Grammatikos et al., 1998). As a result a combination of the guanosine triphosphate precursor guanosine and the hexose mannose was expected to yield a synergetic increase in both GDP-Man and GDP-Fuc and perturb the network sufficiently to yield data for subsequent modelling efforts.

Mannose has previously been shown to be a good addition to or even substitute for glucose as a carbon source for cell culture (Berrios et al., 2011) and thus, little detrimental effect with respect to cell culture dynamics was expected. The Berrios et al. experiment was carried out at 10 mM of mannose, which proved to be sufficient to elicit a clear response. Further increases in the concentration were avoided to prevent high osmolarity in the extracellular environment. Guanosine, on the other hand, has been reported to arrest cell growth (Carvalhal et al., 2003). Additionally, guanosine has very poor solubility in pH neutral aqueous solutions and hence, guanosine required dissolution in dimethyl sulfoxide (DMSO), which is known to also arrest cell growth in CHO cells at concentrations of 1-2% v/v (Fiore et al., 2002). As a result, guanosine additions have been kept at low concentrations and equivalent amounts of DMSO have been added to the control culture to isolate the effect of mannose and guanosine additions only. The cell culture feeding was

carried out on day 5 of the experiment to ensure a balance between sufficiently high cell density and exponentially growing cells. At this stage of the culture cell metabolism is not expected to be hindered by any limitations in nutrients such that any metabolic changes can be attributed to the feeding alone. In order to allow for the quantification of the dynamic response of cells to feeding, readings in two hour time intervals were taken after feeding. All cultures were conducted with CD-CHO as the basal medium and in fed-batch mode with Feed C being supplemented every 48 hours starting on day 2 as per the manufacturer's instructions. All cultures were cultivated as triplicates (N = 3) and error bars indicate standard deviation (ER = SD). The final experiment conditions were:

- **Control –** 35.2mM (0.25% v/v) DMSO in cell culture after feeding.
- High Guanosine (**High G) –** 35.2mM (0.25% v/v) DMSO, 10mM Mannose and 1mM Guanosine in cell culture after feeding.
- Low Guanosine (**Low G**) – 35.2mM (0.25% v/v) DMSO, 10mM Mannose and 0.25mM Guanosine in cell culture after feeding.

All fed-batch cultures were also supplemented with CD EfficientFeed C® on even days of cell culture. The CD EfficientFeed C® (Feed C®) additions are referred to as "supplementation" of Feed C as opposed to "feeding", which is indicative of the guanosine and/or uridine additions on day 5 of culture.

4.1. Cell dynamics and extracellular environment

Measurements of the extracellular environment include viable cell and dead cell densities. The viable cell density allows for the calculation of the IVCC and represents a means of comparison of accumulated cell life time. This enables a systematic comparison of cell proliferation and cell lifetime between cultures and thus, highlights the effects of the various feeding strategies on cell culture dynamics. The dead cell density introduces a further means of monitoring these effects as well as allowing for the calculation of a total cell

density. This total density gives an indication of the absolute increase in cell densities and possible cell lysis. The antibody titer shows the concentration of the final product of the cell culture. Its concentration profile enables the tracking of specific productivity and how it is influenced by the cell environment and the various feeding strategies. Glucose and its metabolic derivative lactate are the main carbon sources and thus, energy source of the culture media. As a result it is crucial to measure their concentration in the cell's extracellular environment. Glutamine plays a crucial role in the biosynthesis of species such as nucleotides and NSDs, where it acts as a nitrogen source. Consequently knowledge of its concentration is crucial for any modelling efforts involving these metabolic networks. In a GS cell line it is synthesised from glutamate and ammonia resulting in the need to monitor the concentration of all three. Ammonia and lactate can also lead to cell growth inhibition and at high concentrations ammonia is known to negatively impact glycosylation and thus, giving further need to monitor their concentrations (Borys et al., 1994, Yang and Butler, 2000).

The outcome of the feeding experiment shows a distinct decrease in cell density after the feeding of the cell culture on day five as compared to the control (figure 4.1). The data in figure 4.1, of the total cell density, i.e. the summation of the viable and dead cell densities, suggests a complete inhibition of cell growth for both the high as well as the low guanosine concentrations. This is very much in line with what was observed by Carvalhal et al. (citation Carvalhal et al., 2003), who observed an accumulation of CHO cells in the S-phase and thus, halting cell division. While DMSO, which was added to all cultures, is also known to arrest cells growth at concentrations of 1-2% v/v (Fiore et al., 2002), there was still notable growth observable after its addition. Mannose substitution as a carbon source has been shown to have no detrimental effect on viable cell density but rather increase it (Berrios et al., 2011). From this, the conclusion is drawn that the cell growth arrest and resulting difference in viable and total cell density is due to the presence of guanosine, where both concentrations of guanosine produced the same effect.

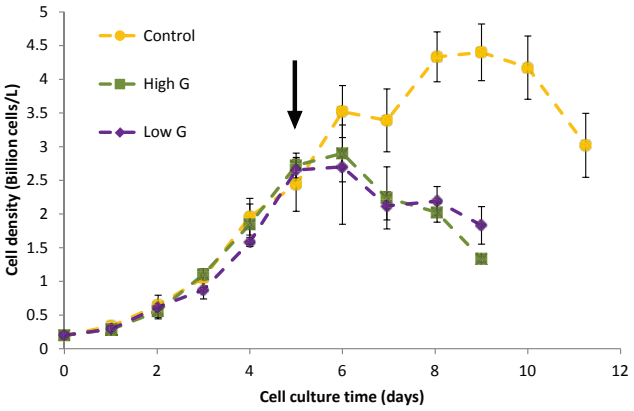


Figure 4.1 Viable cell density with respect to culture time of the three experimental runs (N = 3, EB = SD).

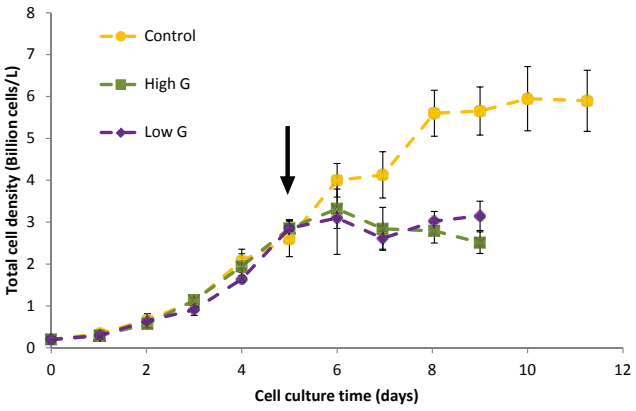


Figure 4.2 Total cell density, including both viable and dead cells, with respect to culture time of the three experimental runs (N = 3, EB = SD).

Interestingly, the antibody titer was not suppressed to the same extent as the viable cell density (figure 4.1) in the presence of guanosine. In fact, the specific antibody production is significantly higher after feeding compared to the control run as shown in figure 4.3. This is in line with the findings by Carvalhal et al., who reported a 1.8-fold increase in specific productivity of recombinant protein after the addition of guanosine to cell culture (Carvalhal et al., 2003). This can also be explained by the cell arrest in the S-phase, where specific productivity is increased. The impact of mannose addition to cell culture has been reported to have a much smaller effect on specific productivity than the changes observed in this study (Berrios et al., 2011). Both concentrations of guanosine produced effects that did not significantly differ from each other.

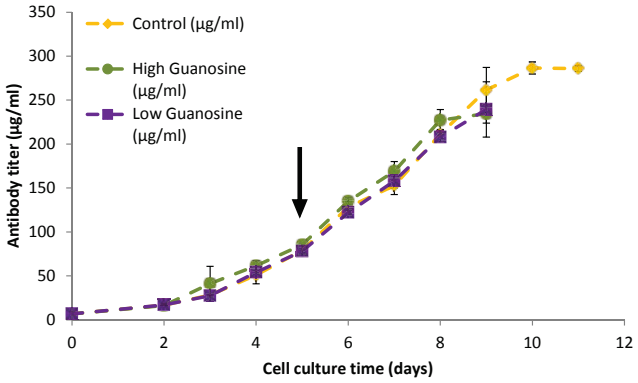


Figure 4.3 Antibody titer for all three experimental runs with respect to cell culture time (N = 3, EB = SD).

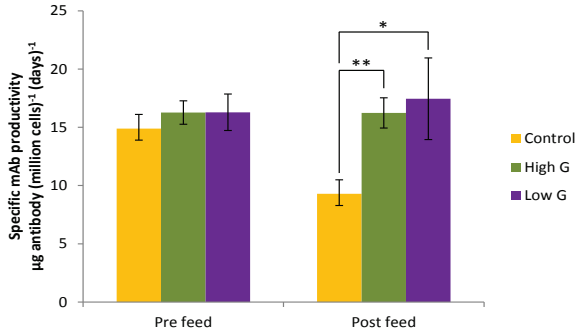


Figure 4.4 Comparison of specific mAb productivity for all three conditions pre feed (days 1 to 5) and post feed (day 5 to end of culture). A significant difference between IVCC values is indicated by asterisks, where * P < 0.05 and ** P < 0.01 (N = 3, EB = SD).

The extracellular guanosine concentrations show a very rapid decrease, where the guanosine was virtually consumed by the cells within the first 48 h and 24 h after the feeding of 1 mM and 0.25 mM of guanosine, respectively (figure 4.5). This suggests an irreversible cell growth arrest at both, the low and high guanosine concentrations, until the end of the culture, as the cells remained arrested despite the depletion of guanosine from the extracellular environment. The chromatography analysis method was not able to detect any levels of guanosine in the cell culture media of the control. The mannose pools, however, did not deplete within the culture time, although consumption was significant. The mannose concentrations measured in the control showed no concentrations outside the experiments error margin. As a result no significant concentrations of mannose can be reported. Lastly, there is no distinguishable difference in mannose consumption between both the High G and Low G culture.

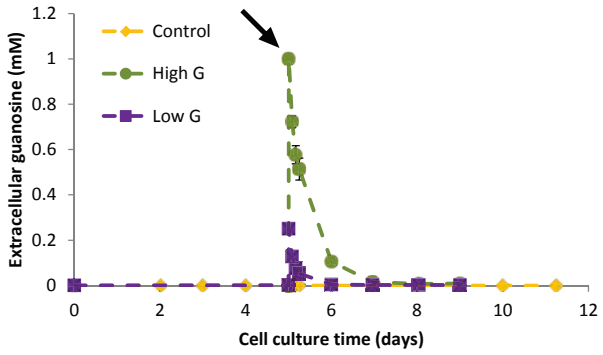


Figure 4.5 Extracellular guanosine with respect to culture time of both guanosine fed culture conditions (N = 3, EB = SD).

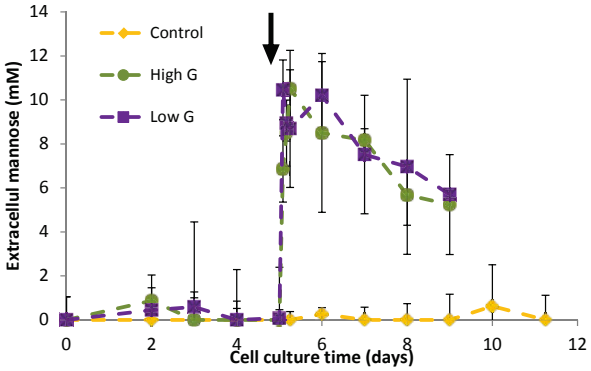


Figure 4.6 Extracellular mannose with respect to culture time of both mannose fed culture conditions (N = 3, EB = SD).

A change in extracellular glucose consumption is observed after feeding of mannose and guanosine, leading to a reduced uptake in the High G and Low G cultures as compared to the control flasks. Due to a reduced cell growth rate as a result of the guanosine feeding and any metabolic changes associated with this, it cannot be concluded whether the changes are due to a substitution of mannose for glucose. However, the total glucose uptake after the feeding is larger than that of mannose, where comparatively little consumption is seen. Hence, the results suggest that the cells do not take up mannose with a strong preference over glucose, yet both are consumed as parallel carbon sources. During the first four days of culture, the cells appear to produce lactate at a high rate before switching to a net

consumption of lactate (figure 4.8). The lactate concentration appears to differ from the control for both High G and Low G setups, where a larger net consumption of lactate is observed in the fed cultures. Berrios et al. reported that a substitution of the carbon source from glucose to mannose decreases the lactate production rate (Berrios et al., 2011). However, it can only be speculated as to whether the same effects are observed here or whether the reduced lactate concentration is a result of growth inhibition or metabolic changes.

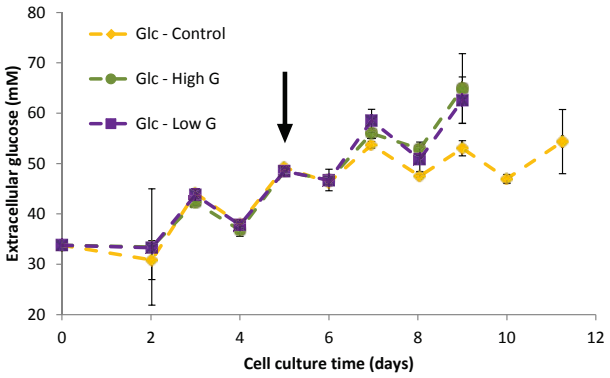


Figure 4.7 Extracellular glucose with respect to culture time for all three experimental conditions (N = 3, EB = SD).

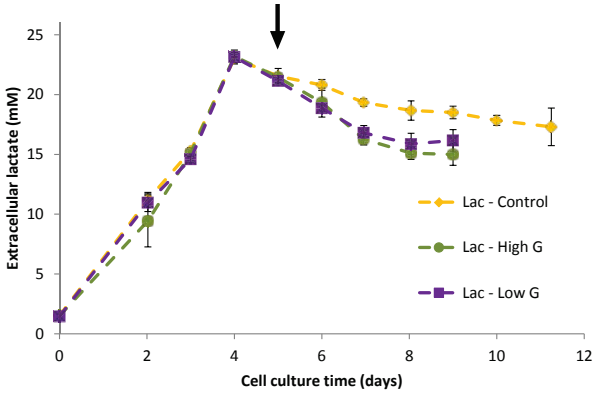


Figure 4.8 Extracellular lactate with respect to culture time for all three experimental conditions (N = 3, EB = SD).

A net consumption of glutamate can be observed at all times for the control run, however, the fed cultures showed a net production of glutamate after day five and only returned to a glutamate consuming regime after day seven (figure 4.9). The culture with the 1 mM guanosine addition shows a much higher increase in extracellular glutamate and little deviation is observed between the Low G and control cultures. This, combined with the timing of the glutamate increase suggests a link between guanosine consumption and glutamate production. The glutamine concentrations on the other hand showed a constant increase for all experimental conditions (figure 4.10). A significantly smaller net production of glutamine was observed when 1 mM guanosine was added to the cell culture media, while glutamate concentrations increased at the same time in the High G culture. This would suggest a decreased glutamine synthetase activity, which links both species in a reaction, where ATP and ammonia are consumed to add an amino group to glutamate thus producing glutamine. The extracellular ammonia measurements (figure 4.11) do not suggest

a significant difference between both guanosine-fed cell cultures, although a deviation from the control can be seen. This suggests that ammonia is not a factor affecting the extracellular glutamate and glutamine concentrations. The higher ammonia concentration in the control run may be an effect of the higher cell density and the resulting higher amount of metabolic by-products of which ammonia is one.

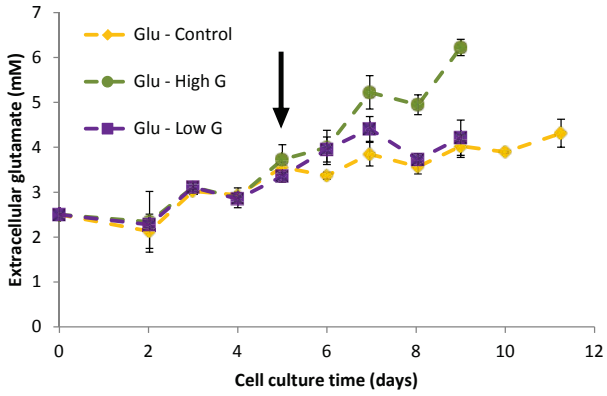


Figure 4.9 Extracellular glutamate with respect to culture time for all three experimental conditions (N = 3, EB = SD).

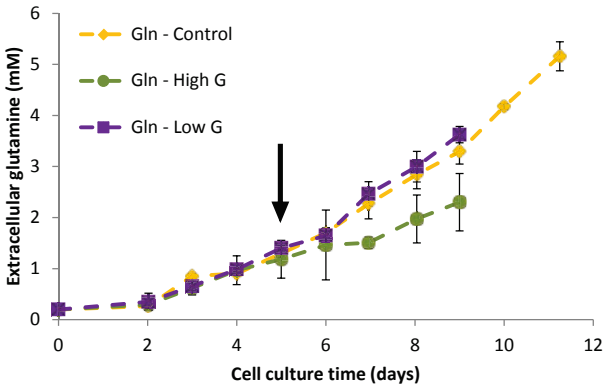


Figure 4.10 Extracellular glutamine with respect to culture time for all three experimental conditions (N = 3, EB = SD).

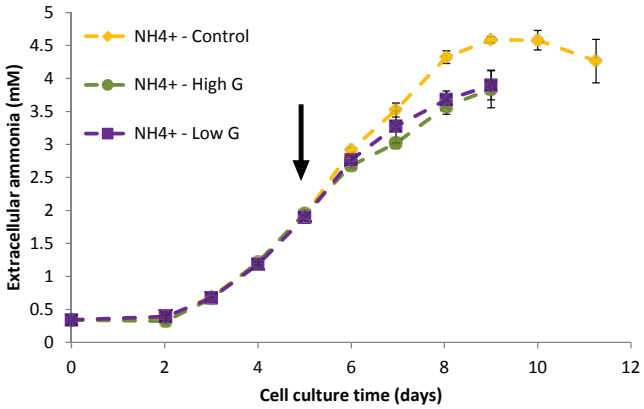


Figure 4.11 Extracellular ammonia with respect to culture time for all three experimental conditions (N = 3, EB = SD).

4.2. Intracellular metabolites

Intracellular concentrations of both hexoses are measured as part of the quantification of metabolites. Knowledge of their extracellular and intracellular concentrations allows identifying constraints of transport or accumulation in the intracellular environment, both of

which can lead to detrimental effects. Furthermore, it can elucidate more accurate knowledge of the cells' immediate response to the feeding strategies and the interactions of the fed species with intracellular metabolites. The same reasons apply to the intracellular glutamine concentration profiles. The concentrations of each nucleotide are known to be a driving force of NSD synthesis and, therefore, the need arises to monitor and model them. The concentration profiles are known to be interdependent and thus all need to be monitored to draw conclusions regarding the control mechanisms and dependencies within the synthesis network. The nucleotide triphosphate ATP is used by cells as a means of intracellular energy transfer and thus, it is the most crucial of the nucleotides with respect to the nucleotide and NSD synthesis networks. The mono- and diphosphate adenine species AMP and ADP are known to be inhibitors of a number of reactions in the NSD network. Consequently, it becomes necessary to monitor ADP and AMP due to their inhibitory role as well as increasing model accuracy of intracellular ATP.

The intracellular glucose concentrations of the control showed a reasonably stable profile with increases resulting from Feed C® supplementations (figure 4.12). On the final day of culture there is an accumulation of intracellular glucose, which suggests a slowdown in consumption due to a reduction in metabolic activity during the decline phase. The mannose fed samples, on the other hand, show an increase in intracellular glucose after the feeding. This may suggest a reduction in glucose consumption in the presence of mannose. Alternatively this may be explained by the fact that both hexoses compete for the same non-specific hexokinase. The increase in mannose would therefore lead to competitive inhibition between the species and thus, concentrations have to increase to maintain the flux into the metabolic network. The second explanation seems more likely as specific glucose transport appears not to have decreased. Again an increase is observed towards the end of the culture with a very pronounced accumulation on the last day of the high guanosine culture. A very similar picture is painted with respect to intracellular mannose (figures 4.13), where the concentration of the control does not vary much throughout culture time. While no extracellular mannose was added to the control cultures, its presence is not surprising due to the cells' ability for *de novo* synthesis as well as the large extent of mannose salvation from native glycans (Fujita et al., 2008). The mannose-fed cultures showed a sharp increase in

intracellular mannose after feeding on day five with prolonged higher levels and an accumulation towards the end of the culture period.

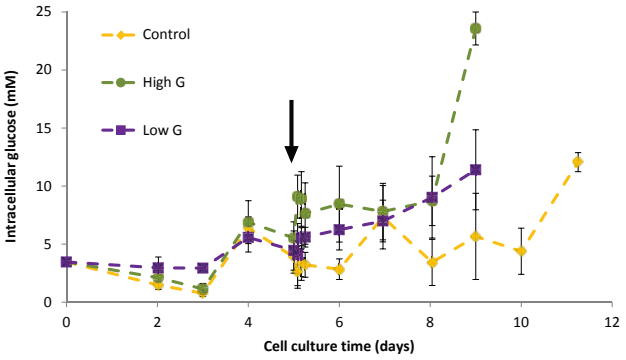


Figure 4.12 Intracellular glucose concentration with respect to culture time (N = 3, EB = SD).

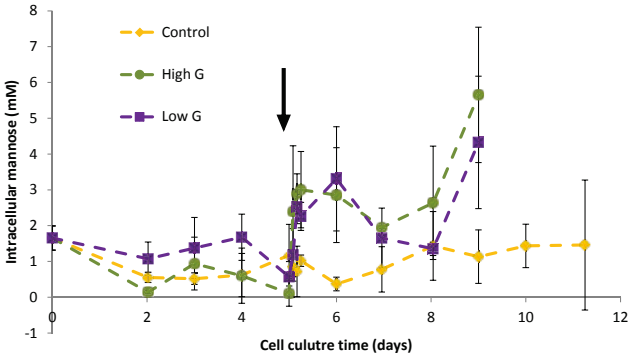


Figure 4.13 Intracellular mannose concentration with respect to culture time (N = 3, EB = SD).

The intracellular glutamine concentrations showed little significant concentration differences among all setups (figure 4.14). An overall increasing trend can be observed under all conditions for the last two days of culture. The High G and Low G cultures show a more rapid accumulation than the control. An accumulation of glutamine in the culture medium is observed during the same time period. This indicates continuing glutamine production towards the end of culture and possibly a reduced glutamine consumption.

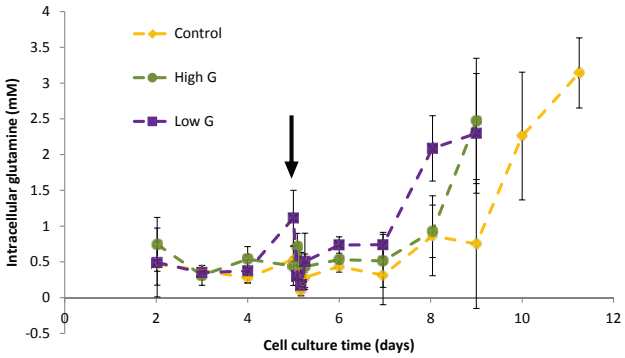


Figure 4.14 Intracellular glutamine concentration with respect to culture time (N = 3, EB = SD).

The intracellular concentrations of pyrimidines - cytidine triphosphate (CTP) and uridine triphosphate (UTP) - as well as the purines adenine monophosphate (AMP), adenine

diphosphate (ADP), adenine triphosphate (ATP) and guanosine triphosphate (GTP), were measured as part of the experiment. Most important with respect to the experimental setup was the dynamic response of the intracellular GTP to guanosine feeding (figure 4.15). The addition of guanosine, the precursor to GTP, led to a 3.9-fold and 3.7-fold increase in GTP over pre feed levels for the High G and Low G condition, respectively. This increase is observed within the space of two hours, while no change was observed in the control culture. Within the space of four hours the intracellular concentration increased further to a 4.4-fold as compared to pre feed levels for the High G condition, indicating further uptake of guanosine. The relatively small differences in the GTP concentration between both runs with guanosine additions indicate that the additions of 0.25 mM and 1 mM of guanosine in the extracellular media were close to a saturation point with respect to potential increases in GTP. However, the High G condition ensured more elevated GTP levels, although eventually a steady decline can be observed for both conditions.

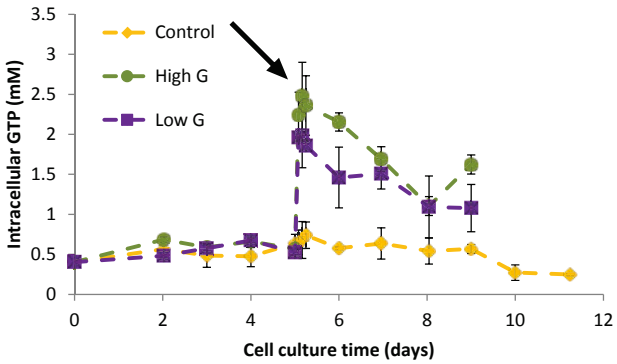


Figure 4.15 Intracellular GTP concentration with respect to culture time (N = 3, EB = SD).

The ATP profiles of the three runs showed minor deviations from each other in concentrations as well as trends (figure 4.16). The control showed a high concentration of ATP from the mid to the late exponential phase with a decline at the end. This decline in ATP, the most significant carrier of directly available energy, may be indicative of a decline in metabolic energy available to the cells leading to the observed drop in viable cell density. The guanosine-fed flasks showed a decrease in ATP after the feeding on day five with signs of recovery towards the end of the culture. This would suggest that cell death did not occur

due to insufficient metabolic energy but was due to other causes. Interestingly, the run with the high guanosine concentration also had a significantly higher ATP concentration after feed addition until the end of the experiment. Both ADP and AMP showed little difference in between the different experimental conditions (figures 4.17 and 4.18). A faster accumulation of ADP can be noted towards the end of the experiment for both the High G and Low G feed. These results seem counterintuitive in the context of elevated GTP concentrations, which is a substrate in the *de novo* synthesis of AMP and would therefore suggest an increase is to be expected. This may indicate saturation of the AMP synthesis reaction with respect to GTP at the lower control levels.

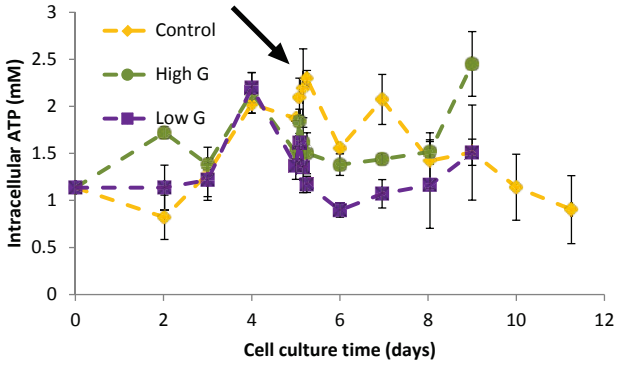


Figure 4.16 Intracellular ATP concentration with respect to culture time (N = 3, EB = SD).

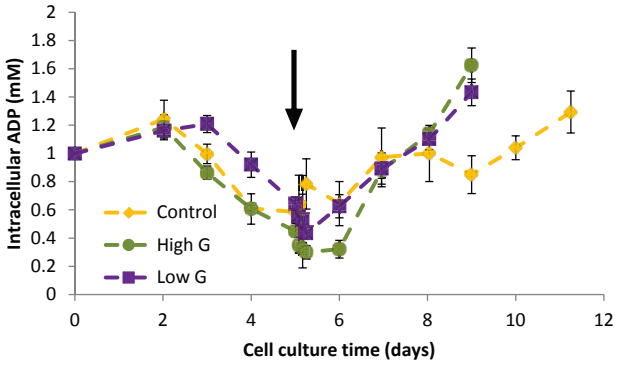


Figure 4.17 Intracellular ADP concentration with respect to culture time (N = 3, EB = SD).

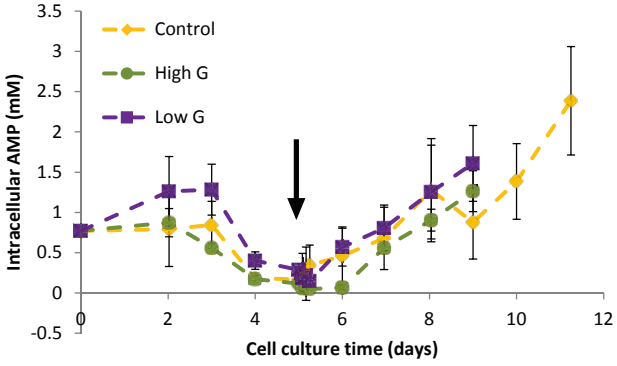


Figure 4.18 Intracellular AMP concentration with respect to culture time (N = 3, EB = SD).

The concentration profiles of both pyrimidine species CTP and UTP share similar profiles, despite the concentration of CTP being lower by roughly an order of magnitude. This is unsurprising given the fact that *de novo* synthesis of CTP is a result of an UTP ammonia ligase reaction step (EC 6.3.4.2). The concentration of both species in the control

culture starts to decline from the feeding day onwards although at a gradual rate. Both experimental runs with guanosine additions on the other hand show a steep drop in CTP and UTP concentrations after feeding with only a slight recovery towards the end of the culture. The concentration profiles for all three conditions seem to resemble those of their respective ATP concentrations, which may be explained by the involvement of ATP in the synthesis of both CTP and UTP. However, it also known that the purine species AMP is an inhibitor of pyrimidine synthesis to ensure a balance between the two nucleoside types (Jones, 1980). It can be speculated that the purine GMP may have a similar effect on pyrimidine synthesis and hence, leading to the concentration profiles observed in CTP and UTP.

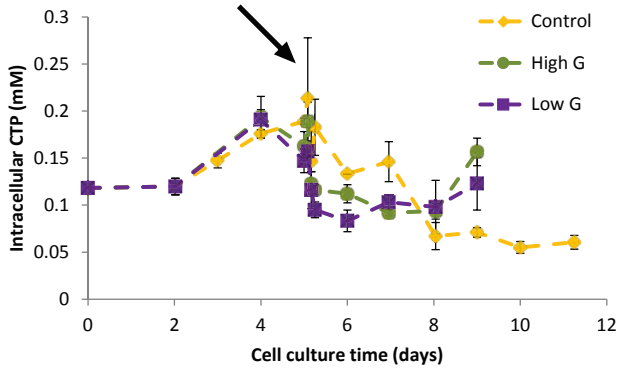


Figure 4.19 Intracellular CTP concentration with respect to culture time (N = 3, EB = SD).

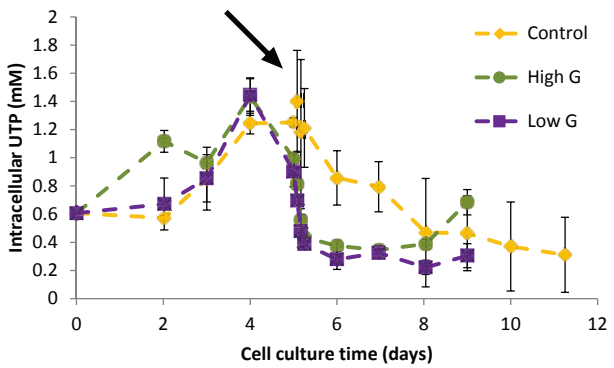


Figure 4.20 Intracellular UTP concentration with respect to culture time (N = 3, EB = SD).

4.3. Intracellular Nucleotide Sugar Donors

A large emphasis was put on the concentration profiles of the intracellular NSD species, specifically GDP-Fucose (GDP-Fuc), GDP-Mannose (GDP-Man), UDP-N-Acetylglucosamine (UDP-GlcNAc), UDP-N-Acetylgalactosamine (UDP-GalNAc), UDP-Glucose (UDP-Glc), UDP-Galactose (UDP-Gal) and CMP-N-Acetylneuraminic acid (CMP-Neu5Ac). Most important with respect to this experiment was the dynamic response of GDP-Fuc and GDP-Man to the feeding of guanosine. After the feeding on day five, a very fast response in GDP-Fuc concentrations was observed, with peak concentrations after four hours and no significant difference between both guanosine concentrations. In comparison

to the control cultures, the feeding produced a 2.7-fold and 2.3-fold increase in GDP-Fuc concentration in the High G and Low G condition, respectively. The concentrations stayed at an elevated level as compared to the control and a small amount of accumulation towards the end of the culture was observed in the High G condition. The control showed a gradual increase in GDP-Fuc towards the end of the culture but remained below the concentrations for the guanosine fed cultures at all times after feeding. The response of the GDP-Man levels to the feeding was also very rapid with maximum concentrations reached after four hours. The increase in GDP-Man was 3.1-fold and 2.2-fold with respect to the control for the High G and Low G condition, respectively. However, a decay in the concentration of the High G run was observable after the feeding, leading to no distinguishable concentration differences with respect to the control on day eight. The control showed an increasing concentration throughout culture time with a very low initial concentration. Guanosine feeding increased the intracellular GTP pools, which in turn seems to have elevated the concentrations of both GDP-Fuc and GDP-Man. The decrease in GTP concentrations (figure 4.15) over the duration of the culture appears to be mirrored by the GDP-Man concentrations where guanosine was fed. However, both NSDs experienced smaller relative concentration increases compared to the GTP nucleotide.

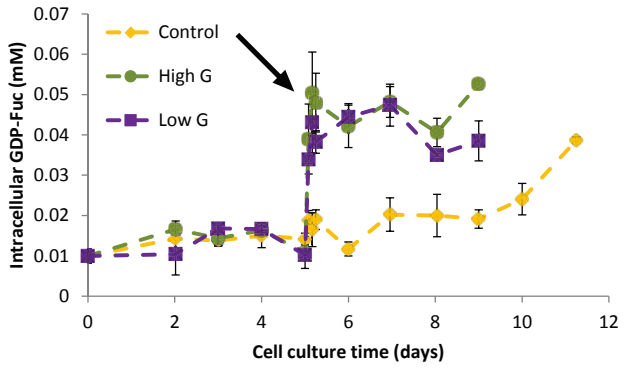


Figure 4.21 Intracellular GDP-Fuc concentration with respect to culture time (N = 3, EB = SD).

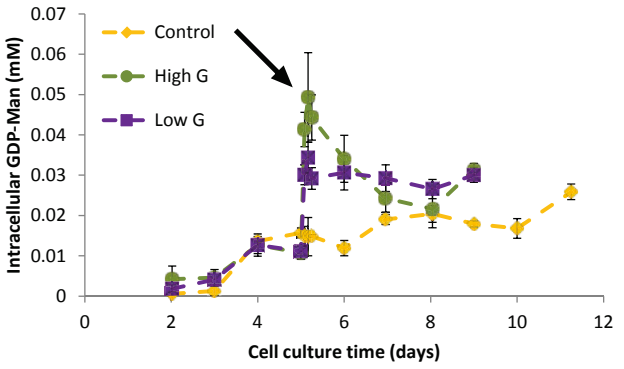


Figure 4.22 Intracellular GDP-Man concentration with respect to culture time (N = 3, EB = SD).

Both UDP-HexNAc species (UDP-GlcNAc and UDP-GalNAc) show a stable concentration in the control until day six of the culture followed by a runaway accumulation until the end of the culture. The High G condition showed an earlier onset in the accumulation starting at day 4, while an increase in the Low G condition was only observed

on the last day of culture as compared to the control. The UDP-HexNAc concentrations exhibit the same trend as their respective intracellular glutamine concentrations (figure 4.10), which seems to suggest a strong dependency. This is not surprising as glutamine is a co-substrate in the *de novo* synthesis of both species and involved in a reaction step that has been indicated as of significant impact by the global sensitivity analysis in section 3.4.2. Both UDP-HexNAc species show a concentration ratio of 1 : 2.75±0.1 UDP-GalNAc to UDP-GlcNAc throughout all experimental conditions and time points. Both species are linked through a single epimerase reaction step and the findings suggest that this step acts as an equilibrium reaction.

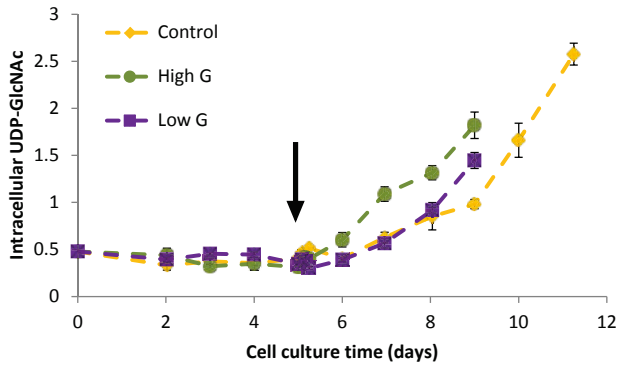


Figure 4.23 Intracellular UDP-GlcNAc concentration with respect to culture time (N = 3, EB = SD).

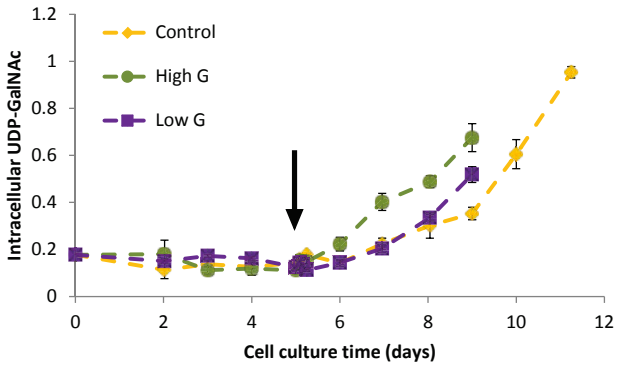


Figure 4.24 Intracellular UDP-GalNAc concentration with respect to culture time (N = 3, EB = SD).

Due to co-elution of UDP-Gal with other species in the chromatographic spectrum and a relatively low concentration, only limited data was collected on this NSD, with no data collected for the Low G condition, as shown in figure 4.25. The data seems to suggest that UDP-Gal concentrations decreased throughout the early and mid-exponential phase, while the feeding caused a lasting increase in the High G condition. The UDP-Glc concentrations on the other hand appeared to increase after Feed C additions with an accumulation towards the end for the control run (figure 4.26). The feeding of guanosine and mannose appears to have decreased UDP-Glc levels until the end of culture. These results are surprising as the reaction is catalysed by the same enzyme as the reaction between the two UDP-HexNAc species. This may indicate an important role played by the enzyme UDP-glucose-hexose-1-phosphate uridylyltransferase (E.C. 2.7.7.12). The reaction step catalysed by this enzyme is situated in parallel to the epimerase. However, the substrates of this

reversible reaction are UDP-Glc and galactose-1-phosphate, which are converted to UDP-Gal and glucose-1-phosphate (r23 in figure 3.6).

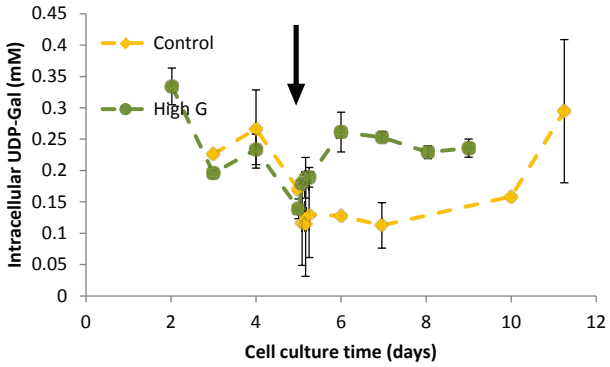


Figure 4.25 Intracellular UDP-Gal concentration with respect to culture time (N = 3, EB = SD).

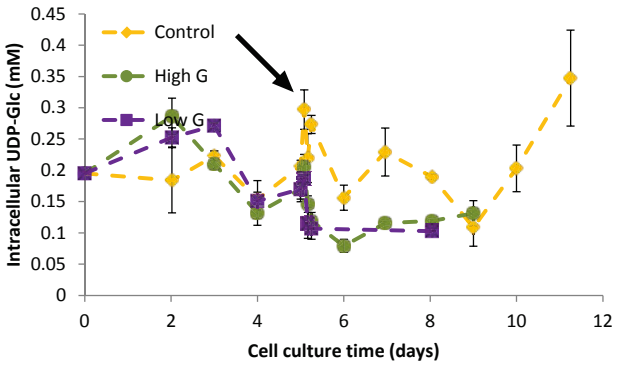


Figure 4.26 Intracellular UDP-Glc concentration with respect to culture time (N = 3, EB = SD).

Sialic acid CMP-Neu5Ac showed very little variation with respect to culture time and media feeding, except for an accumulation at the final culture day in the High G run. Despite an increase in UDP-GlcNac, a precursor in the *de novo* synthesis of CMP-NeuAc, sialic acid concentrations did not vary significantly. This can be explained by a very strong co-operative product inhibition mechanism by CMP-Neu5Ac as well as un-cooperative binding behaviour with respect to UDP-GlcNAc in the synthesis pathway (Kornfeld et al., 1964). The minor accumulation in the High G condition may be explained by a slight increase in intracellular CTP concentration (figure 4.19) towards the end of the culture as compared to the control.

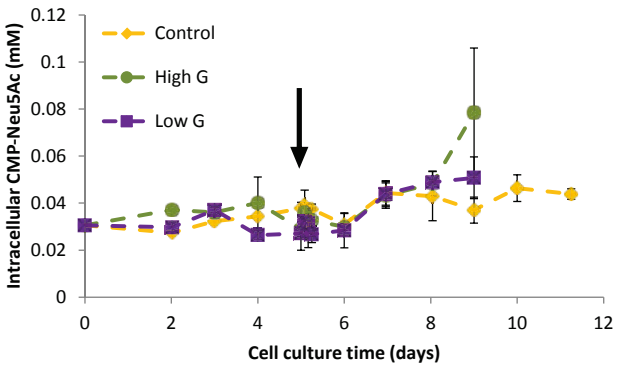


Figure 4.27 Intracellular CMP-Neu5Ac concentration with respect to culture time (N = 3, EB = SD).

4.4. Product glycoform

Lastly the antibody product glycoform at the Asn297 position was examined. A comparison of the product glycoform on day seven of the culture showed minor differences between each condition tested (figure 4.28). Most notably, the control appears to have a smaller proportion of the G0F glycan species and instead a higher abundance of the under-processed Man5 species. In all three test runs very little galactosylation has been observed. Again there can only be speculations about the cause of this as there was no direct evidence of UDP-Gal depletion in the cytoplasm (figure 4.25). While there are spatial constraints of the antibody Fc region, limiting the complexity of the IgG glycoform, Sou et al., achieved a higher degree of galactosylation using the same cell line and antibody product (Sou et al., 2015b). It has to be noted that this experiment was carried out in a bioreactor setup, which makes a direct comparison more difficult. At this point it cannot be concluded whether the lower degree of galactosylation pointed towards the influence of the difference in the experimental setup, the DMSO additions or a combination of both. On the final day there was a negligible amount of glycan structures with two galactose sugars attached as well as a decrease in G1F glycans, in comparison to day seven of the cultures, which translated into a lower degree of galactosylation of the glycoform. At no point throughout all conditions were any detectable amounts of G1 observed. This showed a strong preference towards fucosylation of the antibody glycoform, which was also observed on day seven of the culture.

At the end of each respective culture an increase in Man5 can be observed and a further decrease in more complex structures. Under-processed structures can arise in the case of NSD depletion or high protein flux through the Golgi apparatus, where glycosylation takes place. However, at no point during the culture time was a depletion of UDP-GlcNAc in the cytoplasm observed (figure 4.23). The specific antibody production rate had dropped in the control as opposed to the fed conditions, where fewer Man5 structures were observed. This leads to the speculation that the under processing was a result of either a depletion in the Golgi apparatus due to a deficiency in NSD transport or an issue with the enzymes involved in the glycosylation process. This is particularly interesting as most

commercial antibody glycoforms have little to no Man5 structures (del Val et al., 2011). It has to be assumed that the most probable cause of the observed effect was the DMSO addition to the cell culture media. DMSO is known to affect the abundance of glycosyltransferases. However, results vary with respect to qualitative trends of the various glycosyltransferases and across mammalian cell lines (Liu et al., 1981, Liu et al., 1983, Liu et al., 1998). The localisation of the enzymes within the Golgi was not investigated. Although Miyata et al. have found no difference in the ultrastructure of the Golgi apparatus as a result of DMSO additions, the effects on glycosyltransferase localisation are not known. As a result it is not unreasonable to speculate on the contribution of DMSO addition towards high abundances of man5 structures in the work presented here.

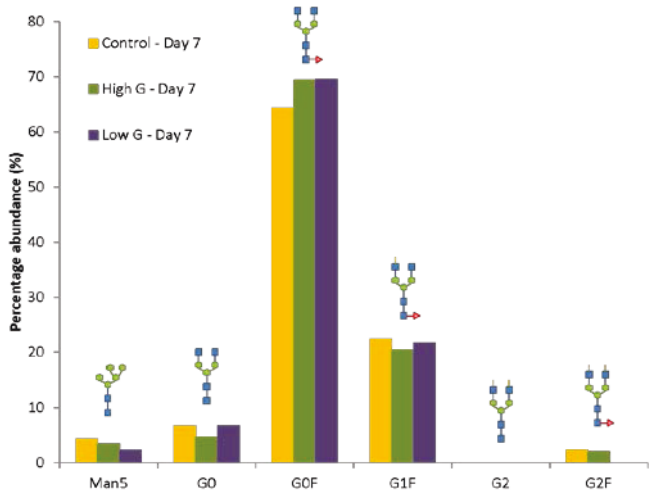


Figure 4.28 Antibody product Fc region glycoform. All detectable glycan structures on day 7 of culture for all feeding strategies (N = 1).

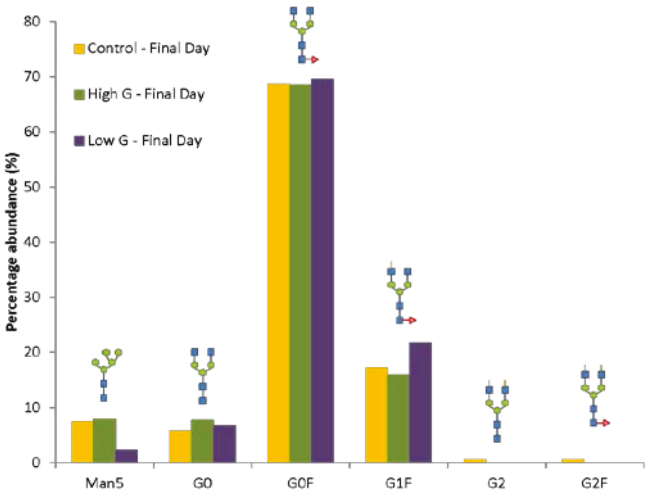


Figure 4.29 Antibody product Fc region glycoform. All detectable glycan structures on final day of culture for all feeding strategies (N = 1).

4.5. Conclusions and Further work

The outcome of the experiment are clear responses of the cells to the guanosine and mannose feeding, which have manifested themselves in terms of changes in cell culture dynamics, extracellular and intracellular metabolites, nucleotides, NSDs and finally the product glycoform. The primary objective of eliciting an increase in GDP-Fuc, GDP-Man and GTP concentrations was achieved and the response was quantified to enable further

model development in chapter 5. A summary of the main effects observed on cell culture dynamics and extracellular species is given below:

- Addition of guanosine was able to inhibit cell growth at both the High G and the Low G guanosine concentrations of 1 mM and 0.25 mM, respectively. The cell growth inhibition has previously been described in literature and has been concluded to be an effect of cell growth arrest in the synthesis phase of the cell cycle (Carvalhal et al., 2003). However, while the cells' growth appeared to have been arrested, the viable cell density only decreased slowly with respect to time.

- The comparatively lower viable cell density of the fed cultures and corresponding lower integral viable cell concentration (IVCC) did not lead to a decrease in product titer. Again, this has been observed by Carvalhal et al. and was attributed to cell growth arrest leading to an increase in specific productivity (Carvalhal et al., 2003).

- Guanosine was taken up rapidly by the cells, such that the extracellular concentrations became negligible in the extracellular media within 24 h to 48 h after feeding. However, the effects on cells persisted and were irreversible after guanosine depletion.

- The presented feeding strategy appears to have slowed down the glutamine synthetase reaction resulting in a smaller consumption of glutamate and a lower amount of glutamine production, compared to the control. The 1 mM guanosine addition led to a brief glutamate production.

- The extracellular mannose was taken up by the cells at a much slower rate than glucose, which appeared to have been consumed preferentially to mannose. Thus, limiting the effect of the mannose feeding on cell metabolism. Consequently, substitution of mannose for glucose is required to produce higher mannose consumption.

The effects of the various feeding strategies have also been able to propagate from the extracellular environment to intracellular species concentrations. This offers valuable insight

into cell metabolism and enables translation to *in silico* mechanisms. The main findings are summarised below:

- With respect to nucleotide synthesis guanosine feeding produced a selective increase in GTP, only. A 4.4-fold increase in GTP was recorded at its maximum four hours after feeding of 1 mM to the cell culture media. The response to both feeding strategies was rapid and prolonged. Despite additions of 1 mM and 0.25 mM of guanosine the difference in concentrations maxima was 15% lower for the Low G condition. This suggests a saturation of the guanosine response in the proximity of the 1 mM guanosine concentration.

- The increased GTP concentrations resulted in an according increases in GDP-Fuc and GDP-Man with 2.7-fold and 3.1-fold maxima, respectively, for the high G condition. The relative differences in maxima for the lower guanosine condition were 15% and 30% lower for GDP-Fuc and GDP-Man, respectively. This is in line with the differences in GTP differences and suggests dependence of species synthesis on GTP availability.

- Little effect was observed on the other NSD species as a result of the feeding. Hence, the experiment confirms that intracellular NSD pools can be selectively increased through feeding of specific nucleotide precursors and hexoses. This gives confidence in the design of experiment and allows for translation of the experimental setup to further feeding strategies.

- A very interesting finding has been made with respect to the UDP-Gal to UDP-Glc reaction step, where two parallel enzymes are known to play a role. The epimerase reaction (r22a in figure 3.6), which also catalyses the UPD-HexNAc epimerase reaction seems to produce an equilibrium of a constant ratio in the UDP-HexNAc species, there are distinct differences in the ratios of the UDP-Hex species. This suggests a strong influence of the transferase reaction step (r23a in figure 3.6) as well as opening up a door to targeted manipulation of one UDP-Hex species over the other.

The effects of the feeding strategies were able to propagate to the glycoform and are summarised below:

- Glycan samples taken on day 7 and the cultures' respective final day showed a prevalence of the G0F glycan structure and a very high degree of fucosylation.

- Despite no evidence of UDP-Gal depletion, very little galactosylation was observed with very minimal amounts of G2 and G2F species, especially towards the end of the culture. This opened the door for an experimental and computational case study to selectively improve product galactosylation, as presented in chapters 6 and 7.

- Glycan under-processing was observed and indicated problems associated either with NSD depletion in the Golgi or with the Golgi machinery. While the first was excluded, the latter was speculated to be the consequence of DMSO addition to the cell culture media. A further investigation into the underlying mechanisms is not warranted at this time as guanosine feeding is not a viable prospect with respect to application in the production of biotherapeutics. Consequently, no DMSO was employed in future experimentation.

The gathered data provides a very good starting point for a further refinement and improvement of the modelling framework. The fed batch data allows a translation of the cell culture dynamics model from a hybridoma model to a more relevant model for GS-CHO cell culture. The successful Feed C additions ensured no depletion of the measured nutrients during the cell culture duration and thus, allowed for the build-up of metabolic by-products leading to an extended stationary phase before causing a drop in viability. This and the measurement of glutamine accumulation in the extracellular medium allows for a further extension of the cell culture dynamics model. Furthermore, the data will allow for the inclusion of a new hexose carbon source, namely mannose, to model its effect on cell culture dynamics and its interaction with the extracellular and intracellular glucose. These benefits also translate to the nucleotide model, where the nucleotides were observed under non-limiting glucose and glutamine concentrations, which allow for an expansion of the nucleotide model to include control mechanisms that prevent nucleotide build up and thus,

increasing model robustness. The guanosine additions were able to perturb the *de novo* nucleotide synthesis network further, to reveal not only its effect on GTP levels but also, how this effect was carried forward to the other triphosphate species to reveal their interdependencies further. The goal of selectively increasing the concentrations of GDP-Fuc and GDP-Man was achieved, which in a modelling context will allow for the estimation of parameters on the metabolic branch leading up to the two NSDs with a much greater confidence. The data is not only of a dynamic nature but also shows the rapid response and gives information about the dependence of GDP-Fuc and GDP-Man on GTP concentrations and the limitations to species build up through the cell's metabolic control mechanisms. The data also suggests a strong dependence of the UDP-HexNAc species on intracellular glutamine, which points towards bottlenecks in the metabolic network and allows for more targeted parameter estimation. Finally, the glycan data will enable a computation estimate of the enzyme concentrations, their dissociation constants and distribution in the Golgi apparatus as described by the del Val et al. model (del Val et al., 2011). On the level of the entire platform, the effect of different antibody production rates, as caused by the guanosine additions can be translated to the modelling platform. This effect propagates to antibody productivity, the outlet fluxes of the nucleotide and NSD model as well as the flux through the Golgi, as described by the del Val et al. model. Translating these findings into the model will give rise to a more robust platform with the outlook of designing feeding strategies to target the glycoform.

Chapter 5

Model Translation and Expansion

The results of chapter 4 showed a clear response to guanosine and mannose supplementation to the cell culture media. The resulting metabolic perturbations have manifested themselves in changes in cell culture dynamics, extracellular and intracellular metabolites, nucleotides, NSDs and finally the product glycoform. The experimental objective was achieved by selectively eliciting an increase in intracellular GDP-Fuc, GDP-Man and GTP concentrations and thus, probing the branch of the NSD metabolic pathway for which previously insufficient data was available (chapter 3). In a modelling context the quantification of the dynamic response, resulting from pulse feeding of guanosine and mannose, enables further development of the NSD model presented in chapter 4. This increases the model robustness with respect to the metabolic branches leading to the *de novo* synthesis of GDP-Man and GDP-Fuc. The guanosine additions also led to perturbations in the *de novo* nucleotide synthesis network and thus, revealing additional species dependencies to permit a further expansion of the nucleotide model leading to greater model accuracy. As part of the work presented in this chapter, the nucleotide model has been expanded to include more structural knowledge of the *in vivo* network. The cell growth model was restructured and expanded to reflect the culture dynamics of the CHO cell line employed in chapter 4 as well as fed-batch culture conditions. However, the modular structure of the model platform presented in the chapter 3 was left unaltered. Lastly, the cell culture dynamics, nucleotide and NSD model were trained using experimental data from chapter 4. The results show good fits for most species for the three experimental conditions.

5.1. Cell culture dynamics

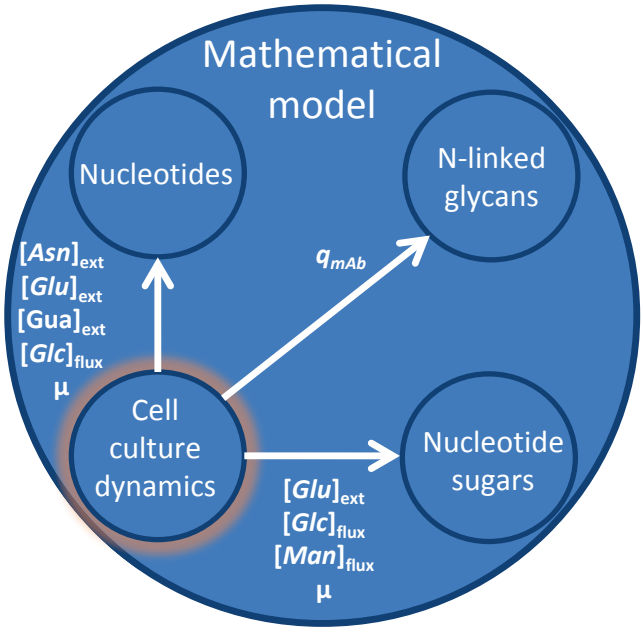


Figure 5.1 Schematic of the model framework depicting the interaction of the cell culture dynamics model with the remaining parts of the framework.

The cell culture dynamics model accounts for the interactions of the cells with their extracellular environment and the resulting cell growth, death, nutrient utilisation as well as fluxes into the intracellular environment (figure 5.1). The model presented herein has been extensively modified as compared to the model described in chapter 3. Changes in the cell line from hybridoma cells to GS-CHO cells, inclusion of intermittent Feed C additions and further metabolites have been included for greater relevance to a biotherapeutic production platform and improvement in model accuracy. Feeding of guanosine and mannose as well as their consumption and irreversible effects on cell growth, metabolism and mAb production rate were taken into account as part of the model expansion. In addition to glucose and glutamine, the redeveloped model considers the extracellular concentrations of ammonia, asparagine, glutamate and lactate, which in turn form inputs to the nucleotide and NSD model (figure 5.1). While asparagine concentrations have not been measured, its consumption leads to the production of ammonia, thus, providing indirect insight into its consumption by the cells. Both the initial concentration of Asparagine and the concentration in the supplemented feed are known, thus, providing sufficient constraints for an estimation of extracellular asparagine concentrations. While the changes to the model in chapter 3 are extensive, its position within the framework and the assumptions of homogeneity with respect to species and cell concentrations remain unchanged.

A fed-batch culture can be defined as a batch process with intermittent additions of nutrients to the cell culture. This implies changes in the total cell culture volume (V in L), which raises the need to reflect the additions of the Feed C (F_{feed} in L/h) and those of the supplementation inlet (F_{in} in L/h) as well as the volumetric reductions due to sampling (F_{out} in L/h), as shown in equation 5.1.

$$\frac{dV}{dt} = F_{in} + F_{feed} - F_{out} \qquad 5.1$$

Accounting for the volumetric changes eliminates the need to modify the expression for the viable cell concentration as shown in equation 3.1. However, the growth expression acquires additional complexity through the inclusion of additional metabolic species including a number of inhibitors. As a result the expression (equation 5.2) for cell growth (μ in h^{-1}) was split into a growth limiting term (f_{lim} no units) due to depletion of nutrients and a growth inhibiting term (f_{inh} no units) due to metabolic by-product accumulation multiplied by the maximum growth rate (μ_{max} in h^{-1}).

$$\mu = \mu_{max}\, f_{lim}\, f_{inh} \qquad 5.2$$

The growth-limiting term features, in addition to glucose and glutamine, also lactate, glutamate and asparagine, which are all known to act as carbon or nitrogen sources in cell metabolism. Equation 5.3 is a multiplication of saturation kinetics terms of the nutrients, featuring dissociation constants ($K_{M,i}$ in mM), where the absence of one species is sufficient to halt cell growth. The inhibition factor is a function of ammonia, DMSO, lactate and mannose contribution terms. All species are known to be detrimental to cell growth except for mannose, for which cell growth inhibition cannot be excluded based on the data presented in chapter 4. Each species contribution term is a function of its concentration and an estimated inhibitory constant ($K_{I,i}$ in mM). The individual terms can take on any value

between 0 and 1, where the extremes indicate total cell growth inhibition and no impact on cell growth, respectively. Again, each individual species is able to arrest cell growth completely. Guanosine is not featured in equation 5.3, as it induced an irreversible cell growth arrest (figure 4.1) after its consumption by the cells. The resulting equations feature a large number of terms, however, only a few nutrients are expected to have a significant impact on cell growth.

$$f_{lim} = \left(\frac{[Glc]_{ext}}{K_{M,\,glc} + [Glc]_{ext}}\right)\left(\frac{[Gln]_{ext}}{K_{M,gln} + [Gln]_{ext}}\right)\left(\frac{[Lac]_{ext}}{K_{M,\,lac} + [Lac]_{ext}}\right) \left(\frac{[Glu]_{ext}}{K_{M,glu} + [Glc]_{ext}}\right)\left(\frac{[Asn]_{ext}}{K_{M,\,asn} + [Asn]_{ext}}\right) \quad 5.3$$

$$f_{inh} = \left(\frac{K_{I,\,amm}}{K_{I,\,amm} + [Amm]_{ext}}\right)\left(\frac{K_{I,\,DMSO}}{K_{I,\,DMSO} + [DMSO]_{ext}}\right)\left(\frac{K_{I,\,lac}}{K_{I,lac} + [Lac]_{ext}}\right)\left(\frac{K_{I,man}}{K_{I,man} + [Man]_{ext}}\right) \quad 5.4$$

The cell death term (k_d in h^{-1}) as featured in equation 5.5, is a summation of the effects of ammonia, asparagine, DMSO and mannose. All of these species are known to impact cell death with the exception of mannose, where early cell death resulting from the presence of extracellular mannose cannot be excluded at this point based on the experimental data. The effects of ammonia, DMSO and mannose are modelled as saturation kinetics, as their accumulation leads to cell death, while asparagine depletion is expect to lead to cell death. The saturation terms ($K_{d,i}$ in mM) and the summation of species terms ensures that each individual species contribution can lead to cell death. This is in contrast to the multiplications featured in the f_{lim} and f_{inh} expressions, where a collective contribution product results from the multiplication of each species contribution.

$$k_d = k_{d,max}\left[\left(\frac{[Amm]_{ext}}{K_{d,amm} + [Amm]_{ext}}\right) + \left(\frac{K_{d,asn}}{K_{d,asn} + [Asn]_{ext}}\right) + \left(\frac{[Man]_{ext}}{K_{d,man} + [Man]_{ext}}\right) + \left(\frac{[DMSO]_{ext}}{K_{d,dmso} + [DMSO]_{ext}}\right)\right] \quad 5.5$$

Due to the fed-batch nature of the model the volume changes resulting from inlet and outlet flows need to be taken into account in the individual species material balances. A representative material balance is shown in equation 5.6 and includes the species consumption/production term with the species rate (q_i in mM/(cell h)), a Feed C inlet term and a sampling outlet term. Data in chapter 4 suggested altered glucose uptake in the presence of mannose and consequently its material balance poses an exception, where a mannose uptake inhibition term is included (equation 5.7). A representative material balance for the supplemented species guanosine and mannose is given by equation 5.8, where a feed supplementation term is used.

$$\frac{dV[i]_{ext}}{dt} = q_i V X_V + F_{feed}[i]_{feed} - F_{out}[i]_{ext} \quad 5.6$$

$$\frac{dV[Glc]_{ext}}{dt} = \left(\frac{K_{c,man}}{K_{c,man} + [Man]_{ext}}\right) q_{glc} V X_V + F_{feed}[Glc]_{feed} - F_{out}[Glc]_{ext} \quad 5.7$$

$$\frac{dV[j]_{ext}}{dt} = q_j V X_V + F_{in}[j]_{ext} - F_{out}[j]_{ext} \quad 5.8$$

The cellular species consumption terms for glucose and asparagine (q_{glc} and q_{asn} in mmol/(cell h)) are shown in equations 5.9 & 5.10. Both follow the form of a growth dependent term with the cell's biomass yield for the glucose and asparagine species ($Y_{Xv/glc}$

and $Y_{Xv/asn}$ in units of cell/mmol) and a corresponding constant metabolic maintenance term (m_{glc} and m_{asn} in units of mmol/(cell h)).

$$q_{glc} = -\left(\frac{\mu}{Y_{Xv/glc}}\right) - m_{glc}\,[Glc]_{ext} \quad 5.9$$

$$q_{asn} = -\left(\frac{\mu}{Y_{Xv/asn}}\right) - m_{asn}\,[Asn]_{ext} \quad 5.10$$

Mannose being a carbon source for cell metabolism has its consumption (q_{man} in mmol/(cell h)) modelled much like that of glucose. However, an additional mannose concentration term was added to the growth term as shown in equation 5.11 to account for concentration dependency in consumption. The guanosine consumption term features a saturation and constant uptake term only, due to its lack of necessity in biomass production (equation 5.12).

$$q_{man} = -\left(\frac{[Man]_{ext}}{K_{M,\,man} + [Man]_{ext}}\right)\left(\frac{\mu}{Y_{Xv/man}}\right) - m_{man} \times [Man_{ext}] \quad 5.11$$

$$q_{gua} = -\left(\frac{[Gua]_{ext}}{K_{M,\,gua} + [Gua]_{ext}}\right) m_{gua}[Gua]_{ext} \quad 5.12$$

The consumption rate of glutamine features again a growth dependent term and a constant contribution to cell maintenance. However, experimental data, as shown in figure 4.5, suggested an increase in glutamine during guanosine consumption. As a result, the guanosine consumption rate has been included as a glutamate producing term (equation

5.13). Glutamine on the other hand has been modelled by a growth-dependent glutamine-consuming term and a glutamine synthesis term as a function of ammonia (s_{gln} in mmol/(cell h)). Glutamate, the co-substrate in the glutamine synthesis reaction, has been assumed to be at saturation and is not featured in the glutamine term (equation 5.14).

$$q_{glu} = -\left(\frac{\mu}{Y_{Xv/gln}}\right) - m_{glu} - q_{gua} \qquad 5.13$$

$$q_{gln} = s_{gln} \times \left(\frac{[Amm]_{ext}}{K_{d,amm} + [Amm]_{ext}}\right) - \left(\frac{\mu}{Y_{Xv/gln}}\right) \qquad 5.14$$

Experimental data indicated a net production of lactate at low concentrations and a switch to lactate consumption at elevated lactate levels (figure 4.8). As a consequence, the lactate term features the familiar growth and constant maintenance consumption term as a function of extracellular lactate levels and an additional glucose yield term linked to cellular glucose consumption (equation 5.15). Finally, the ammonia production term 5.16 features consumption due to glutamine synthesis as well as production as a result of cell growth and asparagine consumption (q_{asn} is negative due to its consumption).

$$q_{lac} = -Y_{lac/glc}\, q_{glc} - \left[\left(\frac{\mu}{Y_{Xv/lac}}\right) + m_{Lac}\,[Lac_{ext}]\right][Lac_{ext}] \qquad 5.15$$

$$q_{amm} = -q_{gln} + \left[\left(\frac{\mu}{Y_{Xv/amm}}\right)\right] - Y_{amm/asn}\, q_{asn} \qquad 5.16$$

The antibody production rate was modified, as antibody production was observed to vary with respect to culture time (figure 4.4) resulting from changes in cell growth phase. Hence, a growth dependent term was introduced in addition to the constant term resulting in equation 5.17 featuring the growth dependent yield coefficient ($Y_{mAb/\mu}$ in mg/cell) and the constant antibody yield coefficient ($Y_{mAb/Xv}$ in mg/(cell h)).

$$q_{mAb} = \mu \times Y_{mAb/\mu} + Y_{mAb/Xv} \qquad 5.17$$

Guanosine clearly had a lasting impact on both the cell growth (figure 4.1) and the antibody production rate (figure 4.4), despite its quick depletion extracellularly (figure 4.5). As a result, a guanosine concentration-dependent term was deemed not to represent the system accurately and a switch was introduced to describe the cells' behaviour more accurately. This switch introduces a new maximum cell growth rate (μ_{max}) and death rate (k_d) as well as the constant and growth-dependent antibody yield coefficients ($Y_{mab/y}$ and $Y_{mab/Xv}$). As no significant difference in cell growth and antibody production rate was found for both guanosine concentrations, a non-concentration dependent switch is activated upon the addition of guanosine to cell culture media. The same set of parameters is therefore used to describe both experimental conditions featuring guanosine.

5.2. Nucleotide model

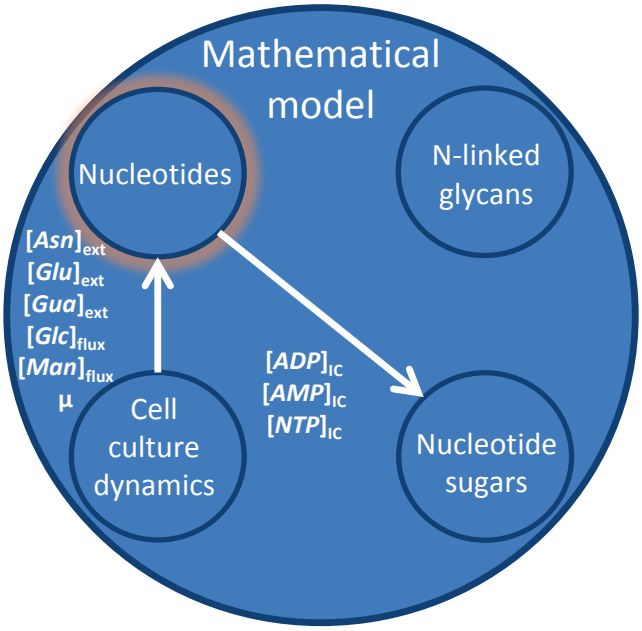


Figure 5.2 a schematic of the nucleotide model and its dependence within the mathematical model platform.

Akin to the cell culture dynamics model, the model of nucleotide *de novo* synthesis was modified from the work presented in chapter 3. The model needs to be extended such that it ensures robustness during fed-batch operation. Furthermore, it must be able to perform well under conditions where glucose and glutamine are not limiting and capture the impact of guanosine on intracellular GTP availability. The inclusion of asparagine in the cell growth model allows exploring further dependence on extracellular species concentrations and their impact on intracellular nucleotide species. Lastly, prolonged culture period and the guanosine perturbation allow for the inclusion of intracellular control mechanisms. The model inputs from the cell culture dynamics model are the extracellular concentrations of asparagine, glutamate, guanosine, the glucose flux into the cell and the cell growth rate (figure 5.2). The model outputs are the intracellular concentrations of adenine diphosphate (ADP), adenine monophosphate (AMP) and the four nucleotide triphosphates (NTP), which are utilized by the nucleotide sugar donor model.

A simplified reaction network of the purine and pyridine synthesis pathway was recreated *in silico* to model the concentrations of adenine monophosphate (AMP), adenine diphosphate (ADP), adenine triphosphate (ATP), cytosine triphosphate (CTP), guanosine triphosphate (GTP) and uridine triphosphate (UTP). The framework is of a semi-structured nature, where mechanistic knowledge of the reaction pathways and enzyme kinetics was utilized when possible (BRENDA, 2015). The resulting network is shown in figures 5.3 & 5.4

and features the reaction steps as well as the inhibitory control mechanisms. While glutamine usually acts as the nitrogen donor in the *de novo* synthesis of nucleotides, extracellular glutamate concentrations were used in this model. It is assumed that the intracellular availability of glutamine is dependent on glutamate, the substrate for its synthesis and, as a result, glutamine will not be limiting, as would be suggested by the extracellular data (figure 4.10). The reaction mechanisms are modelled using saturation type Michaelis-Menten kinetics, assuming a random order of reaction and derived as outlined in chapter 3.4.1. Dissociation constants (K_m in mM), maximum reaction rates (v_{max} in mM/h) and inhibition constant (K_i in mM) were all estimated based on experimental data presented in chapter 4. The same set of assumptions listed in chapter 3 were used to derive all reaction rate expressions.

5.2.1. Purine synthesis

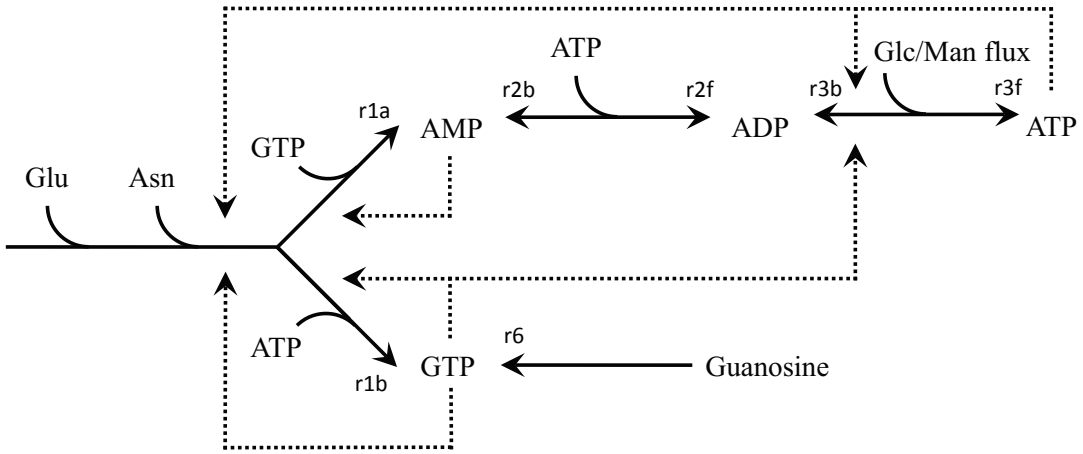


Figure 5.3 a semi structured reaction network of the de novo purine synthesis. Reaction steps are indicated in dark lines, while dashed lines indicate inhibitory mechanisms.

The purine *de novo* synthesis leads to the creation of ADP, AMP, ATP and GTP via the common intermediate nucleoside inosinic acid (IMP). As a result the first reaction in the *in silico* recreation is split into r1a and r1b (figure 5.3) leading to the synthesis of AMP and a second lumped reaction to GTP from its common intermediate. Both reactions have been modelled to share dissociation constants for extracellular asparagine and glutamate. Reaction r1a, as represented by equation 5.18, features uncompetitive control by ATP and GTP as well as AMP production inhibition through competition with GTP. Reaction r1b

(equation 5.19) includes the same uncompetitive ATP and GTP terms. However, the product inhibition term features GTP competing with ATP as the co-substrate to GTP synthesis. The competitive product inhibition terms serve as regulatory mechanism preventing the accumulation of one purine species over the other.

$$\text{r1a} = \frac{v_{max,\,1a}[Asn_{ext}][Glu_{ext}][GTP_{IC}]}{(K_{M1,asn}+[Asn_{ext}])(K_{M1,glu}+[Glu_{ext}])\left(K_{M1,GTP}\left(1+\frac{[AMP_{IC}]}{K_{I1,AMP}}\right)+[GTP_{IC}]\right)\left(1+\frac{[GTP_{IC}]}{K_{I1,GTP}}+\frac{[ATP_{IC}]}{K_{I1,ATP}}\right)} \quad 5.18$$

$$\text{r1b} = \frac{v_{max,\,1b}[Asn_{ext}][Glu_{ext}][ATP_{IC}]}{(K_{M1,asn}+[Asn_{ext}])(K_{M1,glu}+[Glu_{ext}])\left(K_{M1,ATP}\left(1+\frac{[GTP_{IC}]}{K_{I1,GTP}}\right)+[ATP_{IC}]\right)\left(1+\frac{[GTP_{IC}]}{K_{I1,GTP}}+\frac{[ATP_{IC}]}{K_{I1,ATP}}\right)} \quad 5.19$$

The reversible phosphorylation of AMP to ADP, where the forward (f) reaction is a function of ATP, is represented by equations 5.20 & 5.21. Both the forward and the reverse (b) reactions are catalyzed by the same enzyme and, hence, feature competitive inhibitory terms in both directions of the reaction.

$$\text{r2f} = \frac{v_{max,\,2f}[AMP_{IC}][ATP_{IC}]}{\left(K_{M2,amp}\left(1+\frac{[ADP_{IC}]}{K_{I2,ADP}}\right)+[AMP_{IC}]\right)(K_{M2,ATP}+[ATP_{ext}])} \quad 5.20$$

$$\text{r2b} = \frac{v_{max,\,2b}[ADP_{IC}]}{\left(K_{M2,amp}\left(1+\frac{[AMP_{IC}]}{K_{I2,AMP}}\right)+[ADP_{IC}]\right)} \quad 5.21$$

The phosphorylation of ADP to ATP is represented by equation 5.22 and is a function of ADP and the flux of glucose and mannose into the cell. This reaction step is regulated through competitive inhibition by the product and GTP, both of which compete with the

substrate ADP. The consumption of ATP to ADP is represented as a single substrate function of ATP only (equation 5.23).

$$\text{r3f} = \frac{v_{max,\,3f}[ADP_{IC}][Glc_{flux}]}{\left(K_{M3,adp}\left(1+\frac{[GTP_{IC}]}{K_{I3,GTP}}+\frac{[ATP_{IC}]}{K_{I3,ATP}}\right)+[ADP_{IC}]\right)\left(K_{M3,glc}+[Glc_{flux}]+[Man_{flux}]\right)} \quad 5.22$$

$$\text{r3b} = \frac{v_{max,\,3b}[ATP_{IC}]}{\left(K_{M3,atp}+[ATP_{IC}]\right)} \quad 5.23$$

Lastly, an independent lumped reaction accounting for the guanosine uptake and conversion to GTP has been included. It is a single substrate reaction of guanosine with no inhibitory control mechanisms.

$$\text{r6} = \frac{v_{max,\,6}[Gua_{ext}]}{\left(K_{M5,gua}+[Gua_{ext}]\right)} \quad 5.24$$

5.2.2. Pyrimidine synthesis

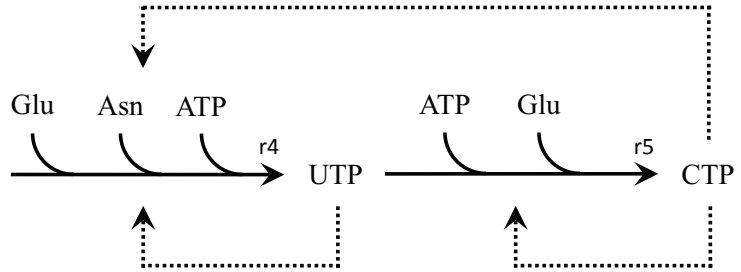


Figure 5.4 simplified reaction network of the *de novo* pyrimidine synthesis network. The inhibition mechanisms are indicated by dashed lines.

The simplified pyrimidine synthesis pathway, as shown in figure 5.4, features two sequential reactions. The first reaction, r4, is a lumped reaction of the *de novo* synthesis of

UTP, where the synthesis rate is determined by the availability of glutamine, asparagine and ATP. The reaction is controlled through uncompetitive inhibition of the reaction product UTP as well as the pyrimidine CTP (equation 5.26). CTP is synthesized from UTP with the co-substrate ATP and glutamine in a single reaction step and is represented by equation 5.26 and features an uncompetitive product inhibition term. An exponential term is featured in the equation to account for the reported allosteric co-operative product inhibition by CTP (Aronow and Ullman, 1987).

$$\mathrm{r4} = \frac{v_{max,\,4a}[Asn_{ext}][Glu_{ext}][ATP_{IC}]}{(K_{M4,asn}+[Asn_{ext}])(K_{M4,glu}+[Glu_{ext}])(K_{M4,ATP}+[ATP_{IC}])\left(1+\frac{[CTP_{IC}]}{K_{I4,CTP}}+\frac{[UTP_{IC}]}{K_{I4,UTP}}\right)} \qquad 5.25$$

$$\mathrm{r5} = \frac{v_{max,\,5}[UTP_{IC}][Glu_{ext}][ATP_{IC}]}{(K_{M5,utp}+[UTP_{IC}])(K_{M5,glu}+[Glu_{ext}])(K_{M1,ATP}+[ATP_{IC}])\left(1+\frac{[CTP_{IC}]^{nCTP}}{K_{I5,CTP}}\right)} \qquad 5.26$$

As in the nucleotide model developed in chapter 33, this updated version is constrained by the same outlet flux equations for the nucleotides ATP, CTP, GTP and UTP (equation 3.34). However, the consumption of species for host cell protein synthesis has been changed and is discussed in detail below.

5.3. Nucleotide Sugar Donor model

The NSD model is of a structured and mechanistic nature, based on cumulative literature data. Consequently, limited room is left for amendments in model structure, where reaction mechanisms and kinetics have been fully characterised. However, changes to the metabolic branch leading to the synthesis of GDP-Fuc were required to obtain good agreement with the experimental data presented in chapter 4. The global sensitivity analysis conducted in chapter 3 showed only parameters featured in reactions r15a and r1a to be significant with respect to GDP-Fuc concentration (figure 5.5). Therefore, reactions r1a and

r15a presented obvious targets for the amendment of reaction kinetics. The dehydratase reaction step (r15a) was originally modelled as random order bi-bi kinetics with uncompetitive product inhibition through GDP-Fuc (Bisso et al., 1999). While the reaction mechanism was left in its original form, exponential Hill-coefficients for both the concentration of GDP-Man and GDP-Fuc were introduced to account for possible allosteric behavior of the substrate binding and product inhibition of the reaction, respectively. This revision was motivated by the inability of the original Michaelis-Menten rate expression to reproduce the experimentally observed concentration profiles.

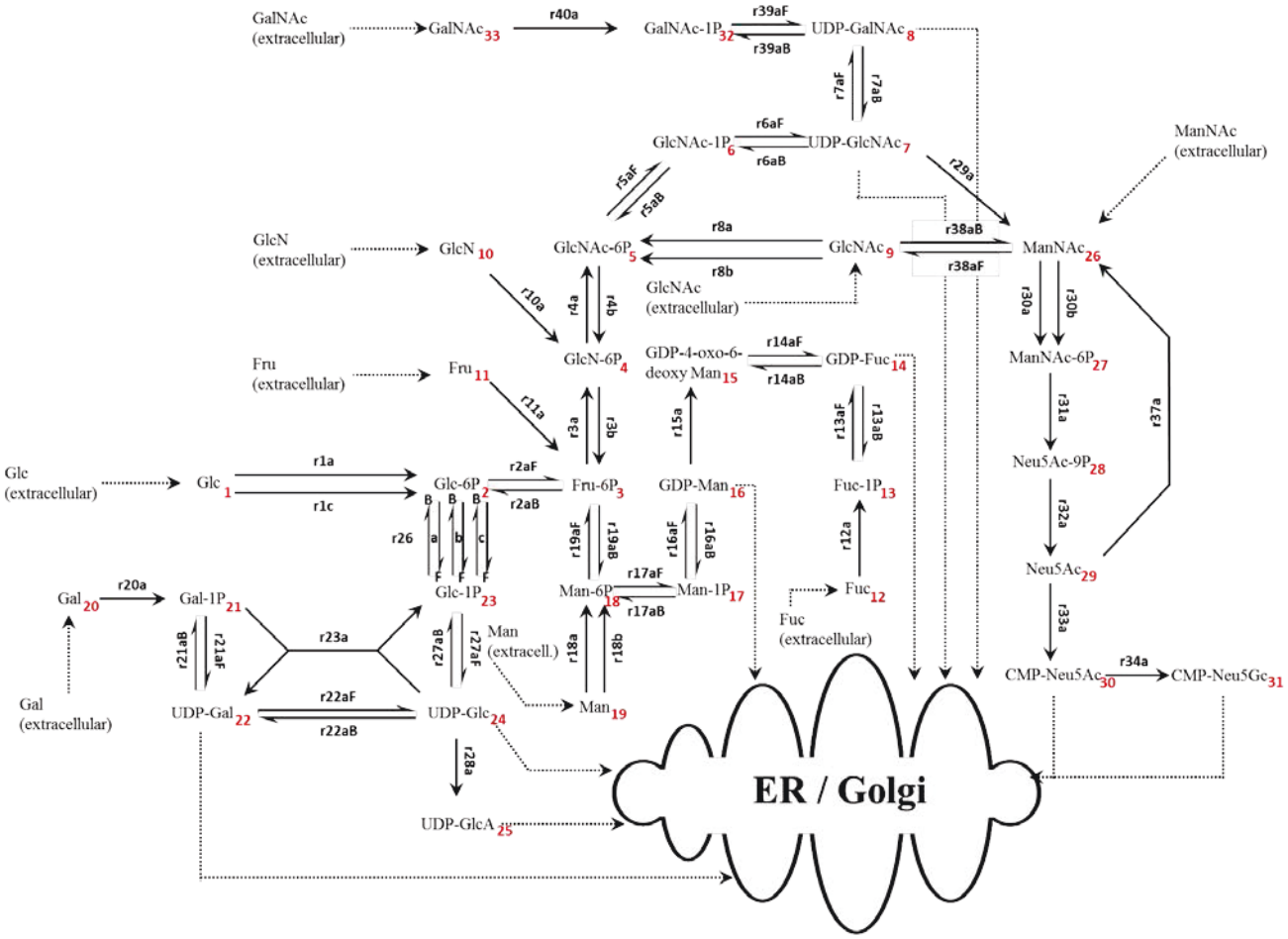


Figure 5.5 The reaction network of the de novo nucleotide sugar donor synthesis pathway, as modelled. Each species is represented as a separate mass balance and the arrows indicate the reaction steps and directions of reaction (Jedrzejewski et al., 2014b).

A further change was made to the rate of NSD consumption resulting from host cell protein production, which also acts as an outlet flux of the nucleotide model. Firstly, the number of N- and O-linked glycans per host cell protein was changed to 2.318×10^{-13} mmol / cell and 1.148×10^{-12} mmol / cell for N- and O-linked glycans, respectively. The numbers are based on literature data of a proteomic analysis of CHO cells (Baycin-Hizal et al., 2012). The numbers represent a reduced flux as compared to the assumed fluxes of chapter 3, as well as a shift towards a larger O-linked to N-linked glycan ratio. Furthermore, a constant host cell volume of 1.615×10^{-12} L/cell was taken, based on an average experimental value across all experimental time points, where little variation was observed with respect to culture time. Lastly, the average host cell glycoform was updated to account for the switch to the CHO cell line from the previous experiment. The glycoform was calculated based on the glycoform data of CHO cells as published by Pamela Stanley on Functional Glycomics and is summarised in table 5.1 (Stanley, 2010).

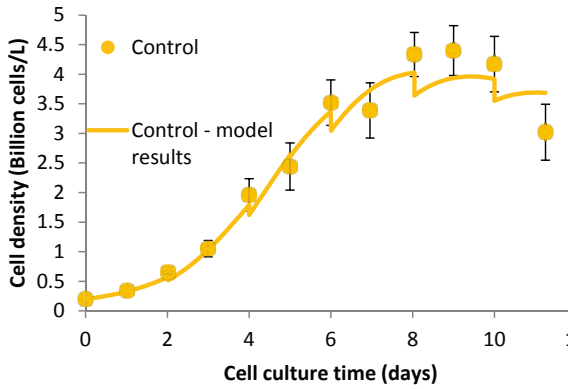
Table 5.1 Frequency of sugar species occurrence in glycans of CHO cells (Stanley, 2010).

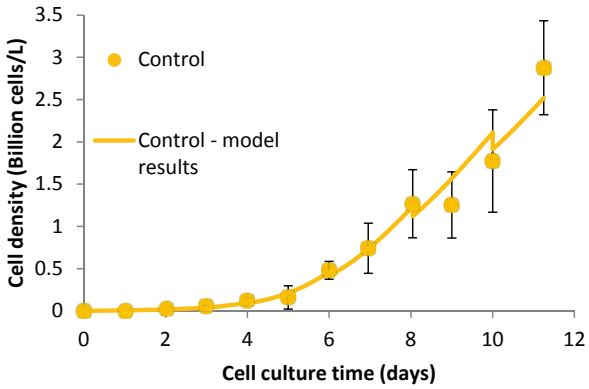
Glycan type	GlcNAc	GalNAc	Man	Gal	Neu5Ac	Fuc
N-linked glycan	3.257	0	4.65	1.405	0.118	0.397
O-linked glycan	0	1	0	1	1.214	0
Glycan average ($N_{NSD,glyc}$)	1.579	0.481	3.018	0.950	1.010	0.173

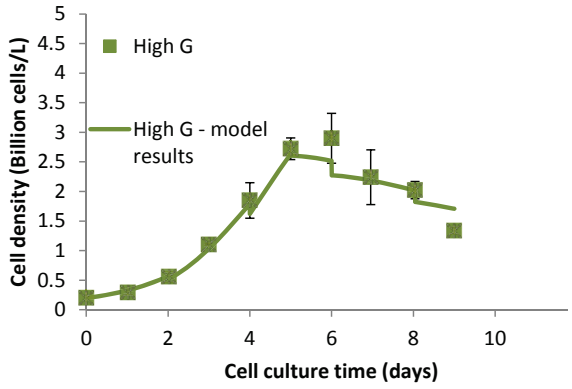
5.4. Model Training, Results and Discussion

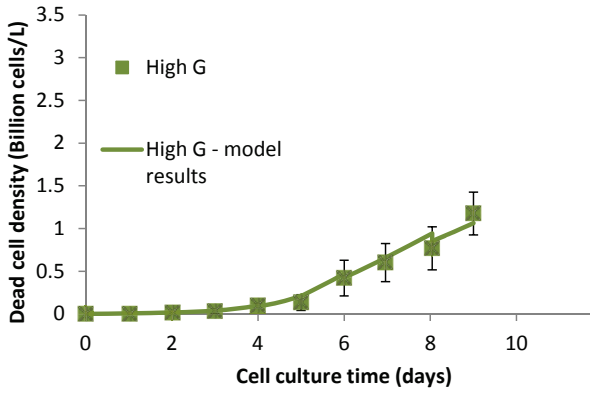
The updated model was trained using the data presented in chapter 4. Particular emphasis was placed on increasing the accuracy of the GDP-Fuc and GDP-Man branch of the NSD model as well as the translation of the model to a fed-batch GS-CHO cell system.

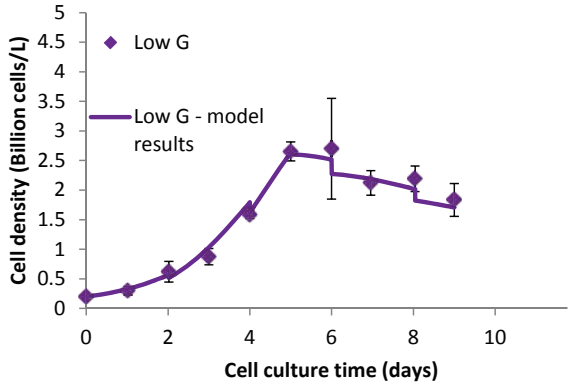
5.4.1. Cell culture dynamics output

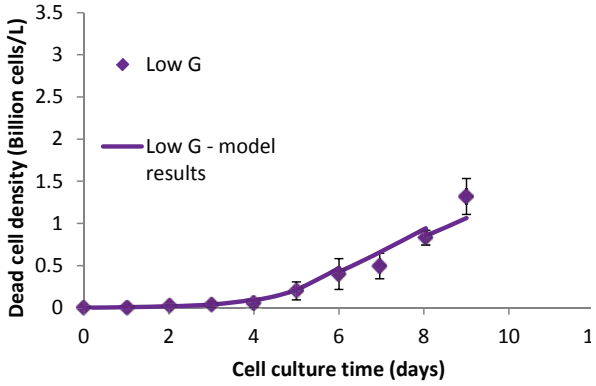












Figures 5.6a-c Experimental data (markers) and computational outputs (lines) of viable cell density for the control, High G and Low G cultures with respect to time.

Figure 5.7a-c Experimental data (markers) and computational outputs (lines) of dead cell density for the control, High G and Low G cultures with respect to time.

The output of the cell culture dynamics model shows a good fit with respect to the experimental viable and dead cell densities of all cultures (figure 5.6a-c). Firstly, a discontinuity in the viable cell density gradient is observed in the mannose and guanosine supplemented cultures. This is a result of the guanosine switch, by which a separate

maximum cell growth term is introduced after feed addition. This term was estimated to be 5-fold lower in the presence of guanosine and thus, explains the sharp change (Appendix D). The cell death (figure 5.7a-c), on the other hand, does not show an equal discontinuity, which is also reflected by the small difference in the estimated parameters of maximum cell death rate pre- and post- feed addition on day 5 of culture (Appendix D). The inhibition parameters ($K_{I,i}$) of the model also suggest strong cell growth inhibition as a result of ammonia accumulation and to a lesser extent due to the presence of galactose, with little to no growth inhibition by other species. Ammonia also appears to be the main contributing factor towards cell death.

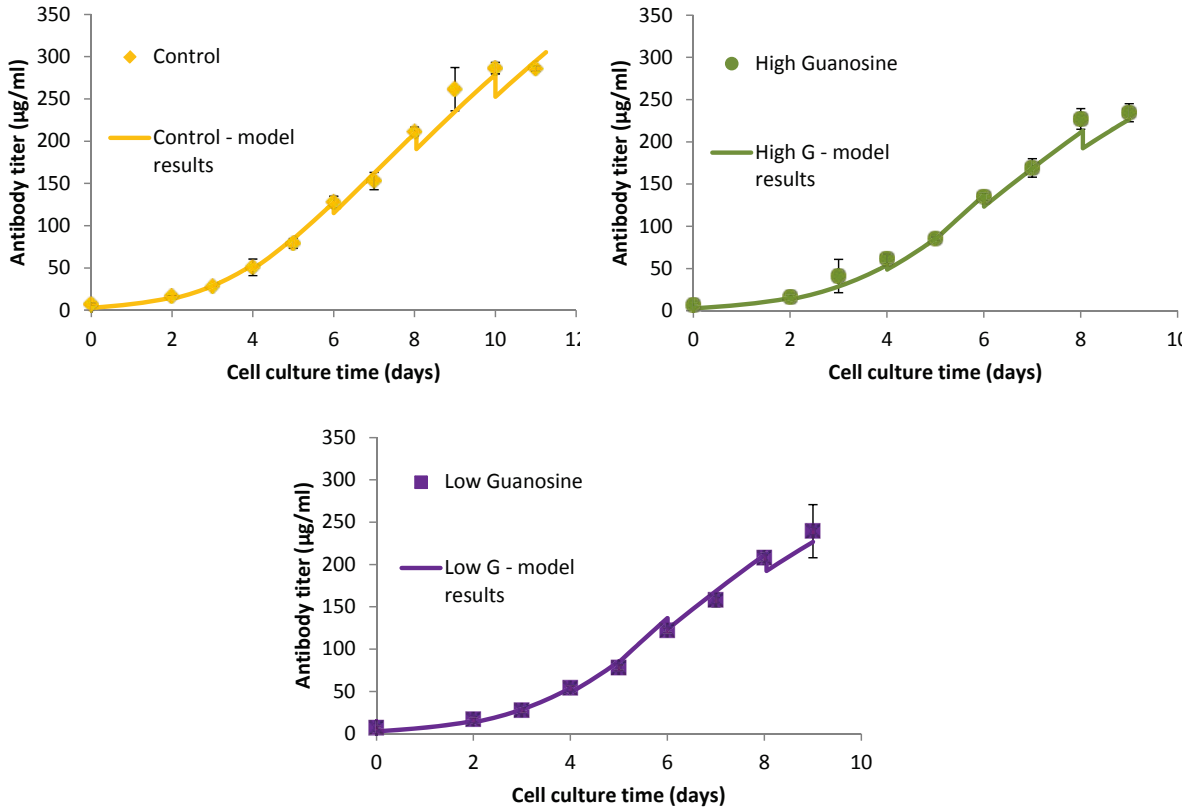
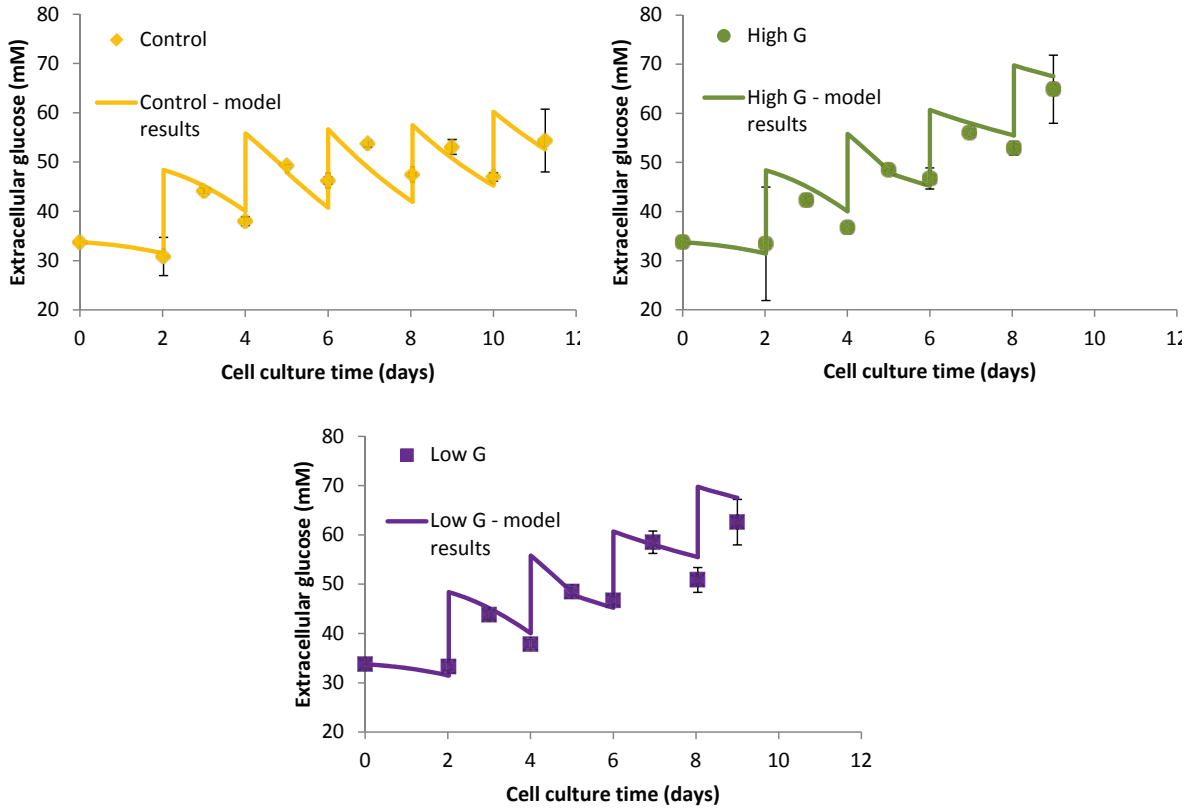


Figure 5.8a-c Experimental data (markers) and computational outputs (lines) of antibody titer for the control, High G and Low G cultures with respect to time.

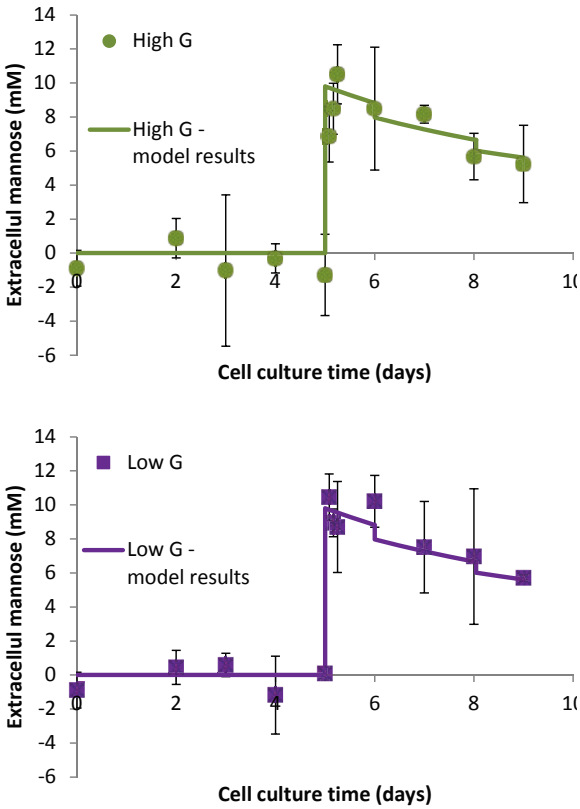
The model output also shows good agreement with respect to the antibody production and its accumulation in the cell culture media (figure 5.8a-c). Again two sets of parameters were estimated for the guanosine supplemented runs. The estimated parameters show a large depends of antibody production on cell growth, when no guanosine is present

(Appendix D). However, the cell density dependent term becomes the dominant factor in antibody production after the guanosine switch.

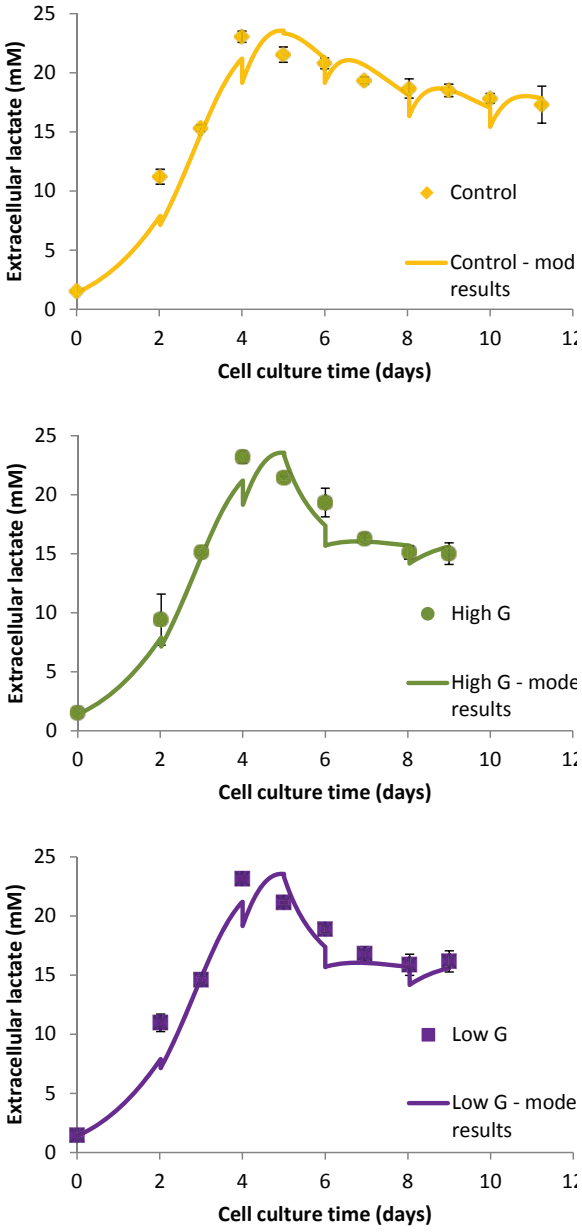
The cell culture dynamics model is also able to capture the consumption of glucose well (figure 9a-c). Again, a discontinuity on day 5 is observed in the guanosine and mannose supplemented cell cultures. This is an effect of the reduced cell growth and subsequently reduced glucose consumption by the cells. The extracellular mannose concentration is also captured by the model, where a slow consumption can be observed after the feeding on day 5 of the culture (figure 5.10a-c). The fits of lactate depicted in figure 11a-c closely track the experimentally obtained data. The model shows a drop in lactate concentration after mannose and guanosine addition on day 5, which is a result of reduced cell growth. This is reflected in the lactate production and consumption expression (equation 5.15), which is a function of cell growth.



Figures 5.9a-c Experimental data (markers) and computational outputs (lines) of extracellular glucose for the control, High G and Low G culture with respect to time.



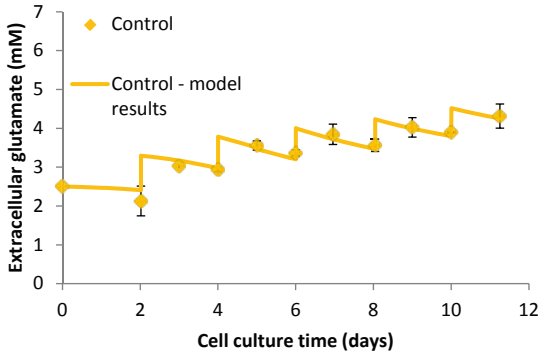
Figures 5.10a-c Experimental data (markers) and computational outputs (lines) of extracellular mannose for the High G and Low G culture with respect to time.

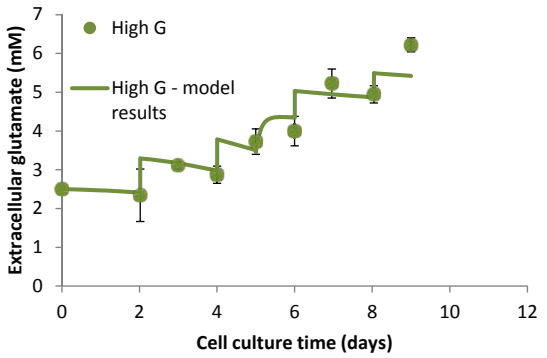


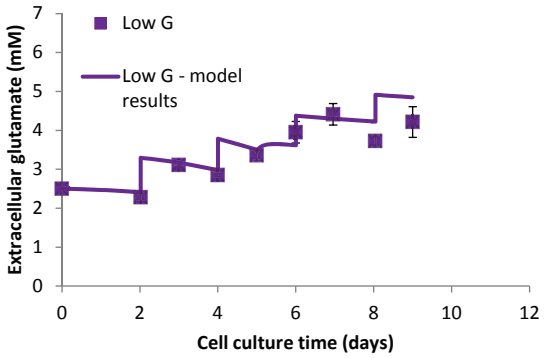
Figures 5.11a-c Experimental data (markers) and computational outputs (lines) of extracellular lactate for the control, High G and Low G culture with respect to time.

The model is able to capture the extracellular glutamate profiles for all cultures well, with the exception of the final points of the guanosine and mannose fed cultures (figure

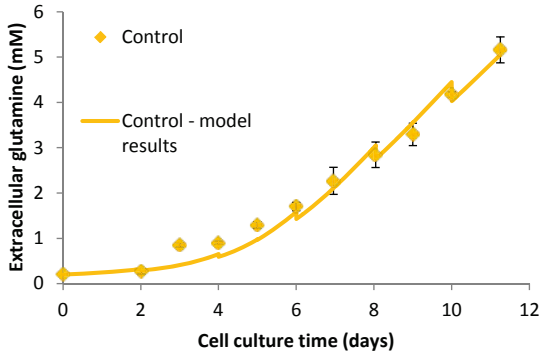
5.12a-c). An increase in glutamate concentration is observed after the feeding of guanosine on day 5 of the culture. The glutamine fits, on the other hand, are less accurate as compared to those of glutamate, with reasonable predictions albeit narrowly outside of the experimental error range (figures 5.13a-c). However, a consistent under-prediction is observed for the LowG condition. This may suggest a guanosine dependent change in glutamine metabolism, which is not captured by the model. Lastly, the ammonia outputs show very good agreement with respect to the experimental data (figure 5.14a-c).

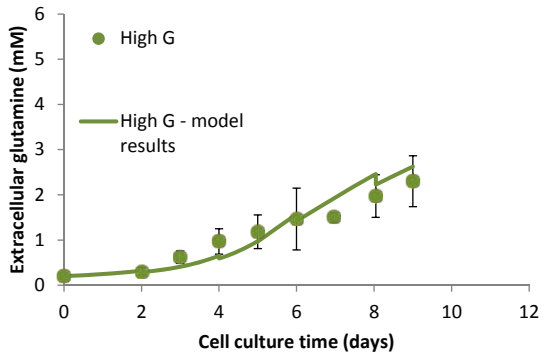






Figures 5.12a-c Experimental data (markers) and computational outputs (lines) of extracellular glutamate for the control, High G and Low G culture with respect to time.





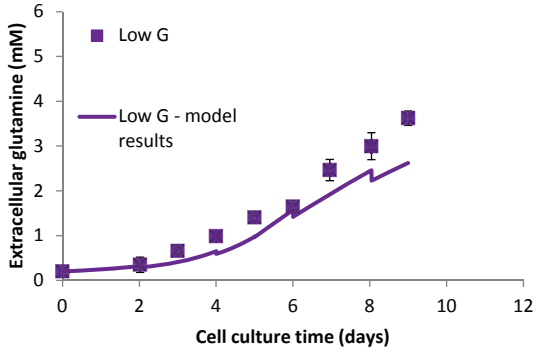
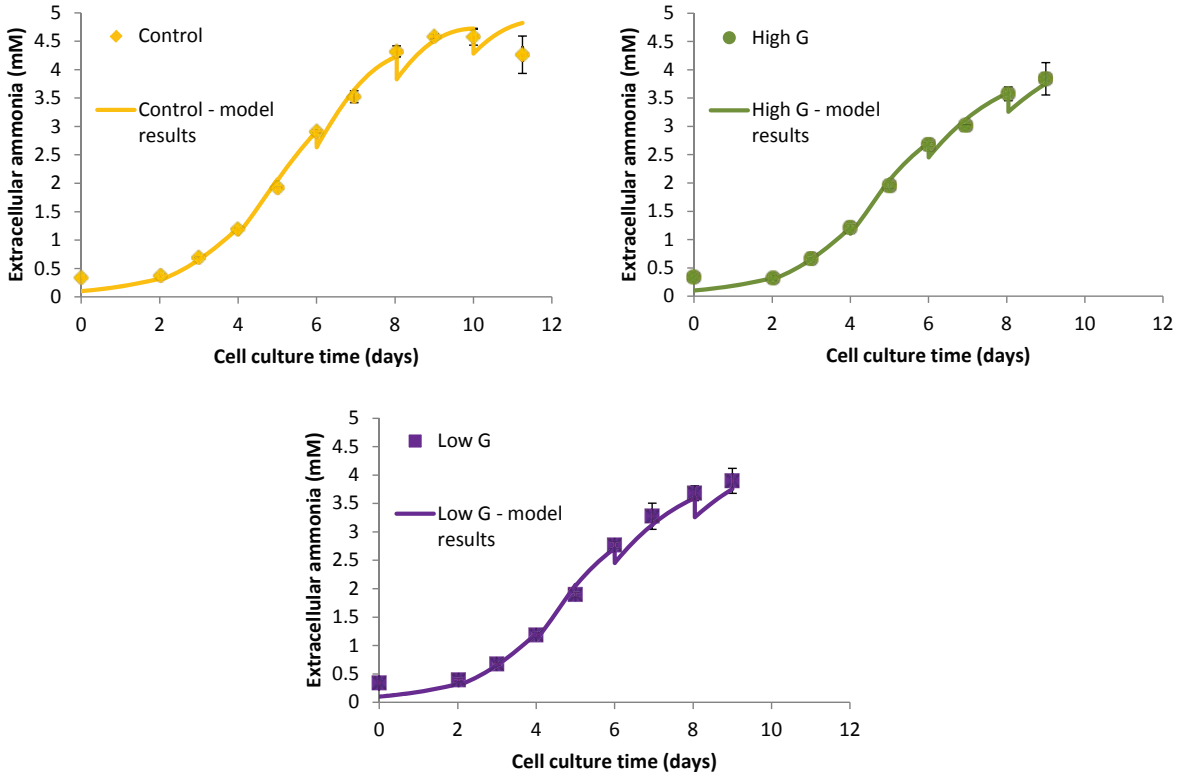


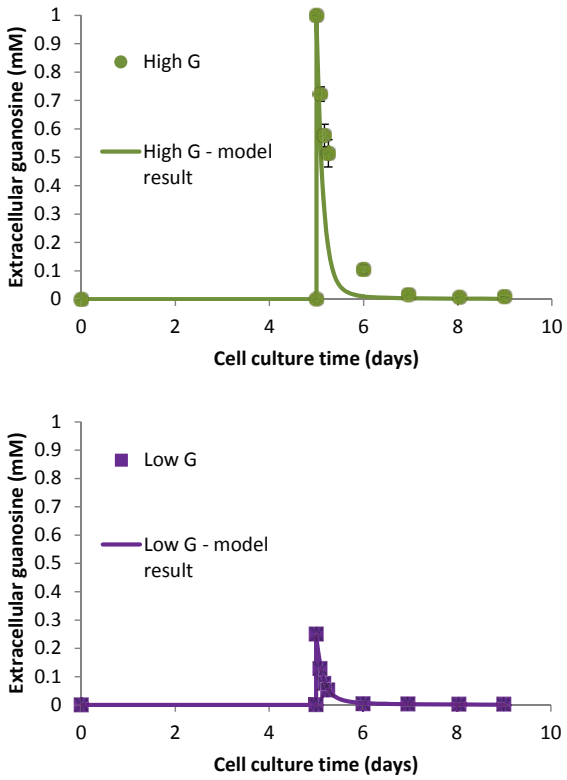
Figure 5.13a-c Experimental data (markers) and computational outputs (lines) of extracellular glutamine for the control, High G and Low G culture.



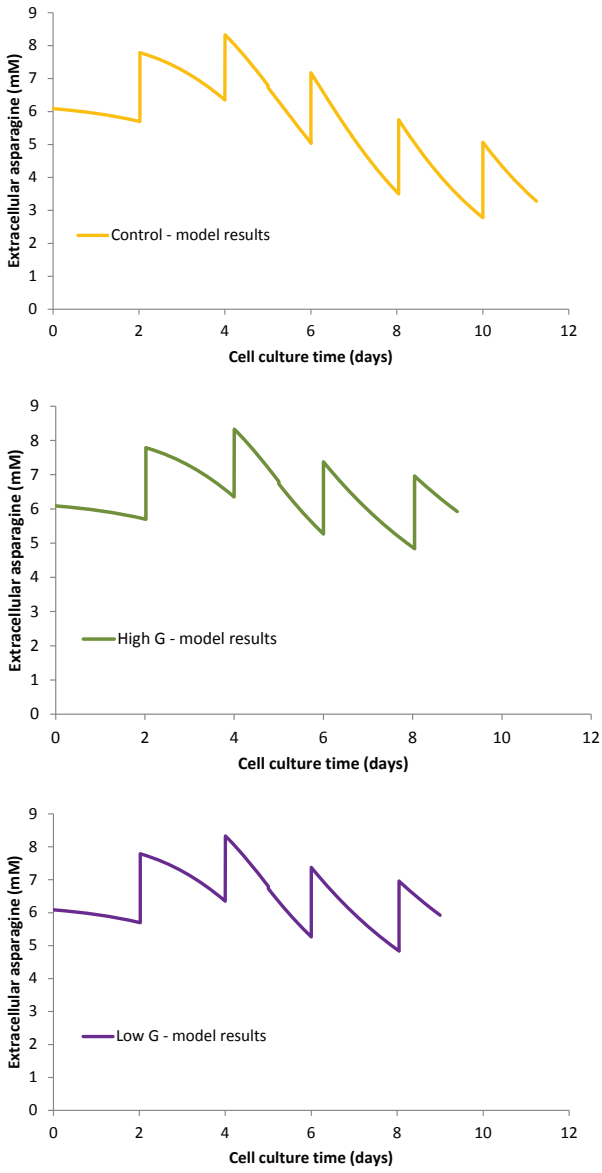
Figures 5.14a-cExperimental data (markers) and computational outputs (lines) of extracellular ammonia for the control, High G and Low G culture with respect to time.

The guanosine outputs of the cell culture dynamics model are in good agreement with the experimental data. However, the model output for the High G condition predicts a marginal overconsumption of guanosine within the first 24 h after feeding, as compared to the experimental data. This suggests a reduction in consumption as compared to the very rapid consumption of the first few hours after feeding. This may indicate saturation in uptake by the cells, which has not been taken into account in the model. Lastly, the cell culture dynamics model produces an output for asparagine (figures 5.16). As discussed in chapter 5.1, no data for asparagine has been collected, however asparagine consumption leads to ammonia consumption and is thus, sufficiently constrained to estimate consumption parameters and produce an output. The model predicts no limitation in asparagine concentration. Limitations in asparagine can be expected in fed-batch cultures of high cell density as it is the most highly consumed amino acid by GS-CHO cells (Carinhas et al., 2013). However, this is not expected to be the case in this set of experiments due to moderately high cell densities for this cell line (Sou et al., 2015a) and relatively short culture

time. This hypothesis is supported by a comparatively higher consumption in the control culture, where a higher IVCC was observed.



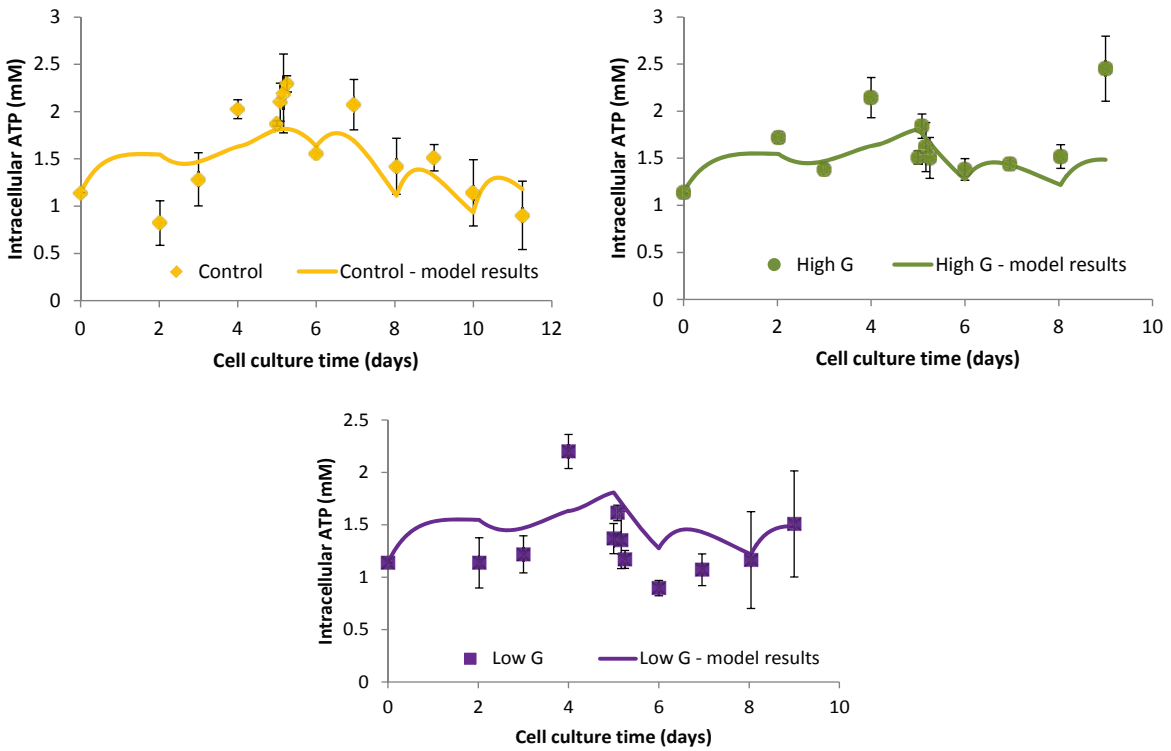
Figures 5.15a-bExperimental data (markers) and computational outputs (lines) of extracellular guanosine for the control, High G and Low G culture with respect to time.



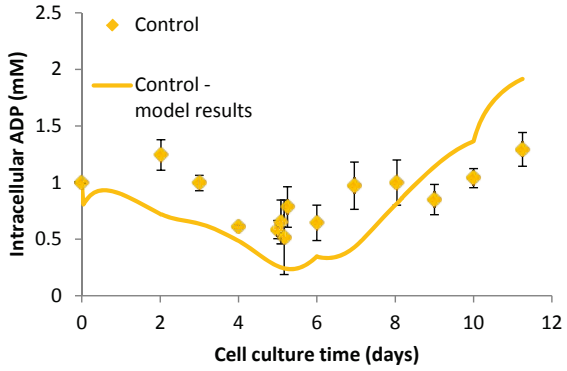
Figures 5.16a-c Experimental data (markers) and computational outputs (lines) of extracellular asparagine for the control, High G and Low G culture with respect to time.

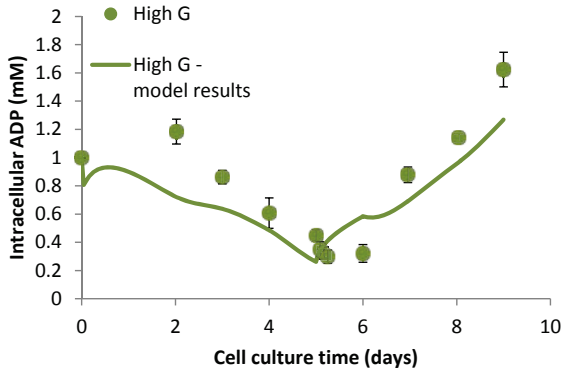
5.4.2. Nucleotide model output

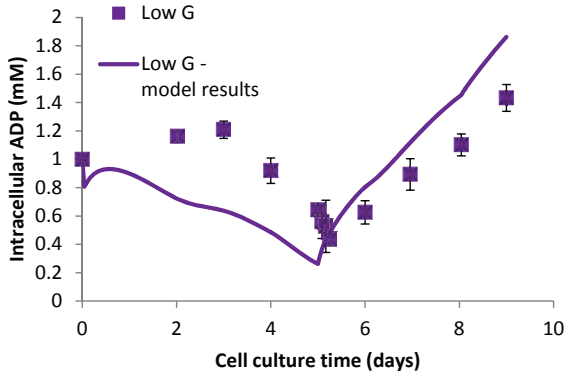
The updated nucleotide model was able to reproduce the intracellular concentrations of most adenine nucleotide species well. The trained model shows good agreement with ATP data for most time points and is able to reproduce the experimentally observed drop upon the feeding on day 5 of culture (figures 5.17a-c). The poorest fits were achieved with respect to the Low G condition, where an over-prediction is observed for a number of time points beyond the experimental error. ADP fits, on the other hand, show poorer agreement than the other two adenine species (figures 5.18a-c). However, the qualitative trend is reproduced, where concentrations are lowest on day 5 for all cultures with an accumulation towards the end of culture. This is steeper under the Low G and High G culture conditions. Lastly, good AMP fits are achieved with most model outputs lying within the experimental error (figures 5.19a-c). This is especially encouraging bearing in mind the lack of data for the metabolic precursors of AMP and thus, justify the choice of AMP as the first species within the *in silico* network reconstruction.



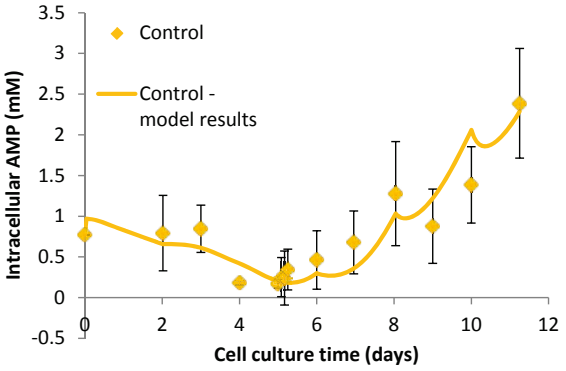
Figures 5.17a-c Experimental data (markers) and computational outputs (lines) of intracellular ATP for the control, High G and Low G culture with respect to time.

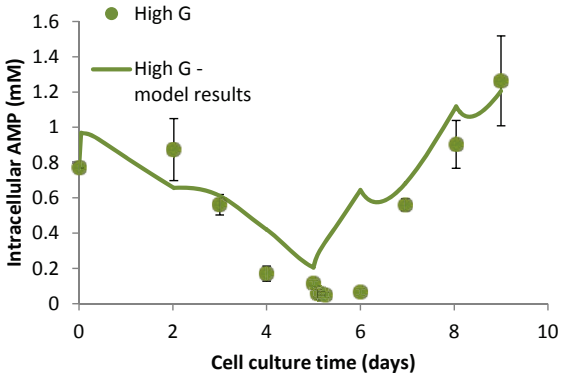


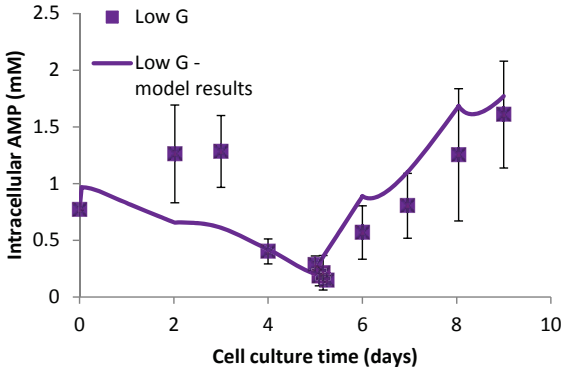




Figures 5.18a-c Experimental data (markers) and computational outputs (lines) of intracellular ADP for the control, High G and Low G culture with respect to time.



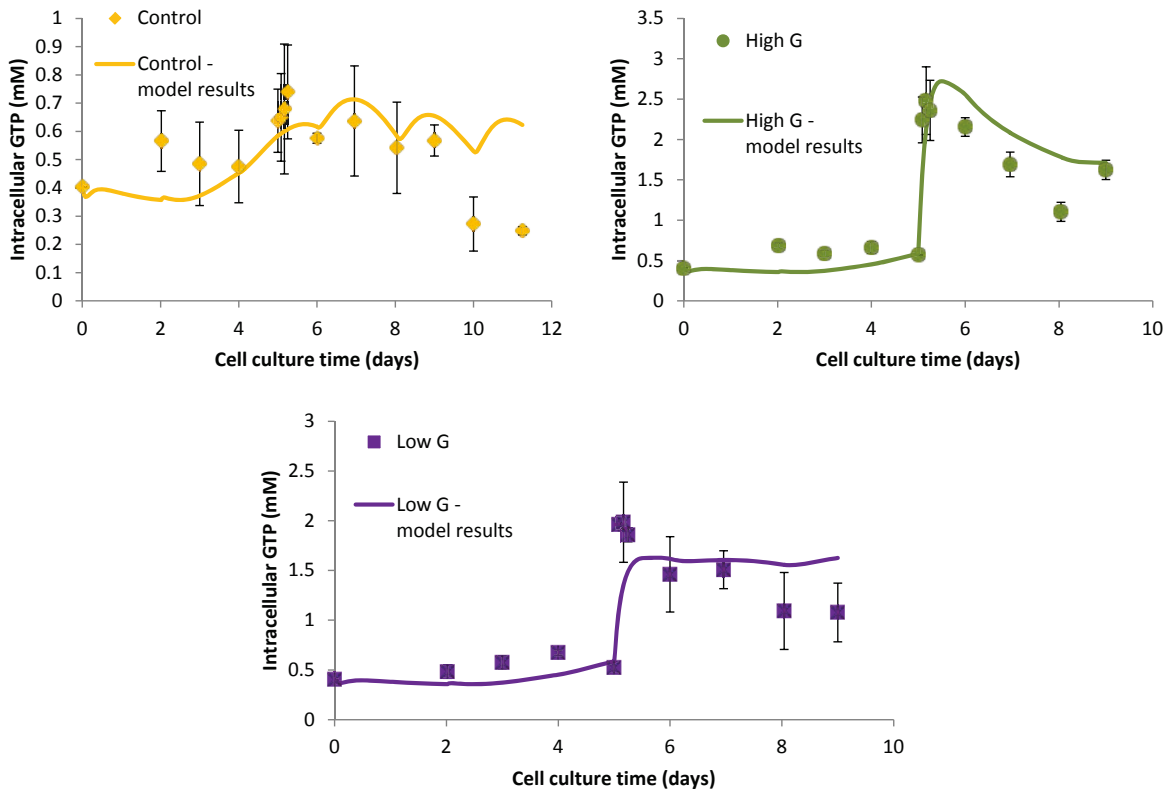




Figures 5.19a-c Experimental data (markers) and computational outputs (lines) of intracellular AMP for the control, High G and Low G culture with respect to time.

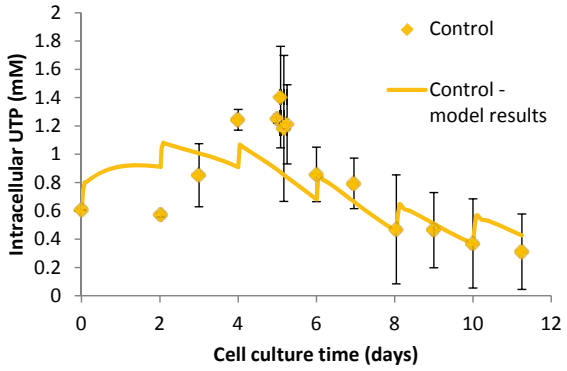
The model output of intracellular GTP concentrations shows fair agreement with experimental data (figures 5.20a-c). The control output is in good agreement until the end of culture, where an experimentally observed steep drop is not reproduced *in silico* by the model. On the other hand both additions of guanosine to the culture media on day 5 are reflected by the model output, where a dose-dependent response can be distinguished

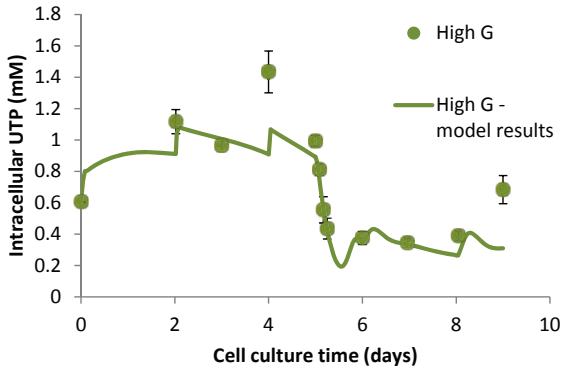
between the 0.25 mM (Low G) and 1 mM (High G) conditions. The computational output is broadly in line with the experimental data for most time points under the High G condition.

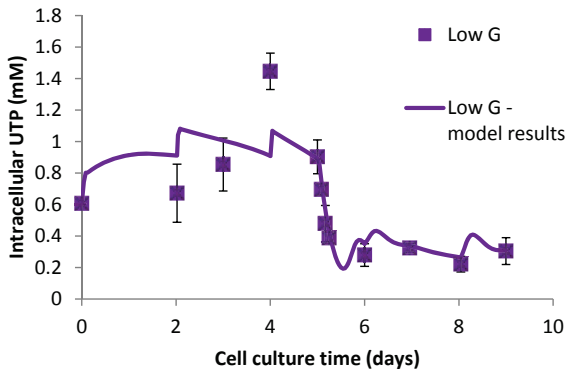


Figures 5.20a-c Experimental data (markers) and computational outputs (lines) of intracellular GTP for the control, High G and Low G culture with respect to time.

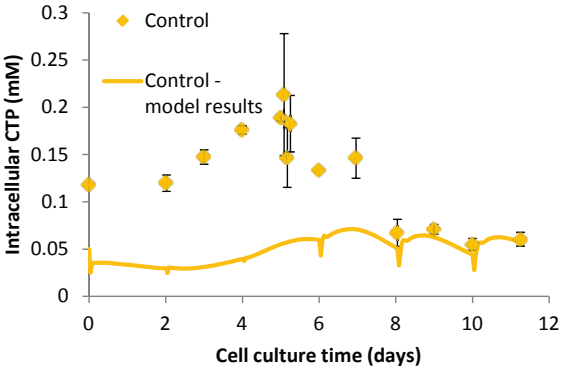
The accuracy of the model output for the pyrimidine species is mixed. The concentrations of UTP are reproduced very well by the model with most points lying within the experimental error (figure 5.21a-c). A drop in UTP can be seen on day 5 after the addition of guanosine to the culture media. This is a result of a decrease in ATP concentrations, the co-substrate to the synthesis reaction, which in turn is the result of the GTP increase due to guanosine feed addition. CTP, on the other hand shows very poor fits with respect to both qualitative and quantitative trends (figures 5.22a-c).

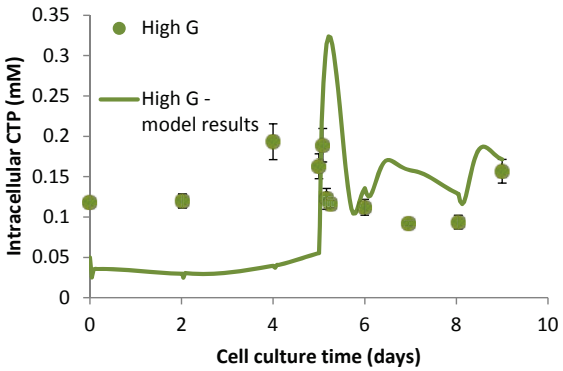


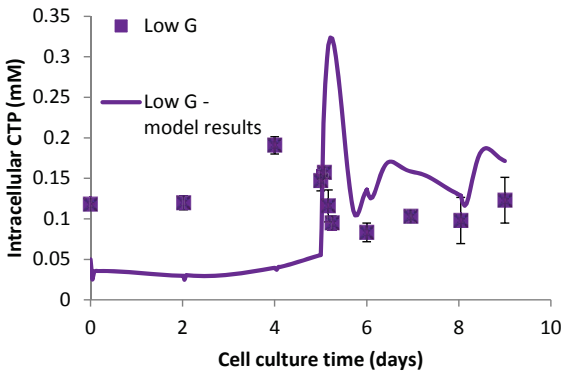




Figures 5.21a-c Experimental data (markers) and computational outputs (lines) of intracellular UTP for the control, High G and Low G culture with respect to time.







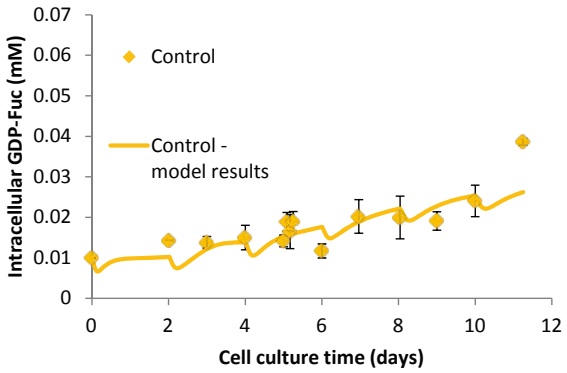
Figures 5.22a-c Experimental data (markers) and computational outputs (lines) of intracellular CTP for the control, High G and Low G culture with respect to time.

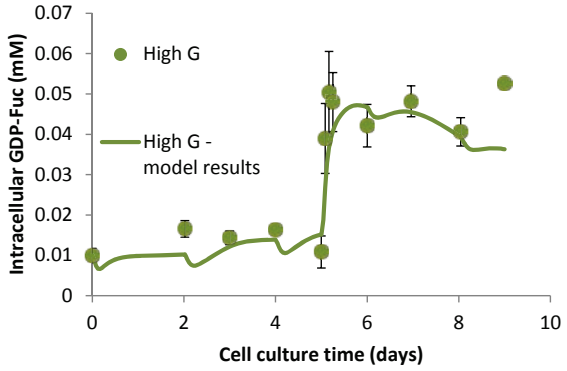
5.4.3. Nucleotide sugar donor model output

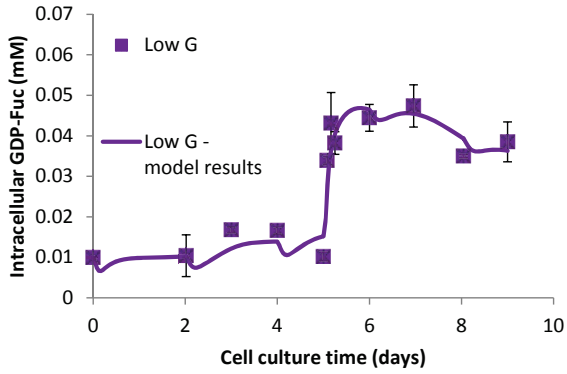
With respect to the nucleotide sugar donor model, the main aim was to improve the performance with respect to GDP-Fuc and GDP-Man to improve the overall accuracy of the *in silico* representation of the NSD *de novo* synthesis network. The trained model is able to capture the changes in GDP-Fuc well with most outputs lying within the experimental error

(figures 23a-c). A sharp increase of GDP-Fuc concentrations is observed upon the addition of mannose and guanosine on day 5 of culture and the dynamic response matches the intracellular data. The fits of GDP-Man are also in good agreement with most of the experimental data, however, the outputs for the control and the High G condition are partially outside the narrow range of the experimental error (figures 24a-c). The exponential Hill-coefficients introduced in the rate limiting reactions r15a (discussed in chapter 4) were estimated to be 2.92 and 3.68 for GDP-Fuc inhibition and the GDP-Man substrate binding, respectively (Appendix D). This indicates highly co-operative behaviour with respect to both the substrate and inhibitor binding. Experimental observations of allosteric behaviour are not reported. However, these values compare well to the experimentally determined Hill-coefficient of 4.1 in the epimerase reaction of UDP-GlcNAc to ManNAc (r29a figure 5.5) (Hinderlich et al., 1997). Hence, the estimates appear to be reasonable and combined with the good fits obtained for GDP-Fuc the modification of the rate expression seems justified.

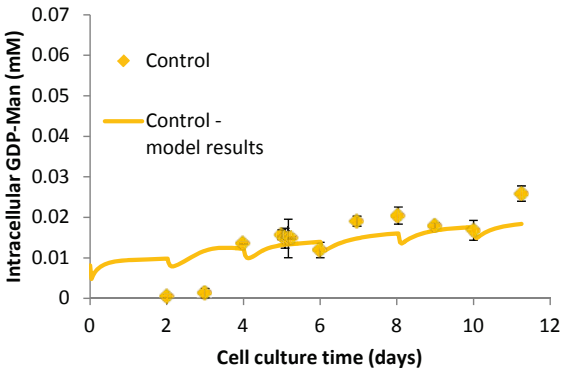
The model outputs of the UDP-Hex species show a mixed quality of results. UDP-Glc model outputs are mostly in agreement with the experimental data and a decrease in concentration is observed after feeding on day 5 in both computational outputs and experimental data (figures 5.25a-c). However, the output for UDP-Gal shows a less good agreement with experimental data (figures 5.26a-c). The computationally determined concentrations of UDP-Hex species appear to follow a similar profile, while the experimental data shows otherwise. This suggests that reaction r22a (figure 5.5), the equilibrium reaction epimerase discussed in chapter 4.3 is the dominant reaction in the *in silico* reconstruction. The experimental data on the other hand suggests an increase in the UDP-Gal concentrations under the High G regime and thus, breaking the similarity in concentration profiles of the UDP-Hex species. No UDP-Gal data was detectable for the Low G condition and thus, a discussion of the model output is not possible.

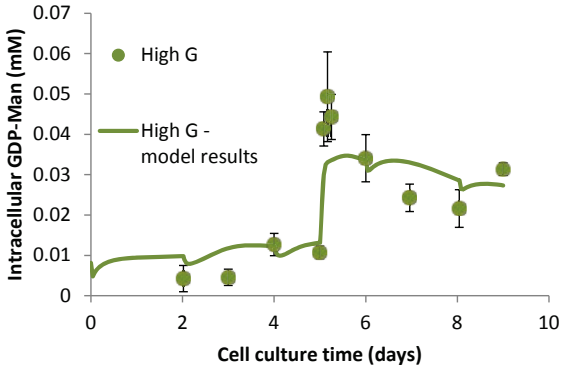


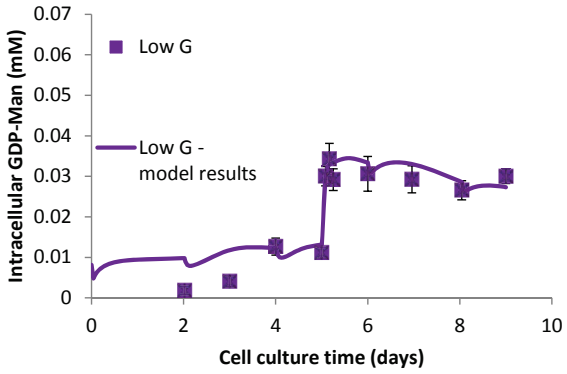




Figures 5.23a-c Experimental data (markers) and computational outputs (lines) of intracellular GDP-Fuc for the control, High G and Low G culture with respect to time.



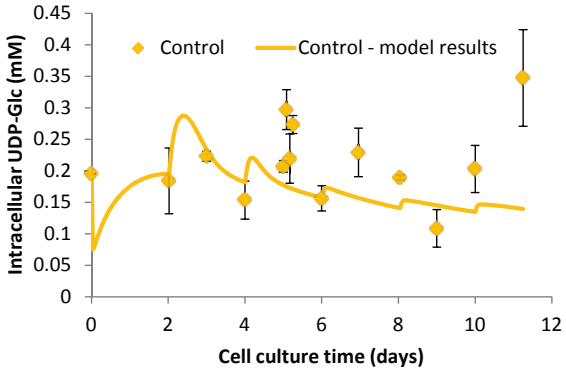


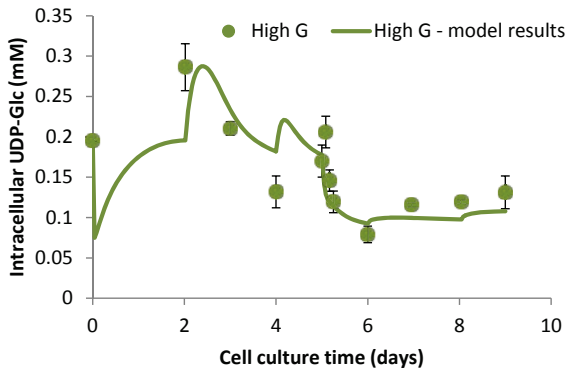


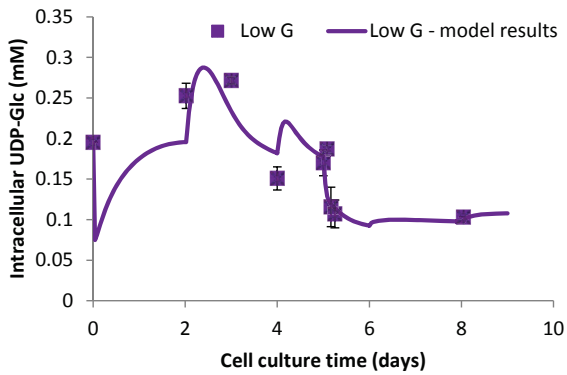
Figures 5.24a-c Experimental data (markers) and computational outputs (lines) of intracellular GDP-Man for the control, High G and Low G culture with respect to time.

Good fits for both UDP-GlcNAc and UDP-GalNAc concentrations are achieved within the first days of culture for each experimental setup (figures 5.27a-c). However, the model does not appear to be able to account for the accumulation of the UDP-HexNAc species observed in the last two to three days of culture and an under-prediction is observed in the model output of all cultures. The model shows an immediate increase in UDP-HexNAc

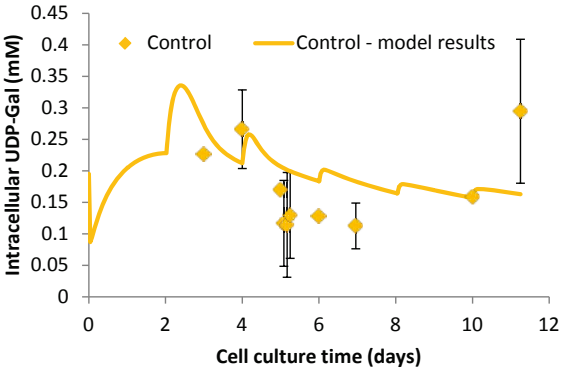
concentrations after the mannose and guanosine feeding on day 5, due to a reduced consumption of species, while the experimental accumulation occurs at a later time. The UDP-HexNAc species follow the same trends in experimental as well as in computational output and thus, it gives confidence in the rate expression of the epimerase reaction connecting both species (r7b figure 5.5).

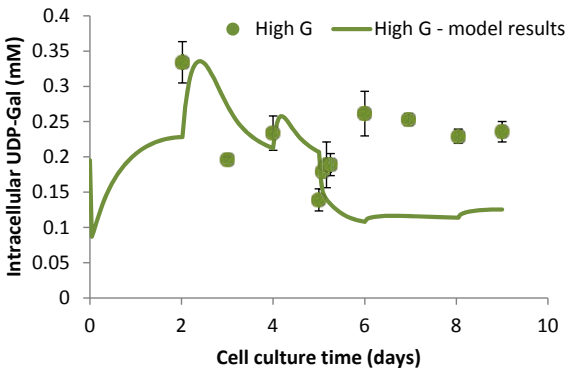


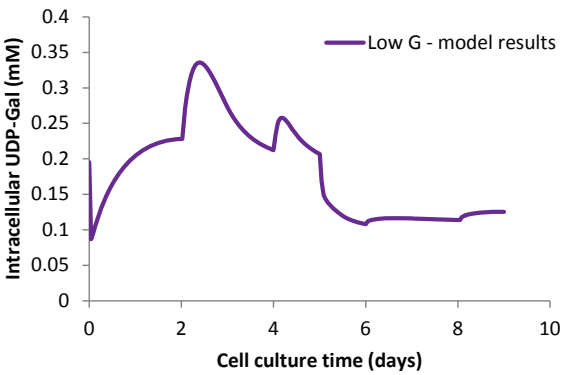




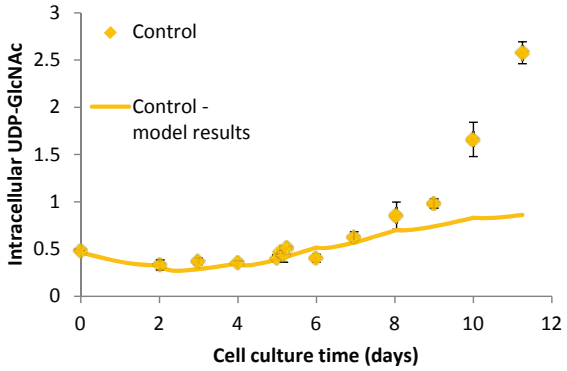
Figures 5.25a-c Figures 5.26a-c Experimental data (markers) and computational outputs (lines) of intracellular UDP-Glc for the control, High G and Low G culture with respect to time.

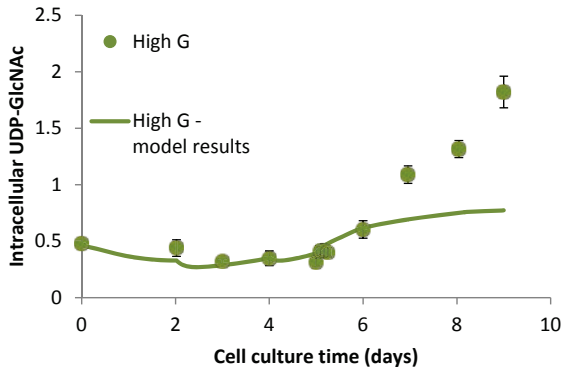


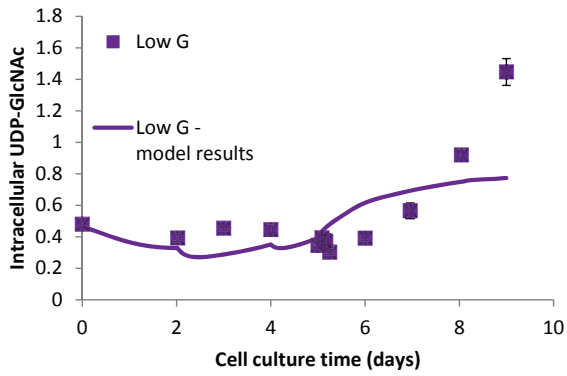




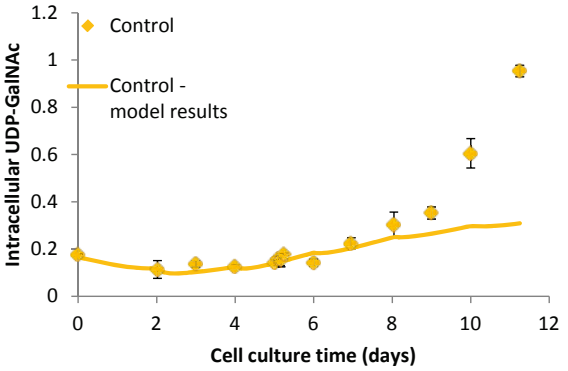
Figures 5.27a-c Experimental data (markers) and computational outputs (lines) of intracellular UDP-Gal for the control, High G and Low G culture with respect to time.

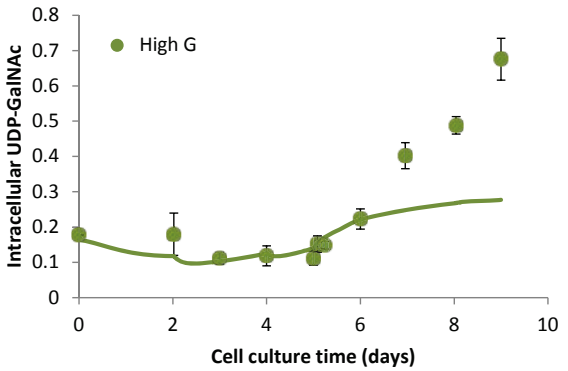


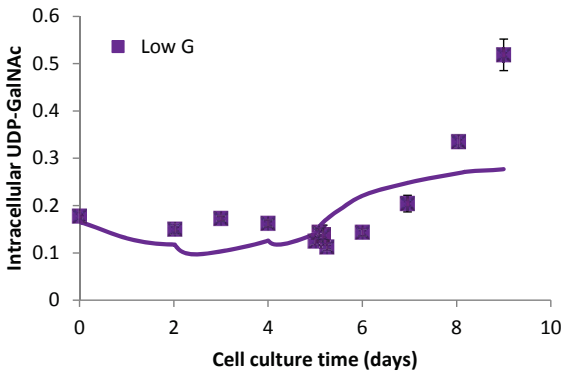




Figures 5.28a-c Experimental data (markers) and computational outputs (lines) of intracellular UDP-GlcNAc for the control, High G and Low G culture with respect to time.



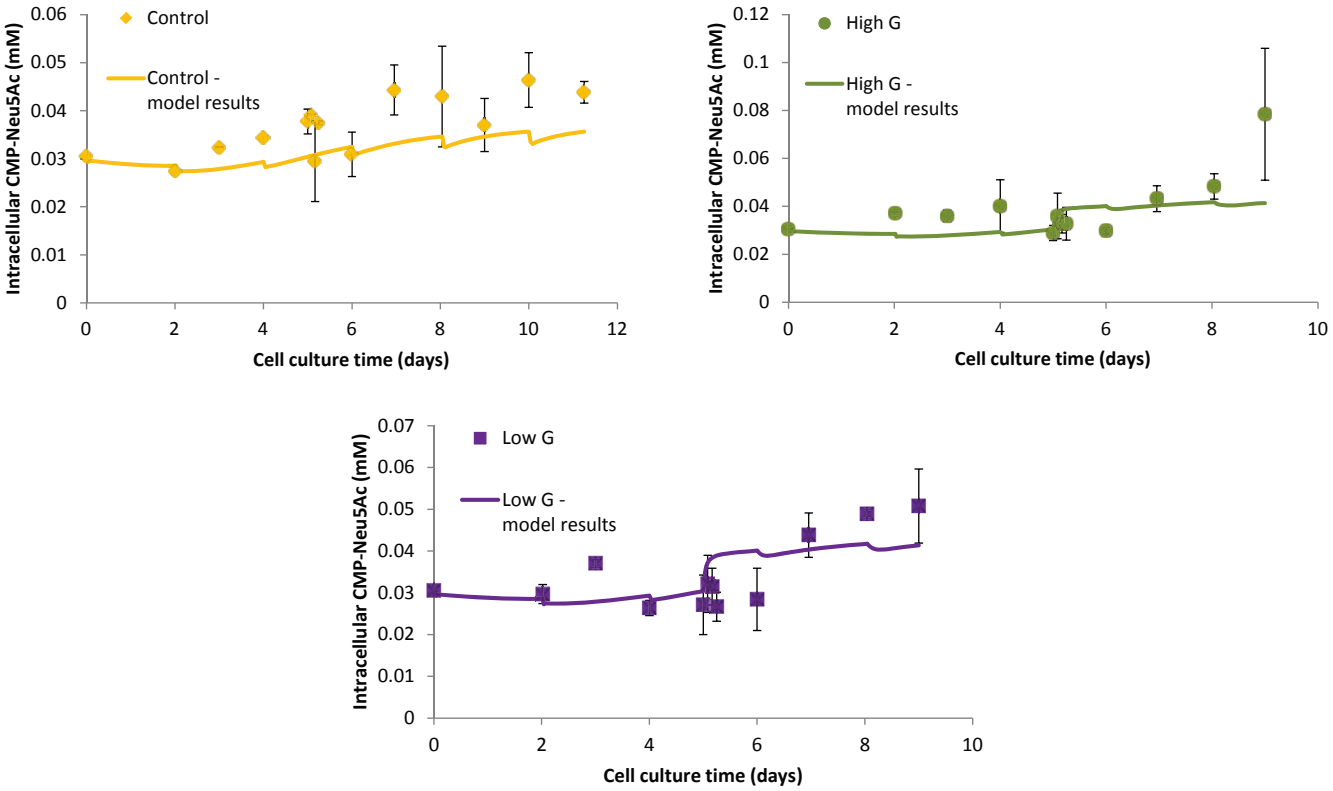




Figures 5.29a-c Experimental data (markers) and computational outputs (lines) of intracellular UDP-GalNAc for the control, High G and Low G culture with respect to time.

Lastly, the fits for the sialic acid-containing NSD CMP-Neu5Ac are in fair agreement with the experimental data (figures 5.29a-c). The model outputs show a reasonably flat profile with a small concentration increase after feeding on day 5, which is thought to be a result of decreased consumption due to growth inhibition. The flat profiles are a result of the strong product inhibition of reaction r29a (figure 5.5). While CTP concentrations were not

accurately reproduced by the nucleotide model, the uncertainty did not propagate to the CMP-Neu5Ac output. This suggests little dependence of the NSD on its nucleotide co-substrate. Furthermore, the concentrations did not increase together with the UDP-GlcNAc concentrations, which is the precursor to this sialic acid-containing NSD. Consequently, the NSD's production appears to be regulated by the strongly co-operative product inhibition indicated by a Hill coefficient of 4.15 (Hinderlich et al., 1997).



Figures 5.30a-c Experimental data (markers) and computational outputs (lines) of intracellular CMP-Neu5Ac for the control, High G and Low G culture with respect to time.

5.5. Conclusions

In this chapter the proof of concept model framework presented in chapter 3 was expanded further and trained using the experimental data presented in chapter 4. The objectives were an increase in model accuracy with respect to *in silico* reconstruction of the NSD metabolic network, the extension of the nucleotide model to capture additional details of species interaction and control of the metabolic network and a translation of the dynamic

cell culture model to a fed-batch operated GS-CHO cell culture. All the former were achieved through structural changes of the individual modules of the computational framework and model training using experimental data.

The cell culture dynamics model presented in this chapter was restructured and extended by the inclusion of glutamate, ammonia, asparagine, lactate, mannose, guanosine and DMSO and their effect on cell culture dynamics. The parameter values estimated based on the experimental data suggest growth inhibition through both galactose and ammonia as well as cell death mostly due to the accumulation of ammonia in the extracellular environment. This is in contrast to the work presented in chapter 3, where data from batch operation was used and cell death occurred due to nutrient depletion. Furthermore, a guanosine dependent switch was included in the model, where a new maximum cell growth rate, death rate and the antibody production constants are introduced in the presence of guanosine. The switch was able to account for cell growth inhibition and the increased specific antibody productivity resulting from metabolic changes after guanosine addition to the culture media, as discussed in chapter 4. The growth rate obtained from the cell culture dynamics model is also an input to both the nucleotide and NSD model, where it constrains the outlet fluxes. Both other modules of the model were also able to reproduce experimental data well and thus, giving confidence in the use of a guanosine dependent switch to simulate cell growth inhibition. The updated cell culture dynamics model was also able to account for operation under fed-batch and the resulting prolonged cell culture time.

The nucleotide model presented in this chapter was largely reconstructed based on knowledge of the metabolic network, as well as experimental findings from chapter 4, resulting in a semi-structured, partially mechanistic model. The reconstructed model is split into the *de novo* synthesis of purine and pyrimidine species, which are interlinked by means of inhibitory control mechanisms. The updated model now also includes glutamate and asparagine dependence as well as the dependency of GTP on extracellular guanosine concentrations. The trained model showed good agreement with experimental data for most nucleotide species. It was able to capture the guanosine induced increase in GTP and the resulting effect of the availability on ATP, which in turn affect UTP and CTP concentrations. Thus, the model structure is able to show interdependence of species within the metabolic

network, which increases model confidence and robustness. However, poor fits for CTP concentrations were achieved and thus, further probing of the network and in particular of CTP is required to improve model reliability further.

Lastly, the NSD model was updated with respect to the synthesis of GDP-Fuc and GDP-Man by changes in the reaction rate expressions and a mannose inlet flux term, while conserving the fully structured metabolic network. Together with the updated consumption rates for the host cell protein glycoform, good agreement with experimental data was achieved for most NSD species. The dynamic response to the addition of both mannose and guanosine on day 5 of culture was captured well by the model framework. Together with these results and estimated Hill-coefficients within a biologically feasible range, gives confidence in the changes made to the reaction rate expression. Good agreement with experimental data was also achieved for the NSD species CMP-Neu5Ac and UDP-Glc. While the concentration profile of UDP-Gal partially agreed with experimental data, deviation was observed after guanosine and mannose feed addition. The model predicted similar concentration profiles for both UDP-Hex species, which was not observed experimentally and thus, indicating either a lack of mechanistic detail or insufficient experimental training data. The UDP-HexNAc species were fitted well by the model with the exception of the final days of culture, where the model was not able to reproduce the species accumulation. It can be concluded that the *in silico* reproduction of the NSD *de novo* synthesis metabolic network is capable of capturing most experimental trends as well as giving sufficient flexibility for adaptation to perturbation scenarios. However, further training and experimental perturbations specifically of the UDP-Hex and UDP-HexNAc species are required to gain more knowledge of species and overall system behaviour to increase model confidence.

The holistic modelling approach achieved by means of the modelling framework, as initially presented in chapter 3, was successfully applied to the data set presented in chapter 4 and was able to reproduce it well. The modular structure allowed sufficiently flexibility with respect to the individual modules, while maintaining the overall platform structure. Consequently the framework is taken forward for further model refinement with the ultimate aim of steering and controlling the product glycoform by means of metabolic control through media supplementation. However, the individual modules leave room for

improvement and greater confidence in the model must be achieved in order to allow for *in silico* optimisation of feeding strategy. The most notable limitations of the model are the CTP output of the nucleotide model and the UDP-Hex and UDP-HexNAc outputs of the NSD model.

To address the overall project aim as well as the remaining model uncertainties a further experiment was designed. The addition of galactose and uridine to the cell culture media is known to improve the galactosylation of monoclonal antibodies, as discussed in chapter 1.6.2 (Wong et al., 2010b, Grainger and James, 2013). Furthermore, antibody galactosylation is a critical quality attribute of many biotherapeutics (Jedrzejewski et al., 2013). Increased product galactosylation is achieved through the increased availability of intracellular UDP-Gal. The addition of uridine is also known to increase UTP concentrations with the knock-on effect of increasing UDP-HexNAc pools intracellularly (Grammatikos et al., 1998). UTP is also the direct metabolic precursor to the synthesis of CTP and would therefore offer valuable insight into pyrimidine synthesis. Consequently, an experimental setup where the cells are probed through additions of varying amounts of galactose and uridine was carried out using GS-CHO cell line and fed-batch operation, as reported in the next chapter 6. The experimental output of this experiment will be able to probe the improved modules presented in this chapter as well as testing the dependence of the del Val glycosylation model on the availability of NSDs and specifically UDP-Gal pools. A further experiment and subsequent computational refinement of the model framework will produce a validated operation space in which *in silico* optimisation can take place.

Chapter 6

Galactose and Uridine Feeding

In this chapter experimental fed-batch culture data obtained from a variety of galactose and uridine feeding strategies is presented. The addition of these two substances is known to lead to an increase in galactosylation of the antibody Fc region due to a synergetic increase in UDP-Gal pools (Wong et al., 2010b, Grainger and James, 2013). Observation of the metabolic response of the cells to the feeding of a combination of galactose and uridine concentrations and the resulting changes in the antibody product glycoform allows for a significant extension of the modelling platform. The appeal of this improvement in the model lies in the relevance of galactosylation to biopharmaceutical production. In the context of biotherapeutic antibodies, galactose terminating glycan structures of the antibody Fc region are known to increase affinity towards the C1q complex, leading to improved complement lysis activity (CDC) (Raju, 2008, Hodoniczky et al., 2005). Thus, the experimental data presented here sets the groundwork, for *in silico* glycoengineering by means of metabolic control.

In order to build on the experimental and computational findings of chapters 4 & 5, the same experimental setup was used as in chapter 4 with regards to the GS CHO cell line, feeding of Efficient Feed C®, extracellular & intracellular metabolite measurements as well as final product glycoform analysis. However, extracellular and intracellular concentrations of galactose and uridine were measured instead of guanosine and mannose. Furthermore galactose and uridine have been added together with Feed C® on days 4 and 8 of the cell culture, as opposed to day 5 as reported in chapter 4. The rationale for an earlier exposure is the amplification of the effects on cell culture growth, when cell densities are still lower. The second addition enabled observation of the metabolic impact during the stationary phase of the cell culture, where antibody productivity is highest as well as amplifying any effects that

may lead to shortened cell culture periods. Additionally, the same concentration of manganese(II) chloride ($MnCl_2$) was supplemented to all cultures at seeding due to its known effect in improving galactosylation in CHO cell lines (Crowell et al., 2007) and even creating a synergetic effect in combination with galactose and uridine (Gramer et al., 2011). As before the intracellular NSD data was collected on a daily basis and in two additional 2 h intervals after each feed addition thus, resulting in a dynamic dataset with emphasis on the metabolic response to feed additions. No DMSO was added in this experiment as uridine was successfully dissolved in larger quantities of Feed C® due to its higher solubility in an aqueous solution than guanosine. The absence of DMSO avoids problems in under-processing of glycan structures and cell growth dynamics as was observed in section 4.4.

The addition of uridine to the cell culture is known to increase UDP-Hex and UDP-HexNAc pools indirectly by firstly increasing the concentration of UTP (Grammatikos et al., 1998). It has previously been observed that elevated UTP concentrations can lead to a reduction in ATP (Rijcken et al., 1995), while increasing CTP pools as CTP is its direct metabolic derivative. This provides an excellent opportunity to further study the interaction and control mechanisms of the various triphosphate species that make up the *de novo* synthesis network of nucleotides. Uridine concentrations of 5mM and 20mM were chosen, when supplemented to the media. The work by Grainger et al. suggested reduced cell growth at concentrations of 10mM of uridine and above, while Wong et al. saw no significant reduction in cell growth at 5mM (Grainger and James, 2013, Wong et al., 2010b). As a result concentrations for this experiment were chosen to give information about the metabolic behaviour of cells at concentrations corresponding to minimal perturbations (5 mM uridine) and high perturbations in cell growth (20 mM uridine), where the latter was essential in investigating detrimental effects, that may offset any benefits in glycosylation.

Large amounts of galactose will increase osmolarity to the point where it will become detrimental to cell growth and antibody production rate (Takagi et al., 2000). However, previous research investigated the substitution of galactose with glucose in the culture media at comparable concentrations and suggested a decrease in cell culture growth, while maintaining viability (Altamirano et al., 2001). On the other hand the findings of Wong et al. suggest no significant effect on cell culture growth or cell metabolism at 10mM galactose

supplementation to glucose containing cell culture media. (Wong et al., 2010b). However, the same study observed improved galactosylation thus, suggesting consumption of galactose in the presence of glucose. Consequently, galactose supplementations equating to concentrations of 10mM in total cell culture media have been made to explore the dynamic effect in the experimental setup. On the other hand large amounts of galactose will increase osmolarity to the point where it will become detrimental to cell growth and antibody production rate (Takagi et al., 2000). To observe the dynamic perturbations in cell metabolism resulting from high galactose supplementation a second condition, with 50mM galactose cell culture media, was investigated.

Research by Grainger et al., suggested an "on/off" response of cells to an addition of manganese ions at a concentration as low as 1µM with no detrimental effect to cell culture dynamics. This concentration was found to be sufficient to increase galactosylation with no further improvement at higher concentrations. As a result of this all flasks were supplemented with 1µM at seeding to enable maximal galactosylation and investigate the cell culture in the best possible process space for galactosylation.

The control cultures were cultivated as triplicates (N_C = 3), while all other remaining experimental conditions were cultivated as duplicates (N = 2) and error bars indicate standard deviation (ER = SD). In summary the following conditions were tested, where the galactose and uridine additions were made on days 4 and 8:

- **Control** – 1µM manganese(II) chloride at seeding

- Low galactose, low uridine (**10G5U**) – 1µM manganese(II) chloride at seeding; additions of 10mM galactose and 5mM uridine

- High galactose, low uridine (**50G5U**) – 1µM manganese(II) chloride at seeding; additions of 50mM galactose and 5mM uridine

- Low galactose, high uridine (**10G20U**) – 1µM manganese(II) chloride at seeding; additions of 10mM galactose and 20mM uridine

- Low galactose, no uridine (**10G**) – 1μM manganese(II) chloride at seeding; additions of 10mM galactose

All fed-batch cultures were also supplemented with CD EfficientFeed C® on even days of cell culture. The CD EfficientFeed C® supplementations are referred to "feeding" of Feed C as opposed to "supplementation", which is indicative of the uridine and/or galactose additions on days four and eight of culture.

6.1. Cell dynamics and extracellular environment

The choices of measurements taken in this section have not been altered from chapter 4, where the experimental strategy has been discussed in full.

The outcome of the feeding experiment showed large variations in the cell dynamics between the 5 conditions. Perhaps most strikingly a near total cell growth arrest and a quick drop in cell viability can be observed in the 10G20U condition (figures 6.1 & 6.2). In comparison to other conditions it can be concluded that this is a direct result of the high concentration uridine addition. This result has previously been reported by Grainger et al. (Grainger and James, 2013). The control cultures on the other hand showed the highest cell density, highest viability as well as a significantly higher IVCC (figure 6.3) as compared to the remaining conditions. The 10G and 10G5U conditions show no significant difference in IVCC and little difference in viable cell density. However, the cell cultures supplemented with only galactose showed an early increase in dead cell density and a resulting drop in viability. The result of this was a drop in viability below 70% and thus, an early termination of the 10G experiment as compared to the 10G5U run, which indicates that uridine in low concentrations negates the negative effects of galactose with respect to cell viability. Lastly the high galactose condition 50G5U showed a suppressed viable cell density, which is reflected by a significantly lower IVCC as compared to both 10G and 10G5U. Yet again the uridine addition appears to have prevented early cell death as compared to the 10G condition.

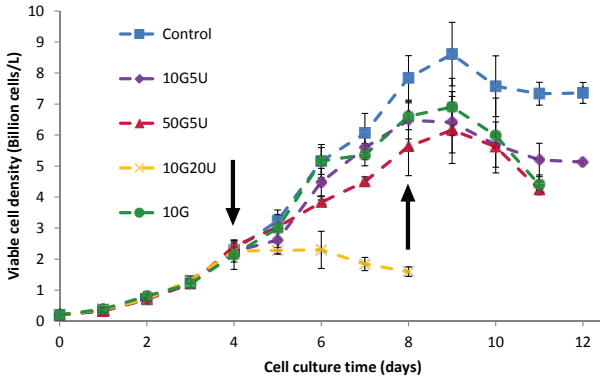


Figure 6.1 Viable cell density with respect to culture time of the three experimental runs (N_C = 3, N = 2, EB = SD).

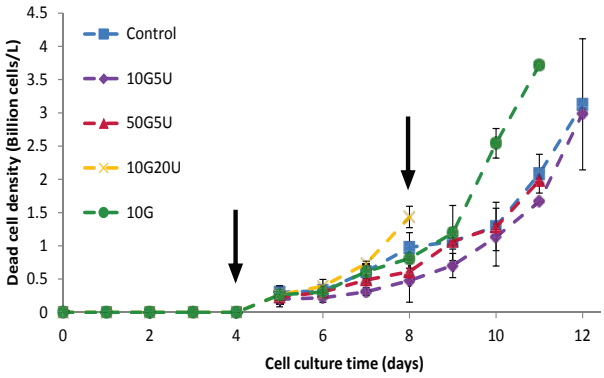


Figure 6.2 Dead cell density with respect to culture time of the three experimental runs (N_C = 3, N = 2, EB = SD).

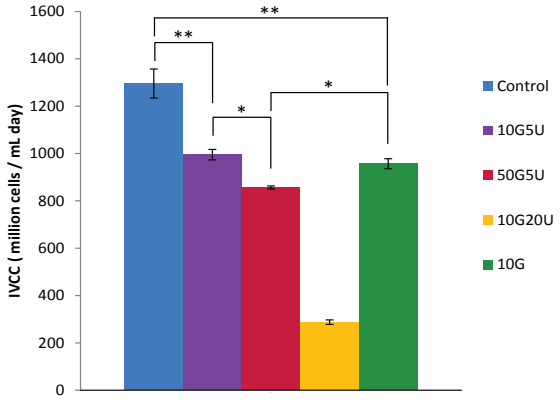


Figure 6.3 Integral viable cell concentration (IVCC). A significant difference between IVCC values is indicated by asterisks, where * P < 0.05 and ** P < 0.01 (N_C = 3, N = 2, EB = SD).

Similarly to the cell growth dynamics a much reduced antibody titer can be observed for the high uridine condition 10G20U compared to all other feeding strategies (figures 6.4 & 6.5). The control culture on the other hand shows a significantly higher titer as compared to all other conditions, which results from a higher cell density and viability during the longer stationary phase of the culture. The decrease in the final antibody titer of the remaining three conditions 10G5U, 50G5U and 10G do not quite show statistical significance, although the data suggests that the final day antibody titer and IVCC for each culture show the same trend. As a result it is not surprising to find that the calculated specific antibody productivity (q_{mAb}) after galactose and uridine feeding on day 8 of culture shows no significant deviation within the set of conditions (figure 6.6). This is in contrast to the findings of chapter 4, where guanosine additions led to an increase in specific mAb productivity. This behaviour has not been replicated in the 10G20U condition, where growth

was halted due to uridine. This suggests a different mechanism of cell growth inhibition compared to guanosine, where the cells were thought to be arrested in the S phase. The culture's q_{mAb} from day 4 to each cultures respective final day shows a reduction in specific mab productivity, despite maintaining good viability cell density until cell culture termination and viability greater than 70%. This suggests a reduction in specific productivity due to changes in cell metabolism in the cell's decline phase or possible changes in the extracellular environment rather than cell viability, cell density or the various feeding strategies.

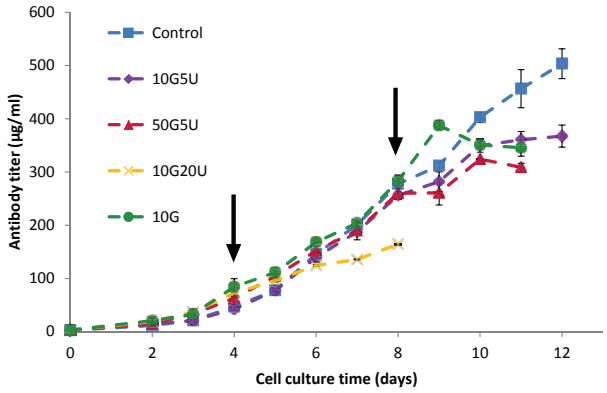


Figure 6.4 Antibody titer with respect to cell culture time (N_C = 3, N = 2, EB = SD).

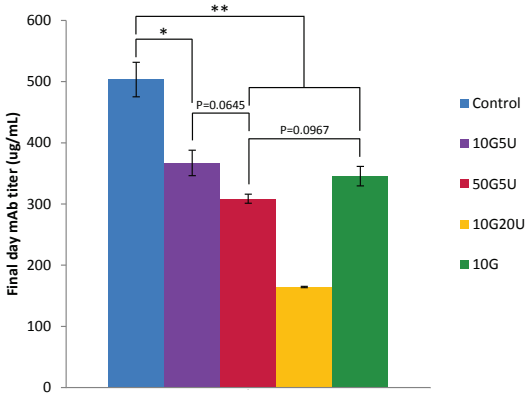


Figure 6.5 Final day Antibody titer for all experimental conditions (N_C = 3, N = 2, EB = SD).

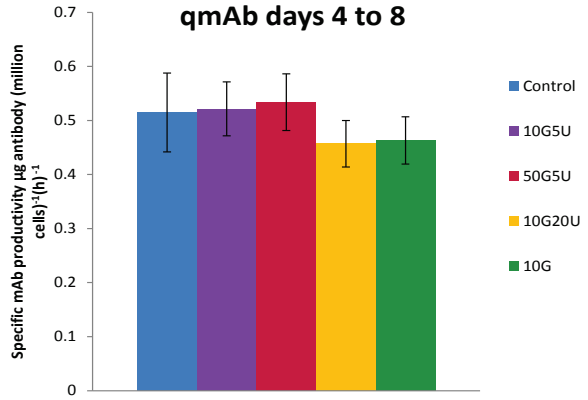


Figure 6.6 Specific mAb productivity in the post feeding interval from day 4 to day 8 (N_C = 3, N = 2, EB = SD).

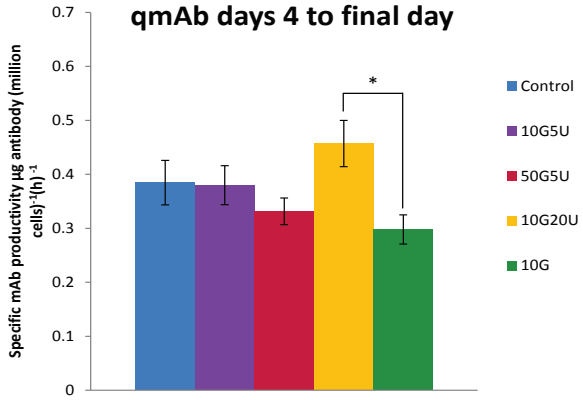


Figure 6.7 Specific mAb productivity in the post feeding interval from day 4 the respective final days of culture (N_C = 3, N = 2, EB = SD).

Measurements of extracellular uridine concentrations reveal little consumption during the duration of the culture, when uridine was added to cultures (figure 6.8). Absolute as well as specific consumption appeared to be larger at the 20 mM concentration despite a reduced

IVCC. At the lower 5 mM concentration both the 10G5U and 50G5U conditions showed no significant difference in consumption and hence, suggest that uridine consumption is not affected by galactose additions. Negligible amounts of uridine were detected in the extracellular environment at late culture stages in the Control and 10G conditions and appear to be the result of cell lysis.

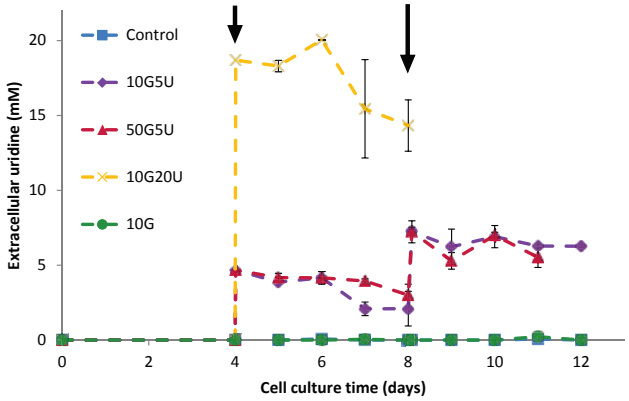


Figure 6.8 Extracellular uridine with respect to culture time (N_C = 3, N = 2, EB = SD).

The extracellular galactose data suggests significant consumption of galactose at both the low and high galactose concentrations (figures 6.9 & 6.10). This finding is contradictory to the work by Altamirano et al., who observed little consumption of galactose with preference for glucose over lactate and lactate over galactose (Altamirano et al., 2004). The consumption observed was especially large in the high galactose environment of 50G5U. The galactose concentrations of the 10G5U, 50G5U and 10G conditions show similar profiles. Bearing in mind the lower cell density in the 50G5U condition suggests a higher galactose uptake per cell. This may indicate transport limitations rather than limitations in consumption and thus, suggests preferential uptake of galactose over glucose. The similarities in the 10G5U and 10G profiles suggest no evidence of interaction of uridine and galactose with respect to consumption from the extracellular environment.

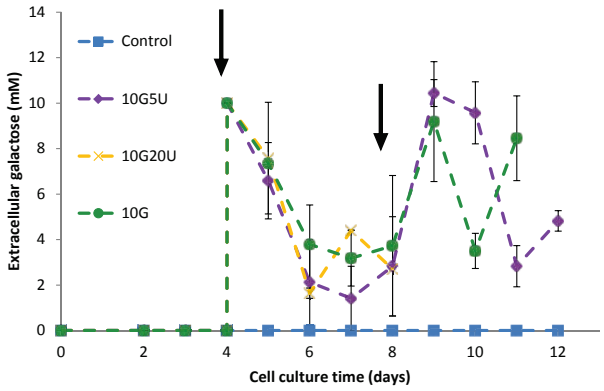


Figure 6.9 Extracellular galactose for control, 10G5U, 10G20U and 10G conditions with respect to culture time (N_C = 3, N = 2, EB = SD).

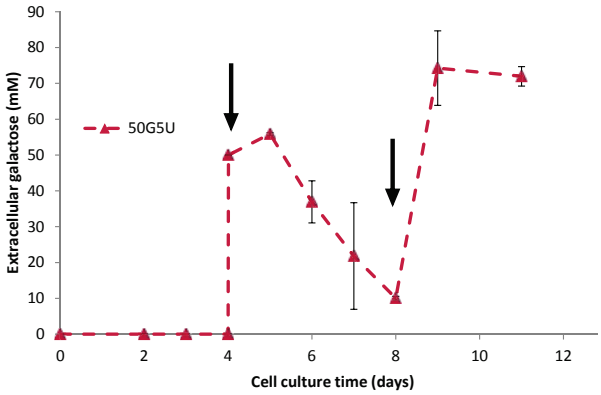


Figure 6.10 Extracellular galactoe for the 50G5U condition with respect to culture time (N_C = 3, N = 2, EB = SD).

The extracellular glucose concentration shows a much higher consumption in the control culture compared to the remaining conditions (figure 6.11). No distinguishable difference is observed in the glucose profile of 10G5U and 10G. The high galactose concentration of the 50G5U condition shows less glucose consumption. This points again towards a preferential consumption of galactose over glucose however, it is also a reflection of each of the IVCCs, as seen by the low glucose consumption of the 10G20U condition. Consequently, the reduced glucose consumption will be a combination of both the preferential galactose uptake and the reduced IVCC. At no point during any of the experiments can glucose limiting conditions be observed.

The overall lactate trend shows a very fast lactate build up until day four of the culture and then a plateau with limited consumption and only minor signs of separation under the different feeding strategies (figure 6.12). Generally signs of net consumption can be observed in the uridine fed samples in the time period of days 4 to 8, where the highest consumption is observed in 10G20U. Towards the late culture stage the control cultures show larger consumption than the galactose fed conditions. This is again in contrast to the work by Altamariano et al. (Altamirano et al., 2004), where a decrease in lactate was observed after galactose supplementation. However these are finding from a low glucose environment and hence, the comparison is limited. In summary, the data presented here shows preference in consumption of galactose over glucose over lactate.

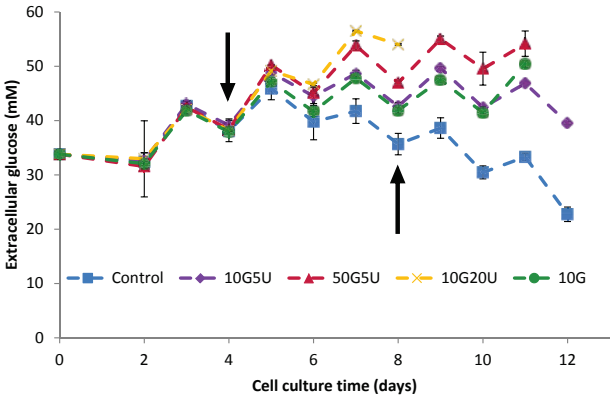


Figure 6.11 Extracellular glucose for all conditions with respect to culture time (N_C = 3, N = 2, EB = SD).

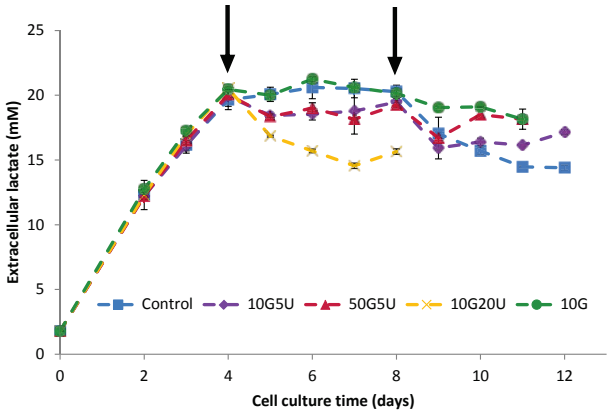


Figure 6.12 Extracellular lactate for all conditions with respect to culture time (N_C = 3, N = 2, EB = SD).

The extracellular concentration of glutamate suggests consumption of the species between increases resulting from the FeedC® supplementation to the cell culture media (figure 6.13). The concentration profiles do not differ significantly for all investigated conditions. Glutamine data on the other hand shows a net production of glutamine at all times under all conditions (figure 6.14). The only condition with significantly higher glutamine accumulation is the 10G, while all others show no significance deviation. The extracellular ammonia concentration profiles can be split into two distinctively different groups of uridine fed and non-uridine fed (figure 6.15). The uridine fed samples show increased net ammonia production after feeding over the non-uridine fed conditions. This suggests either a metabolic breakdown of the nitrogen containing uridine by the cells, resulting in ammonia production or an increased metabolism of amino acids leading to the increased ammonia concentration. The latter is not supported by the limited amino acid data containing glutamine and glutamate, only. The near identical ammonia and glutamate data of the control cultures vs 10G, which are the precursors of glutamine, indicates that the increased glutamine concentration may be the effect of reduced consumption in cell metabolism. This would mean that more glutamine is transported to the extracellular environment in the scenario where production is not altered.

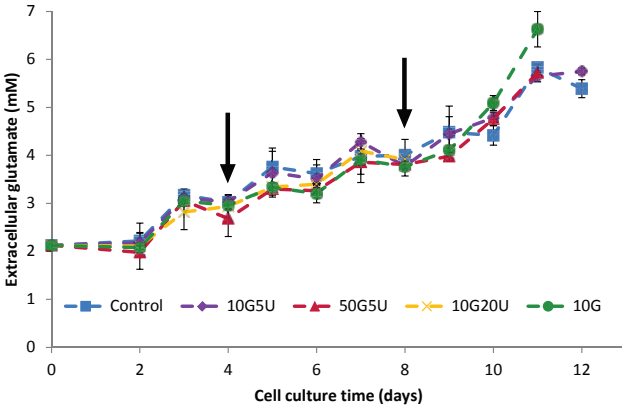


Figure 6.13 Extracellular glutamate for all conditions with respect to culture time (N_C = 3, N = 2, EB = SD).

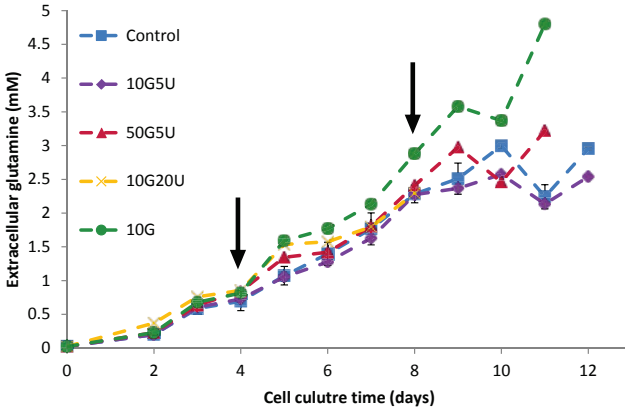


Figure 6.14 Extracellular glutamine for all conditions with respect to culture time (N_C = 3, N = 2, EB = SD).

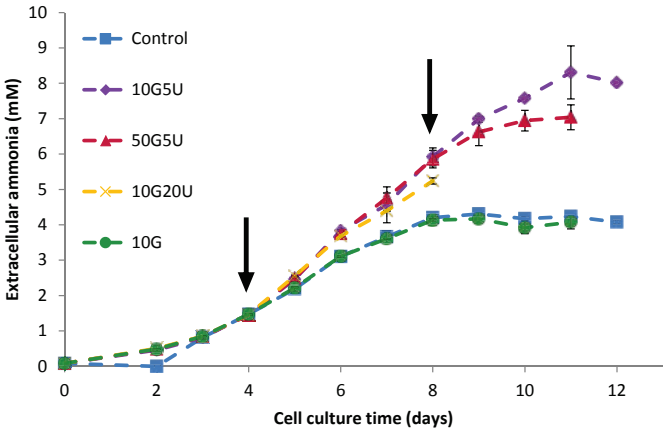


Figure 6.15 Extracellular ammonia for all conditions with respect to culture time (N_C = 3, N = 2, EB = SD).

6.2. Intracellular metabolites

The intracellular galactose concentrations show a clear peak after galactose feeding under the 50G5U condition (figure 6.16). The galactose concentration increases within the space of 2 hours and supports the extracellular data, which suggested a rapid uptake of galactose into the intracellular environment. The concentration remains significantly higher under this condition than for any other experimental run. Galactose spikes can also be seen after galactose feeding for the remaining galactose fed conditions 10G5U, 10G20U and 10G, while none are observed in the control cultures. Furthermore an accumulation of galactose towards the end of culture can be observed in all runs other than 50G5U. The accumulation in the control cultures suggests the action of the synthesis and salvage pathways of galactose as no significant amounts of galactose were observed in the extracellular environment. The intracellular glucose concentrations can be broadly split into groups. The first group is the control, G10 and 50G5U conditions, where similar concentrations were observed, which fluctuated between 10 mM and 20 mM during most of the culture (figure 6.17). No accumulation is apparent towards the end of the culture for these conditions. The second group consisting of the conditions 10G5U and 10G20U, showed an accumulation of intracellular galactose towards the end of the culture and concentrations, consistently above 20 mM from day 4 onwards (figure 6.18). The second group may shows signs of limited glucose accumulation as a consequence of metabolic slowdown due to uridine addition. However, the same cannot be said for 50G5U, which was also supplemented with uridine. This may be explained by the high galactose consumption of 50G5U and resulting galactose accumulation, which may have acted competitively with glucose uptake and thus, prevented its accumulation. All feeding strategies exhibit visible glucose concentration spikes after Feed C® supplementation and no total depletion is observed at any point throughout the experiment.

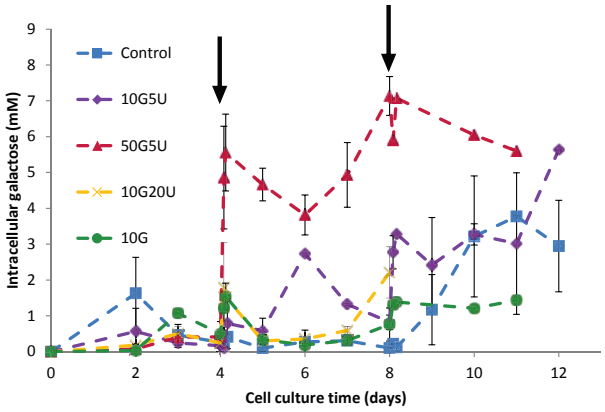


Figure 6.16 Intracellular galactose for all conditions with respect to culture time (N_C = 3, N = 2, EB = SD).

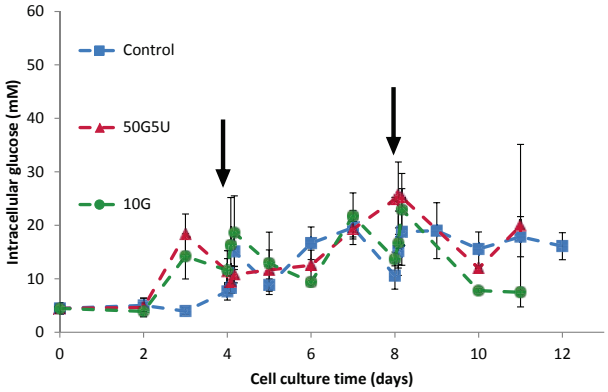


Figure 6.17 Intracellular glucose for the control, 50G5U and 10G with respect to culture time (N_C = 3, N = 2, EB = SD).

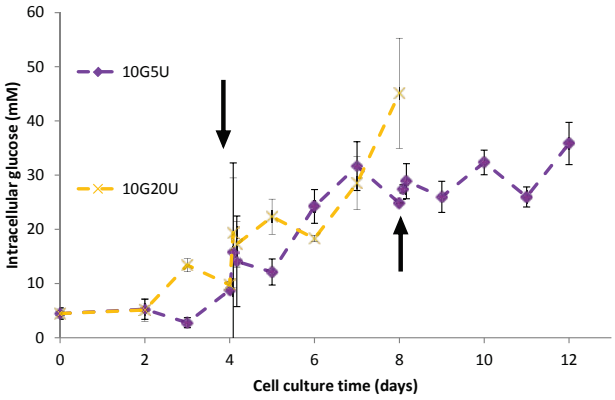


Figure 6.18 Intracellular glucose for the 10G5U and 10G20U with respect to culture time (N_C = 3, N = 2, EB = SD).

The intracellular uridine concentrations (figure 6.19) reflect those of the extracellular environment for each of the test conditions (figure 6.8) with the control cultures and 10G showing no significant amounts. The 10G5U and 50G5U show rapid increases after both additions but do not vary from each other in their concentrations profiles. This suggests no interference of galactose with the uptake and accumulation of uridine intracellularly. The high uridine condition 10G20U shows a slower uridine uptake in relative terms, where a plateau is not reached within the first 4 hours after feeding. The data indicates that the membrane transport of uridine is not a limiting factor with respect to uridine uptake and subsequent metabolism.

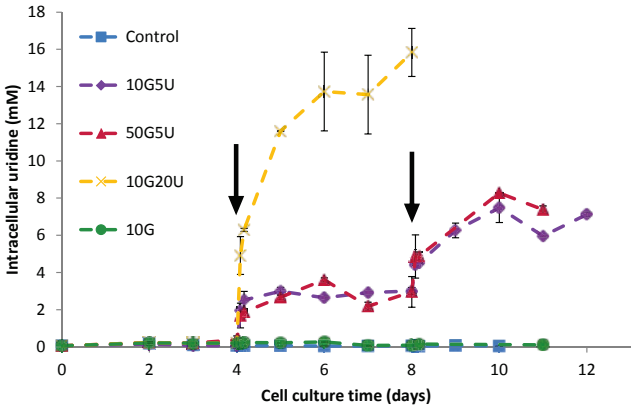


Figure 6.19 Intracellular uridine for all conditions with respect to culture time (N_C = 3, N = 2, EB = SD).

The uridine additions have successfully increased the UTP concentrations in the intracellular environment (figure 6.20). The control cultures and 10G condition show similar concentration profiles with little fluctuation except for the final days, where a decrease in UTP can be noted for 10G as compared to the Control. Both the 10G5U and 50G5U show very similar concentration profiles, where a rapid increase in UTP is observed on the first uridine addition but only a limited response to the second feeding. The 10G20U high uridine condition generated the largest response to the feeding with a constant plateau at 11 mM UTP from day 5 until the end of the culture. The UTP profiles appear to follow those of the intracellular uridine, where uridine was fed. On day 5 a stable concentrations of UTP are observed with increases of 4.62 ± 0.48 and 4.49 ± 0.34 fold over the control for 10G5U and 50G5U, respectively (table 6.1). The increase of the 50G20U condition is 8.73 ± 0.72 and thus, approximately twice higher than the conditions with 5 mM uridine supplementation. This indicates partial saturation as the uridine addition does not translate to an equivalent UTP increase. The CTP profiles follow those of UTP very closely (figure 6.19). The concentration of 10G does not differ significantly from the control cultures with only a slight decrease towards the end of the culture. Again both the 10G5U and 50G5U form a pair of highly similar concentrations with a rapid increase upon feeding and little response to the second uridine addition. Lastly, the 10G20U condition shows the highest increase in CTP with a relatively slower increase before reaching a constant concentration of just over 1mM from day 5 onwards. The relative increases of CTP are approximately 3-fold for both 10G5U and 50G5U and 4.1-fold for the 10G20U condition (table 6.2) and consequently suggesting

further limitations due to saturation. The results show a high dependency of UTP on uridine and CTP on UTP. The latter dependency is a result of UTP being the metabolic precursor to CTP in the *de novo* synthesis of nucleotides. It can be seen that the effect of uridine addition to the cell culture media propagates in a diminishing manner, where the effects are the least pronounced in CTP however, they remain significantly with respect to the control cultures.

Table 6.1 Relative increase of UTP with respect to the control on day 5 of the culture

	Relative UTP increase
Control	1± 0.08
10G5U	4.62 ± 0.48
50G5U	4.49 ± 0.34
10G20U	8.73 ± 0.72
10G	1.05 ± 0.11

Table 6.2 Relative increase of CTP with respect to the control on day 5 of the culture

	Relative CTP increase
Control	1 ± 0.06
10G5U	3.07 ± 0.30
50G5U	2.96 ± 0.20
10G20U	4.14 ± 0.32
10G	1.09 ± 0.09

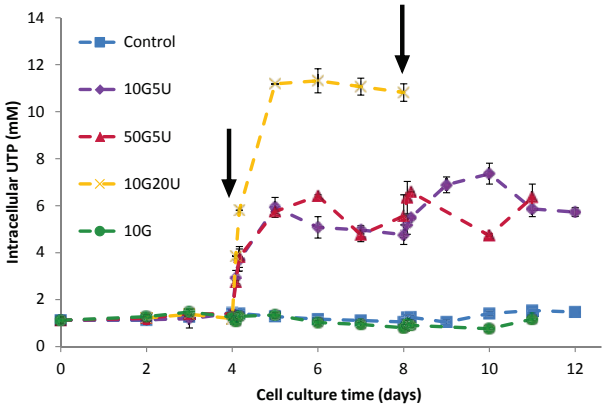


Figure 6.20 Intracellular UTP for all conditions with respect to culture time (N_C = 3, N = 2, EB = SD).

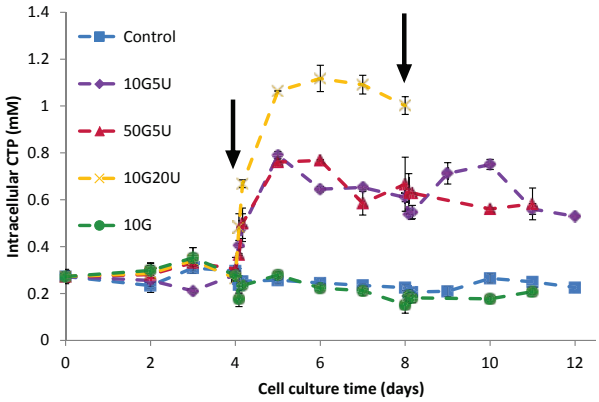


Figure 6.21 Intracellular CTP for all conditions with respect to culture time (N_C = 3, N = 2, EB = SD).

The ATP concentrations show a much more limited response to uridine additions than the pyrimidines CTP and UTP (figure 6.22). However, a decrease in ATP can be observed as a result of the uridine additions, where the higher 20 mM concentration results in a larger drop in ATP as compared to the 10G5U and 50G5U conditions. The observation of a reduction of ATP as a result of increased UTP after uridine addition was also made by

Rijcken et al (Rijcken et al., 1995). The control cultures show a profile with an almost constant concentration of approximately 2 mM. The galactose feeding in the condition 10G appears to have marginally reduced ATP with a more pronounced drop towards the later stages of the culture. However, the higher supplementation of 50 mM galactose in 50G5U shows little additional detrimental effect as compared to 10G5U. A similar picture is painted with both ADP and AMP, where the data shows a split into uridine free and uridine fed cultures (figures 6.23 & 6.24). The uridine fed cultures show a drop after feeding and thus, indicating an overall drop in adenine synthesis as compared to cultures with no uridine. The control and 10G cultures show a peak on day 2 for both ADP and AMP with little change in concentration until the end of the culture period, where an accumulation can be observed that is more pronounced with AMP. The accumulation at the end of the culture can also be observed for the uridine fed cultures although, to a lesser extent.

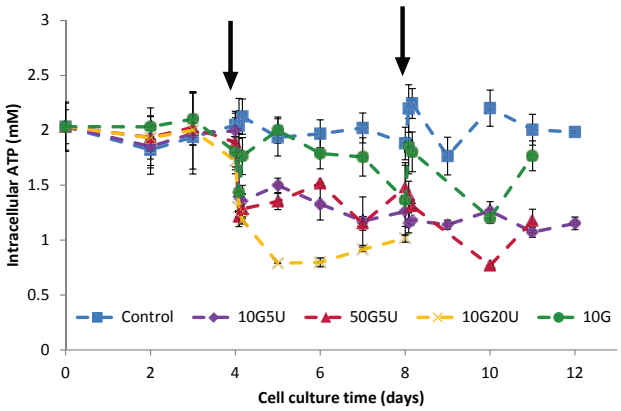


Figure 6.22 Intracellular ATP for all conditions with respect to culture time (N_C = 3, N = 2, EB = SD).

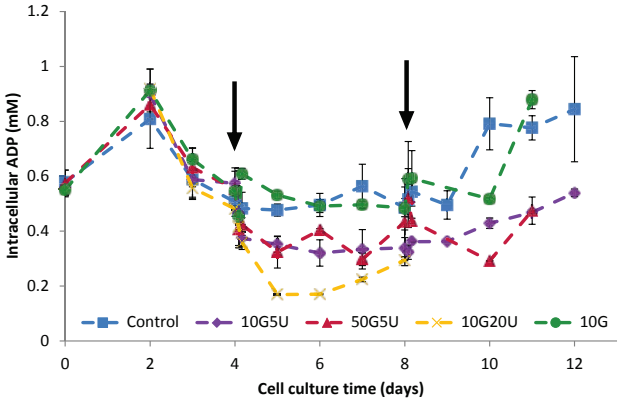


Figure 6.23 Intracellular ADP for all conditions with respect to culture time (N_C = 3, N = 2, EB = SD).

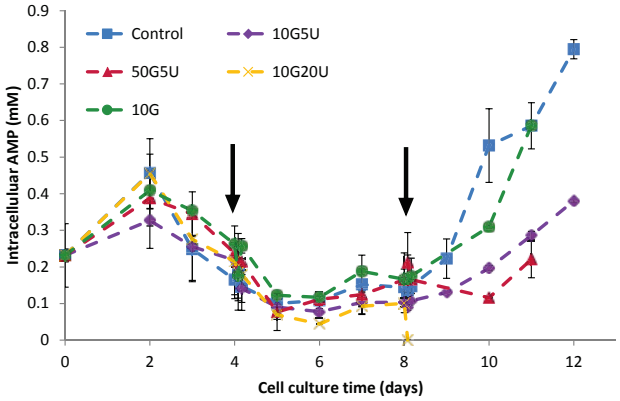


Figure 6.24 Intracellular uridine AMP for all conditions with respect to culture time (N_C = 3, N = 2, EB = SD).

The GTP concentrations for all cultures show little variation with concentrations ranging between 0.5 mM and 0.8 mM for all conditions at all time points (figure 6.25). A drop in GTP concentration can be observed upon the first uridine addition for the uridine fed cultures however, the concentrations converge with the Control and 10G on days 5 and 6. A second, although smaller drop, can be observed as a result of the second uridine addition.

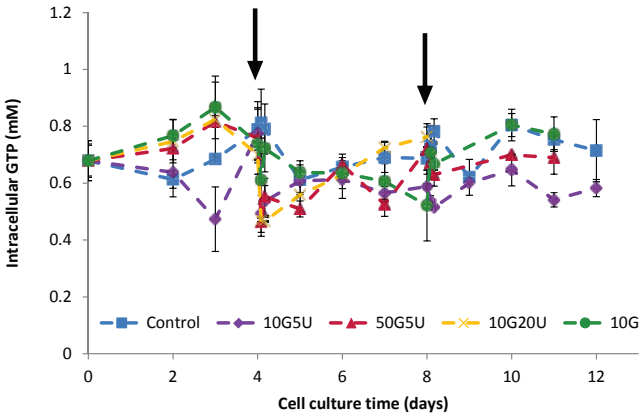


Figure 6.25 Intracellular GTP for all conditions with respect to culture time (N_C = 3, N = 2, EB = SD).

6.3. Intracellular Nucleotide Sugar Donors

The main focus of the investigation was to find the effect of the different feeding strategies on the dynamic availability of UDP-Gal. The concentrations of all cultures prior to day 4 were too low to allow for quantification and thus, data from day 4 onwards only is presented. The results show that each of the test conditions was able to achieve a significant increase in UDP-Gal concentration over the control cultures (figure 6.26). In all cases the effect was rapid with the quickest and highest peak resulting from the 10G condition. 10G is also notable for achieving a high peak immediately after feeding and then going into a steady decline with a much smaller peak resulting from the second addition. The 10G20U culture produced an accumulation of UDP-Gal from day 4 until the end of the culture, where the concentration rose to 2.30 mM, which corresponds to an increase by a factor of 34.2 ± 4.6 when compared to the concentrations in the control cultures on day 8. The

conditions 10G5U and 50G5U both showed a fast increase in UDP-Gal on day 4, as compared to the Control and remained at a steady concentration of 0.8 mM to 1 mM until the second feeding. After this a significant accumulation can be observed until the end of the culture, where the increase by the 50G5U condition is more rapid. The control cultures showed a steady concentration profile with little fluctuation with unquantifiable amounts of UDP-Gal on the final two days of the culture and thus, no evidence of accumulation as opposed to the fed cultures. Interestingly the concentration profiles of UDP-Glc paint a different picture (figure 6.27) to those of UDP-Gal despite both species being separated by only a single reaction step in the metabolic network of *de novo* NSD synthesis. The Control shows little variation with respect to time with a ratio of UDP-Glc to UDP-Gal of 3.54 ± 0.57 from days 4 to 10 of the culture. The galactose fed condition 10G shows a UDP-Glc profile that is very similar to the Control. However, an increase in UDP-Gal means a very different and varying ratio of UDP-Glc to UDP-Gal, which ranges from 0.25 ± 0.06 on day 4 two hours after galactose feeding and a maximum of 1.02 ± 0.29 just prior to feeding on day 8. This shows a selective increase in UDP-Gal in the intracellular environment as a result of galactose additions. At the high uridine 10G20U condition an accumulation of UDP-Glc can be observed after the addition, which may be due to high uridine conditions but also a reduced consumption due to the slowdown in cell growth. The conditions 10G5U and 50G5U show UDP-Glc profile that appears to follow that of the uridine additions very closely with little variation between the two. This is a very interesting observation, as the uridine additions were reflected to a lesser extent in the UTP concentrations. This suggests a reduced consumption of UDP-Glc as a result of reduced growth due to the uridine additions. It is also important to note that no accumulation of UDP-Glc takes place towards the end of the culture, as opposed to UDP-Gal. This together with the selective increase in the 10G condition confirms the findings of chapter 4 that suggested that both the epimerase and the transferase enzymes are involved in the catalysis of the UDP-Hex species (reactions 22 & 23 in figure 5.5). While the UDP-glucose 4-epimerase (EC 5.1.3.2) produces a constant ratio for the UDP-Hex and UDP-HexNAc species this is not the case in the presence of galactose. This suggests either a bottleneck in the epimerase or greater involvement of UDP-glucose-hexose-1-phosphate uridylyltransferase (E.C. 2.7.7.12) in the presence of galactose.

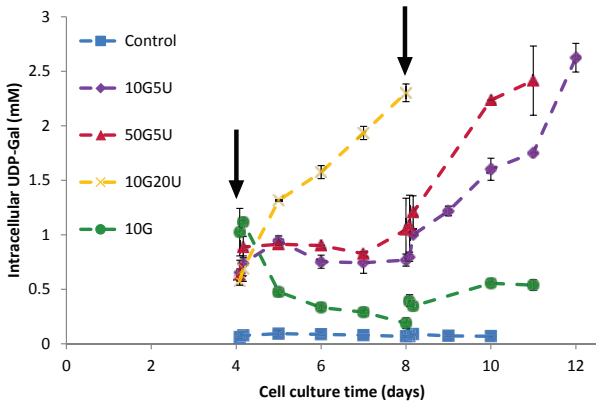


Figure 6.26 Intracellular UDP-Gal for all conditions with respect to culture time (N_C = 3, N = 2, EB = SD).

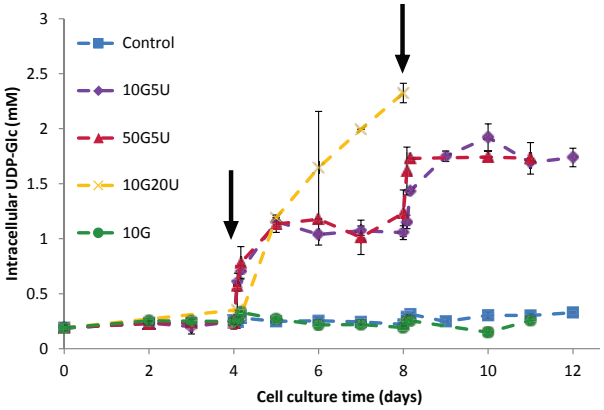


Figure 6.27 Intracellular UDP-Glc for all conditions with respect to culture time (N_C = 3, N = 2, EB = SD).

Both UDP-HexNAc species show mirrored each other's concentrations for all conditions with accumulation towards the end of the culture (figures 6.28 & 6.29). The Control and 10G appear to follow the same trend, which was already observed in chapter 4 with respect to UDP-HexNAc with an increase towards the end of culture. It was argued that the UDP-HexNAc profiles follow that of intracellular glutamine, which acts as the nitrogen source in the *de novo* synthesis of both species. A rapid increase in UDP-HexNAc after uridine supplementation suggests that increased UTP concentrations leads to a further concentration increase, where the steepest increase is observed in 10G20U. A somewhat faster increase in 50G5U can be observed over 10G5U, which may indicate reduced consumption as a contributing factor, as the growth observed in 50G5U was reduced compared to 10G5U. The ratio of UDP-GlcNAc to UDP-GalNAc for all culture conditions across the entire range of sample points is 2.66 ± 0.09. This shows that the epimerase reaction joining both species together acts as an equilibrium reaction with a ratio independent of culture conditions. The epimerase (EC 5.1.3.7) also links the UDP-Hex species and thus, the varying ratio in the UDP-Hex concentration suggests greater involvement of the transferase reaction in NSD metabolism. The bottleneck is the result of all extracellular galactose passing through this reaction step on the way to glycolysis and thus, creating a large flux.

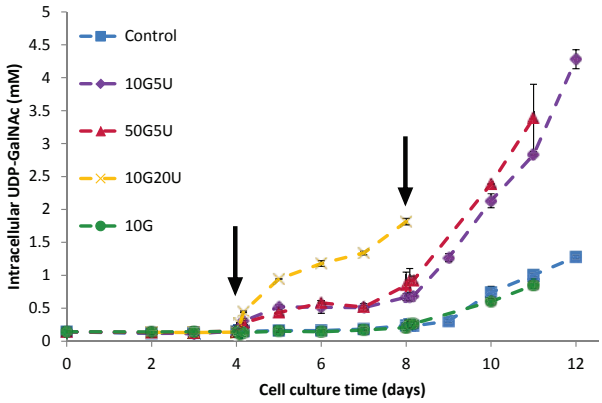


Figure 6.28 Intracellular UDP-GlcNAc for all conditions with respect to culture time (N_C = 3, N = 2, EB = SD).

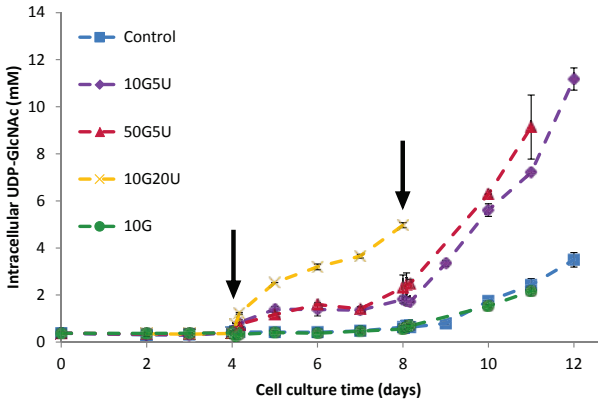


Figure 6.29 Intracellular UDP-GalNAc for all conditions with respect to culture time (N_C = 3, N = 2, EB = SD).

Limited data is available for CMP-Neu5Ac due to co-elution with a much larger uridine peak in the chromatographic spectrum. Thus, no data is available after uridine supplementation however, previous studies have shown that large increases in UDP-HexNAc due to uridine and glucosamine supplementation to the culture media led to limited increases in CMP-Neu5Ac (Baker et al., 2001). The limited propagation of the effect is due to a strong allosteric feedback control mechanism by which CMP-Neu5Ac is inhibits the conversion of UDP-GlcNAc to ManNAc (reaction 29 figure 5.5). Consequently an increase in UDP-GlcNAc of larger magnitude than that of CMP-Neu5Ac was anticipated but cannot be confirmed. The control cultures show a marginally higher concentration during the late exponential phase as compared to the 10G (figure 6.30). Both show minor accumulation towards the end of the culture, which may be an effect of the increase in UDP-GlcNAc or slowdown of growth.

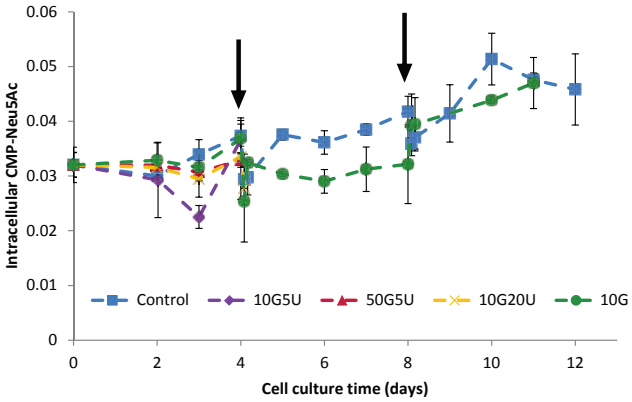


Figure 6.30 Intracellular CMP-Neu5Ac for all conditions with respect to culture time (N_C = 3, N = 2, EB = SD).

Intracellular GDP-Fuc concentrations show little variation with respect to the different feeding strategies (figure 6.31). Broadly speaking a minor amount of accumulation can be seen towards the end of the culture especially regarding the 10G and 50G5U conditions. Due to low concentration levels GDP-Man was not quantifiable for a number of time points, thus painting an incomplete picture (figure 6.32). Broadly speaking the GDP-Man profiles reflect those of GDP-Fuc, where the highest concentrations were observed during the late culture stages in the 50G5U and 10G conditions. The accumulation under the conditions of high galactose concentration and galactose addition only, may be the result of competition for enzymes shared by the UDP-Hex and GDP-Fuc and GDP-Man synthesis branch of the NSD network. The concentrations profiles of GDP-Fuc and GDP-Man in the control cultures appear to be lower than those of the control cultures in chapter 4 during the later culture stages. This suggests the influence of DMSO in the accumulation in the Control of the guanosine and mannose feeding experiments in chapter 4.

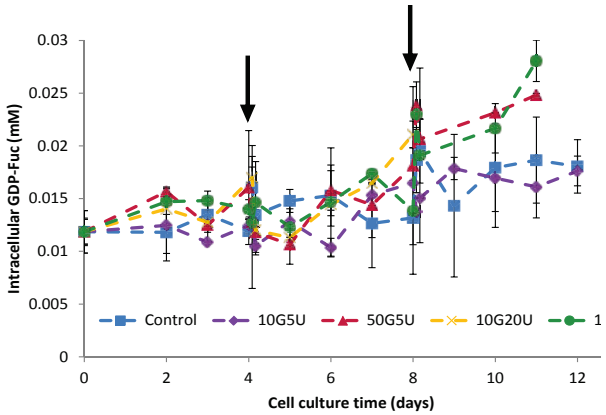


Figure 6.31 Intracellular GDP-Fuc for all conditions with respect to culture time (N_C = 3, N = 2, EB = SD).

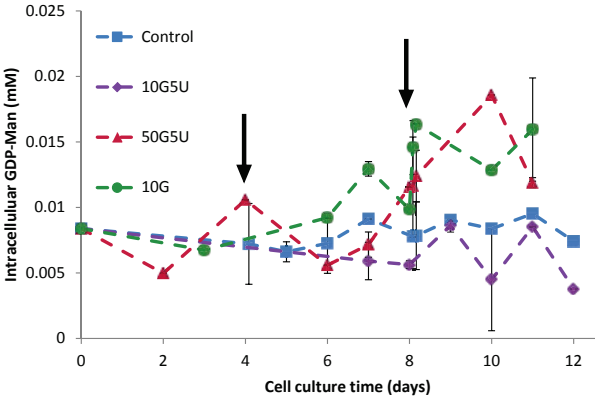


Figure 6.32 Intracellular GDP-Man for all conditions with respect to culture time (N_C = 3, N = 2, EB = SD).

6.4. Product glycoform

The experimental work aimed at quantifying the effect of a number of different feeding strategies on cell culture dynamics and metabolism with the final aim of finding the impact of the various feeding strategies on product galactosylation to further develop the modelling platform. The data shows that the desired outcome, of an increase in the abundance of galactose bearing structures, was indeed achieved for all culture conditions as compared to the Control (figures 6.33 & 6.34). Varying amounts of under-processed Man5 structures can be observed for different conditions. The highest absolute abundance was observed in the high uridine condition 10G20U on day 7 of culture with 4.44 ± 0.75 %. A higher degree of under-processing was also observed under the 50G5U condition and 10G5U on the final day. All the uridine supplemented conditions showed significantly enlarged UDP-GlcNAc pools, as such depletion can be excluded as a possible cause of high Man5 abundance. Furthermore, the qmAb did not differ significantly from those of the other conditions and hence, is not a contributing factor. This points towards a stressed Golgi environment due to the metabolic burden of uridine supplementation. Conditions 50G5U and 10G20U also resulted in increased osmolarity due to high concentrations of galactose and reduced consumption of extracellular nutrients, respectively. This has previously been reported to increase the abundance of Man5 structures in mAb producing CHO cell cultures (Pacis et al., 2011). The highest concentrations of G0 structures were observed in the control

cultures on both day 7 and the final day of culture, while the lowest abundance was found under the 10G20 and 50G5U conditions. This indicates a high rate of further processing towards galactosylated and/or fucosylated structures, which may be explained by high concentrations of UDP-Gal and GDP-Fuc under these conditions as compared to the Control. The highest degree of G0F structure abundance was observed in the Control at both days 7 and the end of the culture. Both 10G20U and 10G showed a reduced abundance of G0F with the lowest abundance displayed by 50G5U on day 7 (41.8 ± 3.6%) and by 10G5U on the final day of culture (40.0 ± 0.3%), respectively. The abundance of the galactosylated species G1F and G2F were highest under the 50G5U condition on day 7 (41.8 ± 1.9% and 7.9 ± 1.0%, respectively) and under the 10G5U condition on the final culture day (43.9 ± 0.6% and 8.9 ± 0.3%, respectively). and the final culture day, respectively. The abundance of G2F on the last day of culture is comparable for both 10G20U and 10G, while that of the Control is consistently the lowest. Lastly the least abundant detectable species was G2, where the highest reading was observed on day 7 in the 50G5U culture with an abundance of just under 1% and thus, making up a negligible to non-detectable fraction of the glycoform with respect to all cultures. Overall a high degree of fucosylation is observed with a minimum of 92.6% in the Control and a maximum of 93.7% in 10G on the final day of culture. The data suggests very little to no impact on fucosylation by the feeding strategies tested.

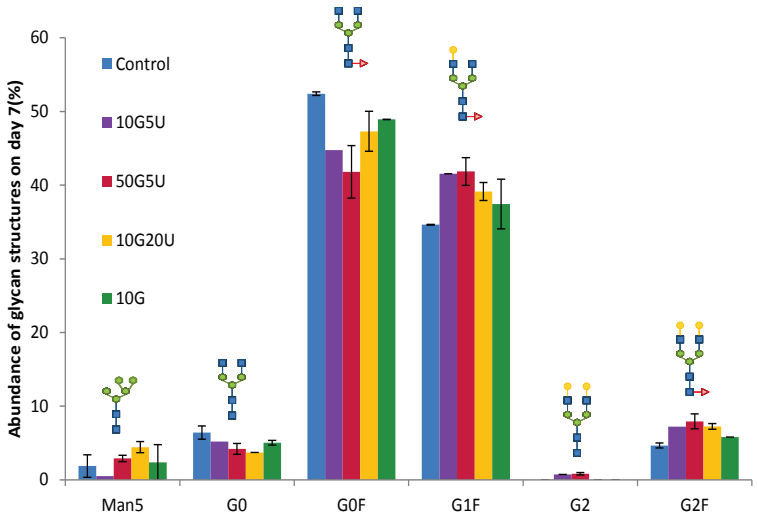


Figure 6.33 Distribution of glycan structures on day 7 of culture for all conditions (N = 2, EB = SD).

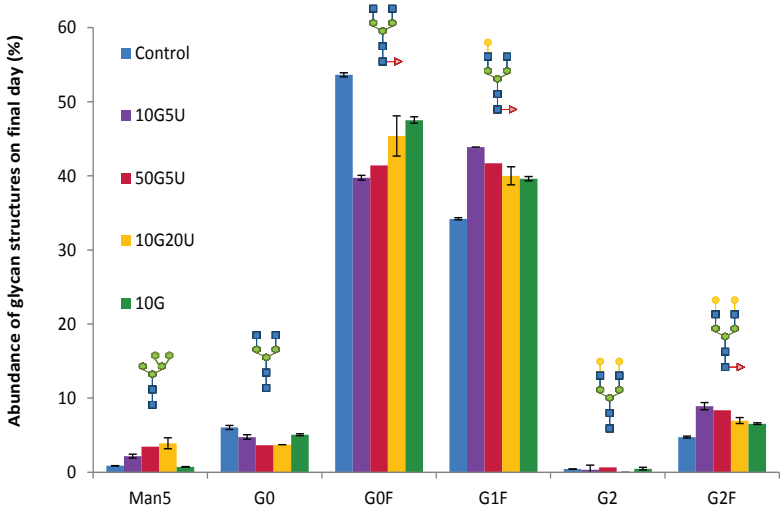


Figure 6.34 Distribution of glycan structures on final day of culture for all conditions (N = 2, EB = SD).

An analysis of the galactosylation shows limited variation within the sample set of each condition, throughout the culture time (figure 6.35). Galactosylation in this context is defined as the average number of galactose molecules per glycan of the antibody constant Fc region. The control shows the lowest galactosylation at all time points other than day 9, when the lowest degree of galactosylation is produced by 10G. The lowest galactosylation was reported on day 11 of the control cultures with 0.427 ± 0.017 and the highest on day 12 of the 10G5U condition with 0.624 ± 0.10. The highest galactosylation is observed under the 10G5U and 50G5U feeding regimes. The lower galactosylation under the 10G20U condition is initially surprising as UDP-Gal concentrations were highest after the first feeding. However, the comparatively high abundance of Man5 structures indicated a stressed Golgi environment, which may have prevented a higher degree of galactosylation despite large UDP-Gal pools. Furthermore, the data reported here is that of the cumulative glycoform and includes the glycoform of antibodies produced prior to the feed addition. This would have impacted the 10G20U condition most, where a reduced growth and titer were observed after feeding. This means that 53% of the antibodies analysed on the final culture day were produced by the cells before feed addition and thus, reducing feed impact on cumulative galactosylation. The galactosylation of the 10G condition indicates an elevation as compared to the Control however, lower than the 10G5U and 50G5U conditions. Further increases under the uridine fed cultures over the 10G condition indicate that a point of saturation was

not yet achieved under the 10G feeding regime and thus, uridine additions present a rational target for further optimisation.

The degree of galactosylation achieved on the final day of culture for the Control was 0.446 ± 0.004, which is much higher than the 0.181 measured in the control cultures of chapter 4. However, the fairness of a comparison between the two controls can be questioned due to the presence of DMSO in the control cultures reported in chapter 4, which was speculated to lead to under-processing. Nonetheless the difference is very substantial and may also indicate the effect that the manganese supplementation has on galactosylation, as a vital cofactor for the activity of the β-1,4-galactosyltransferase, the enzyme responsible for the addition of galactose to terminal GlcNAc on growing glycans in the Golgi (Witsell et al., 1990). The elevated level of galactosylation in the Control also reduces the scope for further increases in galactosylation due to spatial constraints on the glycan in the Fc region. The maximal reported levels of galactosylation upon optimisation vary strongly from as low as 0.29 (Gramer et al., 2011) to as high as 1.07 galactose per glycan (Grainger and James, 2013) in antibody producing GS-CHO cell lines. This produces a problem of fair comparison of results as well as the quantitative extrapolation of the results to other cell lines.

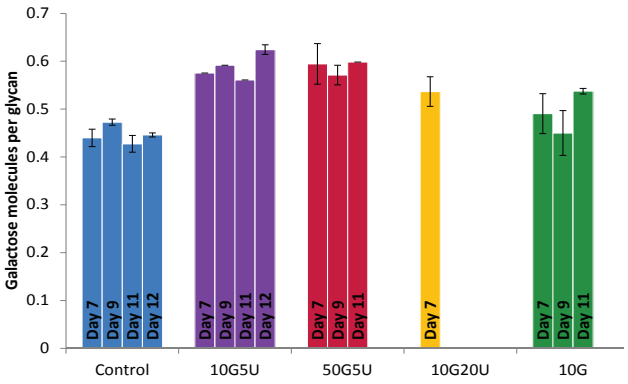


Figure 6.35 Average number of galactose molecules per product glycan structure for all conditions for culture days 7, 9, 11 and 12. (N = 2, EB = SD).

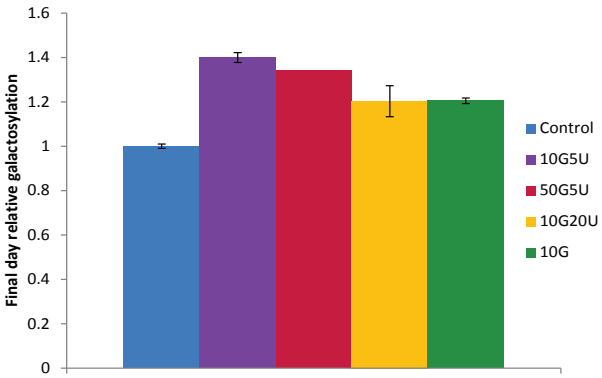


Figure 6.36 Normalised galactosylation per product glycan for all conditions for each respective final culture day. (N = 2, EB = SD).

A comparison of the final day galactosylation of each condition to the control reveals an overall enhanced galactosylation under all conditions (figure 6.36). The highest increase in galactosylation, over the control cultures, was achieved by the 10G5U condition by a

margin of 39.9 ± 2.2 %, which presents a very significant improvement. The remaining increases in galactosylation were 34.1 %, 20.4 ± 1.3 % and 20.3 ± 6.9 %, over the control cultures, for 50G5U, 10G and 10G20U, respectively. This indicates that over-saturation in both uridine and galactose concentration was achieved leading to a reduction in beneficial effects with respect to final day product galactosylation. However, the over-saturation may be due to secondary effects, such as increased osmolarity as a result of metabolic slowdown. No significant changes in qmAb were observed during the duration of the culture periods and thus, indicating a successful manipulation of the glycoform towards higher galactosylation through increased UDP-Gal concentrations.

6.5. Conclusions and Further work

The experimental work presented in this chapter was aimed at determining the response of cell cultures to varying additions of galactose and uridine to maximise the galactosylation of the antibody Fc region glycan structures. The work successfully demonstrated improved galactosylation at all feed conditions to varying degrees. Effects with respect to cell culture dynamics, the extracellular environment, intracellular metabolites and finally the product glycoform were observed. The aim was to provide a set of data to build on the modelling efforts presented in chapter 5 and allow for a further expansion of the model to devise an optimal feeding strategy to maximise antibody galactosylation. A summary of the main effects observed on cell culture dynamics and extracellular species is given below:

- The additions of both uridine and galactose had a significant negative impact on cell culture dynamics with a 20 mM addition of uridine during the exponential growth phase leading to inhibited cell growth and early cell death. A high uridine environment is therefore clearly undesirable for the optimisation of culture conditions.

- Addition of only galactose to the cell culture media resulted in a reduction in cell growth and earlier cell death. This effect was reduced in the presence of uridine in

addition to galactose. However, despite accelerated cell death leading to an early cell culture termination, the IVCC did not differ significantly to that of the 10G5U culture. A large shift in UDP-Hex ratios was observed for the 10G condition and was speculated to cause the accelerated cell death. High galactose additions in the presence of uridine resulted in supressed IVCC, which was attributed to an increase in osmolarity, as few other changes were observed as compared to the 10G5U culture.

- The antibody titer of all cultures appeared to have been largely a function of the IVCC and was not significantly impacted by the presence of uridine and galactose in culture media. However, the specific antibody production rate declined with progressing cell culture time suggesting growth dependent productivity.

- Extracellular uridine was shown to be consumed by the cells with little impact on consumption by the IVCC. It was observed that uridine consumption was linked to increases in extracellular ammonia concentrations. This was speculated to be either a result of metabolic break-down of uridine or a shift in metabolism

- Extracellular galactose was shown to be taken up very readily especially at the high 50 mM concentration. It appears to be taken up preferentially to glucose, as glucose uptake was reduced although not stopped as a result of galactose additions. This is in contrast to the findings of chapter 4, where mannose was not readily taken up by the cells in the presence of glucose. Galactose uptake was not impacted by uridine additions to culture media.

The effects of the various feeding strategies have also been able to propagate from the extracellular environment to intracellular species concentrations. This offers valuable insight into cell metabolism and enables further refinement of the model structure. The main findings are summarised below:

- The additions of galactose have been shown to lead to increases in intracellular galactose especially in the 50G5U condition, where the concentration extracellularly

was highest. Concentrations did not follow extracellular profiles and accumulation was observed towards the end of culture for all conditions. This points towards the contribution of the synthesis and salvage pathways to intracellular pools.

- Intracellular uridine concentrations on the other hand traced those of the extracellular environment. Increases were observed immediately after uridine addition to the media on days four and eight. Hence, transport limitations can be excluded with respect to this metabolite.

- The concentration profiles of uridine translated directly to those of UTP and eventually CTP with concentration profiles following those of extracellular uridine. However, a diminishing propagation of the effects was observed indicating partial saturation along the synthesis pathway and/or the existence of control mechanisms. The feeding of uridine appeared to inhibit adenosine nucleotide synthesis, where the lowest adenine species concentrations were observed for the highest fed uridine culture 10G20U.

- Galactose proved to have no measurable effect on UTP concentrations. No impact was also observed on the concentrations of other nucleotide triphosphate species as a result of varying galactose feed concentrations.

- Significant changes in UDP-Gal pools were observed as a consequence of the various feeding strategies. Firstly, the concentration profiles of UDP-Gal in the uridine fed cultures followed those of the intracellular UTP with a rapid increase after feeding. This suggested a strong dependence of UDP-Gal synthesis on its nucleotide precursor. The 10G condition produced the fastest and initially highest peak after feeding with a subsequent decline that still remained above the levels of the control culture. An accumulation was observed for all uridine supplemented cultures towards the end of the culture, where the highest concentration was observed in the 50G5U condition. UDP-Glc levels were shown to be affected by uridine addition but not by galactose leading to a shift in UDP-Hex ratios.

- The UDP-HexNAc species were also impacted by the uridine feeding and showed an immediate increase in concentration upon feeding. This suggests a dependence of UDP-HexNAc synthesis on uridine concentrations. The UTP dependent reaction step (r6a in figure 5.5) must therefore be of significant impact on UDP-HexNAc model output despite the GSA of chapter 3 not highlighting this reaction step. This may indicate dependence on UTP at elevated concentrations. The impacts of the feeding strategies on the remaining NSD concentrations were either minimal or indistinguishable from the control culture.

Lastly, the effects of the various feeding strategies propagated to changes in the glycoform. This confirms again the established hypothesis that the glycoform can be influenced through manipulation of the precursor pools of the glycosylation reactions, i.e. NSDs. A summary of the findings is shown below:

- The overall experimental aim was achieved, as feeding resulted in a stable increase in galactosylation of at least 20% for all cultures as compared to the control. The highest level of galactosylation was observed on the final day of the 10G5U culture with 0.624 ± 0.010 galactose molecules per glycan, which presented an increase of galactosylation of 39.9 ± 2.2 % over the control. As a result it can be concluded that the increase in UDP-Gal concentrations were translated to increases in the degree of galactosylation of the antibody product. However, high concentrations of uridine and galactose led to a decrease in beneficial effects to product galactosylation.

- A degree of under processing, resulting in an increase in Man5 glycan structures was observed most strongly in 10G20U. Increased Man5 concentrations were also observed in 50G5U and to a lesser extent in 10G5U. These conditions demonstrated elevated UDP-HexNAc concentration and thus, excluding substrate limitations. This indicated a stressed Golgi environment, which may be an effect of increased osmolarity. It has previously been hypothesised that increased osmolarity reduces the activity of the glycosyltransferase GnTI, which processes Man5 structures further (Pacis et al., 2011). The same study also proposed that increased Man5 abundance can also result from elevated ammonia concentrations, which were observed under

the uridine fed regimes. Consequently, high uridine concentrations become unfavourable for process optimisation.

- A high degree of fucosylation was observed for all cultures with abundances no lower than 92.6% for all cultures and very little variation with respect to time and culture conditions. This was unsurprising as GDP-Fuc levels showed little variation. This also suggests little to no impact on fucosyltransferase by the addition of galactose and uridine to cell culture media.

The experimental data presented in this chapter was successful in perturbing the cell cultures and their metabolic systems to elucidate control mechanisms, adverse culture effects, interaction of species and saturation of systems. The data provides excellent insights into the effect of uridine and galactose additions with respect to further computational work. The extracellular galactose data and its consumption allow its inclusion into the cell culture dynamics model and as an additional flux into the NSD model. Likewise the extracellular uridine data can be used to include uridine and its consumption into the cell dynamics model as well as the nucleotide model. With respect to the whole system the various feeding strategies were able to show beneficial effects with respect to galactosylation as well as a number of detrimental effects in excess concentrations. These include reduced cell growth, premature cell death and under processing of glycans. The data provided allows incorporating further structural elements into the cell dynamics model as well as further metabolic system control mechanisms and reactions into the semi-structured nucleotide model. Furthermore, the data provides valuable input for improved model training especially with respect to the highly perturbed UDP-Hex branch, where model outputs were previously poor (chapter 5). The experimental data for this branch of the NSD model has previously been sparse and the targeted perturbations have been able to give rich information regarding the involvement of the various reactions, control mechanisms and metabolic bottlenecks. With respect to the glycosylation model the data was able to demonstrate that increases in UDP-Gal concentrations will lead to increases in antibody product galactosylation. This data is crucial in providing more information about the operation range at near saturation and highlight boundaries, beyond which no further galacotyslation improvements are achieved and thus, narrowing down a windows for an *in*

silico design of experiment. The detrimental effects on the various aspects of cell culture resulting from feed additions provide further restrictions for a good operating space. This is especially valuable in view of the *in silico* optimisation of process conditions, where a restricted operating space is essential to constrain the system sufficiently to arrive at an optimised feeding strategy. With the picture painted in this chapter, sufficient data has been collected to improve the model further and find optimal process conditions to produce an optimised *in silico* feeding strategy to maximise galactose profile by means of metabolic control through targeted galactose and uridine additions.

Chapter 7

Model refinement and *in silico* optimisation

The work presented in this chapter builds on the computational work presented in chapter 5. The original framework of chapter 3 is taken forward combined with the updated models of chapter 5 as well as the del Val glycosylation model. Here the entire framework is expanded and trained further using the experimental data shown in chapter 6 to obtain a calibrated operating space with respect to galactose and uridine supplementation to the cell culture. This operating space then serves as a base for the optimisation of galactose and uridine supplementation to maximise the galactosylated product. Specifically the function of product galactosylation as well as antibody titer is maximised such that both the glycosylation process as well as the cell culture dynamics are accounted for. This case study provides a practical example of the application of the model platform to the Quality by Design (QbD) paradigm, whereby more knowledge of the critical quality attribute (cQA), i.e. galactosylation, is obtained through upfront experimentation to eventually exercise control over it. This addresses the ultimate project aim of steering the glycoform of a monoclonal antibody during its synthesis by the host cell.

The model outputs presented in chapter 5 give confidence in the overall modular model platform structure. Hence, the structure is taken forward to be refined further based on the experimental findings of chapter 6. However, improvements in model accuracy must be achieved over the outputs as presented in chapter 5 to ensure a sufficiently calibrated operating range for feeding strategy optimisations. With respect to the NSD model improvements in UDP-Hex and UDP-HexNAc species are necessary, while the nucleotide

model requires an improved intracellular CTP concentration output. The experimental data of chapter 6 elucidates the effects of additions of varying galactose and uridine concentrations to the cell culture media and the resulting metabolic and cell culture dynamics changes. The direct perturbations of UTP synthesis and the UDP-Hex branch as well as the propagation of these effects to UDP-HexNAc and CTP synthesis are used in this chapter to improve on the previous model structure and provide rich data for further model training. The data also allows extending the cell culture dynamics model to capture the effects of feeding on cell culture dynamics and nutrient consumption/production by the cells. The resulting updated and trained framework provides an improved *in silico* representation of the macroscopic and microscopic cell environment as well as enabling the subsequent *in silico* optimisation of feeding to maximise galactosylation.

7.1. Cell culture dynamics model

The cell culture dynamics model accounts for the interactions of the cells with their extracellular environment and the resulting cell growth, death, nutrient utilisation as well as fluxes into the intracellular environment (figure 7.1). The model presented herein has been modified from the model described in chapter 5 to account for the impacts of galactose and uridine supplementations to cell culture media. Changes in cell culture dynamics have been observed ranging from cell growth to nutrient utilisation. Furthermore, parameters are re-estimated, as no DMSO was used in the experimental setup of chapter 4, which is known to

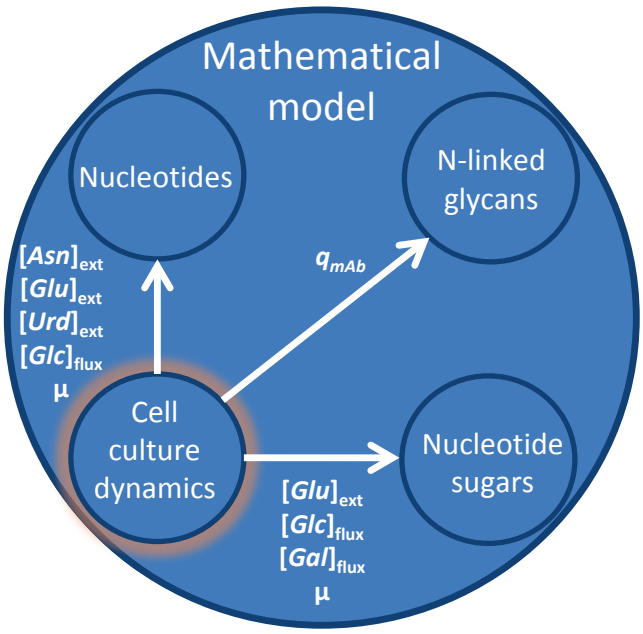


Figure 7.1 Schematic of the model framework depicting the interaction of the cell culture dynamics model with the remaining parts of the framework.

be detrimental to cell proliferation and metabolic activity and hence, impact estimated parameters. Shown below are all modified and newly added expressions of the cell culture dynamics model. All remaining cell culture dynamics equations of chapter 5 that are not discussed below have not been altered from their original form.

Firstly, the growth inhibiting term has been altered to reflect the effects of extracellular galactose and uridine on cell proliferation (equation 7.1). As previously, a multiplication of all species contributions forms the growth inhibition term, such that growth inhibition can arise from each individual species. All species contribution terms are modelled as saturation type kinetics depending on the individual estimated inhibitory constant ($K_{I,i}$ in mM). This includes the newly added galactose and uridine contribution terms. However, experimental viable cell density data presented in chapter 6 suggested a sharp increase in cell growth inhibition from the 5 mM uridine to 20 mM uridine conditions. This suggested co-operative cell growth inhibition by uridine, which is reflected by the exponential term $n_{I,urd}$ (no units).

$$f_{inh} = \left(\frac{K_{I,\,amm}}{K_{I,\,amm} + [Amm]_{ext}}\right)\left(\frac{K_{I,\,lac}}{K_{I,lac} + [Lac]_{ext}}\right)\left(\frac{K_{I,man}}{K_{I,man} + [Man]_{ext}}\right) \left(\frac{K_{I,gal}}{K_{I,gal} + [Gal]_{ext}}\right)\left(\frac{K_{I,urd}}{K_{I,urd} + [Urd]_{ext}^{n_{I,urd}}}\right) \quad 7.1$$

The modified cell death term (k_d in h^{-1}) is still a summation of the effects of ammonia, asparagine and mannose with the addition of uridine and galactose (equation 7.2). The newly included uridine and galactose contributions are modelled as saturation kinetics, as their accumulation leads to cell death. Again, an exponential term is applied in the uridine contribution term to account for co-operative behaviour ($n_{d,urd}$ no units). It was noted in chapter 6, that feeding uridine together with galactose, as opposed to galactose only, was able to reduce the toxic effect of galactose supplementation. This is reflected by the uridine term featured in the galactose contribution, which effectively acts as an inhibitory term to the cell death contribution by galactose ($K_{d,urd/gal}$ in mM).

$$k_d = k_{d,max}\left[\left(\frac{[Amm]_{ext}}{K_{d,amm} + [Amm]_{ext}}\right) + \left(\frac{K_{d,asn}}{K_{d,asn} + [Asn]_{ext}}\right) + \left(\frac{[Man]_{ext}}{K_{d,man} + [Man]_{ext}}\right) + \left(\frac{[Urd]_{ext}^{n_{d,urd}}}{K_{d,urd} + [Urd]_{ext}^{n_{d,urd}}}\right) + \left(\frac{[Gal]_{ext}}{K_{d,gal}\left(1 + \frac{[Urd]_{ext}}{K_{d,urd}/_{gal}}\right) + [Gal]_{ext}}\right)\right] \quad 7.2$$

The material balance of glucose was altered to account for the reduced glucose uptake observed in chapter 6 in the presence of galactose in the extracellular environment (equation 7.3). This is reflected by the inclusion of a galactose competing term in the glucose material balance, which requires estimation of the saturation parameter $K_{c,gal}$ (in mM).

$$\frac{dV[Glc]_{ext}}{dt} = \left(\frac{K_{c,gal}}{K_{c,gal} + [Gal]_{ext}}\right)\left(\frac{K_{c,man}}{K_{c,man} + [Man]_{ext}}\right) q_{glc} V X_V + F_{feed}[Glc]_{feed} - F_{out}[Glc]_{ext} \quad 7.3$$

A new material balance is introduced to account for the addition and consumption of galactose in the cell culture media (equation 7.4). The material balance features terms accounting for consumption by cells, supplementation in the feed inlet and loss from the outlet, respectively. The species consumption term (q_{gal} in mmol/(cell h)) contains a cell growth and cell maintenance contribution term. However, an additional galactose concentration term was added to the growth term as shown in equation 7.5 to account for concentration dependency in consumption.

$$\frac{dV[Gal]_{ext}}{dt} = q_{gal} V X_V - F_{in}[Gal]_{in} - F_{out}[Gal]_{ext} \quad 7.4$$

$$q_{gal} = -\left(\frac{[Gal]_{ext}}{K_{M,\,gal} + [Gal]_{ext}}\right)\left(\frac{\mu}{Y_{Xv/gal}}\right) - m_{gal}[Gal]_{ext} \quad 7.5$$

The material balance representing the extracellular uridine concentration takes the same form as that of galactose (equation 7.6). However, the species cellular consumption term (q_{urd} in mmol/(cell h)) contains a growth dependent saturation term only (equation 7.7). Lastly, the expression for the cellular ammonia production term was altered to reflect the increase in ammonia resulting from the uptake of uridine from the extracellular environment (equation 7.8 of q_{amm} in mmol/(cell h)). This has been reflected by the inclusion of the negative cellular uridine consumption term and hence, as an ammonia producing term.

$$\frac{dV[Urd]_{ext}}{dt} = q_{urd}VX_V - F_{in}[Urd]_{in} - F_{out}[Urd]_{ext} \quad 7.6$$

$$q_{urd} = -\left(\frac{[Urd]_{ext}}{K_{M,\,urd} + [Urd]_{ext}}\right)\left(\frac{\mu}{Y_{Xv/urd}}\right) \quad 7.7$$

$$q_{amm} = -q_{gln} + \left(\frac{\mu}{Y_{Xv/amm}}\right) - Y_{amm/asn} \times q_{asn} - q_{urd} \quad 7.8$$

No switch mechanism akin to that in chapter 5 was implemented in the model structure. Consequently, only a single set of parameters is estimated to reproduce the full range of experimentally obtained data points in chapter 6. Manganese is not featured in the

cell dynamics model, as it was reported not to have any significant impact on cell growth in the low concentration used in the experimental setup (Grainger and James, 2013).

7.2. Nucleotide synthesis model

Similarly to the cell culture dynamics model, the nucleotide *de novo* synthesis model was refined based on the experimental findings of chapter 6 and extended further to include the contributions of galactose and uridine. The nucleotide model is a function of the cell culture dynamics model outputs, which include extracellular amino acid concentrations, extracellular uridine, the hexose fluxes and the cell growth rate (figure 7.2). The model outputs are the intracellular concentrations of the four nucleotide triphosphates (NTP) as well as ADP and AMP, which are fed into the NSD model. The original reaction network was left unchanged from the model presented in chapter 5 with the exception of the addition of a further reaction step accounting for the CTP synthesis from extracellular uridine. The experimental data presented in chapter 6 suggested a system wide impact of increased UTP concentrations on the various nucleotide pools, which has been reflected in the updated reaction rate expressions. Furthermore, it was concluded in chapter 6, that transport limitation of uridine from the extracellular environment to the cells' cytosol does not exist at the experimental concentration range. This finding makes it a reasonable assumption for the nucleotide model to be based on extracellular uridine concentrations instead of those of the cytosol.

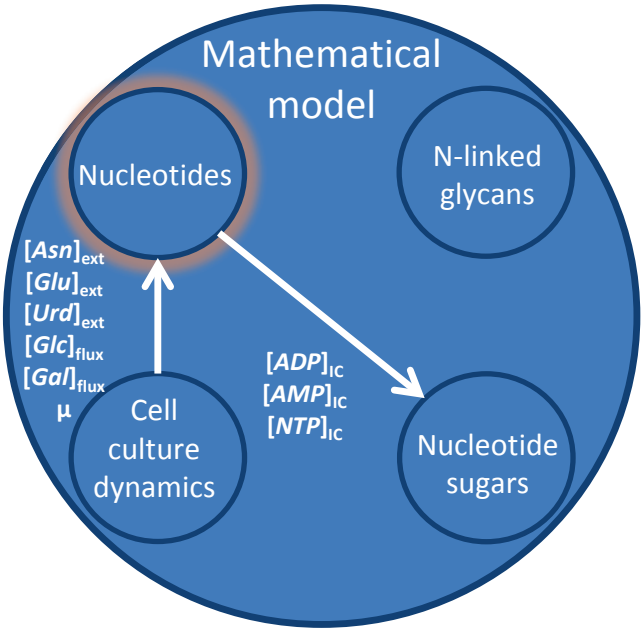


Figure 7.2 a schematic of the nucleotide model and its dependence within the mathematical model platform.

7.2.1. Purine synthesis

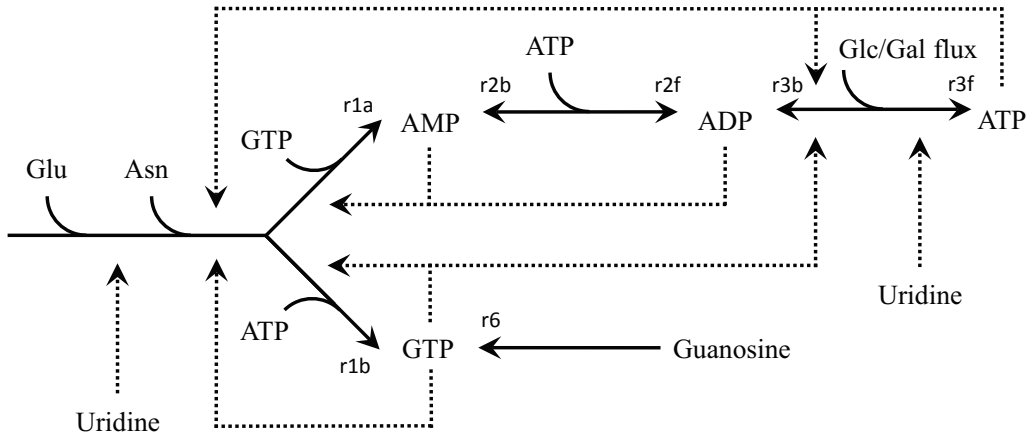


Figure 7.3 A semi structured reaction network of the de novo purine synthesis. Reaction steps are indicated in dark lines, while dashed lines indicate inhibitory mechanisms.

The *in silico* representation of the purine *de novo* synthesis network, leading to the synthesis of adenosine and guanosine nucleotides, was left structurally unchanged. However, additional inhibitory mechanisms were included to achieve better model performance (figure 7.3). An uncompetitive uridine inhibitory mechanism was included in equations r1a and r1b leading to the synthesis of AMP and GTP, respectively (equations 7.9 and 7.10). This was motivated by the experimentally observed decrease in GTP and adenosine nucleotide species concentrations resulting from the addition of uridine to cell culture media (chapter 6). Furthermore, the inhibition of AMP and GTP synthesis by ADP has previously been reported in literature and has been included into the respective rate expressions (Matsuda et al., 1980).

$$\text{r1a} = \frac{v_{max,\,1a}[Asn]_{ext}[Glu]_{ext}[GTP]_{IC}}{(K_{M1,asn}+[Asn]_{ext})(K_{M1,glu}+[Glu]_{ext})\left(K_{M1,GTP}\left(1+\frac{[AMP]_{IC}}{K_{I1,AMP}}\right)+[GTP]_{IC}\right)\left(1+\frac{[GTP]_{IC}}{K_{I1,GTP}}+\frac{[ATP]_{IC}}{K_{I1,ATP}}+\frac{[ADP]_{IC}}{K_{I1,ADP}}+\frac{[Urd]_{ext}}{K_{I1,Urd}}\right)} \quad 7.9$$

$$\text{r1b} = \frac{v_{max,\,1b}[Asn]_{ext}[Glu]_{ext}[ATP]_{IC}}{(K_{M1,asn}+[Asn]_{ext})(K_{M1,glu}+[Glu]_{ext})\left(K_{M1,ATP}\left(1+\frac{[GTP]_{IC}}{K_{I1,GTP}}\right)+[ATP]_{IC}\right)\left(1+\frac{[GTP]_{IC}}{K_{I1,GTP}}+\frac{[ATP]_{IC}}{K_{I1,ATP}}+\frac{[ADP]_{IC}}{K_{I1,ADP}}+\frac{[Urd]_{ext}}{K_{I1,Urd}}\right)} \quad 7.10$$

The phosphorylation reaction of ADP to ATP has also been altered to reflect the decrease in intracellular ATP pools as a result of uridine addition to culture media (equation 7.11). This has been modelled as an inhibition term competing with the ADP reaction substrate. The hexose flux term has also been updated to include the flux of galactose into the cell.

$$\text{r3f} = \frac{v_{max,3f}[ADP]_{IC}\left([Glc]_{flux}+[Gal]_{flux}\right)}{\left(K_{M3,adp}\left(1+\frac{[GTP]_{IC}}{K_{I3,GTP}}+\frac{[ATP]_{IC}}{K_{I3,ATP}}+\frac{[Urd]_{ext}}{K_{I3,Urd}}\right)+[ADP]_{IC}\right)\left(K_{M3,glc}+[Glc]_{flux}+[Gal]_{flux}\right)} \quad 7.11$$

7.2.2. Pyrimidine synthesis

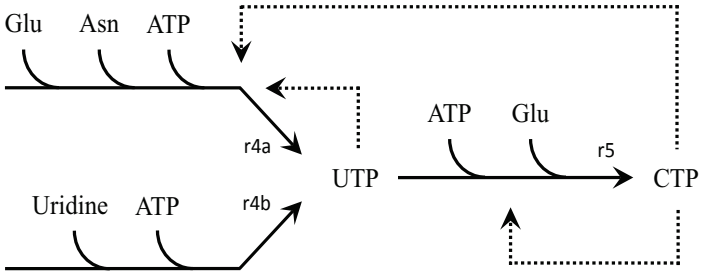


Figure 7.4 simplified reaction network of the de novo pyrimidine synthesis network. The inhibition mechanisms are indicated by dashed lines.

The simplified *de novo* pyrimidine synthesis reaction network has been expanded to include an additional reaction step, where UTP is synthesised from extracellular uridine and intracellular ATP (figure 7.4). The synthesis of UTP from uridine follows a separate pathway to the *de novo* synthesis from the amino acids and hence, a separate reaction rate was used for a more accurate *in silico* representation. The resulting reaction expression takes into account co-operative behaviour of intracellular uridine as well as un-competitive product inhibition by CTP and UTP (equation 7.12). The amino acid-driven UTP synthesis reaction was also altered to include an un-competitive GTP inhibition term (equation 7.13), while the CTP synthesis reaction has been left unaltered.

$$\text{r4a} = \frac{v_{max,\,4a}[Asn]_{ext}[Glu]_{ext}[ATP]_{IC}}{(K_{M4,asn}+[Asn]_{ext})(K_{M4,glu}+[Glu]_{ext})(K_{M4,ATP}+[ATP]_{IC})\left(1+\frac{[CTP]_{IC}}{K_{I4,CTP}}+\frac{[GTP]_{IC}}{K_{I4,GTP}}+\frac{[UTP]_{IC}}{K_{I4,UTP}}\right)} \quad 7.12$$

$$\text{r4b} = \frac{v_{max,\,4b}[Urd]_{ext}^{n4,Urd}[ATP]_{IC}}{\left(K_{M4,urd}+[Urd]_{ext}^{n4,Urd}\right)(K_{M4b,ATP}+[ATP]_{IC})\left(1+\frac{[CTP]_{IC}}{K_{I4b,CTP}}+\frac{[UTP]_{IC}}{K_{I4b,UTP}}\right)} \quad 7.13$$

7.3. Nucleotide sugar donor model

The reaction network of the NSD *de novo* synthesis model was left unchanged, as the network is fully characterised and does therefore not allow for any structural changes, while maintaining a fully mechanistic *in silico* representation. However, a number of reaction mechanisms were altered to allow for a more accurate recreation of the experimental data obtained in chapter 6. Furthermore, the galactose flux as computed by the cell culture dynamics model has been included as an inlet flux to the NSD model in addition to the glucose flux (figure 7.5).

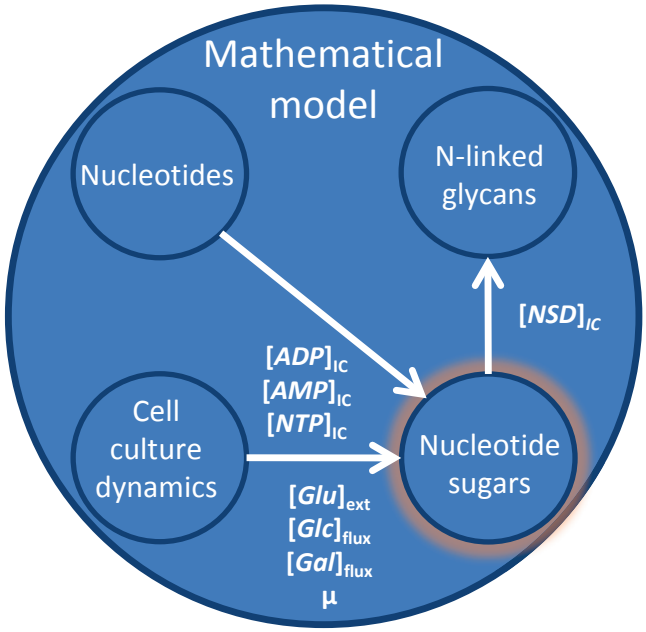


Figure 7.5 a schematic of the NSD model and its dependence within the mathematical model platform.

Firstly, the reaction expression of galactose 1-phosphate uridylyltransferase (GALT) was modified to account for inhibition by intracellular UTP. As was observed in chapter 5, uridine supplemented concentrations led to UDP-Hex concentration profiles that were

similar for both UDP-Gal and UDP-Glc. This suggested that the epimerase reaction step (r22a in figure 7.6) was dominant path for the Gal to glycolysis flux. However, under conditions of high galactose and no uridine supplementation, the similarity in UDP-Hex concentration profiles was not observed. This suggested a higher flux through the GALT reaction (r23a in figure 7.6) at lower UTP concentrations. This inhibitory mechanism of the GALT reaction, which was shown to exist in rat (*rattus norvegicus)* cells is able to explain the experimental UDP-Hex profile observations (Rogers and Segal, 1991). Furthermore, Rogers and Segal propose that other nucleotide species, such as ATP, are inhibitors competing with UDP-Gal. The inhibitory mechanisms were included accordingly in the rate expression of reaction r23a and the inhibitory terms $K_{I23a,UTP}$ and $K_{I23a,ATP}$ (units of mM) were included in the parameter estimation (equation 7.14). Additionally, an exponential factor has been included ($n_{23a,UTP}$ no units) to account for any possible co-operative inhibitory effects.

$$\text{r23a} = \frac{k_{23a}[E]_{23a}[Gal1P]_{IC}[UDPGlc]_{IC}}{[Gal1P]_{IC}\,K_{M23a,UDPGlc}+[UDPGlc]_{IC}\,K_{M23a,Gal1P}\left(1+\frac{[UDPGlc]_{IC}}{K_{I23a,UDPGlc}}+\frac{[ATP]_{IC}}{K_{I23a,ATP}}+\frac{[UTP]_{IC}}{K_{I23a,UTP}}\right)+[Gal1P]_{IC}[UDPGlc]_{IC}} \quad 7.14$$

The reaction rate expressions leading to the synthesis of UDP-HexNAc have also been modified to improve model accuracy. The GSA carried out as part of chapter 3, was able to demonstrate that the transaminase reaction r3a was a rate limiting step of UDP-GlcNAc synthesis together with the hexokinase reaction r1c (figure 7.6). Consequently, the product inhibition term by UDP-GlcNAc on the transaminase reaction was included as an additional parameter to be estimated, to allow for more degrees of freedom in the parameter estimation. Furthermore, the experimental results of chapter 6 showed a dependence of UDP-HexNAc concentrations on the availability of intracellular UTP. Consequently, the UTP dependent phosphorylase reaction (r6a in figure 7.6) was modified to reflect the impact of uridine supplementation. An exponential term was included ($n_{6a,UTP}$ no units) to account for possible co-operative behaviour and the dissociation constant $K_{m6a,UTP}$ (in mM) was included in the parameter estimation.

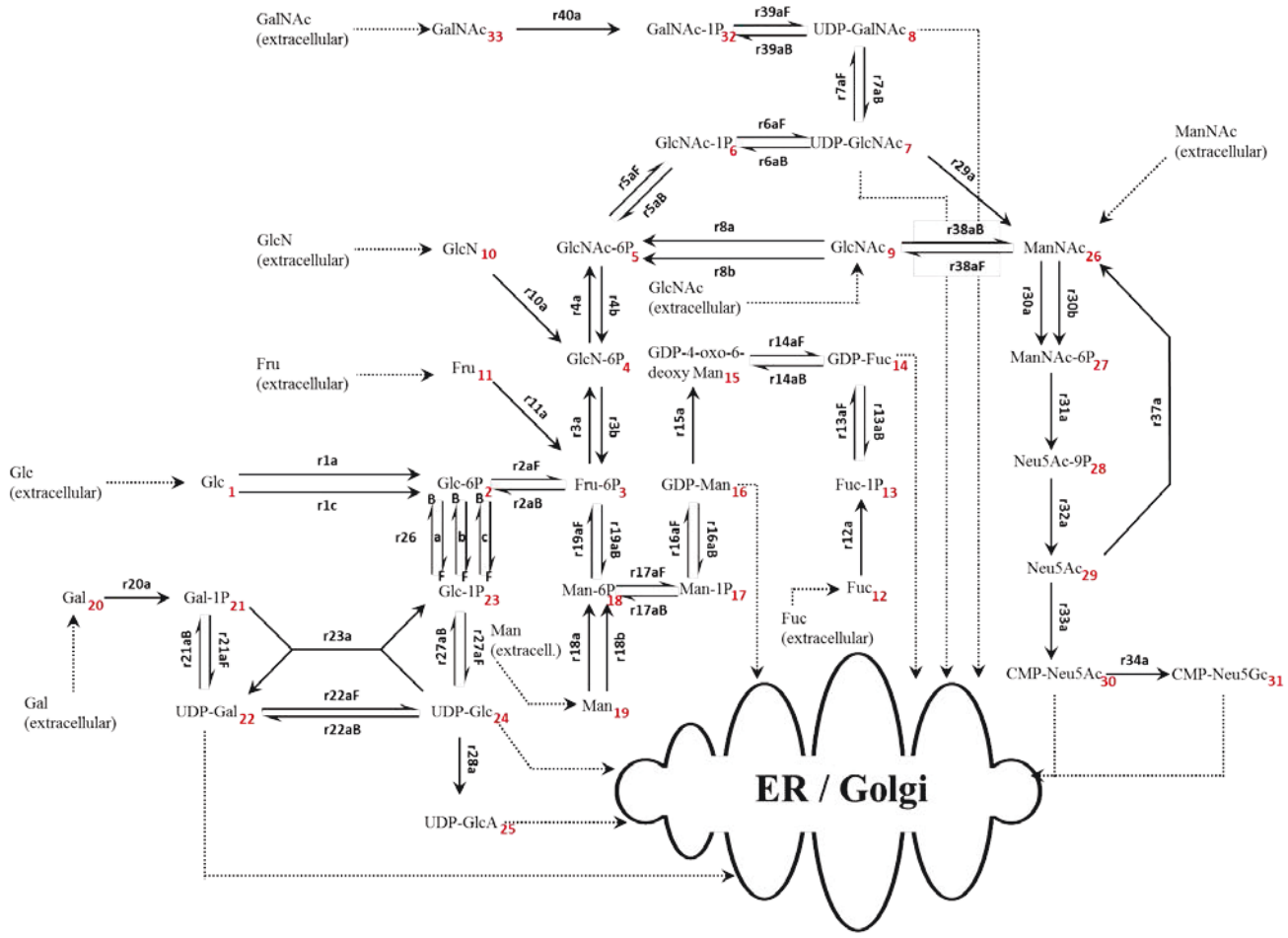


Figure 7.6 The reaction network of the de novo nucleotide sugar donor synthesis pathway, as modelled. Each species is represented as a separate mass balance and the arrows indicate the reaction steps and directions of reaction (Jedrzejewski et al., 2014b).

A number of further parameters were included in the parameter estimation to improve model accuracy with respect to galactose metabolism. Reactions r20a, r21a, r22a, r23a and r27a (figure 7.6) make up together the Leloir pathway, which is responsible for catabolism of galactose from intracellular galactose to glucose-1-phosphate in mammalian cells. The enzyme concentration of each of the above (E20a, E21a, E22a and E23a in mM), where r21a and r27a share the same enzyme, were included in the parameter estimation to enable more degrees of freedom to reproduce experimental UDP-Hex more accurately. Additionally, the dissociation constant $K_{m22a,UDPGlc}$ (in mM) of UDP-Glc for the epimerase reaction r22a was estimated as well as the turnover rate of the uridylyltransferase k27aB (in h^{-1}). On the other hand the enzyme concentration, dissociation constants and exponential factors of the GDP-

Fuc and GDP-Man branch E_{15a}, $K_{m17a,Man6P}$, $K_{m19a,Fru6P}$, $n_{15a,GDPFuc}$ and $n_{15a,GDPMan}$ values, which have been previously estimated in chapter 5, have been left unchanged.

7.4. N-linked glycosylation model

The model describing the N-linked glycosylation of the antibody Fc region employed in chapter 3, has been left unaltered. The model still represents the most appropriate and accurate choice to reproduce the antibody glycan data presented in chapter 6. As previously, it was assumed that transport of NSD species into the Golgi is not limiting. This allows for the transport rate expressions of the del Val model to be bypassed and the glycosyltransferase rate expressions to become a function of the cytosolic NSD concentrations, as opposed to those of the Golgi lumen. This allows for the mathematical model structure to be reduced from a complex partial differential system (PDEs) to a simpler system of ordinary differential equations (ODEs). Consequently, computational cost is reduced and model simulation time is significantly lowered. However, this forces re-estimation of glycosyltransferease dissociation constant for all NSD species, as the literature values used in the del Val model will no longer hold.

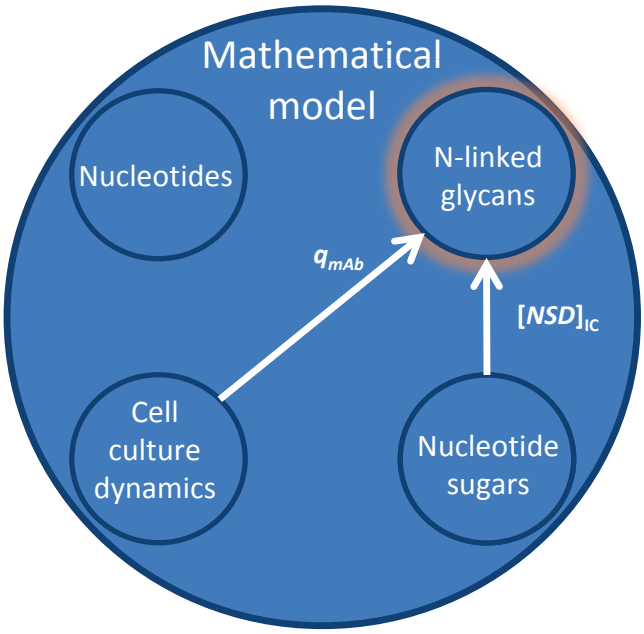


Figure 7.7 a schematic of the glycan model and its dependence within the mathematical model platform.

7.5. *In silico* feeding strategy optimisation

The trained model was used to find an optimal dynamic feeding strategy of galactose and uridine to the cell culture media to maximise product galactosylation. Galactosylation

was defined as the sum of all galactose molecules per product glycan multiplied by product titer (equation 7.15). This means that all galactosylated structures are accounted for, where G2 and G2F structures are counted as two galactose molecules per glycan structure. The optimisation problem was setup to maximise equation 7.15. To distinguish the product of equation 7.15 from the percentage abundance of "galactosylation" of the product glycoform, it is referred to as "titer galactosylation". The titer galactosylation takes not only the glycosylation process and its underlying metabolic factors into account but also cell productivity, which is a function of cell growth as well as cell density. Consequently, the titer galactosylation expression becomes a function of the viable cell density and all the underlying parameters affecting it. Hence, negative effects of galactose and uridine additions on cell culture dynamics are balanced with the benefits in increased galactosylation resulting from increased NSD precursor pools.

$$Galactosylation = [G1F]_{ext} + 2\,[G2]_{ext} + 2\,[G2F]_{ext} \qquad 7.15$$

Feeding was assumed to take place together with Feed C additions on every odd day of culture starting from day 2 of culture. Species were assumed to be dissolved in Feed C such that no volume changes occur. Cell cultures were assumed to be terminated on day 12 of culture, such that the last supplementation occurs on day 10 of culture. Daily sampling was assumed to be 3 mL in a total working volume of 100 mL, where double the sampling volume is taken on days 7, 9, 11 and 12 to allow for the quantification of the glycoform.

7.6. Model Training, Results and Discussion

The updated model was trained using the data presented in chapter 6, against which the model output is compared below. Particular emphasis was placed on increasing the model's ability to reproduce the impact of galactose and uridine feed additions on cell

culture dynamics and product galactosylation via UTP and UDP-Gal concentration profiles to create an accurate operating space for the subsequent optimisation.

7.6.1. Cell culture dynamics model output

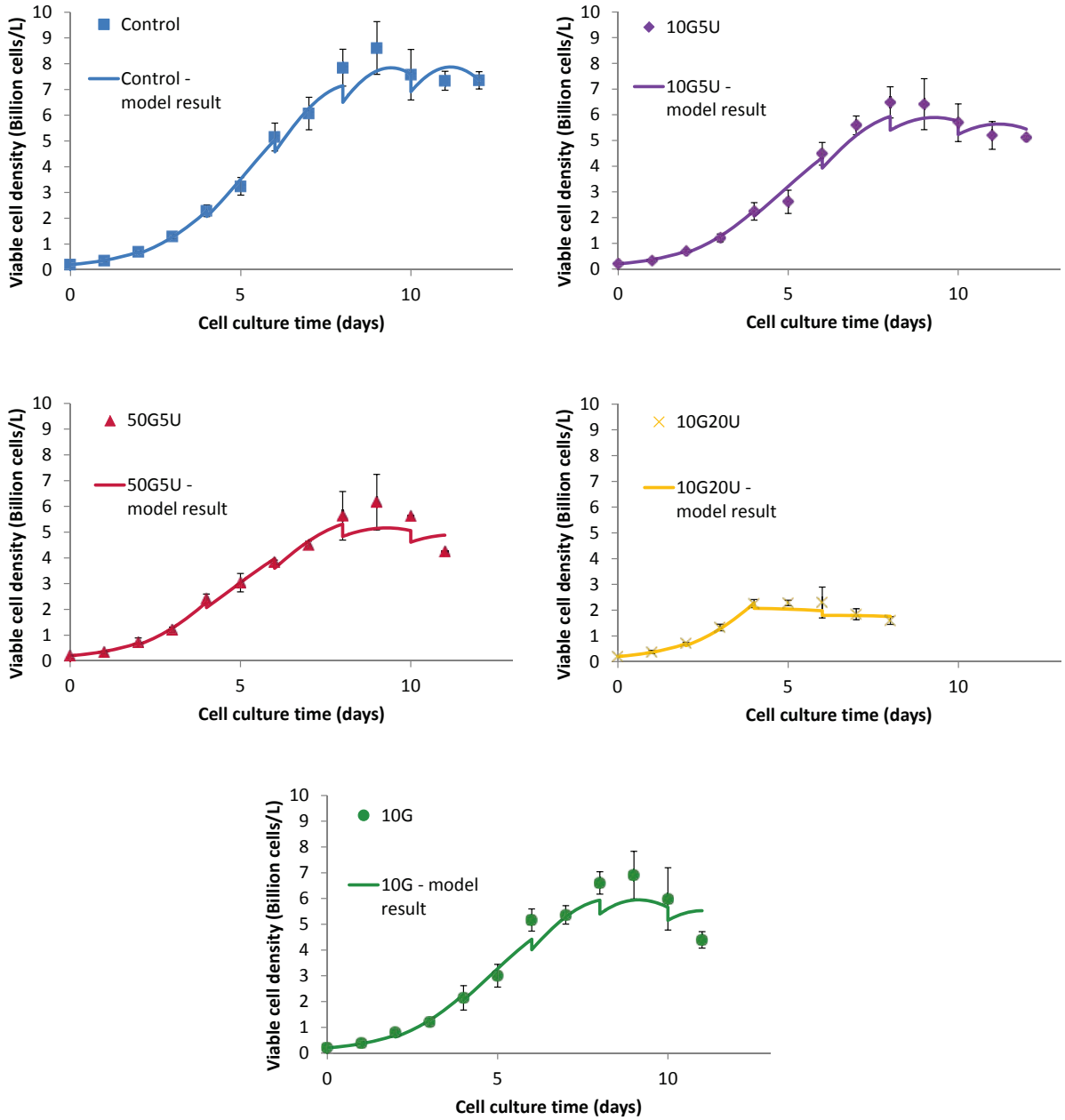
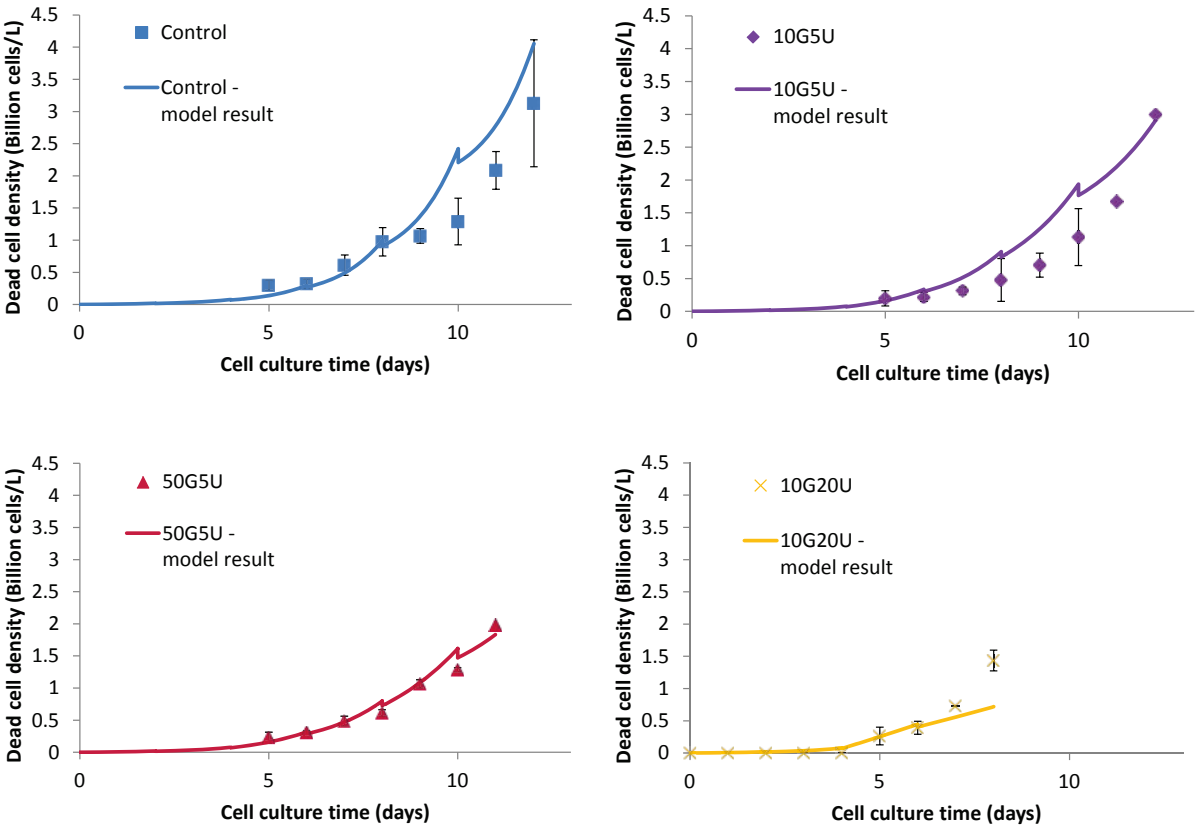
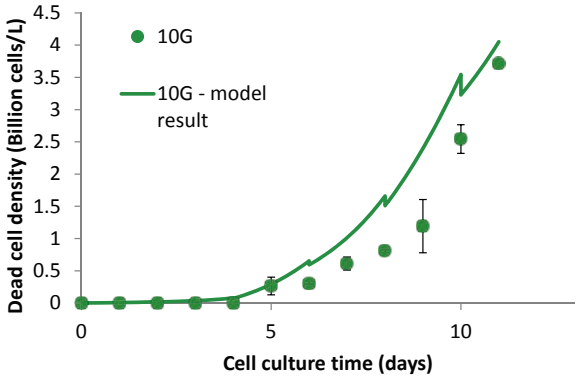


Figure 7.8a-e Experimental data (markers) and computational outputs (lines) of viable cell density for all culture conditions with respect to time.

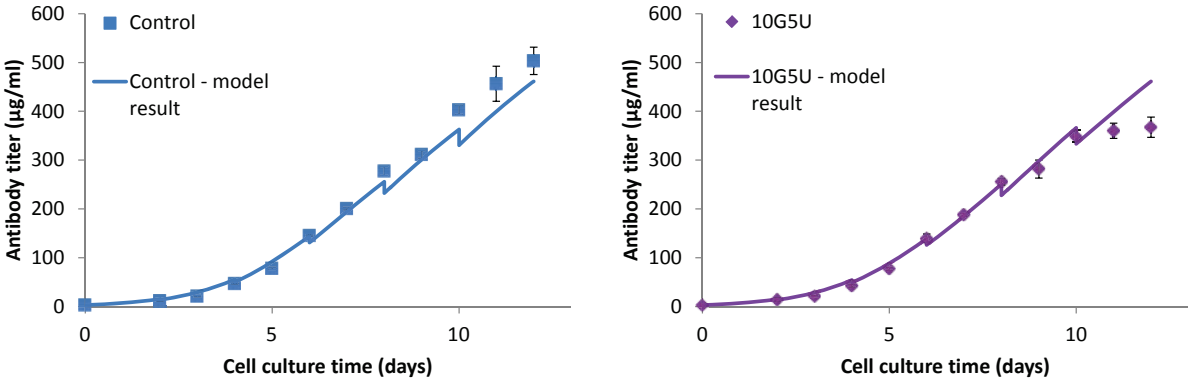
The computational outputs of the viable cell density match the experimental data very well (figure 7.8a-e). Most outputs are within the experimental error range with the exception of final culture days for the 50G5U and 10G culture conditions, where an overestimation is observed. The model is able to capture the cell growth inhibition under the high guanosine condition 10G20U, which can be observed after feeding on day 4 of culture. The model is able to capture the reduced growth resulting from high galactose as well as galactose only feeding for the 50G5U and 10G conditions, respectively. The model output is able to capture the quantitative trend of cell death well (figure 7.9 a-e). However, overestimation of cell death can be observed at the late stages for the control culture, 10G5U and 10G conditions. Very good agreement can be observed for the 50G5U and 10G20U cultures. The estimated parameters (Appendix E) suggest dependence on asparagine depletion, uridine and galactose supplementation. However, due to the nature of cell death expression (equation 7.2), galactose contribution is reduced in the presence of uridine.

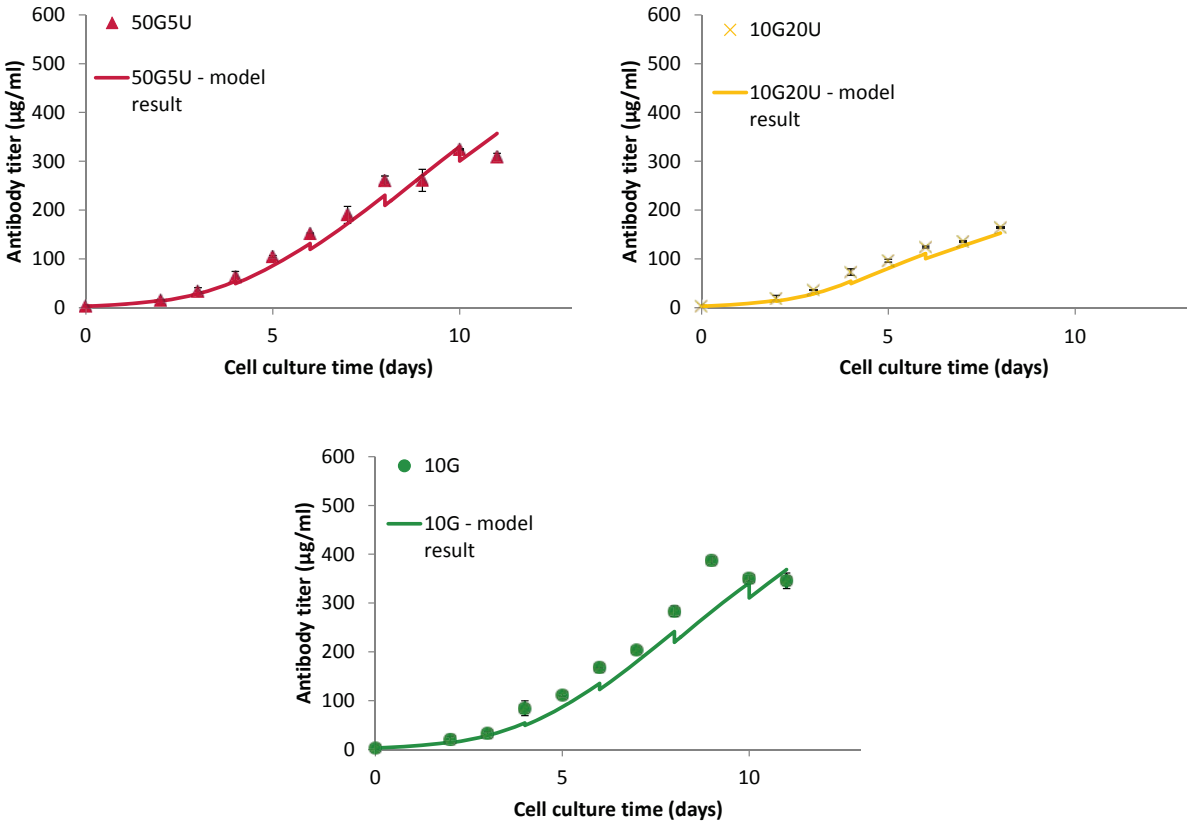




Figures 7.9a-e Experimental data (markers) and computational outputs (lines) of dead cell for all culture conditions with respect to time.

Overall good fits for antibody titer were achieved by the model (figure 7.10). The control, 50G5U and 10G20U cultures show very good agreement. An over-prediction of the final two days of culture can be observed for the 10G5U condition. A poorer fit can also be observed for the 10G condition. However, the experimental data point on day 9 of culture shows a higher titer than on the final two days of culture, which seems unlikely and may be a result of an experimental error. As in chapter 5, the estimated parameters (Appendix E) suggest a dependence of antibody production on both, the cell growth and constant contribution term (equation 5.17).

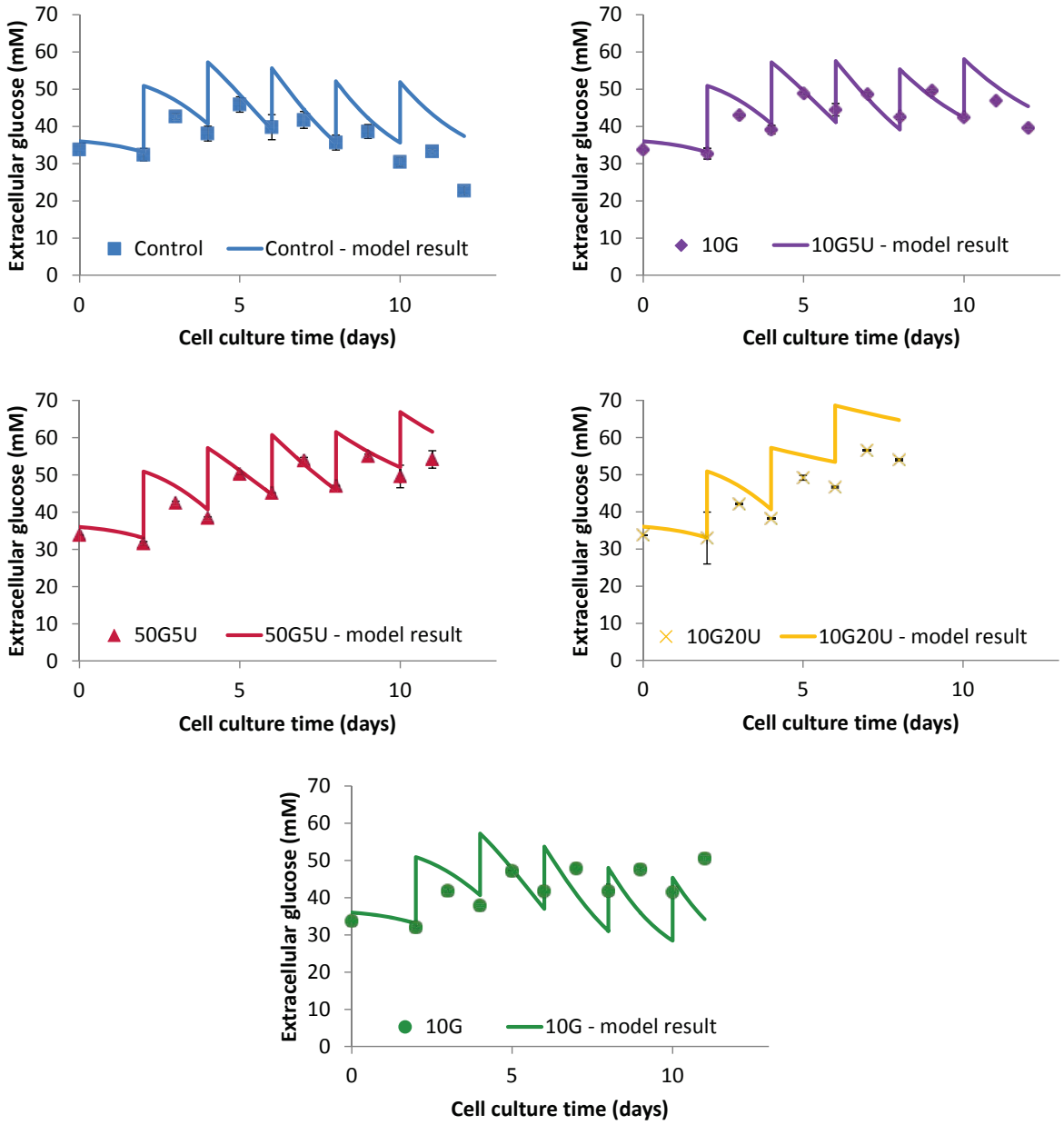




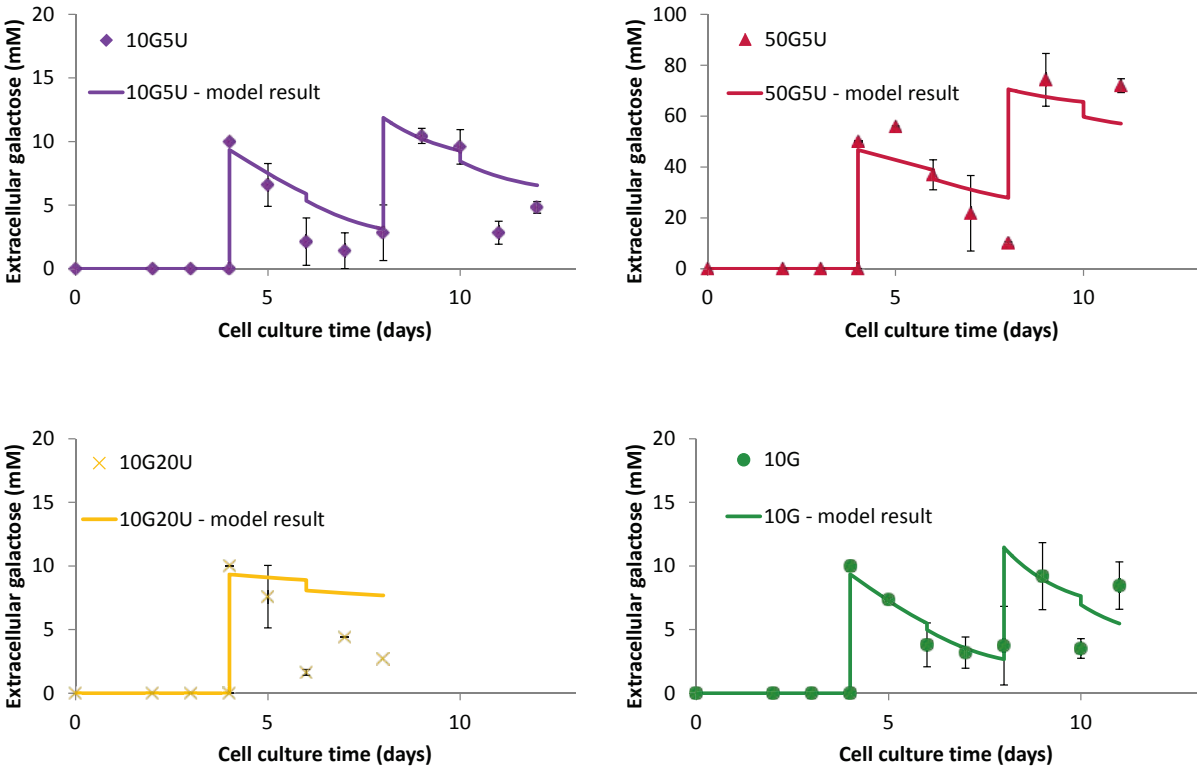
Figures 7.10a-e Experimental data (markers) and computational outputs (lines) of antibody titer for all culture conditions with respect to time.

Overall good quantitative trends of extracellular glucose concentrations were obtained from the model output (figure 7.11a-e). Very good fits were obtained for the 10G5U and 50G5U feed conditions. However over-predictions are observed for the control cultures and the 10G20U condition and a flattening of the glucose concentration gradient can be observed for the late culture stages. This together with the estimated parameter values (Appendix E) suggests a large dependence of glucose consumption on the growth dependent term. An under-prediction of glucose concentrations can be observed for the 10G culture. Good quantitative model outputs were produced by the model for extracellular galactose concentrations (figure 7.12a-e). Particular good fits are observed for the 10G5U and 10G fed conditions, where a concentration dependent consumption is observed. The model output for the 50G5U condition shows lesser agreement with experimental data. However, some of the experimental data points paint an unrealistic picture, where a jump from 10 mM galactose to 80 mM galactose is observed after the 50 mM feeding on day 8. Hence, model

output accuracy cannot be fully compared to experimental data. Lastly, poor agreement with experimental data is observed for the 10G20U model output. Galactose consumption is under-predicted due to the low viable cell density. Under-prediction of glucose and galactose consumption under the 10G20U condition may suggest a uridine induced metabolic shift leading to high cellular hexose consumption metabolism, which the cell dynamics model is not able to capture.

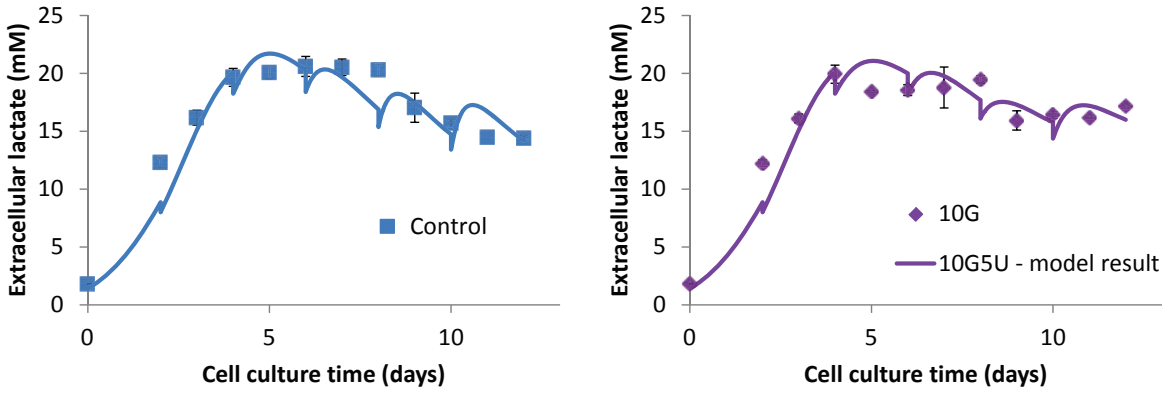


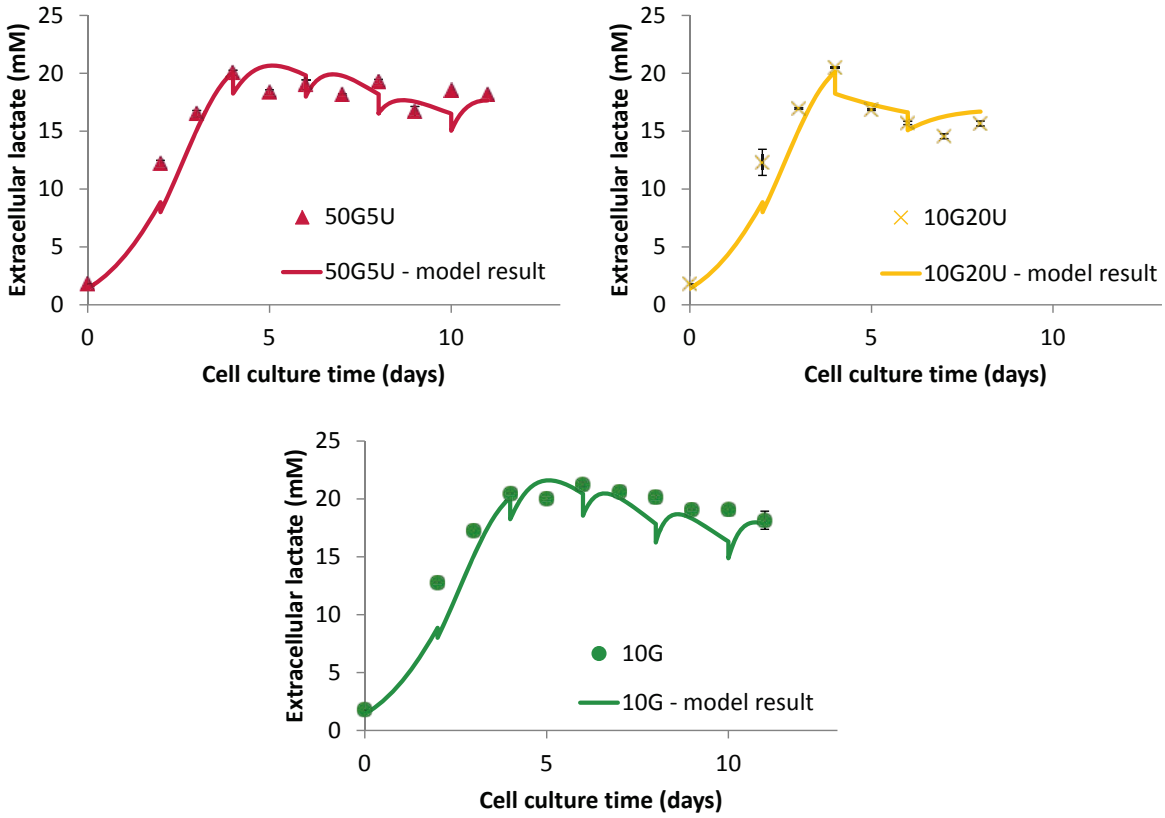
Figures 7.11a-d Experimental data (markers) and computational outputs (lines) of extracellular glucose for all culture conditions with respect to time.



Figures 7.12a-d Experimental data (markers) and computational outputs (lines) of extracellular for all galactose fed culture conditions 10G5U, 50G5U, 10G20U and 10G with respect to time.

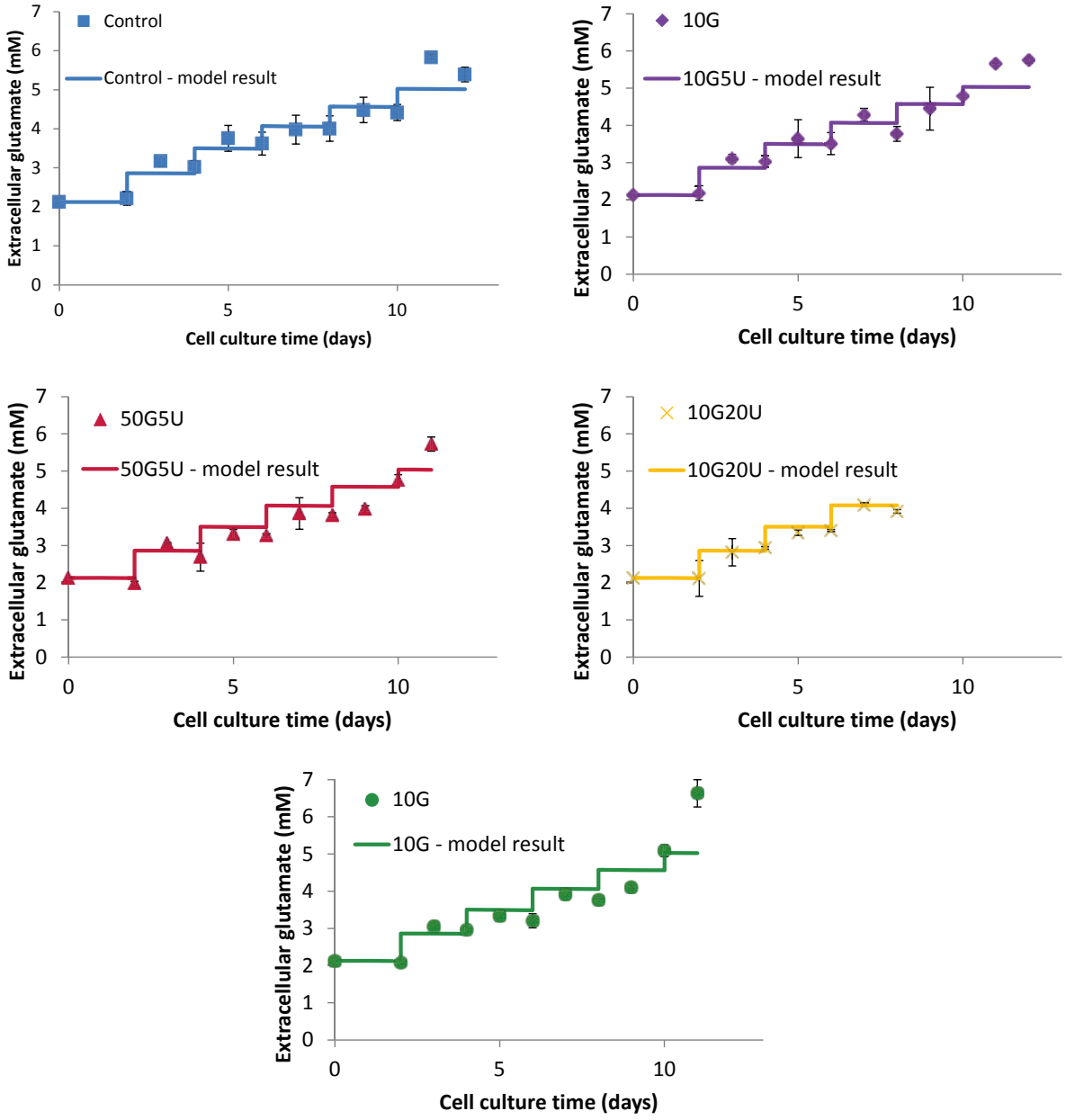
The extracellular lactate concentration model outputs are in very good agreement with experimental data (figure 7.13a-e). The model is able to predict the drop in lactate concentration under the 10G20U condition, where the high uridine feed addition led to cell growth arrest. For all other conditions the model is able to predict the slow decline in lactate concentration with the progression of the cell culture.



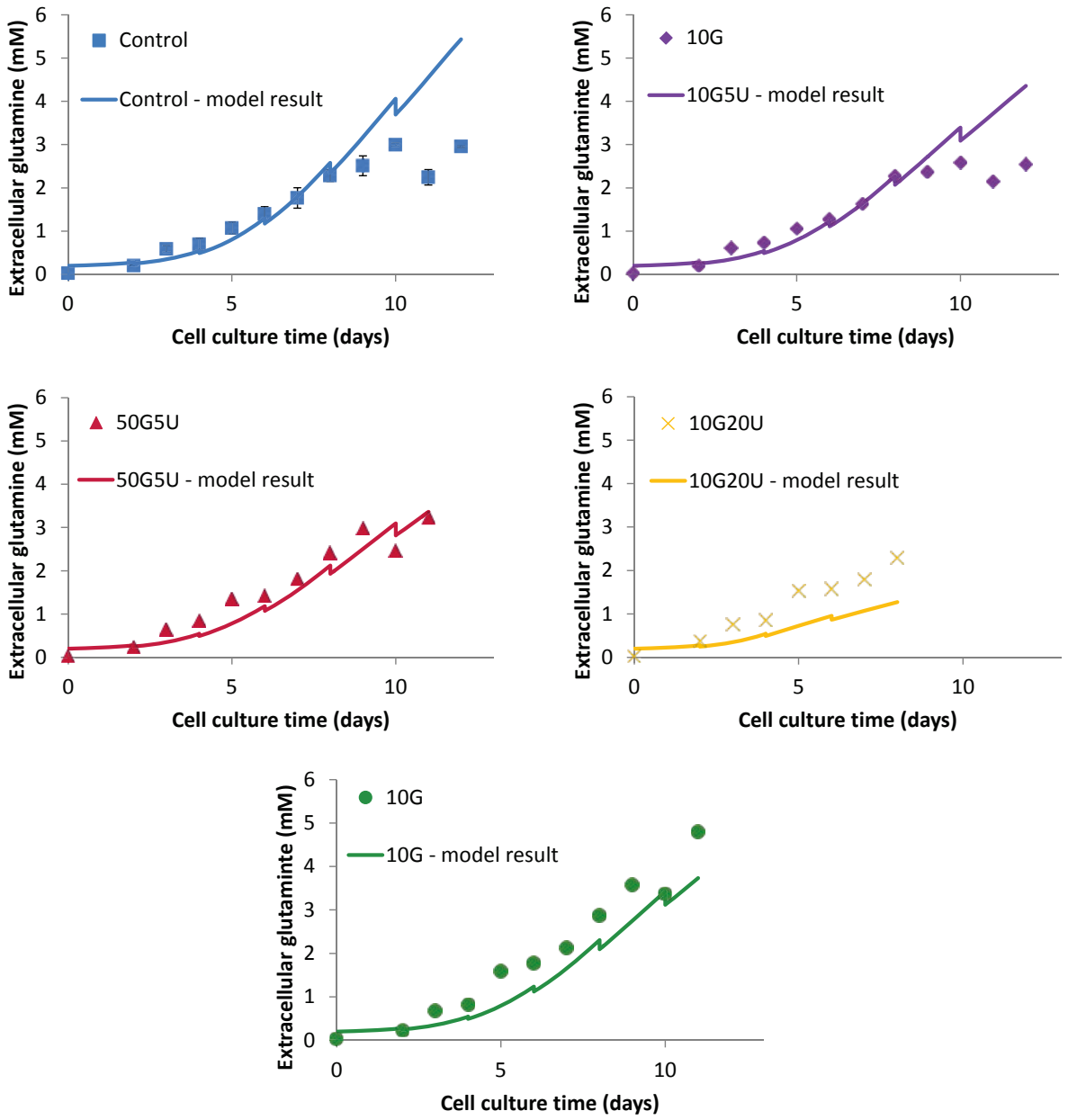


Figures 7.13a-e Experimental data (markers) and computational outputs (lines) of extracellular lactate for all culture conditions with respect to time.

The model is able to reproduce the extracellular glutamine data well (figure 7.14a-e) for all conditions. The model predicts little consumption of glutamate by the cells and gradual accumulation resulting from feed additions. However, the model consistently under-predicts the glutamate concentrations on days eleven and twelve of culture, where a large increase in glutamate is observed. Glutamine concentration profiles showed mixed output accuracy (figure 7.15a-e). Good fits are obtained for early culture stages under all culture conditions. However, poor fits are achieved for the final culture days, where the model predicts an ongoing accumulation, while the experimental data suggests a plateau at a concentration of approximately 3 mM for all concentrations other than the 10G culture. The data suggests a reduced glutamine production at the late culture stages, which coincides with an accumulation of glutamate. This suggests a metabolic shift in glutamine metabolism that is not captured by the cell culture dynamics model.



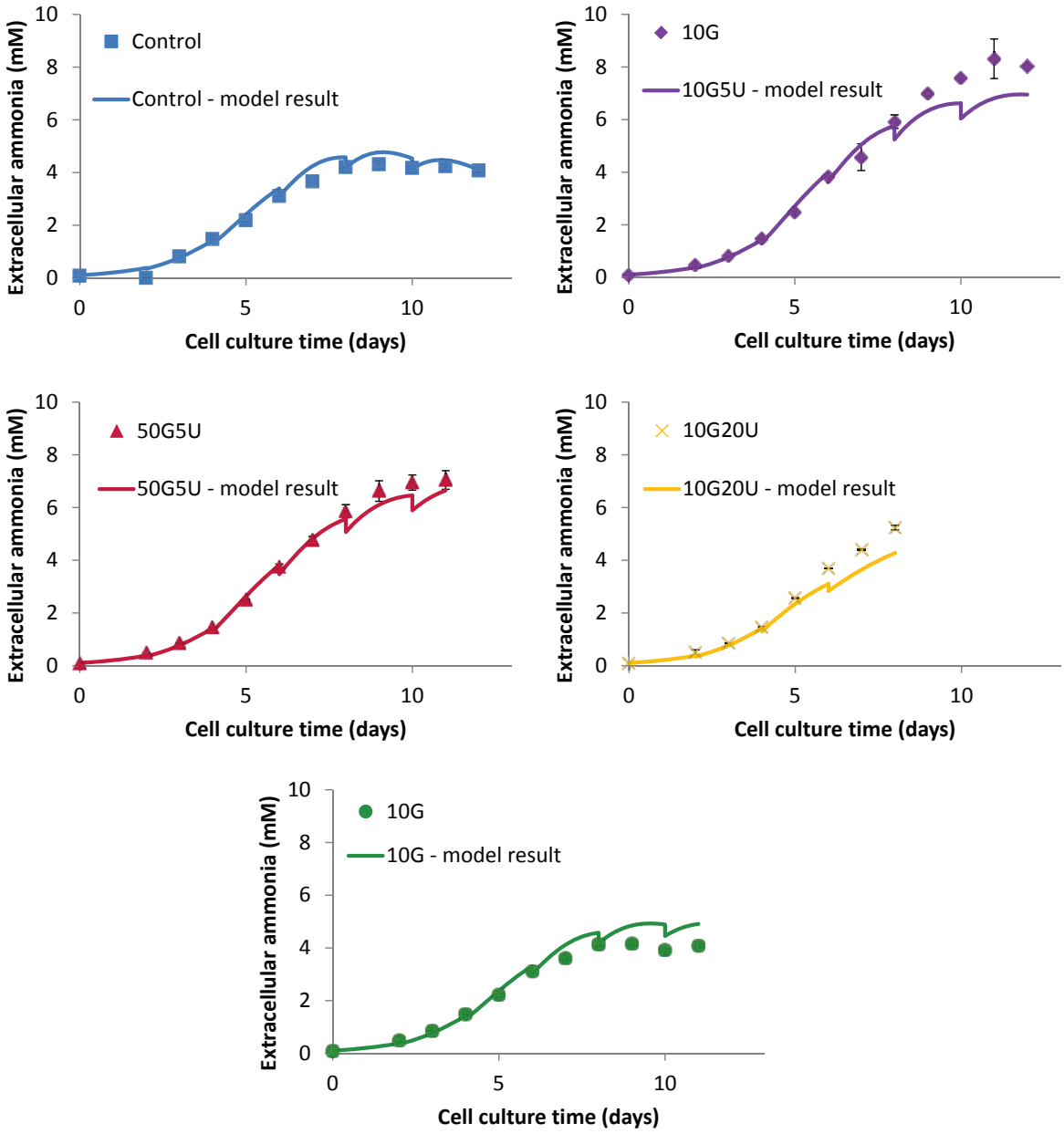
Figures 7.14a-e Experimental data (markers) and computational outputs (lines) of extracellular glutamate for all culture conditions with respect to time.



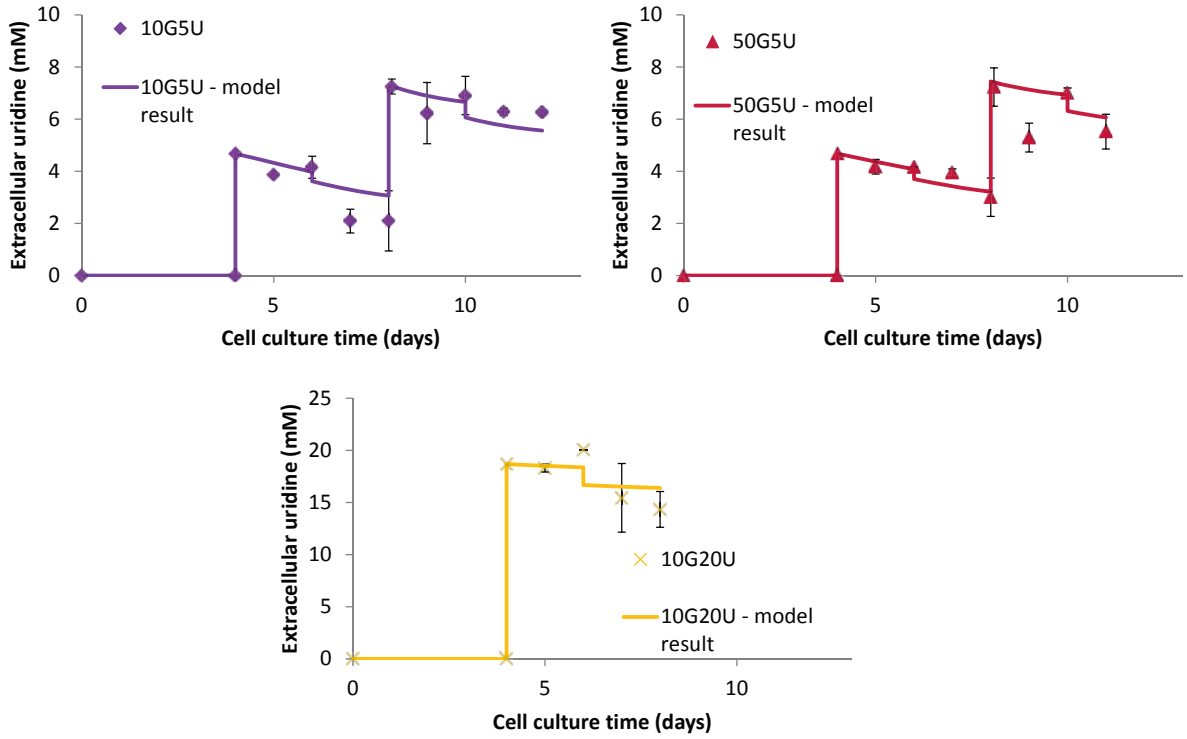
Figures 7.15a-e Experimental data (markers) and computational outputs (lines) of extracellular glutamine for all culture conditions with respect to time.

Very good model outputs are achieved for extracellular ammonia concentrations (figure 7.16a-e). The model is able to account for increased ammonia production resulting from uridine addition to the cell culture media in cultures 10G5U and 50G5U. A minor under-prediction is observed under the 10G5U feeding condition. Good experimental fits are also achieved for extracellular uridine concentrations, where model outputs trace

experimental data closely (figure 7.17a-c). The model is able to account for consumption by the cells as was experimentally observed.

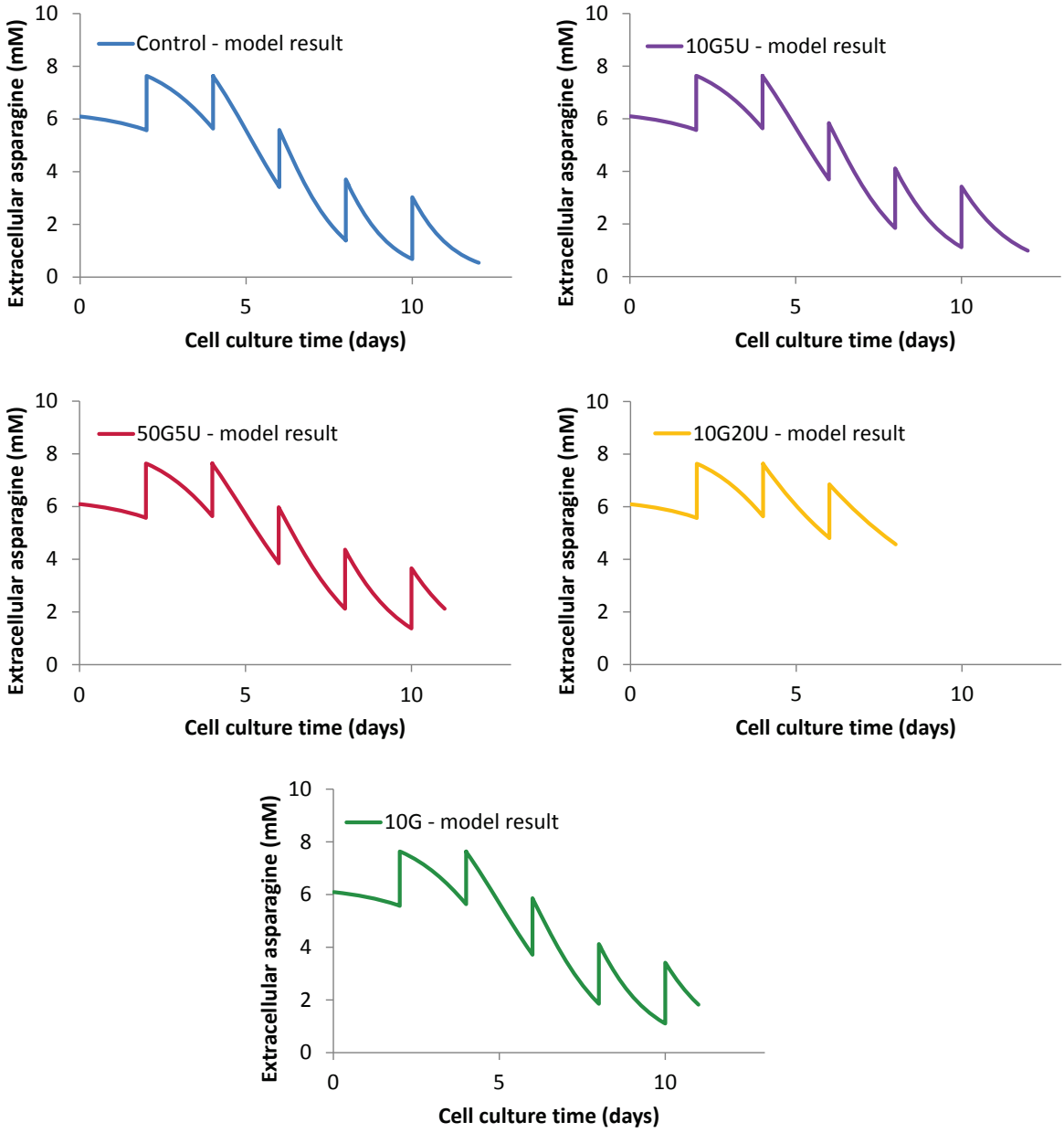


Figures 7.16a-e Experimental data (markers) and computational outputs (lines) of extracellular ammonia for all culture conditions culture with respect to time.



Figures 7.17a-c Experimental data (markers) and computational outputs (lines) of extracellular uridine for the uridine fed culture conditions 10G5U, 50G5U and 10G20U with respect to time.

As discussed in chapter 5, no data for asparagine has been collected (figure 7.18a-e. However, asparagine consumption leads to ammonia production and hence, is sufficiently constrained through the ammonia production term to estimate asparagine consumption parameters. The asparagine concentration starts to deplete in the control culture, where high cell densities were observed. Together with its impact on cell death and growth inhibition, it suggests being a limiting factor in the control culture and possibly to a lesser extent in the 10G5U, 50G5U and 10G cultures. Little consumption is observed by the low cell density 10G20U culture. This is in line with the model outputs of chapter 5, where the extracellular asparagine concentration showed little consumption at lower cell densities.

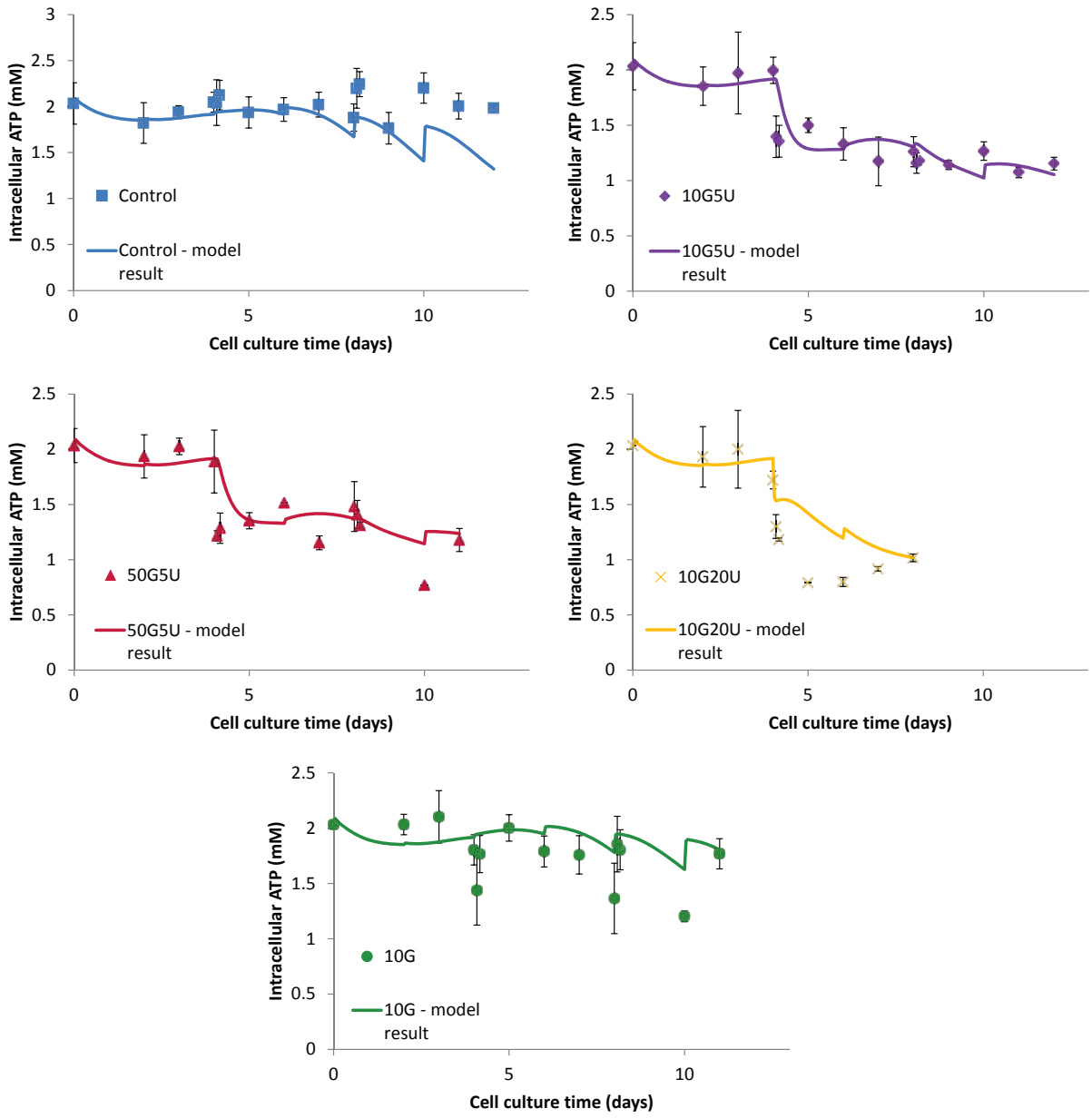


Figures 7.18a-e Experimental data (markers) and computational outputs (lines) of extracellular asparagine for all culture conditions with respect to time.

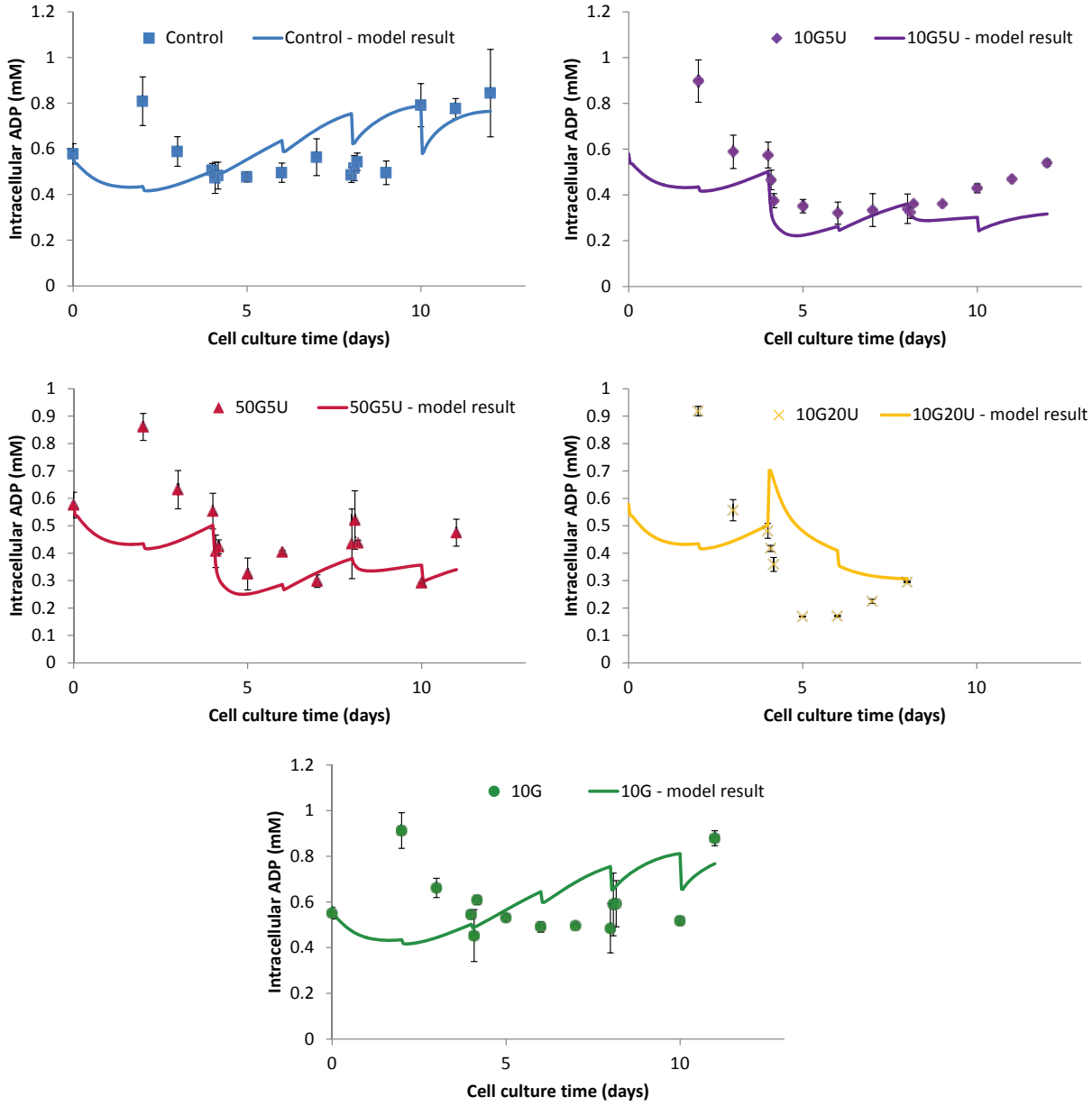
Overall, a good performance is achieved for the cell culture dynamics model. Most importantly, the model is able to compute the consumption of the supplemented galactose and uridine well. Furthermore, it is able to capture the impact of the various feed additions on cell growth and cell death as well as the various metabolic changes reflected in the concentrations of the extracellular metabolites.

7.6.2. Nucleotide synthesis model output

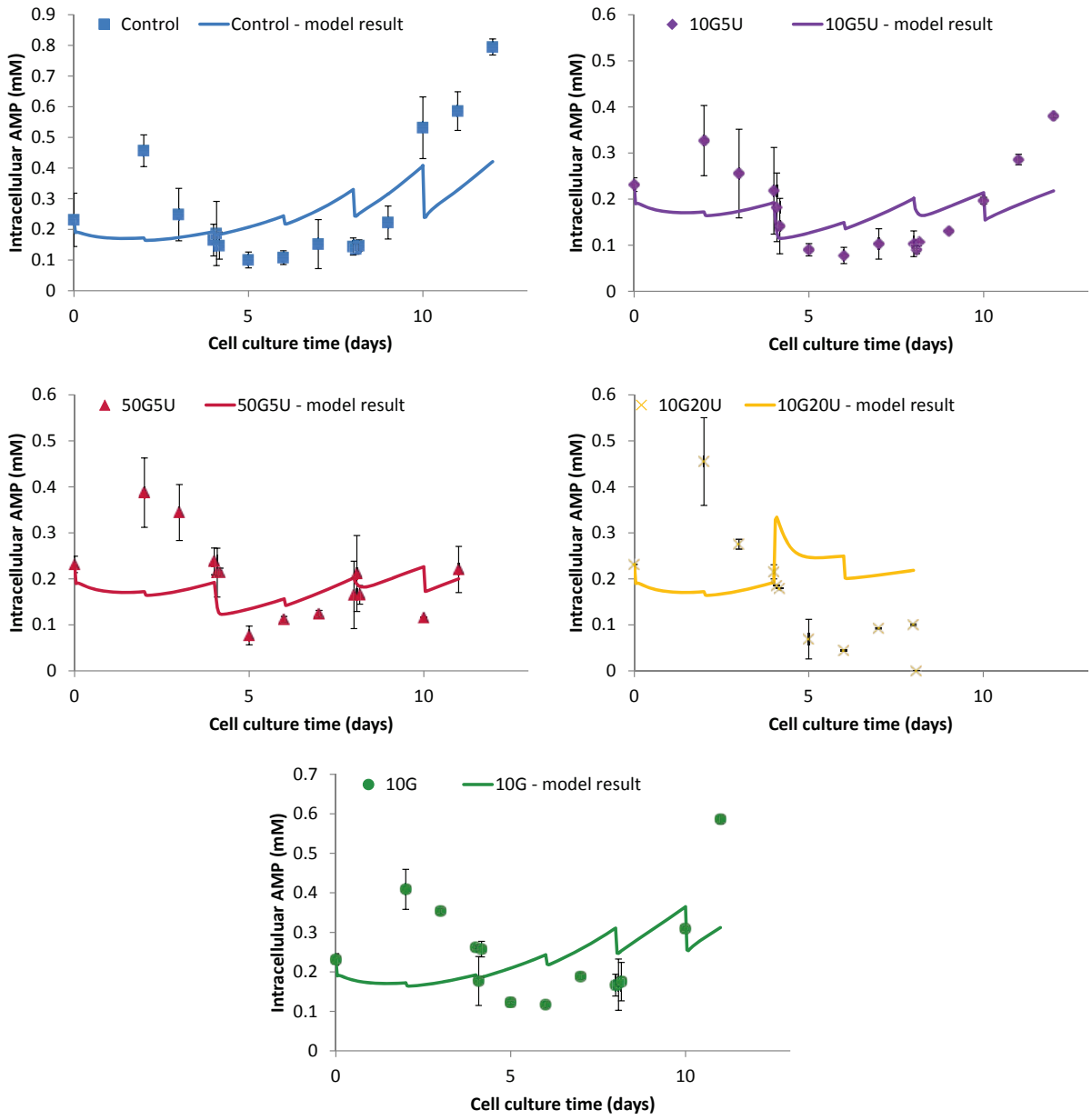
The updated purine model was trained using experimental intracellular data from chapter 6 and was able to reproduce most intracellular ATP concentration profiles well (figure 7.19a-e). The model reproduced the experimentally observed drop in ATP as a result of uridine addition to the cell culture media. An exception to this is the 10G20U condition, where the model was not able to reproduce a sufficiently large drop in ATP concentrations. This is explained by a reduction in the model's ATP consumption for the growth inhibited 10G20U condition, which is a function of growth. The control and the 10G culture outputs show a slight drop towards the end of culture. Reasonable fits are also achieved for intracellular ADP concentrations (figure 7.20a-e). Again a drop is observed as a result of uridine addition to the cell culture media, which is reproduced well under the 10G5U and 50G5U condition but less so for the 10G20U cultures. The model is not able to reproduce the initial increase in ADP concentrations after seeding and the subsequent slow decline. The experimental ADP profile results most likely from the adaptation phase of the cell culture, which the model is not able to account for. Increases in ADP concentrations are observed towards the end of the culture for the control and 10G cultures. Lastly, good quantitative mode outputs are achieved for AMP. While the increase of the adaptation phase is again not captured by the model, accumulation towards the end of the culture can be observed. Again poor fits are achieved for the 10G20U condition. Decreases in late stage AMP can be observed as a result of feed additions. This behaviour propagates particularly to ADP, while the reverse is observed in ATP and is most strongly observed for the control and 10G cultures. This is explained by the inhibitory effect on AMP synthesis by increased ATP concentrations, resulting from increased hexose flux after feed addition.



Figures 7.19a-e Experimental data (markers) and computational outputs (lines) of intracellular ATP for all culture conditions with respect to time.

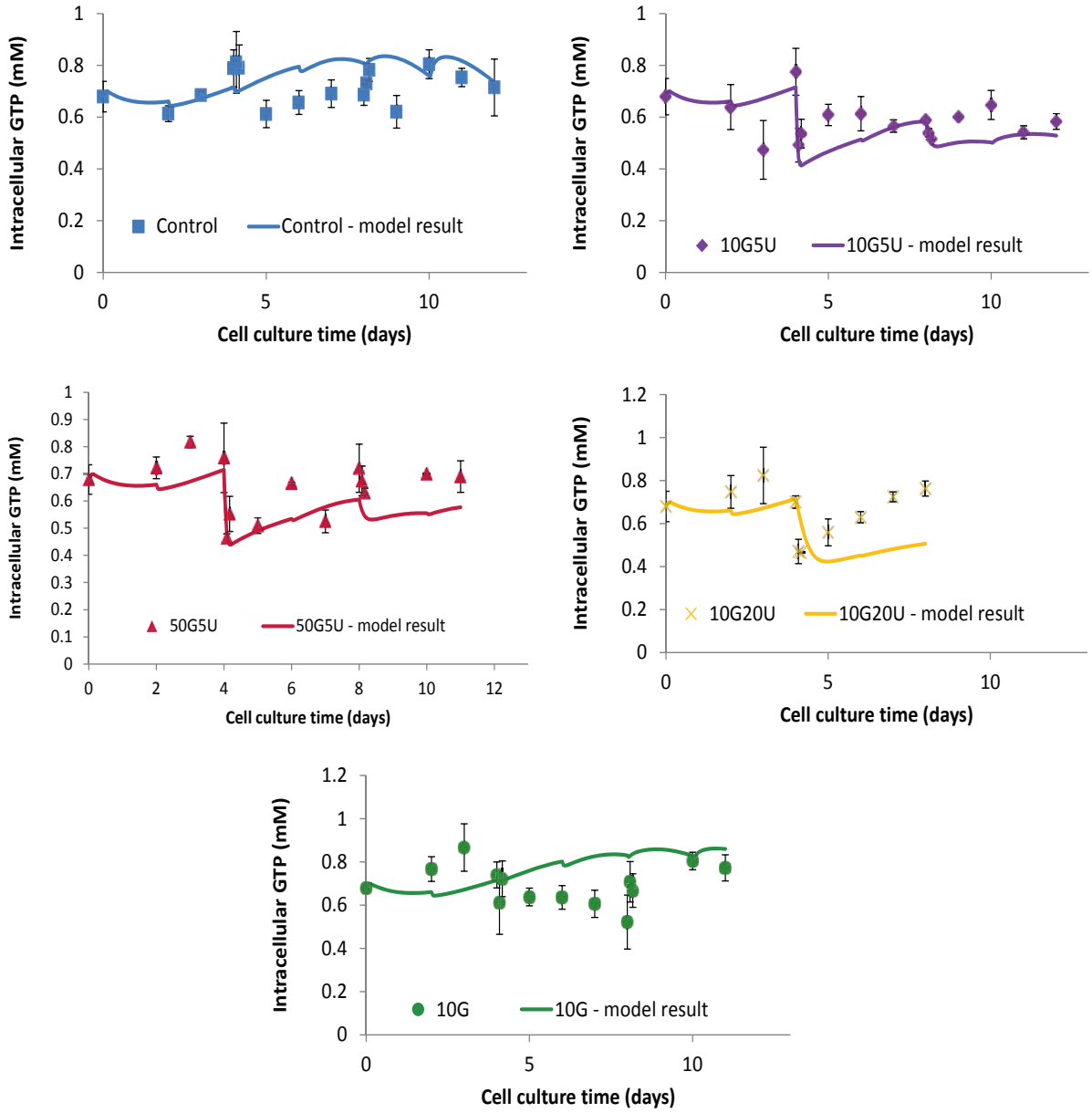


Figures 7.20a-e Experimental data (markers) and computational outputs (lines) of intracellular ADP for all culture conditions with respect to time.



Figures 7.21a-e Experimental data (markers) and computational outputs (lines) of intracellular AMP for all culture conditions with respect to time.

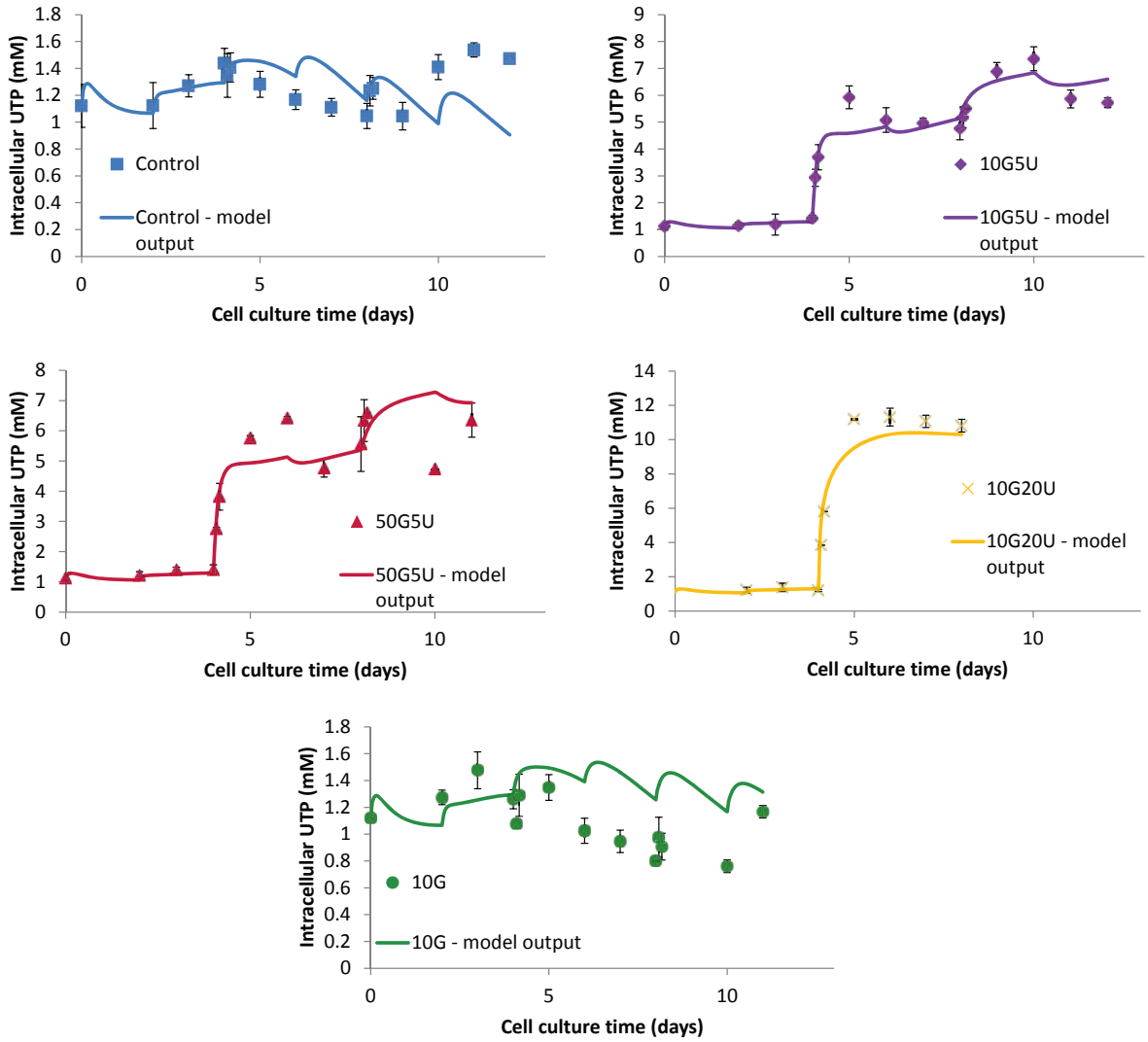
The model output of intracellular GTP is in good agreement with experimental GTP concentrations (figure 7.22a-e). A drop in GTP can be observed as a result of uridine additions to culture media with a slow recovery. However, the large recovery of 10G20U that was observed experimentally was not sufficiently reproduced computationally.



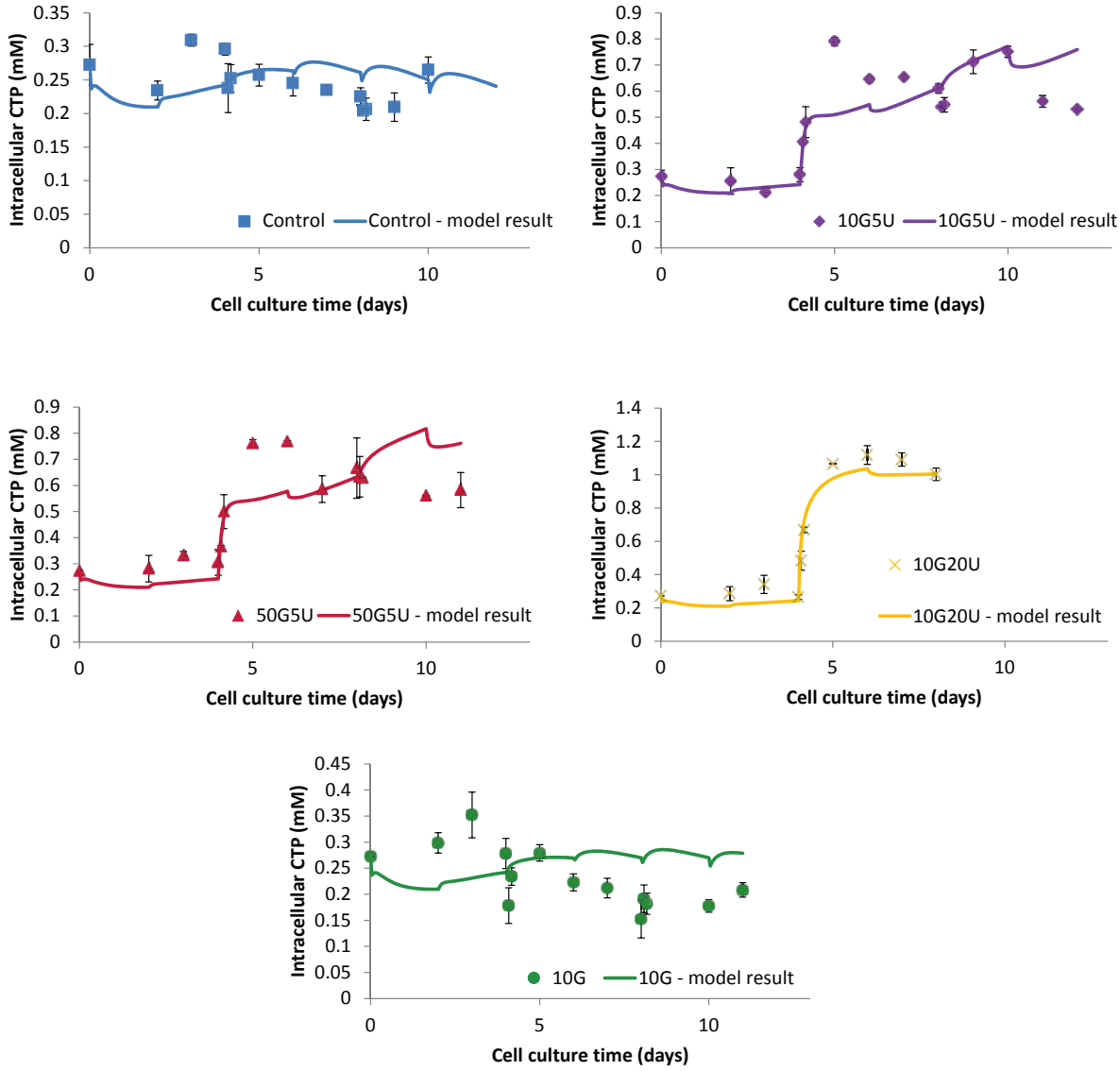
Figures 7.22a-e Experimental data (markers) and computational outputs (lines) of intracellular GTP for all culture conditions with respect to time

Emphasis was paid on the improvement of the pyrimidine model and capturing the response to uridine media supplementation. Overall good fits have been achieved for UTP (figure 7.23a-e). The dynamic response to uridine feed addition has been captured well by the model, which was able to reproduce the rapid increase observed experimentally. A smaller second uridine concentration dependent response can also be observed on day eight of culture. Increases in UTP concentrations can be observed for the control and 10G cultures

after feed addition at the late culture stages. This is explained by the increase in extracellular asparagine resulting from feed addition. The model also reproduces intracellular CTP concentrations well (figure 7.24a-e). Increases in CTP concentration can be observed after uridine addition, which result from increased UTP concentrations, the substrate to CTP synthesis. The experimental data showed a slow decline in CTP concentrations on days 6, 7 and 8 of the 10G5U and 50G5U cell culture, which is not reflected by the model. A similar decline, although to a lesser extent, is also observed in the experimental UTP data and maybe the either the result of the reduction in extracellular uridine concentration due to consumption or the result of changes in enzyme concentration due to gene regulation.



Figures 7.23a-e e Experimental data (markers) and computational outputs (lines) of intracellular UTP for all culture conditions with respect to time.



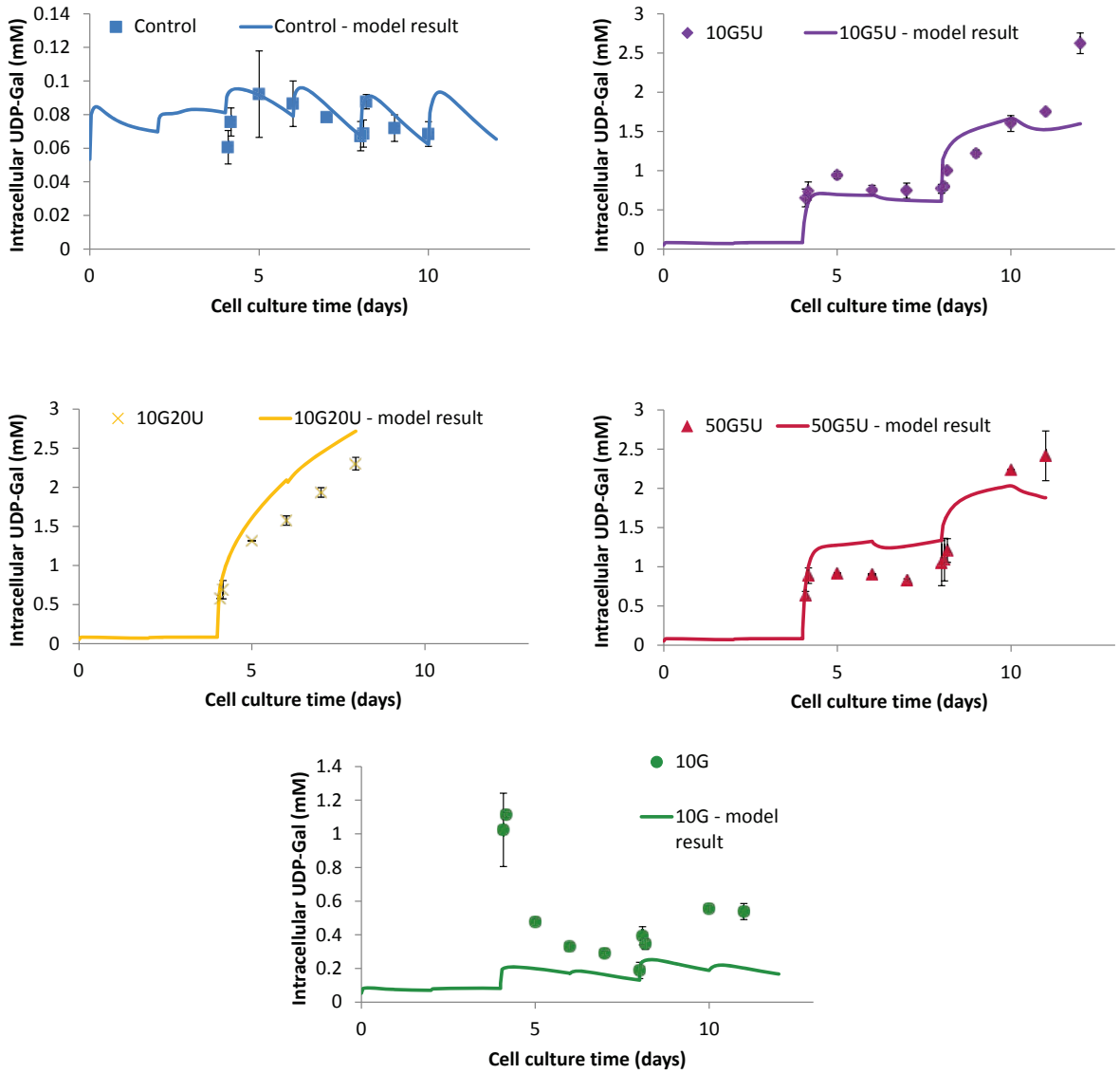
Figures 7.24a-e Experimental data (markers) and computational outputs (lines) of intracellular CTP for all culture conditions with respect to time.

Overall, the improved nucleotide model performs well in comparison with experimental data. The exceptions to this are ADP and AMP, where qualitative trends are largely preserved as well as a number of model outputs of the 10G20U condition. The latter may be the result of metabolic changes resulting from the high uridine concentration, which the model does not account for. In conclusion, it can be said that the nucleotide model is able to capture the effects of galactose and moderate uridine addition to the culture media well. With respect to the optimisation problem the issues encountered by the high uridine

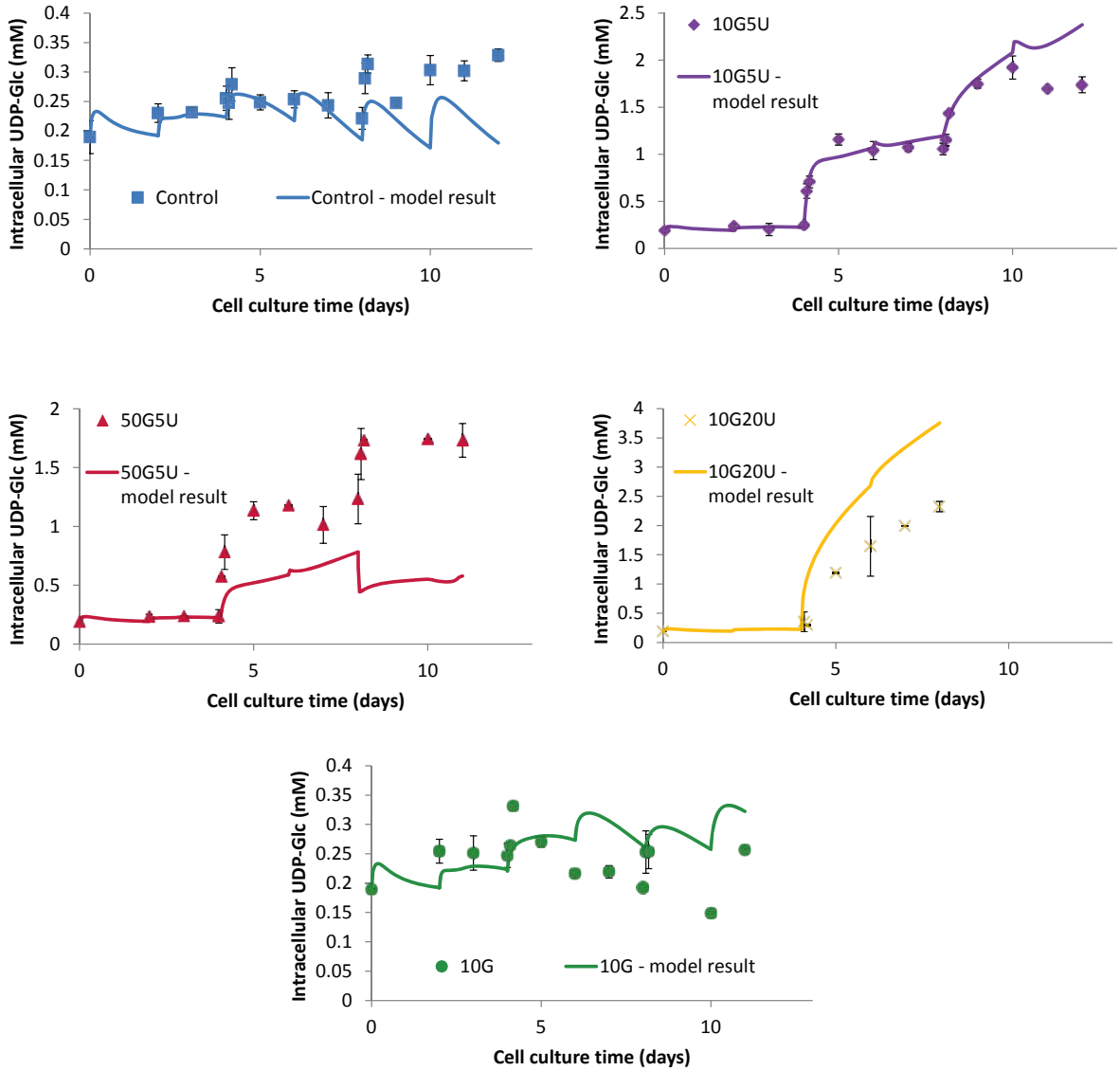
concentration pose no greater problem, as high uridine concentrations are not sought out due to inhibited cell growth and reduced antibody production rate.

7.6.3. Nucleotide sugar donor model output

The main goal of the model training with respect to the nucleotide sugar donor model was to capture the effect of galactose and uridine supplementation to the culture media on intracellular UDP-Galactose concentrations. The model was mostly able to capture the UDP-Gal concentration profiles well and capture the dynamic changes resulting from the various feed additions (figure 7.25a-e). An exception to this was observed under the 10G feeding condition, where the model was not able to reproduce the initial sharp increase in the UDP-Gal profile. However, the model output still shows an increase in UDP-Gal concentrations as compared to the control condition. Under all uridine supplemented conditions increases in UDP-Gal are observed immediately after feed addition on day four of culture and a slower increase is observed on day eight. The model is also able to reproduce the accumulation of UDP-Gal observed for the 10G20U culture, albeit somewhat over-predicted. Good model fits are also obtained for intracellular UDP-Glc (figure 7.26a-e). An exception is observed for the 50G5U feed condition, where a quantitative deviation in model output to experimental data is observed. This may be explained by the large galactose flux, leading to increased Gal-1P concentrations, which drives reaction r23a. The substrate to the double displacement reaction r23a is UDP-Glc and hence, a large reaction rate will lead to a decrease in its concentration in the model output. As for UDP-Gal, the model is able to recreate the accumulation observed in the 10G20U cultures, albeit somewhat over-predicted.



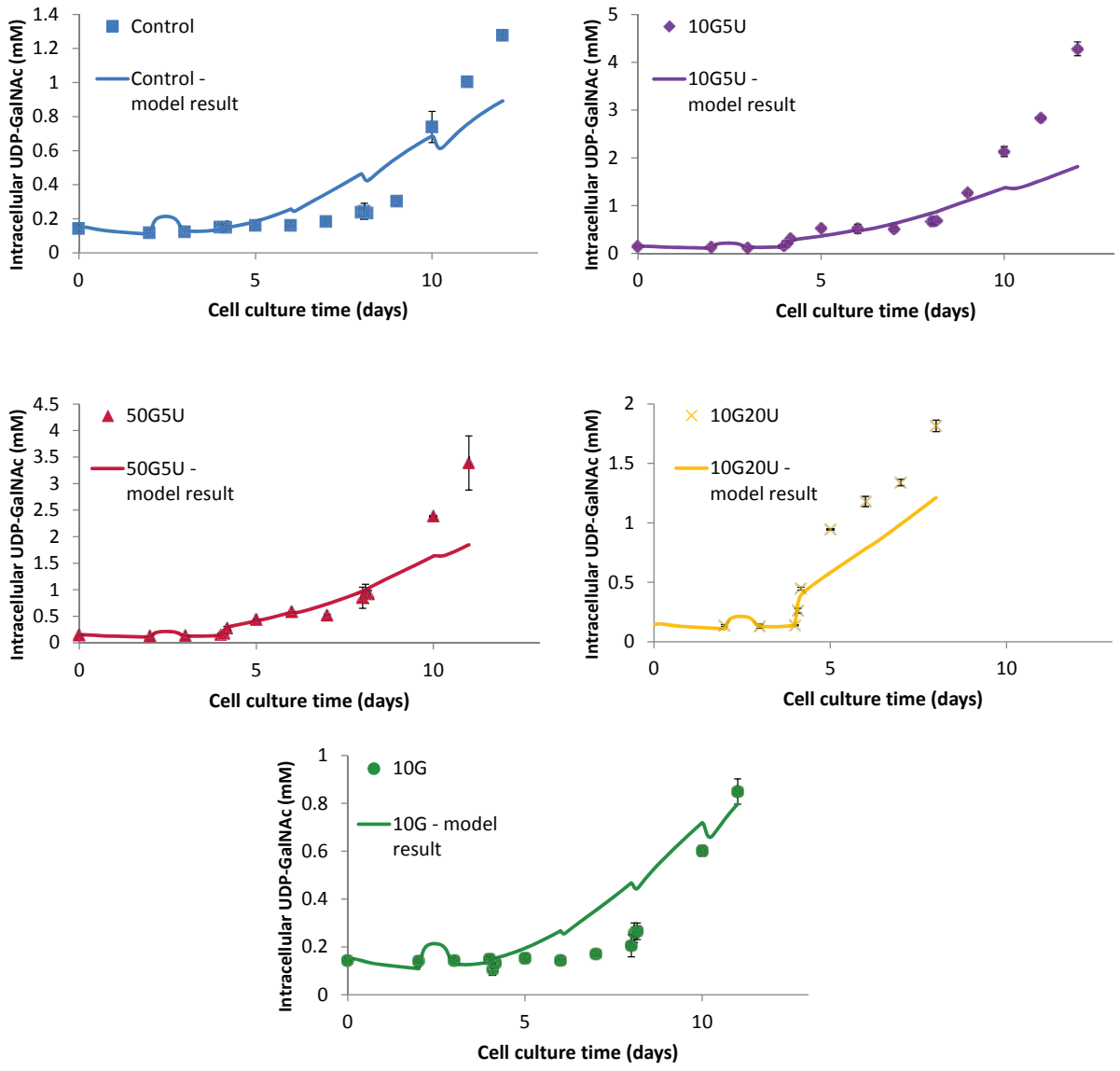
Figures 7.25a-e Experimental data (markers) and computational outputs (lines) of intracellular UDP-Gal for all culture conditions with respect to time.



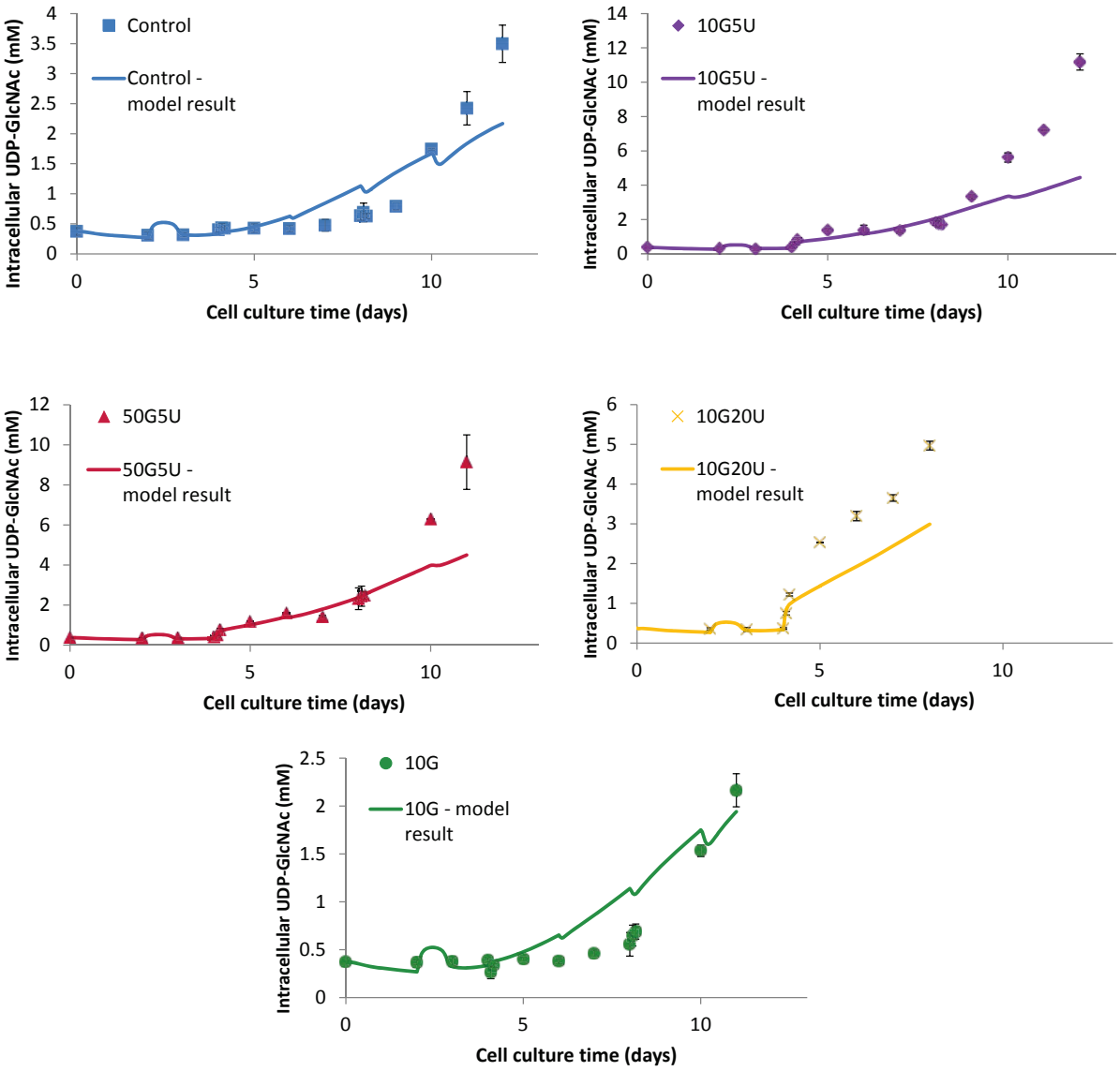
Figures 7.26a-e Experimental data (markers) and computational outputs (lines) of intracellular UDP-Glc for all culture conditions with respect to time.

Good quantitative fits are achieved for the UDP-HexNAc species (figures 7.27a-e and 7.28a-e). As already observed in chapter 5, the model is able to recreate the experimentally observed similarities in concentration profiles for both UDP-HexNAc species. Good fits for both species are achieved for the control and 10G cultures. The early accumulation after feed addition in the 10G20U culture is somewhat under-predicted by the model. The very high late culture stage accumulation of the UDP-HexNAc species under the 10G5U and 50G5U feed conditions are not captured well by the model. However, no UDP-GlcNAc related changes in the glycoform data were observed for the late culture stages of the 10G5U and

50G5U conditions. This points towards saturation of the glycosylation reactions with respect to UDP-GlcNAc throughout most of the culture period. Hence, the model's shortcoming is not expected to impact the optimisation with respect to galactosylation.



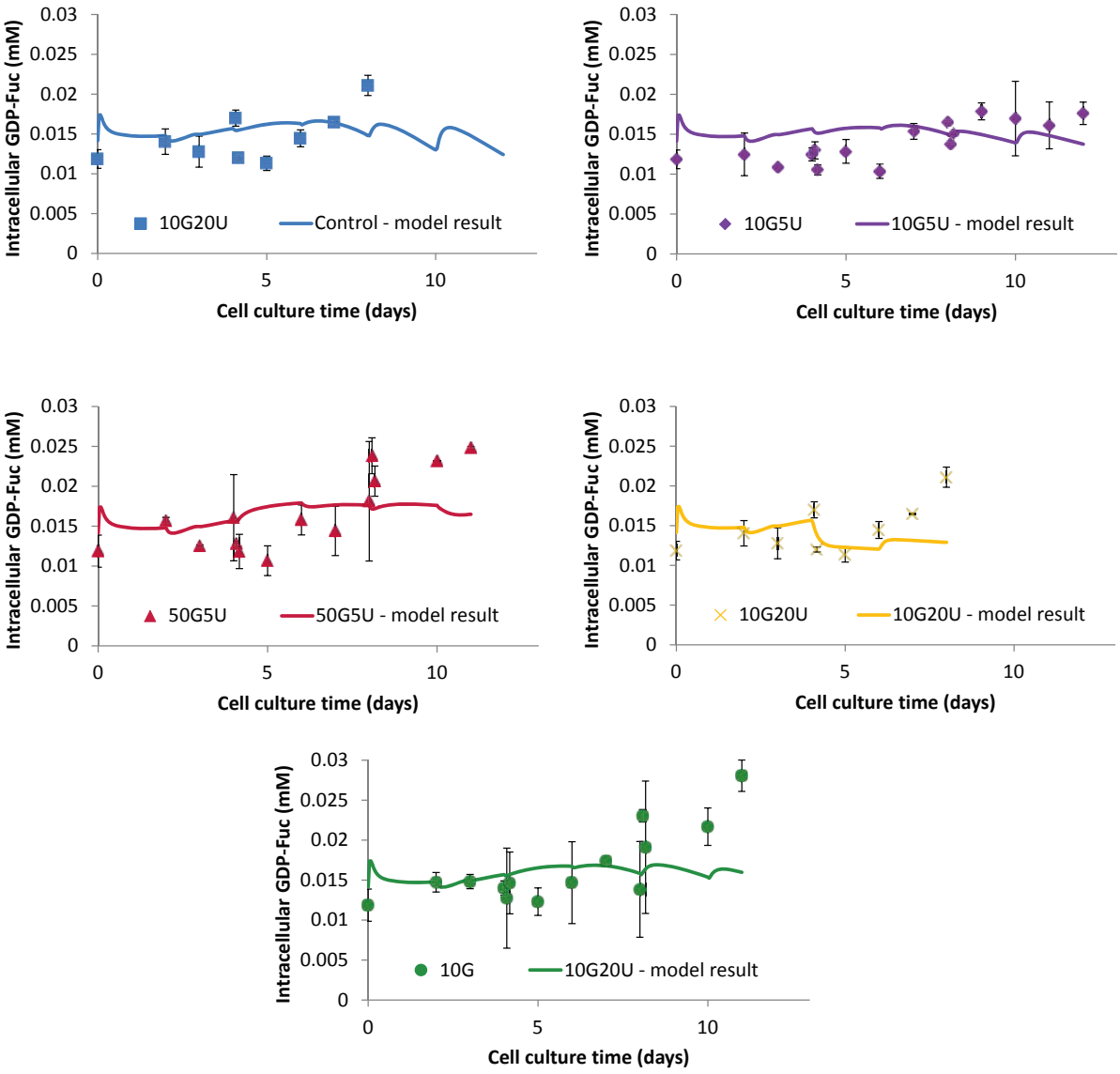
Figures 7.27a-e Experimental data (markers) and computational outputs (lines) of intracellular UDP-GalNAc for all culture conditions with respect to time.



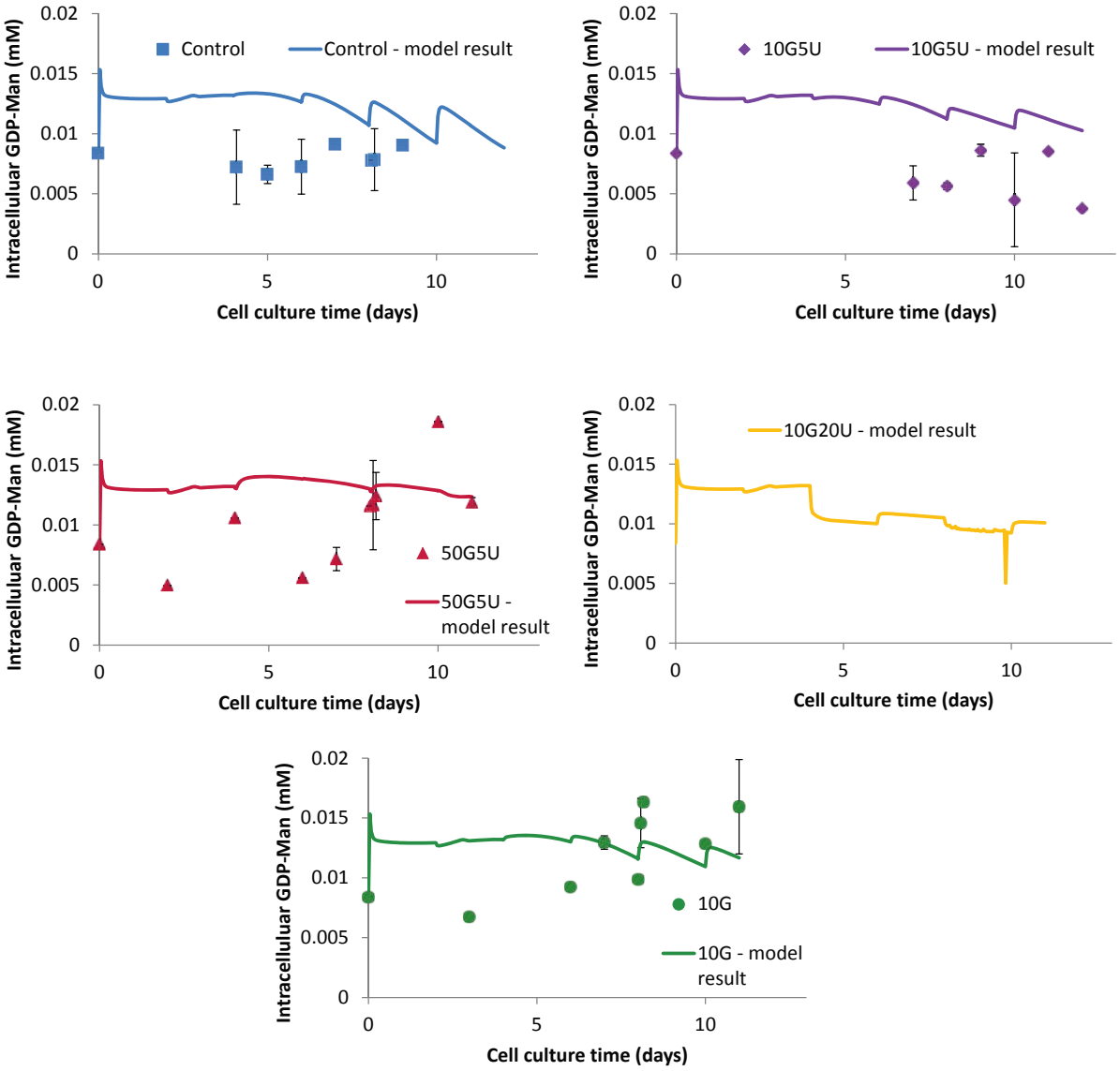
Figures 7.28a-e Experimental data (markers) and computational outputs (lines) of intracellular UDP-GlcNAc for all culture conditions with respect to time.

As discussed in section 7.3, a number of parameters of the GDP-Fuc and GDP-Man branch of the NSD metabolic network were left unchanged from the estimation carried out in chapter 5. Based on these parameters, the model was able to reproduce intracellular GDP-Fuc concentrations well (figure 7.29a-e) and thus, giving confidence in the structural changes and parameters of chapter 5. However, the model outputs for GDP-Man show lesser accuracy (figure 7.30a-e). While the quantitative trend is recreated *in silico*, an over-prediction can be seen for the control and 10G5U cultures. However, datasets are limited

due to very low intracellular concentration levels, which were partially not quantifiable. Consequently, only a limited comparison of model output against experimental GDP-Man data can be made.



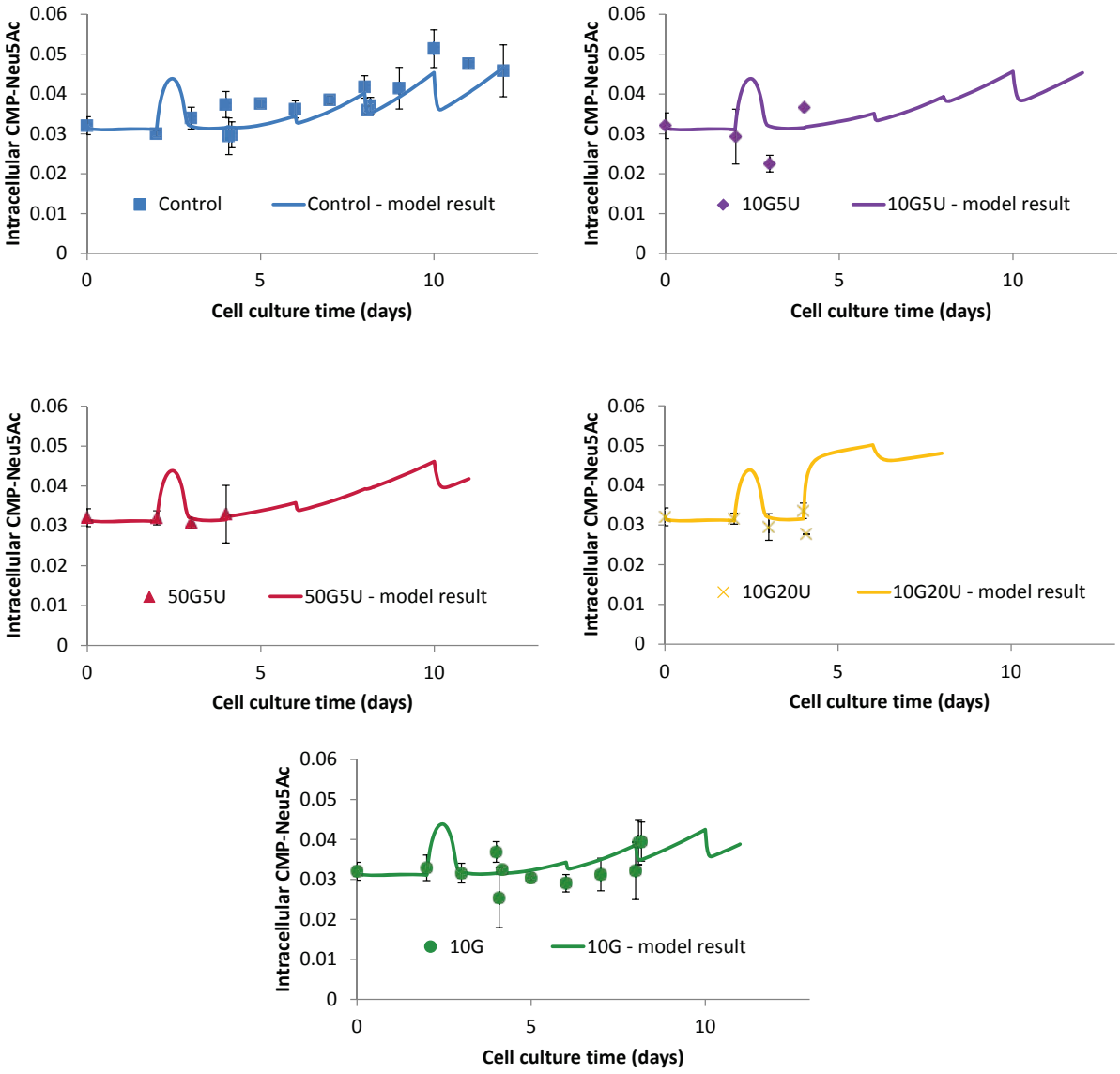
Figures 7.29a-e Experimental data (markers) and computational outputs (lines) of intracellular GDP-Fuc for all culture conditions with respect to time.



Figures 7.30a-e Experimental data (markers) and computational outputs (lines) of intracellular GDP-Man for all culture conditions with respect to time.

Lastly, the model was trained with experimental data of CMP-Neu5Ac and was able to recreate the concentration profiles well. Due to limitations of the analytical method, as discussed in the section 7.31, no CMP-Neu5Ac data was captured after uridine addition to cell culture media. The model predicts a gradual increase in CMP-Neu5Ac levels towards the end of the culture and a more rapid increase after feed addition to the 10G20U culture. As the model does not predict the same behaviour for the other uridine supplemented

cultures, it can be concluded that the increase results from reduced consumption after cell growth inhibition.



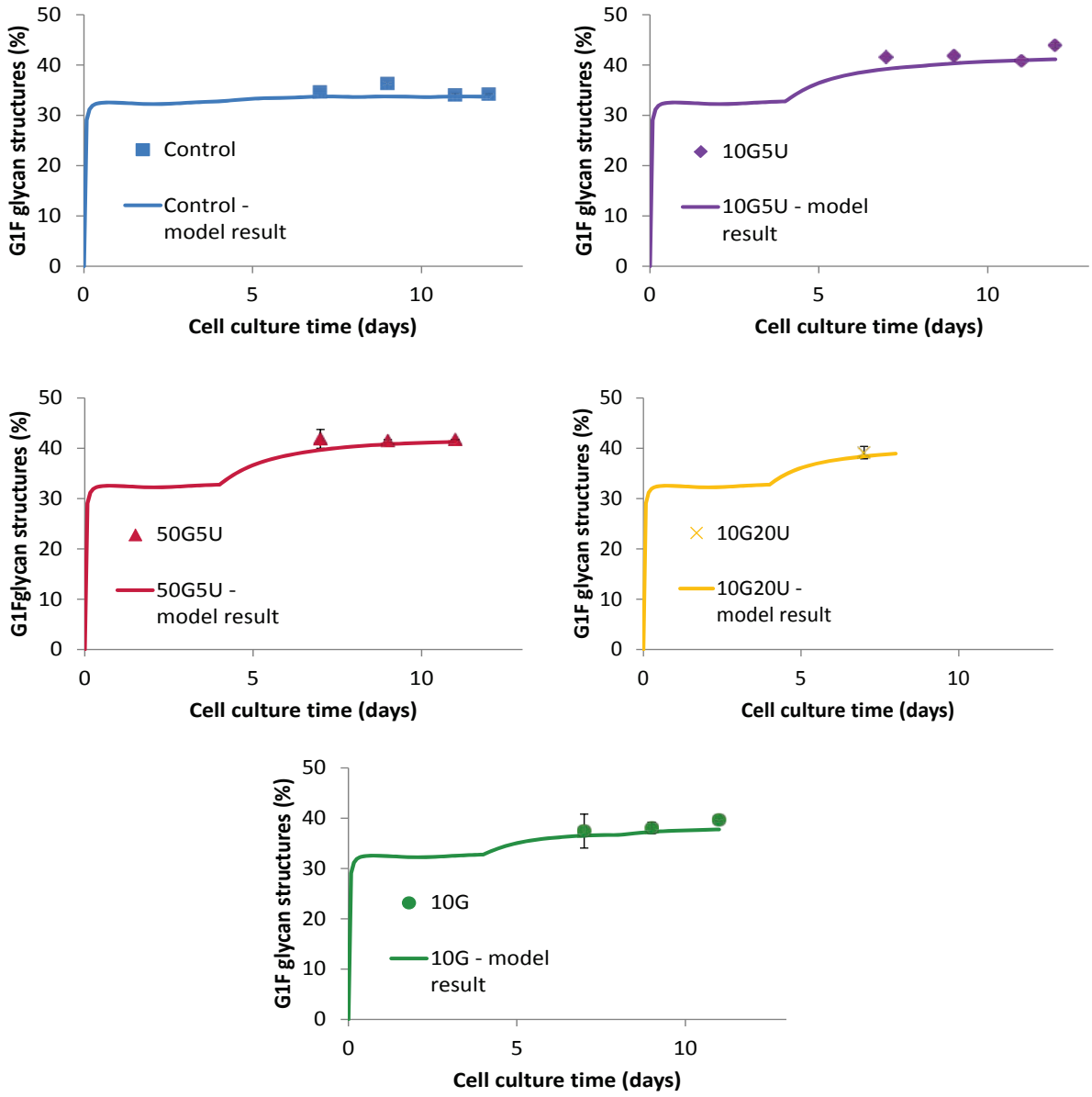
Figures 7.31a-e Experimental data (markers) and computational outputs (lines) of intracellular CMP-Neu5Ac for all culture conditions with respect to time.

Overall, the nucleotide sugar donor model is able to reproduce intracellular NSD data well and shows improved accuracy for the UDP-Hex branch, as compared to the model output of chapter 5. Thus, the main aim with respect to the refinement of the NSD model was achieved. Consequently, the NSD model appears to be sufficiently trained and calibrated to allow the subsequent optimisation with respect to varying galactose and

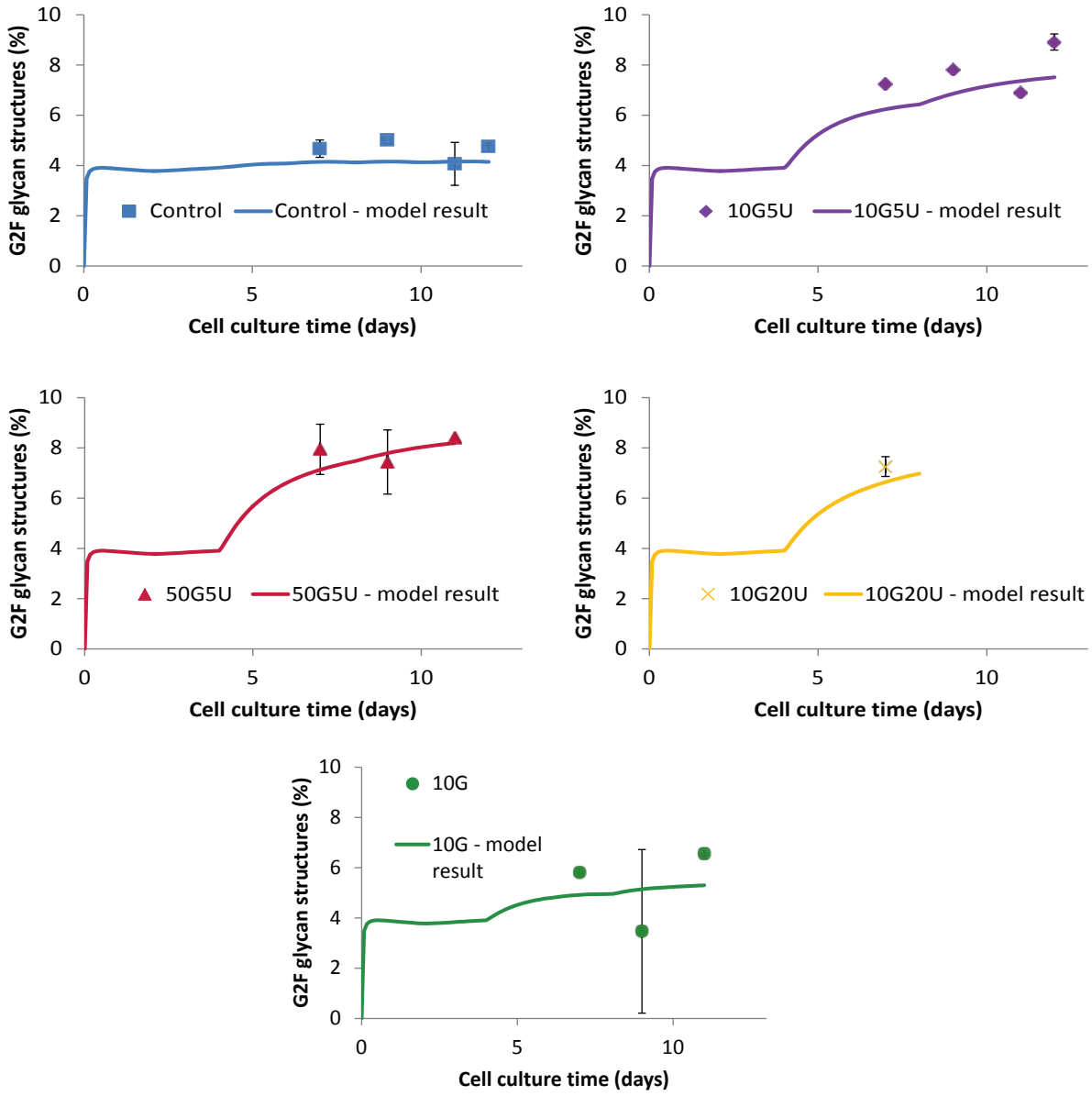
uridine feed conditions. Limitations are still observed for the 10G culture condition, where the decreased accuracy may be explained by changes in enzyme expression levels due to the presence of galactose in the cell culture media and the resulting redistribution of carbon fluxes.

7.6.4. Glycan model output

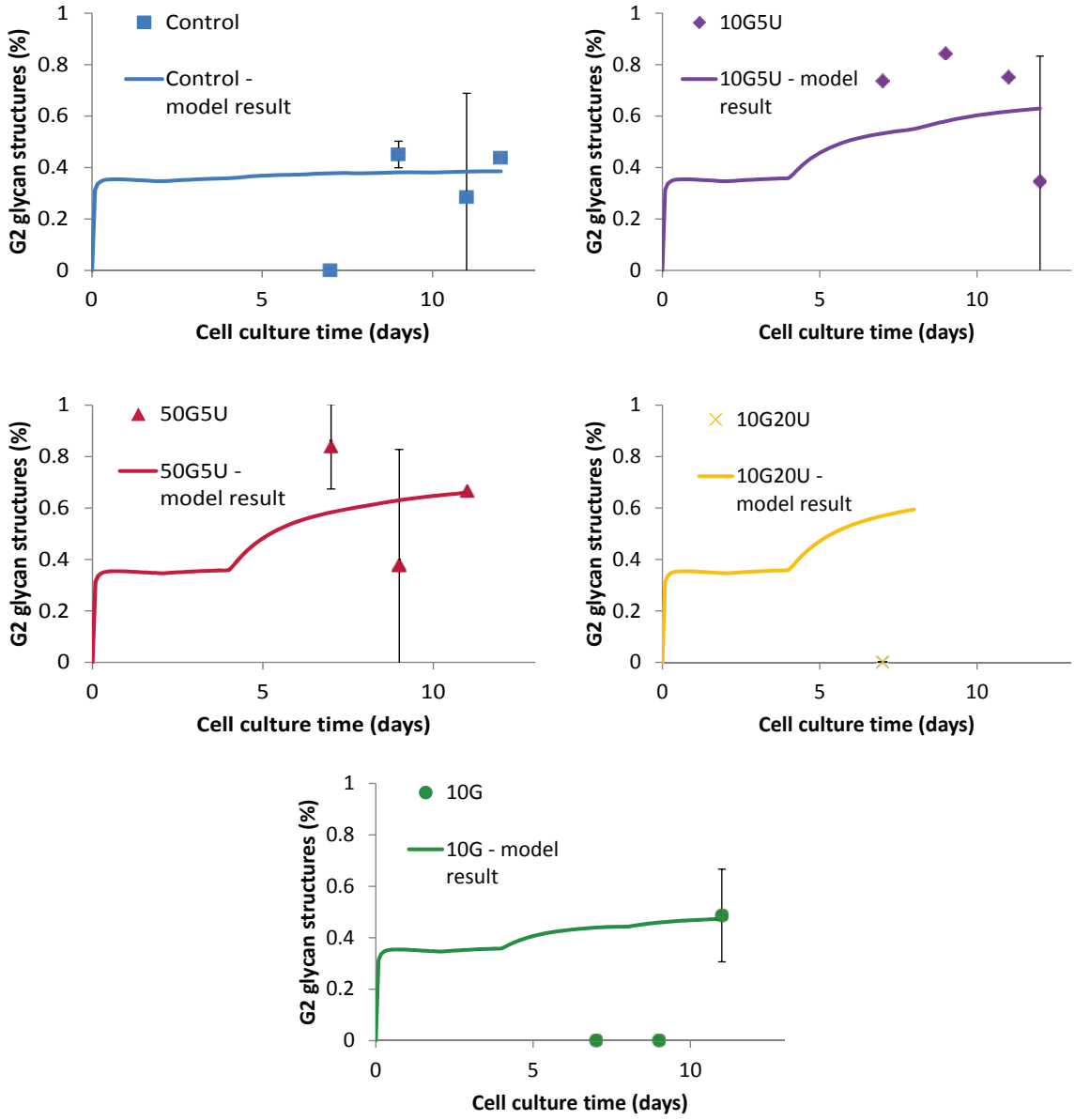
The final part of the model training consists of the estimation of the parameters of the del Val model. Here the model was trained against the cumulative glycan species fractions presented in chapter 6. Of particular importance is the model's ability to reproduce the galactosylated fractions of the glycoform as a function of intracellular UDP-Gal availability. The model outputs for the G1F species, was able to trace the profiles for all conditions very well (figure 7.32a-e). While the control culture shows a rather steady profile throughout the duration of the culture, all supplemented conditions show a clear response to feeding on day 4 of culture. After the initial increase the cumulative G1F fraction appears to plateau towards the end of culture. Despite the under-prediction of UDP-Gal concentrations under the 10G condition by the NSD model, the increase over the control was sufficient to reproduce the G1F profile well. The model is also able to recreate the G2F profiles for all culture conditions well (figure 7.33a-e). Again an increase is observed for all supplemented cultures after feeding and a further increase is observed after the second feeding of the 10G5U and 50G5U cultures on day 8. This suggests that saturation of the galactosylatransferase is not yet achieved with respect to the UDP-Gal concentrations for these conditions. A mixed fit is achieved by the model for the abundance of the G2 species (figure 7.34a-e). However, it has to be noted that the experimentally determined abundance was below 1% of the total glycoform. This led to uncertainty in experimental data as well as difficulties in species detection such, that G2 was partially not quantifiable. Overall, the G2 profiles show strong similarities to those of the G2F glycan species.



Figures 7.32a-e Experimental data (markers) and computational outputs (lines) of G1F glycan abundance with respect to culture time.



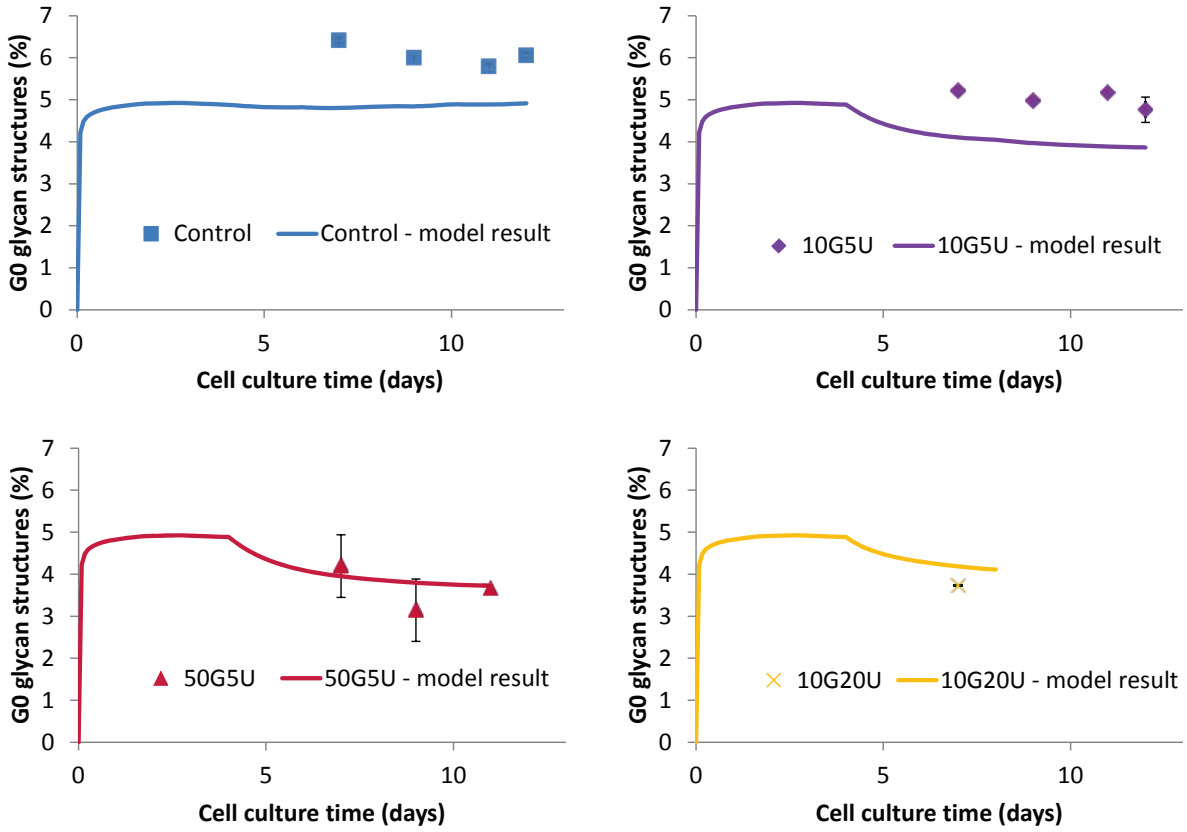
Figures 7.33a-e Experimental data (markers) and computational outputs (lines) of G2F glycan abundance with respect to culture time.

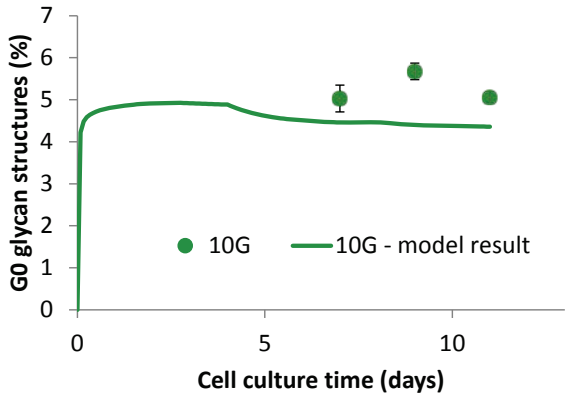


Figures 7.34a-e Experimental data (markers) and computational outputs (lines) of G2 glycan abundance with respect to culture time.

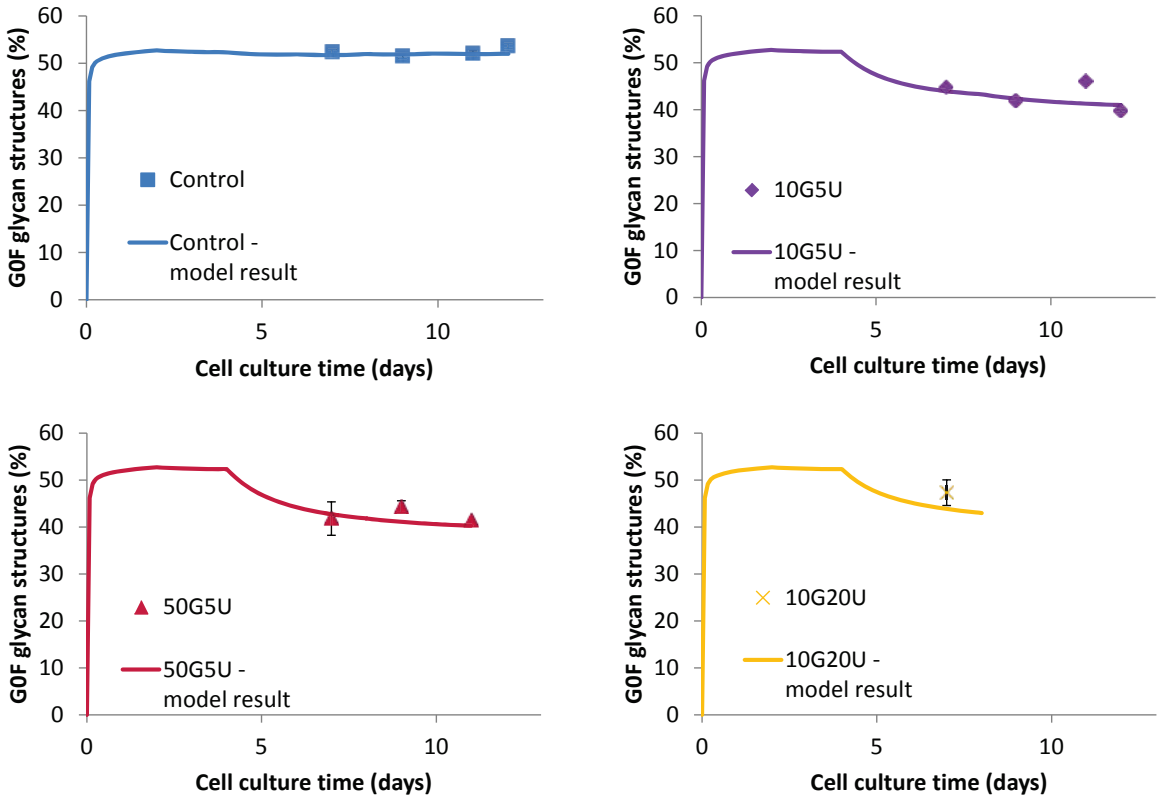
For the afucosylated and agalactosylated species G0, mixed model outputs were achieved (figure 7.35a-e). An under-prediction can be observed especially for the control and 10G5U cultures, while better fits are achieved for the 50G5U and 10G20U cultures. The under-estimation is explained by the model predicting further processing of G0 to form the afucosylated G1 glycan species, which was not experimentally observed. Bearing in mind the experimental observations of the afucosylated G2 species, a limited amount of its precursor, the glycan G1, is expected to be found in the antibody product glycoform. The

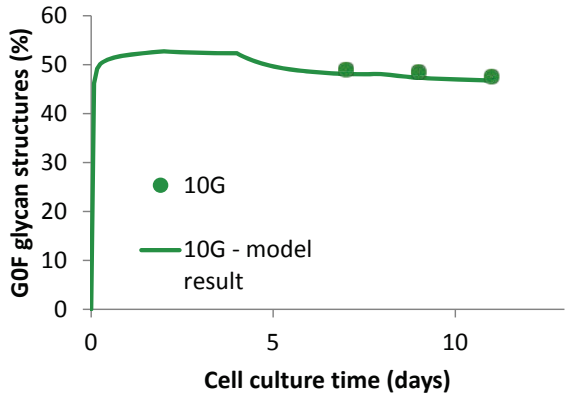
formation of G1 structures by the glycan model leads necessarily to under-predictions for one or a number of the remaining glycans species. Despite this shortcoming, the model is able to produce a good quantitative trend for all species, where a decrease in G0 is observed as result of uridine and/or galactose addition. This is particularly pronounced for the 50G5U culture condition, where also the lowest experimental abundance of G0 was observed. Good model outputs are achieved for the outputs of G0F, which is the most abundant glycan species of the antibody product (figure 7.36a-e). The profiles of G0F resemble those of G1F closely, where the control is not seen to change much during the duration of the cell culture and the most pronounced decrease is again observed in the 50G5U cultures.





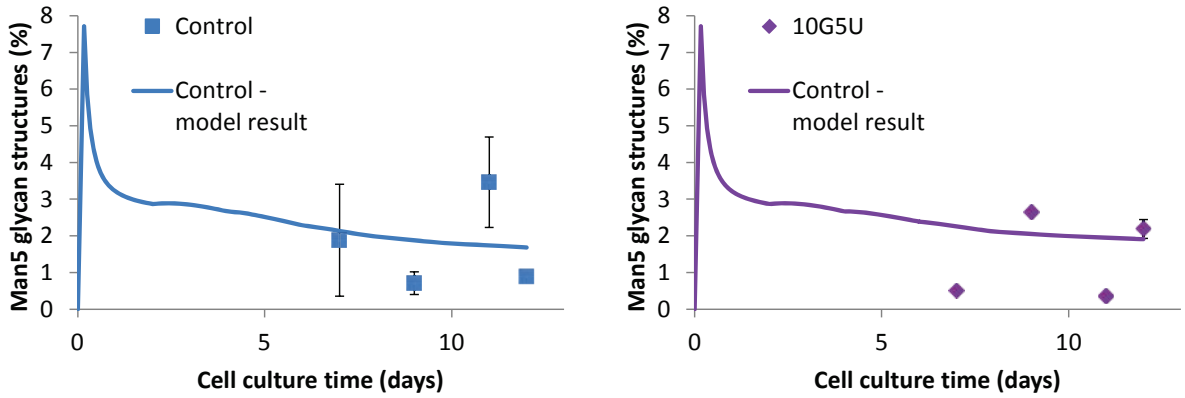
Figures 7.35a-e Experimental data (markers) and computational outputs (lines) of G0 glycan abundance with respect to culture time.

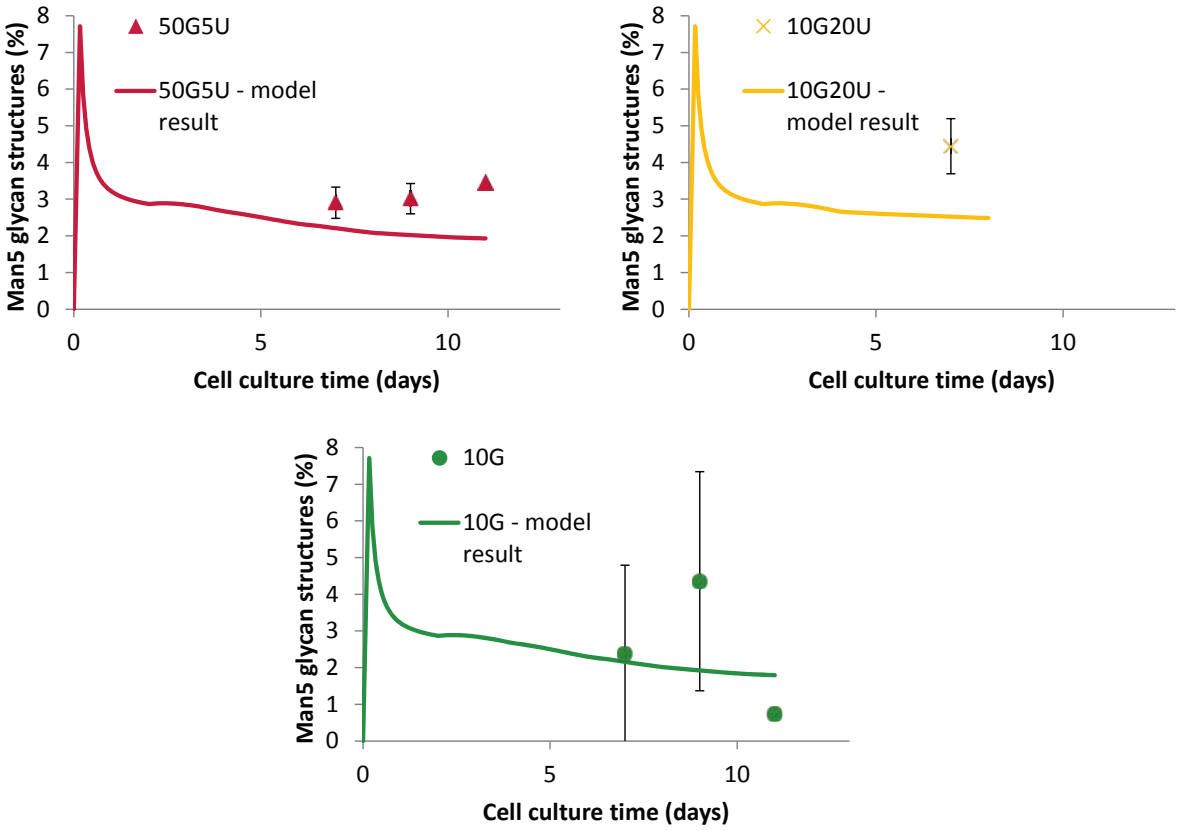




Figures 7.36a-e Experimental data (markers) and computational outputs (lines) of G0F glycan abundance with respect to culture time.

Lastly, significant amounts of the high mannose structure Man5 were observed experimentally and formed a further dataset for model training (figure 7.37a-e). Due to a low abundance of the Man5 species, large uncertainties in experimental data were observed and hence, a fair comparison against model outputs becomes difficult. The model output for the abundance of Man5 structures shows little variation between feed conditions. The highest abundance is observed for the 10G20U condition. Under this feeding regime reduced antibody production was observed after feed addition. Combined with a proportionally large production of Man5 structures during the early culture stages, the higher Man5 abundance can be explained.





Figures 7.37a-e Experimental data (markers) and computational outputs (lines) of Man5 glycan abundance.

Overall, the glycan model was able to reproduce the experimentally observed glycoform very well. This is especially true for the galactosylated species, which were of particular importance. These outputs are able to build confidence in the overall model platform structure and show that the effects of galactose and uridine feed addition to the culture media was able to propagate through all model parts and produce a substantial impact on the overall model output, i.e. the glycoform.

7.7. *In silico* feeding strategy optimisation

The model platform and the parameters estimated to produce the above model outputs were used to design an optimal *in silico* feeding strategy with respect to product galactosylation. The dynamic feeding strategy was optimised for titer galactosylation, as discussed in section 7.5, and galactose and uridine feed concentrations were used as input

variables. Feeding was assumed to take place together with Feed C® additions on all even culture days. The galactose feed additions to cell culture media, as a concentration in total culture volume, are shown in figure 7.38. Concentrations were allowed to vary from 0 mM to 50 mM in total culture volume. The model output suggests no feed addition on day 2 of culture with subsequent additions ranging between 6.53 mM and 9.30 mM in total culture media on days 4 and day 6 of culture, respectively. Uridine additions were allowed to vary between 0 mM and a maximum of 10 mM. A lower uridine concentration was used, as the high concentration of 20 mM appeared to have led to a metabolic shift, which was partially not reproduced by the model structure. However, the high concentration also led to growth inhibition and was hence, well outside an optimal range such that a lower upper bound of 10 mM was not expected to restrict optimisation. The optimised uridine additions suggest no feeding on day 2 of culture and subsequent additions ranging from 0.76 mM to 10 mM in total culture media on days 4 and 10, respectively (figure 7.39). The output suggests no feeding of either galactose or uridine on day 2 of culture. This suggests that the benefit of increased galactosylation at the early culture stage is outweighed by the negative impact on cell growth during the early exponential phase. Subsequently, the uridine additions are increased stepwise, while galactose feed additions don't vary strongly between culture days. This suggests that the model predicts little inhibitory effect on cell culture growth by galactose in the presence of small amounts of uridine during mid to late exponential culture growth phase. Lastly, the output suggests the maximum permissible addition of 10 mM uridine on day 10, the final feeding day corresponding to late stationary phase. The high uridine feed may be explained by little impact through inhibited growth at this culture stage and the benefit of high galactosylation of antibody product outweighing the impact on viable cell density.

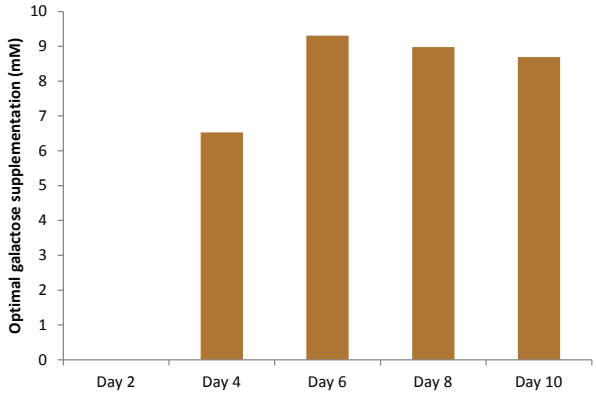


Figure 7.38 optimised galactose feed additions, in total culture volume, for all feeding days starting on day 2 of culture. The output concentrations of $[Gal]_{feed,day2}$ = 0 mM, $[Gal]_{feed,day4}$ = 6.53 mM, $[Gal]_{feed,day6}$ = 9.30 mM, $[Gal]_{feed,day8}$ = 8.98 mM and $[Gal]_{feed,day10}$ = 8.69 mM,

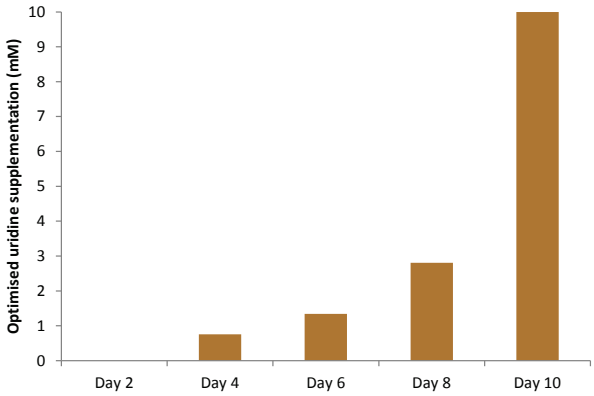


Figure 7.39 optimised uridine feed additions, in total culture volume, for all feeding days starting on day 2 of culture. The output concentrations of $[Urd]_{feed,day2}$ = 0 mM, $[Urd]_{feed,day4}$ = 0.76 mM, $[Urd]_{feed,day6}$ = 1.34 mM, $[Urd]_{feed,day8}$ = 2.81 mM and $[Urd]_{feed,day10}$ = 10 mM

A comparison of titer galactosylation, as defined in equation 7.15, of the control output against the optimised model output shows a large increase in galactosylation (figure 7.40). As expected the two profiles diverge on day 4, when the first pulse feeding of galactose and uridine is made. Decreases in the profile are observed resulting from media dilution on Feed C® feeding days. An overall increase in titer galactosylation of 46.9% is predicted by the optimised feeding strategy on the final day of culture, as compared to the control cultures. This is a further increase over the previously highest *in silico* titer galactosylation of the 10G5U feed condition, where an increase of 34.2% over the control was achieved.

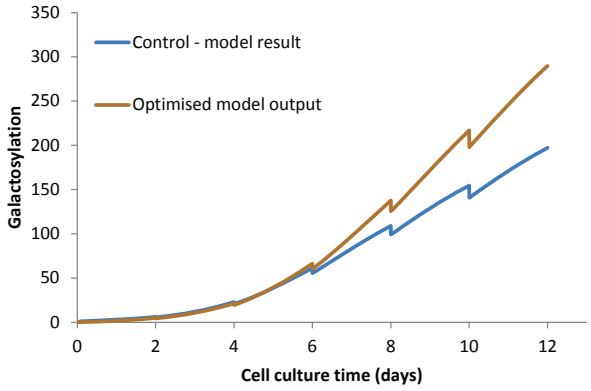


Figure 7.40 Comparison of galactosylation, as defined by expression 7.15, with respect to culture time for the control and the optimised feed outputs.

Furthermore, viable cell density and intracellular UDP-Gal concentrations are compared for the optimised strategy and the control cultures (figures 7.41 & 7.42). The viable cell densities start to diverge slowly from day 6 of culture with more pronounced changes occurring after the last feed addition on day 10. As previously discussed, initial uridine and to a lesser extent galactose feed additions are kept low for the earlier supplementations to ensure little impact on growth during the exponential growth phase. The noticeable decrease in cell density at the end of the optimised culture appears to be caused by the final uridine feed at the high 10 mM uridine concentration. The various feed additions are also reflected in intracellular UDP-Gal concentrations, where a stepwise increase can be observed after each feed addition, as compared to the control culture. As with the viable cell density initial impacts are limited due to lower additions of uridine. The initial profile resembles those of the 10G5U and 50G5U conditions, where stepwise increases are observed. However, an accumulation can be observed at the end of the culture after the 10 mM uridine addition, which resembles the accumulated encountered in the 10G20U culture. The final UDP-Gal concentration approaches 3 mM intracellularly, which is in line with the experimentally observed maxima in chapter 6 for the uridine supplemented cultures (figure 6.26). Hence, the UDP-Gal profile appears physiologically attainable.

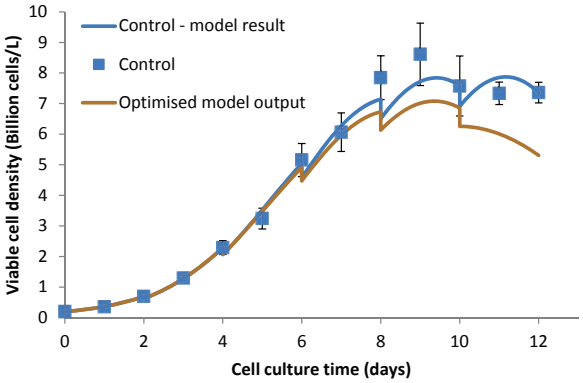


Figure 7.41 viable cell density as predicted for the optimal feed condition with respect to time compared to experimental control results and computational outputs.

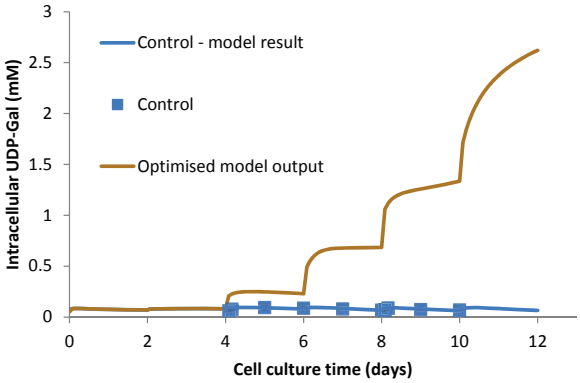


Figure 7.42 intracellular UDP-Gal concentrations as predicted for the optimal feed condition with respect to time compared to experimental control results and computational outputs.

7.8. Conclusion

In this chapter the model framework presented in chapter 5 was expanded and refined further to improve the accuracy of the individual model components of the framework. Furthermore, the experimental data obtained in chapter 6 was used to include the effects of galactose and uridine addition to the culture media and capture their effects on cell growth and cell metabolism *in silico.* Based on this structural changes were made to individual parts of the framework and the model was trained further to obtain a single set of parameters to reproduce the experimental data for all feed conditions. This set of parameters was able to achieve satisfactory results for the whole model framework and created a calibrated operating space with respect to galactose and uridine feed additions for the subsequent optimisation. The dynamic *in silico* optimisation of dynamic galactose and uridine additions to cell culture media was able to produce a strategy with 4 pulse additions of varying feed concentrations projecting a 46.9% increase in final day galactosylation.

The cell culture dynamics model was able to perform well with respect to most outputs including the newly added galactose and uridine species. The only exceptions to this were the glutamine and glutamate species, which showed deviation from experimental data at the late culture stage. This may be the result of a metabolic shift occurring during the stationary phase and is not captured in the model structure. To gain greater understanding and improve the model experiments can be carried out with varying degrees of glutamate and glutamine concentrations at saturating and limiting conditions. This would allow elucidating species dependence and whether such a metabolic shift with respect to these species does in fact occur.

The nucleotide model was able to perform well with respect to the key nucleotide species required to run a successful optimisation. However, the model consistently performed less accurately with respect to the 10G20U outputs. It was proposed that a metabolic shift occurs at high uridine concentrations leading to cell growth inhibition, which in turn impacts nucleotide synthesis strongly. The model is not able to account for such shifts in metabolism and may require a second switch based set of parameters similar to the

strategy used in chapter 5. Furthermore, the nucleotide model is constrained by growth dependent outlet terms and does not account for maintenance type species consumption. However, constraining and determining the magnitude of the outlet terms experimentally can be quite challenging, as it requires the tracing of specific metabolites and would require flux datasets for various stages of cell culture. Furthermore, an adaptation phase was observed for ADP and AMP concentrations for the first few culture days. Modelling of cell adaptation is proving to be a challenging research field, where no simple and universal solution has yet been established for mammalian cell culture. An experimental setup, where culture media or culture conditions are changed during cell culture, may be able to provide a starting point for further modelling efforts. However, both of the proposed experimental investigations are hardly warranted due to difficult experimental setups or uncertain experimentation outcomes for improvements in performance. Any improvements made to the model would be for the undesirable 10G20U feed condition and ADP and AMP, which are of lesser importance to the overall model structure.

The NSD model performed very well overall. However, shortcomings were found for the UDP-Gal concentrations under the 10G condition and for UDP-Glc for the 50G5U condition. While it might be difficult to identify the problem leading to these difficulties, a carefully designed set of experiments may be able to shed light on the possible causes. One of these may be changes in enzyme expression rates as a function of galactose feed addition to allow the cells to adapt to the additional carbon source. Obvious targets are the enzyme concentrations of the Leloir pathway. While directly measuring enzyme concentrations can be experimentally challenging, mRNA levels can be determined more easily and may give information to changes in enzyme expression rates by the cells. The same strategy can also be employed to key enzymes of the UDP-HexNAc synthesis pathway, where the model was not able to estimate the extent of accumulation under the uridine fed conditions. However, further accuracy may also be achieved by modelling the rate limiting steps r3a using intracellular glutamine data, which has been suggested to correlate to UDP-HexNAc concentrations in chapter 4.

The last part of the model framework, the glycan model by del Val, has been able to perform very well. Minor under-predictions were observed for the G0 species, which was

consumed by the model to produce G1 and eventually G2 glycan species. However, experimentally G1 was not observed and hence, resulting in under-prediction of the G0 species. A higher fidelity glycan detection method may be able to provide a more accurate picture of the abundance of these species, as well as some of the other species of low abundance, such as Man5. However, the above did not impact the fits for the dominant galactosylated glycan species G1F and G2F, which formed the basis of the optimisation.

Lastly, the optimisation was able to produce a dynamic feeding strategy that is predicted to improve titer galactosylation by 46.9% over the control culture. This is predicted to be higher than any of the tested conditions of chapter 6. Experimental verification of this result is required for further validation of the model and the optimisation output. Model accuracy can be compared against predicted viable cell densities, UDP-Gal concentrations. However, many other measures can be used for model validation, such as individual glycan species outputs or computational versus experimental consumption of extracellular galactose and uridine. While all the model predictions appear within physiologically attainable boundaries, limitations in model accuracy may be expected. As was discovered in chapter 6, high uridine and galactose levels were detrimental to product galactosylation. Detrimental effects were most strongly observed at the high uridine and galactose concentrations of 20 mM and 50 mM, respectively. The optimised pulse additions are all below these concentrations, however, the cumulative effect of a number of smaller additions may become significant at the end of culture. This is especially the case for uridine, where the final uridine addition is closest to approaching the detrimental concentrations. The effects of high uridine concentrations on the glycosylation reaction steps of Golgi are not taken into account by the model structure. This may lead to limitations by the model and consequently, limit the benefits of the optimised feeding strategy at the late culture stage. Furthermore, transport of NSD species from the cytosol to the Golgi was assumed not to be limiting. However, this may become a bottleneck at the much increased UDP-Gal concentrations proposed as part of this feeding strategy. Hence, the model may predict further benefits to galactosylation resulting from increased UDP-Gal pools, where there are physiological limitations.

The final output of this chapter and hence this thesis is a model platform that was calibrated and applied in a galactosylation case study. The optimisation criteria can be

modified further to add addition constraints. These could include maintaining cell viability above a designated threshold value or limiting the maximum extracellular or intracellular species concentrations impacted by galactose or uridine feed addition. It was demonstrated that the model platform is a holistic tool for quantitative analysis and steering of the glycoform through feeding strategies and thus, bridging the gap from the extracellular environment to product glycoform. This presents a novel and exciting tool in line with the QbD approach allowing planning for product quality at the design stage. As was demonstrated in this thesis the model was able to be trained and applied to a case study based on a reasonable number of experiments. It is expected that adaptation to further cell lines will be streamlined through the refinements made to the model structure as part of the model platform development in this chapter and chapter 5. The application of this framework to hybridoma and CHO cells has been demonstrated as part of this thesis and hence, successful adaptation of the model framework to further cell lines is expected to be achievable.

Chapter 8

Final Conclusions and Future Work

8.1. Project summary

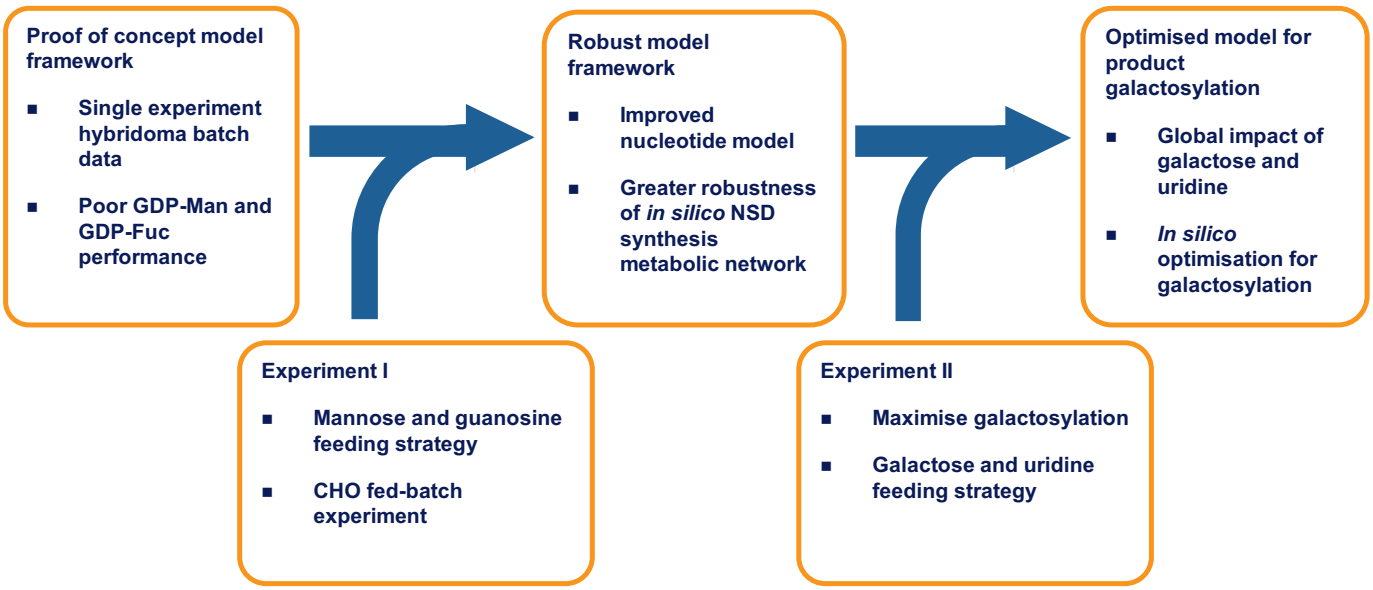


Figure 8.1 A graphic representation of the thesis chronology, where each box represents one of the result chapters (chapters 3 to 7 from left to right) and their contribution towards the final thesis output.

The work presented in this thesis culminated in a modelling platform linking the extracellular environment to antibody glycosylation. This calibrated tool was then used for the *in silico* design of a dynamic feeding strategy to maximise antibody product galactosylation, while maintaining high product titer. This constitutes a new and unique contribution to the literature, as was reviewed in chapter 1 and discussed in section 1.10. While the topic of glycosylation is an area of ongoing fundamental research, much is already

known about the mechanisms of glycosylation and the factors impacting it. This enabled previously the creation of a number of mathematical models describing the glycosylation process, as discussed in section 1.9. Of these the del Val model is the most accurate, with respect to therapeutic antibody glycosylation, and provided a starting point, on which this thesis was able to build further (del Val et al., 2011). A modelling platform was designed with the aim of providing a holistic approach towards optimising process conditions to control the product glycoform. The framework comprises a modified adaptation of the established Monod kinetics approach to model cell culture dynamics and makes use of mass balances to recreate the nucleotide and NSD *de novo* synthesis metabolic networks. While both the nucleotide and NSD model draw on knowledge of the reaction network to establish the model structure, the NSD model incorporated the full mechanistic knowledge available. The sum of the four model parts amounts to a proof-of-concept platform, which was able to link the extracellular environment, via intracellular metabolites to the antibody product glycoform.

As discussed in section 1.6, various studies investigated and established the effect of hexose and nucleotide precursors feeding on the glycosylation process. This work was able to build on existing knowledge of feeding strategies, to partially drive the glycosylation process (section 1.6.2). Utilising this knowledge enabled the design of dynamic feeding strategy experiments, in order to perturb specific branches of the NSD *de novo* synthesis network to maximise dynamic knowledge of reaction kinetics, control mechanisms and system behaviour. In a two-step approach a calibrated model with respect to uridine and galactose feeding strategies was established for a GS-CHO cell line. Firstly, a novel guanosine and mannose feeding experiment was designed to elucidate the synthesis of GDP-Fuc and GDP-Man further and hence, improve NSD model accuracy. Secondly, an experiment was designed to investigate the effect of galactose and uridine on product galactosylation as well as cell culture dynamics. The experimental data enabled a final iteration of the individual model structures and additional data set for parameter estimation. This resulted in a calibrated model platform with respect to product galactosylation enhancement through galactose, uridine and manganese precursor feeding. This platform was finally able to produce an optimal dynamic feeding strategy *in silico* with a predicted increase in galactosylation of 46.9% through an addition of four feed pulse additions on days

4, 6, 8 and 10 of culture. This presence a further improvement of galactosylation over experimental data presented in chapter 6.

8.2. Overall thesis achievements

The achievements realised in this project can be separated into those of an experimental and computational nature. Each of the achievements listed and discussed below describes the novel contributions of the individual aspects of this thesis.

8.2.1. Experimental achievements

- Dynamic effects of mannose and guanosine additions to cell culture media – The experiment, as presented in chapter 4, represent a novel feeding strategy. The results showed that low concentrations of extracellular guanosine are readily utilised by the cells. However, despite depletion within 24h of supplementation, an irreversible cell growth inhibition was observed at both guanosine concentrations that were investigated. The experiment was also able to produce dynamic concentration profiles for intracellular GTP, GDP-Fuc and GDP-Man. Lastly, the effects propagated to show a large proportion of Man5 glycan structures, which increased further with culture time. However, the findings are of no direct application to antibody manufacture, due to cell growth inhibition resulting from guanosine addition to cell culture.

- Dynamic effects of galactose, uridine and manganese(II) additions to cell culture media – The design of experiment, as presented in chapter 6, builds on previous feeding strategy experiments, that are summarised in section 1.6.2. However, a novelty is found in the dynamic pulse feeding and the collection of dynamic cell response data. A novel finding was the observation of reduced toxicity at moderate galactose and uridine levels, as opposed to moderate levels of galactose, only. Furthermore, a slow consumption of extracellular uridine was observed and a quick uptake of galactose was observed. The dynamic intracellular concentration profiles for UTP, UDP-Gal, UDP-Glc and the other NSD species reveal the dynamic response to pulse feeding during exponential and late

exponential/early stationary growth phase. Lastly, dynamic profiles of the product glycoform were captured.

8.2.2. Computational achievements

- Modified Monod kinetics cell dynamics model – While the model is based on established Monod kinetics, it presents a novelty by accounting for the effects of the various feeding strategies on the cell culture. The additions of the hexoses and nucleotide precursors are reflected in the model structure, such that consumption of the species, the effect on other metabolites as well as cell growth, is accounted for. Importantly, with respect to the experimental findings of chapter 5, the model accounts for synergetic interaction of galactose and uridine feed additions.

- Nucleotide model – A novel nucleotide model has been developed as part of this work and is able to reproduce the intracellular concentrations of nucleotide triphosphates ATP, CTP, GTP and UTP as well as those of ADP and AMP. The model structure was based on known reaction network structures, although simplified. In an iterative top-down approach, the model structure and reaction mechanisms were revised and improved, as further knowledge emerged from the feeding experiments.

- Nucleotide sugar donor model – A novel NSD *de novo* synthesis model was constructed as part of this thesis. The fully mechanistic *in silico* representation of the reaction network forms one of the major contributions of the work presented in this thesis. Available biological knowledge was utilised to derive individual reaction mechanism and experimental literature data was used, where available. This bottom-up reconstruction of the network comprises 34 species, represented as individual mass balances, and linked through a total of 60 reaction steps. The model is able to reproduce dynamic concentration profiles of all experimentally determined NSD species in the CHO cell experiments. In an iterative approach the experimental data obtained in chapters 4 and 6 was used to further refine the model structure and improve estimated parameter values, resulting in greater model accuracy. A global sensitivity analysis was able to highlight

parameters with significant impact on model outputs and reduce the number of parameters to be estimated.

- Model platform – The above model parts together with the previously developed del Val model were linked together to form a novel modular modelling platform that is able to link the extracellular environment to product glycoform. The individual modules are interlinked by means of extracellular and intracellular species fluxes, as well as cell growth rate and antibody titer. An initial proof-of-concept model platform was developed based on hybridoma cells. Based on the experimental data presented here, the platform was readily translated to a GS-CHO cell production platform. This suggests sufficient flexibility within the framework, allowing for translation to other production platforms.

- Optimised dynamic feeding strategy – The final cumulative outcome of the work presented is an optimised dynamic feeding strategy with respect to product galactosylation. The calibrated model platform was able to suggest a strategy for the optimal feeding on all even culture days, starting on day 4 of culture. The optimisation takes into account the product titer, as well as the abundance of galactose bearing glycan species to maximise the product of both. The model produced outputs for viable cell densities and the key metabolite UDP-Gal, which compare well with experimental data obtained in chapter 6. Hence, the predicted increase of 46.9% over the control culture presents an achievable outcome.

While each of the above represents a novel aspect of the work presented here, the model platform is thought to be the most significant advancement. The importance of glycosylation with respect to product safety and efficacy of biotherapeutics is extensively discussed and illustrated in chapter 1.4. Consequently, exerting control over the glycoform of biotherapeutic antibodies becomes a desirable goal. The model platform provides a novel tool to produce a feeding strategy to achieve this goal. While most previous efforts of glycan control focused on qualitative control, this modelling platform represents a qualitative method of glycan control. The mathematical models presented in section 1.9 focused on an *in silico* reproduction of the glycosylation process by various means, but were not able to

provide a bridge to the extracellular environment, a gap which this model platform addresses. An exception to this was the statistical model developed by Grainger and James based on a series of experiments, also exploring galactose, uridine and manganese additions to cell culture media (Grainger and James, 2013). While, this investigation offered excellent insight into the effects of feeding strategies on product galactosylation, the statistical approach is limited to feeding on the culture seeding day, only. As suggested by the optimisation output in chapter 7, early stage feed additions are not optimal with respect to final day product galactosylation. The work presented in this thesis was able to build on the knowledge of Grainger and James and utilise mechanistic knowledge to develop a strategy for dynamic optimisation. Dynamic pulse feeding enables much greater control over the feeding to improve final day galactosylation further. Moreover, the platform was shown to be easily translatable to other cell lines and culture modes due to its modular nature. This is helped by the mechanistic nature, which allows for rational guidance in design of experiment to maximise experimental output and reduce number of experiments. This is very much in line with the QbD approach under which up-front experimentation and in depth knowledge of the process is required to rationally design process conditions and include product quality at the design stage. The application of the model was demonstrated in chapter 7, where an optimal feeding strategy was designed to maximise product galactosylation. However, it is argued that the usefulness of the model goes beyond feeding strategy optimisation for galactosylation as discussed below.

8.3. Future work and application

The model platform, which is presented in this thesis provides a holistic approach towards the quantitative control of glycosylation and the author argues, that much practical application can be found, which is listed and discussed below

- Validation experiment – Firstly, and foremost an experimental validation of optimised feeding strategy is required. An experimental comparison of a suitable control and the optimised feeding strategy, as presented in chapter 7, will be able to confirm *in silico* observations and give greater certainty in the model outputs and capability.

- Translation to other cell lines – The framework was able to translate well from a hybridoma to a GS-CHO cell line. However, to demonstrate applicability across a range of production platforms, a translation to other CHO cell lines is desirable. These could include other CHO cell types or cell lines expressing a different recombinant glycoprotein product. Translation to other cell lines requires specific cell line dependent experimental data. Further experimental work involving other cell lines is required to find a general design of experiment for easy translation and application of the framework to other cell systems. The experimental work presented in chapters 4 and 6 presents a framework for future experimentation with respect to the experimental setup and the number of experiments to be conducted for sufficient model training data.

- Further feeding strategies – While the application of the model was demonstrated for the case of product galactosylation, the mechanistic model structures allows for a shift in focus onto other glycan characteristics. Other desired glycan structures may include increased glycan antennarity and/or sialylation, which may be achieved by an increase in UDP-GlcNAc and/or CMP-Neu5Ac species abundance. While, the model is currently able to capture the UDP-GlcNAc and CMP-Neu5Ac concentrations well, further experiments may be required for greater model accuracy.

- Interaction of hexose and nucleotide precursors – As discussed in chapter 1.6, glycan control with respect to certain glycan characteristics, such as product sialylation, requires the feeding of more than a single hexose and nucleotide precursor. This raises the need to account for interactions between different hexoses and nucleotide precursors. This may include interference in the uptake of different hexoses or possible synergetic effects encountered by the addition of multiple nucleotide species precursors. Investigation of these effects and inclusion into the model framework requires further carefully designed experimentation. With respect to sialylation this would require feeding of the uridine as well as galactose and ManNAc to investigate the effect of the two additional sugars on each other's respective metabolism.

- Enzyme concentration measurements – A global sensitivity analysis (GSA) was performed as part of the model development described in chapter 3. The GSA was not

only able to reduce the number of parameters to be estimated but also highlighted enzyme concentrations with significant impact on the model output. Based on the above, experiments can be designed to determine dynamic enzyme concentrations, which are expected to vary within the space of a cell culture experiment (Wong et al., 2010a). This would allow abolishing the assumption of constant enzyme concentrations with respect to key reaction steps and hence, include further mechanistic detail and improve model accuracy.

- *In silico* cell line engineering – The mechanistic nature of the NSD model provides an excellent opportunity for the study of the effect of cell line engineering on product glycosylation. In combination with a GSA of the entire model framework, a calibrated model may be used to identify reaction/transport steps with significant impact on specific model outputs and consequently, flag up bottlenecks. While computationally very expensive, this strategy may be able to allow for quantitative *in silico* experimentation. A framework with known and ranked bottlenecks would allow for a series of in silico experiments to remove the identified bottlenecks step by step. This would provide a very powerful tool to guide cell line engineering and bypass lengthy exploratory experimental work. Targets for cell line engineering may include overexpression or knock down of various enzymes of the NSD metabolic pathway or the glycosyltransferases of the Golgi apparatus.

- Model reduction – Lastly, the GSA and its insight into key reaction steps opens up the door for a reduction of the NSD model. A heuristic model reduction approach may be used, where reactions of no significant impact, with respect to model outputs, are removed. While, this may produce a more manageable model structure, it may also lead to local solutions, which would be not universally applicable to all model applications. Hence different reduced model structures may be required to account for different feeding strategies or other model applications.

- Control System – The model framework presented here may also be adapted as a control system to maintain or control the glycoform during cell culture campaigns. Due to the long running times of cell cultures and infrequent additions of supplements to cell

culture media, the complexity of the model and the lengthy computations incurred, do not pose an obstacle in its implementation. To enable a practical application of this kind, high data density and ongoing parameters estimations/corrections based on online cell culture data, become necessary. High throughput experimental methodologies exist to take experimental measurements akin to the data presented in chapters 4 & 6. Together with sufficient computational power parameter corrections and optimisation can be performed within the feeding intervals, i.e. a time period of 48 hours.

Overall the work presented has been able to address the objectives outlined in chapter 1.10 and provide a novel contribution towards steering the glycoform of biotherapeutics in line with the QbD paradigm. The model provides much scope for further model extension for a wide range of model application. This is believed to ultimately lead to improvements in the manufacture of biotherapeutics to provide a safer, more efficacious and cheaper product for the patient.

List of Publications

Journal Papers

1. Jedrzejewski P. M., del Val I. J., Constantinou A., Dell A., Haslam S. M. , Polizzi K. M., and Kontoravdi C. 2014. Towards controlling the glycoform: a model framework linking extracellular metabolites to antibody glycosylation. *International Journal of Molecular Sciences.* 15, 4492-522

2. Jedrzejewski P. M., del Val I. J., Polizzi K. M., and Kontoravdi C. 2013. Applying Quality by Design (QbD) to Glycoprotein Therapeutics: Experimental and Computational Efforts towards Glycoform Control. *Pharmaceutical Bioprocessing,* 1, 51-69

Book Chapters

1. del Val I. J., Jedrzejewski P. M., Exley K., Sou S. N., Kyriakopoulos S., Polizzi K. M., and Kontoravdi C. 2012 Application of Quality by Design Paradigm to the Manufacture of Protein Therapeutics. in Glycosylation, S. Petrescu, (Ed.), *InTech*. ISBN *978-953-51-0771-2*

List of Abstracts

1. Jedrzejewski P. M., Polizzi K. M., Kontoravdi C. 2015. An improved model framework linking the extracellular environment to antibody glycosylation. *24th ESACT Meeting Proceedings, 2015*

2. Jedrzejewski P. M., del Val I. J., Constantinou A., Dell A., Haslam S. M. , Polizzi K. M., and Kontoravdi C. 2014. Towards Controlling the Glycoform: Bridging the Gap from the Extracellular Environment to Antibody Glycosylation. *Annual Meeting of the AIChE, 2014*

Bibliography

ABEL, C. A., SPIEGELBERG, H. L., AND GREY, H. M. 1968. The carbohydrate content of fragments and polypeptide chains of human >G-myeloma protein of different heavy chain subclasses. *Biochemistry and Cell Biology-Biochimie Et Biologie Cellulaire,* 7**,** 1271-1278.

AGGARWAL, S. 2011. What's fueling the Biotech Engine - 2010 to 2011. Nature Biotechnology.

ALLEN, A. C., HARPER, S. J. & FEEHALLY, J. 1995. Galactosylation of N-Linked and O-Linked Carbohydrate Moieties of Iga1 and Igg in Iga Nephropathy. *Clinical and Experimental Immunology,* 100**,** 470-474.

ALTAMIRANO, C., CAIRO, J. J. & GODIA, F. 2001. Decoupling cell growth and product formation in Chinese hamster ovary cells through metabolic control. *Biotechnology and Bioengineering,* 76**,** 351-360.

ALTAMIRANO, C., PAREDES, C., ILLANES, A., CAIRO, J. J. & GODIA, F. 2004. Strategies for fed-batch cultivation of t-PA producing CHO cells: substitution of glucose and glutamine and rational design of culture medium. *Journal of Biotechnology,* 110**,** 171-179.

ANGATA, T. & VARKI, A. 2002. Chemical diversity in the sialic acids and related alpha-keto acids: An evolutionary perspective. *Chemical Reviews,* 102**,** 439-469.

ANTHONY, R. M., NIMMERJAHN, F., ASHLINE, D. J., REINHOLD, V. N., PAULSON, J. C. & RAVETCH, J. V. 2008. Recapitulation of IVIG anti-inflammatory activity with a recombinant IgG fc. *Science,* 320**,** 373-376.

ANTONIEWICZ, M. R. 2013. Dynamic metabolic flux analysis - tools for probing transient states of metabolic networks. *Current Opinion in Biotechnology,* 24**,** 973-978.

APWEILER, R., HERMJAKOB, H. & SHARON, N. 1999. On the frequency of protein glycosylation, as deduced from analysis of the SWISS-PROT database. *Biochimica Et Biophysica Acta-General Subjects,* 1473**,** 4-8.

ARONOW, B. & ULLMAN, B. 1987. Insitu Regulation of Mammalian Ctp Synthetase by Allosteric Inhibition. *Journal of Biological Chemistry,* 262**,** 5106-5112.

BAILEY, J. E. 1998. Mathematical modeling and analysis in biochemical engineering: Past accomplishments and future opportunities. *Biotechnology Progress,* 14**,** 8-20.

BAKER, K. N., RENDALL, M. H., HILLS, A. E., HOARE, M., FREEDMAN, R. B. & JAMES, D. C. 2001. Metabolic control of recombinant protein N-glycan processing in NS0 and CHO cells. *Biotechnology and Bioengineering,* 73**,** 188-202.

BALAQUER, E. & NEUSUSS, C. 2006. Intact glycoform characterization of erythropoietin-alpha and erythropoietin-beta by CZE-ESI-TOF-MS. *Chromatographia,* 64**,** 351-357.

BATT, B. C. & KOMPALA, D. S. 1989. A Structured Kinetic Modeling Framework for the Dynamics of Hybridoma Growth and Monoclonal-Antibody Production in Continuous Suspension-Cultures. *Biotechnology and Bioengineering,* 34**,** 515-531.

BAYCIN-HIZAL, D., TABB, D. L., CHAERKADY, R., CHEN, L., LEWIS, N. E., NAGARAJAN, H., SARKARIA, V., KUMAR, A., WOLOZNY, D., COLAO, J., JACOBSON, E., TIAN, Y., O'MEALLY, R. N., KRAG, S. S., COLE, R. N., PALSSON, B. O., ZHANG, H. & BETENBAUGH, M. 2012. Proteomic Analysis of Chinese Hamster Ovary Cells. *Journal of Proteome Research,* 11**,** 5265-5276.

BECK, A., SANGLIER-CIANFERANI, S. & VAN DORSSELAER, A. 2012. Biosimilar, biobetter, and next generation antibody characterization by mass spectrometry. *Anal Chem,* 84**,** 4637-46.

BERRIOS, J., ALTAMIRANO, C., OSSES, N. & GONZALEZ, R. 2011. Continuous CHO cell cultures with improved recombinant protein productivity by using mannose as carbon source: Metabolic analysis and scale-up simulation. *Chemical Engineering Science,* 66**,** 2431-2439.

BISSO, A., STURLA, L., ZANARDI, D., DE FLORA, A. & TONETTI, M. 1999. Structural and enzymatic characterization of human recombinant GDP-D-mannose-4,6-dehydratase. *Febs Letters,* 456**,** 370-374.

BONARIUS, H. P. J., HATZIMANIKATIS, V., MEESTERS, K. P. H., DEGOOIJER, C. D., SCHMID, G. & TRAMPER, J. 1996. Metabolic flux analysis of hybridoma cells in different culture media using mass balances. *Biotechnology and Bioengineering,* 50**,** 299-318.

BORYS, M. C., LINZER, D. I. H. & PAPOUTSAKIS, E. T. 1994. AMMONIA AFFECTS THE GLYCOSYLATION PATTERNS OF RECOMBINANT MOUSE PLACENTAL LACTOGEN-1 BY CHINESE-HAMSTER OVARY CELLS IN A PH-DEPENDENT MANNER. *Biotechnology and Bioengineering,* 43**,** 505-514.

BOSQUES, C. J., COLLINS, B. E., MEADOR, J. W., SARVAIYA, H., MURPHY, J. L., DELLORUSSO, G., BULIK, D. A., HSU, I. H., WASHBURN, N., SIPSEY, S. F.,

MYETTE, J. R., RAMAN, R., SHRIVER, Z., SASISEKHARAN, R. & VENKATARAMAN, G. 2011. Chinese hamster ovary cells can produce galactose-alpha-1, 3-galactose antigens on proteins (vol 28, pg 1153, 2010). *Nature Biotechnology,* 29**,** 459-459.

BOYD, P. N., LINES, A. C. & PATEL, A. K. 1995. The effect of the removal of sialic acid, galactose and total carbohydrate on the functional activity of Campath-1H. *Molecular Immunology,* 32**,** 1311-1318.

BRENDA. 2015. *BRENDA (BRaunschweig ENzyme DAtabase)* [Online]. Available: http://www.brenda-enzymes.info/ [Accessed January 2015.

BRINKS, V., HAWE, A., BASMELEH, A. H., JOACHIN-RODRIGUEZ, L., HASELBERG, R., SOMSEN, G. W., JISKOOT, W. & SCHELLEKENS, H. 2011a. Quality of original and biosimilar epoetin products. *Pharm Res,* 28**,** 386-93.

BRINKS, V., HAWE, A., BASMELEH, A. H. H., JOACHIN-RODRIGUEZ, L., HASELBERG, R., SOMSEN, G. W., JISKOOT, W. & SCHELLEKENS, H. 2011b. Quality of Original and Biosimilar Epoetin Products. *Pharmaceutical Research,* 28**,** 386-393.

BROWNE, J. K., COHEN, A. M., EGRIE, J. C., LAI, P. H., LIN, F. K., STRICKLAND, T., WATSON, E. & STEBBING, N. 1986. Erythropoietin - Gene Cloning, Protein-Structure, and Biological Properties. *Cold Spring Harbor Symposia on Quantitative Biology,* 51**,** 693-702.

BURLEIGH, S. C., VAN DE LAAR, T., STROOP, C. J. M., VAN GRUNSVEN, W. M. J., O'DONOGHUE, N., RUDD, P. M. & DAVEY, G. P. 2011. Synergizing metabolic flux analysis and nucleotide sugar metabolism to understand the control of glycosylation of recombinant protein in CHO cells. *Bmc Biotechnology,* 11.

BUTLER, M. 2006. Optimisation of the cellular metabolism of glycosylation for recombinant proteins produced by mammalian cell systems. *Cytotechnology,* 50**,** 57-76.

CAMPBELL, M. P., ROYLE, L., RADCLIFFE, C. M., DWEK, R. A. & RUDD, P. M. 2008. GlycoBase and autoGU: tools for HPLC-based glycan analysis. *Bioinformatics,* 24**,** 1214-1216.

CAMPBELL, M. P., ROYLE, L. & RUDD, P. M. 2015. GlycoBase and autoGU: resources for interpreting HPLC-glycan data. *Methods Mol Biol,* 1273**,** 17-28.

CARINHAS, N., DUARTE, T. M., BARREIRO, L. C., CARRONDO, M. J. T., ALVES, P. M. & TEIXEIRA, A. P. 2013. Metabolic Signatures of GS-CHO Cell Clones Associated With Butyrate Treatment and Culture Phase Transition. *Biotechnology and Bioengineering,* 110**,** 3244-3257.

CARVALHAL, A. V., SANTOS, S. S., CALADO, J., HAURY, M. & CARRONDO, M. J. T. 2003. Cell growth arrest by nucleotides, nucleosides and bases as a tool for improved production of recombinant proteins. *Biotechnology Progress,* 19**,** 69-83.

CAZZOLA, M., MERCURIALI, F. & BRUGNARA, C. 1997. Use of recombinant human erythropoietin outside the setting of uremia. *Blood,* 89**,** 4248-4267.

CHA, Y., HOLLAND, S. M. & AUGUST, J. T. 1990. The Cdna Sequence of Mouse Lamp-2 - Evidence for 2 Classes of Lysosomal Membrane-Glycoproteins. *Journal of Biological Chemistry,* 265**,** 5008-5013.

CHEN, N., DEL VAL, L. J., KYRIAKOPOULOS, S., POLIZZI, K. M. & KONTORAVDI, C. 2012a. Metabolic network reconstruction: advances in in silico interpretation of analytical information. *Current Opinion in Biotechnology,* 23**,** 77-82.

CHEN, N., KOUMPOURAS, G. C., POLIZZI, K. M. & KONTORAVDI, C. 2012b. Genome-based kinetic modeling of cytosolic glucose metabolism in industrially relevant cell lines: Saccharomyces cerevisiae and Chinese hamster ovary cells. *Bioprocess and Biosystems Engineering,* 35**,** 1023-1033.

CHO, S. K. & CUMMINGS, R. D. 1997. A soluble form of alpha 1,3-galactosyltransferase functions within cells to galactosylate glycoproteins. *Journal of Biological Chemistry,* 272**,** 13622-13628.

CHUNG, C. H., MIRAKHUR, B., CHAN, E., LE, Q., BERLIN, J., MORSE, M., MURPHY, B. A., SATINOVER, S. M., HOSEN, J., MAURO, D., SLEBOS, R. J., ZHOU, Q. W., GOLD, D., HATLEY, T., HICKLIN, D. J. & PLATTS-MILLS, T. A. E. 2008. Cetuximab-induced anaphylaxis and IgE specific for galactose-alpha-1,3-galactose. *New England Journal of Medicine,* 358**,** 1109-1117.

COLOMA, M. J., TRINH, R. K., MARTINEZ, A. R. & MORRISON, S. L. 1999. Position effects of variable region carbohydrate on the affinity and in vivo behavior of an anti-(1 -> 6) dextran antibody. *Journal of Immunology,* 162**,** 2162-2170.

COMBE, C., TREDREE, R. L. & SCHELLEKENS, H. 2005. Biosimilar epoetins: an analysis based on recently implemented European medicines evaluation agency guidelines on comparability of biopharmaceutical proteins. *Pharmacotherapy,* 25**,** 954-62.

CONRADT, H. S., EGGE, H., PETERKATALINIC, J., REISER, W., SIKLOSI, T. & SCHAPER, K. 1987. Structure of the Carbohydrate Moiety of Human Interferon-Beta Secreted by a Recombinant Chinese-Hamster Ovary Cell-Line. *Journal of Biological Chemistry,* 262**,** 14600-14605.

CONSTANTINESCU, S. N., GHAFFARI, S. & LODISH, H. F. 1999. The erythropoietin receptor: Structure, activation and intracellular signal transduction. *Trends in Endocrinology and Metabolism,* 10**,** 18-23.

CROWELL, C. K., GRAMPP, G. E., ROGERS, G. N., MILLER, J. & SCHEINMAN, R. I. 2007. Amino acid and manganese supplementation modulates the glycosylation state of erythropoietin in a CHO culture system. *Biotechnology and Bioengineering,* 96**,** 538-549.

DANDREA, A. D., LODISH, H. F. & WONG, G. G. 1989. Expression Cloning of the Murine Erythropoietin Receptor. *Cell,* 57**,** 277-285.

DAVIES, J., JIANG, L. Y., PAN, L. Z., LABARRE, M. J., ANDERSON, D. & REFF, M. 2001. Expression of GnTIII in a recombinant anti-CD20 CHO production cell line: Expression of antibodies with altered glycoforms leads to an increase in ADCC through higher affinity for Fc gamma RIII. *Biotechnology and Bioengineering,* 74**,** 288-294.

DEL VAL, I. J., KONTORAVDI, C. & NAGY, J. M. 2010. Towards the Implementation of Quality by Design to the Production of Therapeutic Monoclonal Antibodies with Desired Glycosylation Patterns. *Biotechnology Progress,* 26**,** 1505-1527.

DEL VAL, I. J., KYRIAKOPOULOS, S., POLIZZI, K. M. & KONTORAVDI, C. 2013. An optimized method for extraction and quantification of nucleotides and nucleotide sugars from mammalian cells. *Analytical Biochemistry,* 443**,** 172-180.

DEL VAL, I. J., NAGY, J. M. & KONTORAVDI, C. 2011. A dynamic mathematical model for monoclonal antibody N-linked glycosylation and nucleotide sugar donor transport within a maturing Golgi apparatus. *Biotechnology Progress,* 27**,** 1730-1743.

DELL, A., GALADARI, A., SASTRE, F. & HITCHEN, P. 2010. Similarities and differences in the glycosylation mechanisms in prokaryotes and eukaryotes. *Int J Microbiol,* 2010**,** 148178.

DELORME, E., LORENZINI, T., GIFFIN, J., MARTIN, F., JACOBSEN, F., BOONE, T. & ELLIOTT, S. 1992. Role of Glycosylation on the Secretion and Biological-Activity of Erythropoietin. *Biochemistry,* 31**,** 9871-9876.

DETREMBLAY, M., PERRIER, M., CHAVARIE, C. & ARCHAMBAULT, J. 1992. Optimization of Fed-Batch Culture of Hybridoma Cells Using Dynamic-Programming - Single and Multi Feed Cases. *Bioprocess Engineering,* 7**,** 229-234.

DRICKAMER, K. & TAYLOR, M. E. 1993. Biology of Animal Lectins. *Annual Review of Cell Biology,* 9**,** 237-264.

DUBE, D. H. & BERTOZZI, C. R. 2005. Glycans in cancer and inflammation. Potential for therapeutics and diagnostics. *Nature Reviews Drug Discovery,* 4**,** 477-488.

DUBE, S., FISHER, J. W. & POWELL, J. S. 1988. Glycosylation at Specific Sites of Erythropoietin Is Essential for Biosynthesis, Secretion, and Biological Function. *Journal of Biological Chemistry,* 263**,** 17516-17521.

DWEK, R. A. 1996. Glycobiology: Toward understanding the function of sugars. *Chemical Reviews,* 96**,** 683-720.

EASTERBY, J. S. & QADRI, S. S. 1982. Hexokinase Type-Ii from Rat Skeletal-Muscle. *Methods in Enzymology,* 90**,** 11-15.

EGRIE, J. C. & BROWNE, J. K. 2001. Development and characterization of novel erythropoiesis stimulating protein (NESP). *British Journal of Cancer,* 84**,** 3-10.

EGRIE, J. C., DWYER, E., BROWNE, J. K., HITZ, A. & LYKOS, M. A. 2003. Darbepoetin alfa has a longer circulating half-life and greater in vivo potency than recombinant human erythropoietin. *Experimental Hematology,* 31**,** 290-299.

EGRIE, J. C., GRANT, J. R., GILLIES, D. K., AOKI, K. H. & STRICKLAND, T. W. 1993. The Role of Carbohydrate on the Biological-Activity of Erythropoietin. *Glycoconjugate Journal,* 10**,** 263-263.

EGRIE, J. C., STRICKLAND, T. W., LANE, J., AOKI, K., COHEN, A. M., SMALLING, R., TRAIL, G., LIN, F. K., BROWNE, J. K. & HINES, D. K. 1986. Characterization and Biological Effects of Recombinant-Human-Erythropoietin. *Immunobiology,* 172**,** 213-224.

ELBEIN, A. D. 1991. Glycosidase Inhibitors - Inhibitors of N-Linked Oligosaccharide Processing. *Faseb Journal,* 5**,** 3055-3063.

ENDO, T. 2009. New Era of Glycoscience: Intrinsic and Extrinsic Functions Performed by Glycans Foreword. *Biological & Pharmaceutical Bulletin,* 32**,** 765-766.

ESCHBACH, J. W., ABDULHADI, M. H., BROWNE, J. K., DELANO, B. G., DOWNING, M. R., EGRIE, J. C., EVANS, R. W., FRIEDMAN, E. A., GRABER, S. E., HALEY, N. R., KORBET, S., KRANTZ, S. B., LUNDIN, A. P., NISSENSON, A. R., OGDEN, D. A., PAGANINI, E. P., RADER, B., RUTSKY, E. A., STIVELMAN, J., STONE, W. J., TESCHAN, P., VANSTONE, J. C., VANWYCK, D. B., ZUCKERMAN, K. & ADAMSON, J. W. 1989. Recombinant Human Erythropoietin in Anemic Patients with End-Stage Renal-Disease - Results of a Phase-Iii Multicenter Clinical-Trial. *Annals of Internal Medicine,* 111**,** 992-1000.

EVALUATEPHARMA 2011a. Beyond the Patent Cliff. *World Preview to 2016,* . EvaluatePharma Ltd.

EVALUATEPHARMA 2011b. World Preview 2016 "Beyond the Patent Cliff".

EVALUATEPHARMA. 2012. *Betaseron* [Online]. EvaluatePharma. Available: http://www.evaluatepharma.com/Universal/View.aspx?type=Entity&entityType=Product&id=13896&lType=modData&componentID=1002 2012].

EVALUATEPHARMA 2014. World Preview 2014, Outlook to 2020. *World Preview.*

FEIL, B., KUCHERENKO, S. & SHAH, N. 2009. Comparison of Monte Carlo and Quasi Monte Carlo Sampling Methods in High Dimensional Model Representation. *Simul: 2009 First International Conference on Advances in System Simulation*, 12-17.

FIORE, M., ZANIER, R. & DEGRASSI, F. 2002. Reversible G(1) arrest by dimethyl sulfoxide as a new method to synchronize Chinese hamster cells. *Mutagenesis,* 17**,** 419-424.

FRAME, K. K. & HU, W. S. 1990. Cell-Volume Measurement as an Estimation of Mammalian-Cell Biomass. *Biotechnology and Bioengineering,* 36**,** 191-197.

FRIESS T, H. F., BAUER S, ET AL. 2008. GA101, a novel therapeutic type II CD20 antibody with outstanding efficacy and clear superiority in subcutaneous non-Hodgkin lymphoma xenograft models as well as superior B cell depletion. . *American Association for Cancer Research.* San Diego, CA. .

FUJITA, N., TAMURA, A., HIGASHIDANI, A., TONOZUKA, T., FREEZE, H. H. & NISHIKAWA, A. 2008. The relative contribution of mannose salvage pathways to glycosylation in PMI-deficient mouse embryonic fibroblast cells. *Febs Journal,* 275**,** 788-798.

FUKUDA, M. & HINDSGAUL, O. 2000. *Molecular and cellular glycobiology,* Oxford ; New York, Oxford University Press.

FUKUDA, M. N., SASAKI, H., LOPEZ, L. & FUKUDA, M. 1989. Survival of Recombinant Erythropoietin in the Circulation - the Role of Carbohydrates. *Blood,* 73**,** 84-89.

GALILI, U., ANARAKI, F., THALL, A., HILLBLACK, C. & RADIC, M. 1993. One Percent of Human Circulating B-Lymphocytes Are Capable of Producing the Natural Anti-Gal Antibody. *Blood,* 82**,** 2485-2493.

GATYAS, G. 2011. IMS Institute Reports U.S. Spending on Medicines Grew 2.3 Percent in 2010, to $307.4 Billion. New York: IMS Institute for Healthcare Informatics.

GAWLITZEK, M., VALLEY, U. & WAGNER, R. 1998. Ammonium ion and glucosamine dependent increases of oligosaccharide complexity in recombinant glycoproteins secreted from cultivated BHK-21 cells. *Biotechnology and Bioengineering,* 57**,** 518-528.

GEIGER, T., VELIC, A., MACEK, B., LUNDBERG, E., KAMPF, C., NAGARAJ, N., UHLEN, M., COX, J. & MANN, M. 2013. Initial Quantitative Proteomic Map of 28 Mouse Tissues Using the SILAC Mouse. *Molecular & Cellular Proteomics,* 12**,** 1709-1722.

GENOMES), K. K. E. O. G. A. Available: http://www.genome.jp/kegg/ [Accessed 10 March 2014.

GLACKEN, M. W., HUANG, C. & SINSKEY, A. J. 1989. Mathematical Descriptions of Hybridoma Culture Kinetics .3. Simulation of Fed-Batch Bioreactors. *Journal of Biotechnology,* 10**,** 39-65.

GOETZE, A. M., LIU, Y. D., ZHANG, Z. Q., SHAH, B., LEE, E., BONDARENKO, P. V. & FLYNN, G. C. 2011. High-mannose glycans on the Fc region of therapeutic IgG antibodies increase serum clearance in humans. *Glycobiology,* 21**,** 949-959.

GOUDAR, C., BIENER, R., BOISART, C., HEIDEMANN, R., PIRET, J., DE GRAAF, A. & KONSTANTINOV, K. 2010. Metabolic flux analysis of CHO cells in perfusion culture by metabolite balancing and 2D [C-13, H-1] COSY NMR spectroscopy. *Metabolic Engineering,* 12**,** 138-149.

GRAINGER, R. K. & JAMES, D. C. 2013. CHO Cell Line Specific Prediction and Control of Recombinant Monoclonal Antibody N-Glycosylation. *Biotechnology and Bioengineering,* 110**,** 2970-2983.

GRAMER, M. J., ECKBLAD, J. J., DONAHUE, R., BROWN, J., SHULTZ, C., VICKERMAN, K., PRIEM, P., VAN DEN BREMER, E. T. J., GERRITSEN, J. & VAN BERKEL, P. H. C. 2011. Modulation of Antibody Galactosylation Through Feeding of Uridine, Manganese Chloride, and Galactose. *Biotechnology and Bioengineering,* 108**,** 1591-1602.

GRAMMATIKOS, S. I., VALLEY, U., NIMTZ, M., CONRADT, H. S. & WAGNER, R. 1998. Intracellular UDP-N-acetylhexosamine pool affects N-glycan complexity: A mechanism of ammonium action on protein glycosylation. *Biotechnology Progress,* 14**,** 410-419.

GRANGER, B. L., GREEN, S. A., GABEL, C. A., HOWE, C. L., MELLMAN, I. & HELENIUS, A. 1990. Characterization and Cloning of Lgp110, a Lysosomal Membrane Glycoprotein from Mouse and Rat-Cells. *Journal of Biological Chemistry,* 265**,** 12036-12043.

GROUP, B. 2011a. Quality by Design in Biomanufacturing. *BIO-G Whitepaper* [Online]. Available: http://www.bio-g.com/whitepapers/download/6.

GROUP, B. 2011b. Quality by Design in Biomanufacturing. *Bio-G Whitepaper*. Bioproduction Group.

HARMONISATION, I. C. O. 2009. Pharmaceutical Development Q8(R2). *ICH Harmonised Tripartite Guideline*.

HARRISON, C. 2011. The Patent Cliff Steepens. Patent Review.

HAYTER, P. M., CURLING, E. M. A., GOULD, M. L., BAINES, A. J., JENKINS, N., SALMON, I., STRANGE, P. G. & BULL, A. T. 1993. THE EFFECT OF THE DILUTION RATE ON CHO CELL PHYSIOLOGY AND RECOMBINANT INTERFERON-GAMMA PRODUCTION IN GLUCOSE-LIMITED CHEMOSTAT CULTURE. *Biotechnology and Bioengineering,* 42**,** 1077-1085.

HELENIUS, A. 1994. How N-Linked Oligosaccharides Affect Glycoprotein Folding in the Endoplasmic-Reticulum. *Molecular Biology of the Cell,* 5**,** 253-265.

HELENIUS, A. & AEBI, M. 2001. Intracellular functions of N-linked glycans. *Science,* 291**,** 2364-2369.

HELENIUS, A. & AEBI, M. 2004. Roles of N-linked glycans in the endoplasmic reticulum. *Annual Review of Biochemistry,* 73**,** 1019-1049.

HILDEBRANDT, S., RADEN, D., PETZOLD, L., ROBINSON, A. S. & DOYLE, F. J. 2008. A top-down approach to mechanistic biological modeling: Application to the single-chain antibody folding pathway. *Biophysical Journal,* 95**,** 3535-3558.

HILLS, A. E., PATEL, A., BOYD, P. & JAMES, D. C. 2001. Metabolic control of recombinant monoclonal antibody N-glycosylation in GS-NS0 cells. *Biotechnology and Bioengineering,* 75**,** 239-251.

HINDERLICH, S., STASCHE, R., ZEITLER, R. & REUTTER, W. 1997. A bifunctional enzyme catalyzes the first two steps in N-acetylneuraminic acid biosynthesis of rat liver - Purification and characterization of UDP-N-acetylglucosamine 2-epimerase/N-acetylmannosamine kinase. *Journal of Biological Chemistry,* 272**,** 24313-24318.

HINES, J., JU, R., DUTSCHMAN, G. E., CHENG, Y. C. & CREWS, C. M. 2010. Reversal of TNP-470-Induced Endothelial Cell Growth Arrest by Guanine and Guanine Nucleosides. *Journal of Pharmacology and Experimental Therapeutics,* 334**,** 729-738.

HIRAYAMA, K., YUJI, R., YAMADA, N., KATO, K., ARATA, Y. & SHIMADA, I. 1998. Complete and rapid peptide and glycopeptide mapping of mouse monoclonal antibody by LC/MS/MS using ion trap mass spectrometry. *Analytical Chemistry,* 70**,** 2718-2725.

HIRSCHBERG, K., MILLER, C. M., ELLENBERG, J., PRESLEY, J. F., SIGGIA, E. D., PHAIR, R. D. & LIPPINCOTT-SCHWARTZ, J. 1998. Kinetic analysis of secretory protein traffic and characterization of Golgi to plasma membrane transport intermediates in living cells. *Journal of Cell Biology,* 143**,** 1485-1503.

HODONICZKY, J., ZHENG, Y. Z. & JAMES, D. C. 2005. Control of recombinant monoclonal antibody effector functions by Fc N-glycan remodeling in vitro. *Biotechnology Progress,* 21**,** 1644-1652.

HOLLAND, M., TAKADA, K., OKUMOTO, T., TAKAHASHI, N., KATO, K., ADU, D., BEN-SMITH, A., HARPER, L., SAVAGE, C. O. S. & JEFFERIS, R. 2002. Hypogalactosylation of serum IgG in patients with ANCA-associated systemic vasculitis. *Clinical and Experimental Immunology,* 129**,** 183-190.

HOLLAND, M., YAGI, H., TAKAHASHI, N., KATO, K., SAVAGE, C. O. S., GOODALL, D. M. & JEFFERIS, R. 2006. Differential glycosylation of polyclonal IgG, IgG-Fc and IgG-Fab isolated from the sera of patients with ANCA-associated systemic vasculitis. *Biochimica Et Biophysica Acta-General Subjects,* 1760**,** 669-677.

HOLST, B., BRUUN, A. W., KIELLANDBRANDT, M. C. & WINTHER, J. R. 1996. Competition between folding and glycosylation in the endoplasmic reticulum. *Embo Journal,* 15**,** 3538-3546.

HOSSLER, P., MULUKUTLA, B. C. & HU, W. S. 2007. Systems Analysis of N-Glycan Processing in Mammalian Cells. *Plos One,* 2.

HUANG, L. H., BIOLSI, S., BALES, K. R. & KUCHIBHOTLA, U. 2006. Impact of variable domain glycosylation on antibody clearance: An LC/MS characterization. *Analytical Biochemistry,* 349**,** 197-207.

HUPPA, J. B. & PLOEGH, H. L. 1998. The eS-Sence of -SH in the ER. *Cell,* 92**,** 145-148.

ICH. 2009. Harmonized Tripartite Guideline on Pharmaceutical Development Q8(R2). Available: http://www.ich.org/fileadmin/Public_Web_Site/ICH_Products/Guidelines/Quality/Q8_R1/Step4/Q8_R2_Guideline.pdf.

IHARA, H., IKEDA, Y., KOYOTA, S., ENDO, T., HONKE, K. & TANIGUCHI, N. 2002. A catalytically inactive beta 1,4-N-acetylglucosaminyltransferase III (GnT-III) behaves as a dominant negative GnT-III inhibitor. *European Journal of Biochemistry,* 269**,** 193-201.

IMPERIALI, B. & O'CONNOR, S. E. 1999. Effect of N-linked glycosylation on glycopeptide and glycoprotein structure. *Current Opinion in Chemical Biology,* 3**,** 643-649.

INC, B. G. 2011. Quality by Design in Biomanufacturing. *Bio-G Whitepaper.* Bioproduction Group.

INOUE, N., WATANABE, T., KUTSUKAKE, T., SAITOH, H., TSUMURA, H., ARAI, H. & TAKEUCHI, M. 1999. Asn-linked sugar chain structures of recombinant human thrombopoietin produced in Chinese hamster ovary cells. *Glycoconjugate Journal,* 16**,** 707-718.

ISHIDA, N., YOSHIOKA, S., CHIBA, Y., TAKEUCHI, M. & KAWAKITA, M. 1999. Molecular cloning and functional expression of the human Golgi UDP-N-acetylglucosamine transporter. *Journal of Biochemistry,* 126**,** 68-77.

ITO, K., TAKAHASHI, N., HIRAYAMA, M., HONDA, H. & TAKAHASHI, A. 1993. Abnormalities in the Oligosaccharide Moieties of Immunoglobulin-G in Patients with Myotonic-Dystrophy. *Journal of Clinical Biochemistry and Nutrition,* 14**,** 61-69.

J. GU, A. KONDO, N. OKAMOTO & WADA, Y. 1994. Oligosaccharide structures of immunoglobulin G from two patients with carbohydrate-deficient glycoprotein syndrome. *Glycosyl. Dis.,* 1**,** 247–252.

J.T., W. D. H. B. 1974. *Methods of Enzymatic Analysis,* New York, NY, USA and London, UK, Verlag Chemie.

JEDRZEJEWSKI, P. M., DEL VAL, I. C. M., POLIZZI, K. M. & KONTORAVDI, C. 2013. Applying quality by design to glycoprotein therapeutics: experimental and computational efforts of process control. *Pharmaceutical Bioprocessing,* 1**,** 51-69.

JEDRZEJEWSKI, P. M., DEL VAL, I. J., CONSTANTINOU, A., DELL, A., HASLAM, S. M., POLIZZI, K. M. & KONTORAVDI, C. 2014a. Towards controlling the glycoform: a model framework linking extracellular metabolites to antibody glycosylation. *Int J Mol Sci,* 15**,** 4492-522.

JEDRZEJEWSKI, P. M., DEL VAL, I. J., CONSTANTINOU, A., DELL, A., HASLAM, S. M., POLIZZI, K. M. & KONTORAVDI, C. 2014b. Towards Controlling the Glycoform: A Model Framework Linking Extracellular Metabolites to Antibody Glycosylation. *Int J Mol Sci,* 15**,** 4492-4522.

JELKMANN, W. 2012. Biosimilar recombinant human erythropoietins ("epoetins") and future erythropoiesis-stimulating treatments. *Expert Opinion on Biological Therapy,* 12**,** 581-592.

JIMENEZ DEL VAL, I., NAGY, J. M. & KONTORAVDI, C. 2011. A dynamic mathematical model for monoclonal antibody N-linked glycosylation and nucleotide sugar donor transport within a maturing Golgi apparatus. *Biotechnology Progress,* 27**,** 1730-43.

JITSUHARA, Y., TOYODA, T., ITAI, T. & YAMAGUCHI, H. 2002. Chaperone-like functions of high-mannose type and complex-type N-glycans and their molecular basis. *Journal of Biochemistry,* 132**,** 803-811.

JONES, A. J. S., PAPAC, D. I., CHIN, E. H., KECK, R., BAUGHMAN, S. A., LIN, Y. S., KNEER, J. & BATTERSBY, J. E. 2007. Selective clearance of glycoforms of a complex glycoprotein pharmaceutical caused by terminal N-acetylglucosamine is similar in humans and cynomolgus monkeys. *Glycobiology,* 17**,** 529-540.

JONES, M. B., NASIRIKENARI, M., LUGADE, A. A., THANAVALA, Y. & LAU, J. T. Y. 2012. Anti-inflammatory IgG Production Requires Functional P1 Promoter in beta-Galactoside alpha 2,6-Sialyltransferase 1 (ST6Gal-1) Gene. *Journal of Biological Chemistry,* 287**,** 15365-15370.

JONES, M. B., TENG, H., RHEE, J. K., LAHAR, N., BASKARAN, G. & YAREMA, K. J. 2004. Characterization of the cellular uptake and metabolic conversion of acetylated N-acetylmannosamine (ManNAc) analogues to sialic acids. *Biotechnology and Bioengineering,* 85**,** 394-405.

JONES, M. E. 1980. Pyrimidine Nucleotide Biosynthesis in Animals - Genes, Enzymes, and Regulation of Ump Biosynthesis. *Annual Review of Biochemistry,* 49**,** 253-279.

JUNOD, S. W. 2007. Celebrating a Milestone: FDA's Approval of First Genetically-Engineered Product. *Food and Drug Law Institute* [Online]. Available: http://www.fdli.org/.

KANEKO, Y., NIMMERJAHN, F. & RAVETCH, E. V. 2006. Anti-inflammatory activity of immunoglobulin G resulting from Fc sialylation. *Science,* 313**,** 670-673.

KARRENBAUER, A., JECKEL, D., JUST, W., BIRK, R., SCHMIDT, R. R., ROTHMAN, J. E. & WIELAND, F. T. 1990. The Rate of Bulk Flow from the Golgi to the Plasma-Membrane. *Cell,* 63**,** 259-267.

KHOLODENKO, B. N., KIYATKIN, A., BRUGGEMAN, F. J., SONTAG, E., WESTERHOFF, H. V. & HOEK, J. B. 2002. Untangling the wires: A strategy to trace functional interactions in signaling and gene networks (vol 99, pg 12841, 2002). *Proceedings of the National Academy of Sciences of the United States of America,* 99**,** 15245-15245.

KIPARISSIDES, A., KOUTINAS, M., KONTORAVDI, C., MANTALARIS, A. & PISTIKOPOULOS, E. N. 2011. 'Closing the loop' in biological systems modeling - From the in silico to the in vitro. *Automatica,* 47**,** 1147-1155.

KIPARISSIDES, A., KUCHERENKO, S. S., MANTALARIS, A. & PISTIKOPOULOS, E. N. 2009. Global Sensitivity Analysis Challenges in Biological Systems Modeling. *Industrial & Engineering Chemistry Research,* 48**,** 7168-7180.

KOCHANOWSKI, N., BLANCHARD, F., CACAN, R., CHIRAT, F., GUEDON, E., MARC, A. & GOERGEN, J. L. 2006. Intracellular nucleotide and nucleotide sugar contents of cultured CHO cells determined by a fast, sensitive, and high-resolution ion-pair RP-HPLC. *Analytical Biochemistry,* 348**,** 243-251.

KOCHANOWSKI, N., BLANCHARD, F., CACAN, R., CHIRAT, F., GUEDON, E., MARC, A. & GOERGEN, J. L. 2008. Influence of intracellular nucleotide and nucleotide sugar contents on recombinant interferon-gamma glycosylation during batch and fed-batch cultures of CHO cells. *Biotechnology and Bioengineering,* 100**,** 721-733.

KOHLER, G. & MILSTEIN, C. 1975. Continuous Cultures of Fused Cells Secreting Antibody of Predefined Specificity. *Nature,* 256**,** 495-497.

KONTORAVDI, C., ASPREY, S. P., PISTIKOPOULOS, E. N. & MANTALARIS, A. 2005. Application of global sensitivity analysis to determine goals for design of experiments: An example study on antibody-producing cell cultures. *Biotechnology Progress,* 21**,** 1128-1135.

KONTORAVDI, C., PISTIKOPOULOS, E. N. & MANTALARIS, A. 2010. Systematic development of predictive mathematical models for animal cell cultures. *Computers & Chemical Engineering,* 34**,** 1192-1198.

KORNFELD, R. & KORNFELD, S. 1985. Assembly of Asparagine-Linked Oligosaccharides. *Annual Review of Biochemistry,* 54**,** 631-664.

KORNFELD, S., KORNFELD, R., NEUFELD, E. F. & O'BRIEN, P. J. 1964. The Feedback Control of Sugar Nucleotide Biosynthesis in Liver. *Biochemistry,* 52**,** 371-379.

KRAMBECK, F. J., BENNUN, S. V., NARANG, S., CHOI, S., YAREMA, K. J. & BETENBAUGH, M. J. 2009. A mathematical model to derive N-glycan structures and cellular enzyme activities from mass spectrometric data. *Glycobiology,* 19**,** 1163-1175.

KRAMBECK, F. J. & BETENBAUGH, M. J. 2005. A mathematical model of N-linked glycosylation. *Biotechnology and Bioengineering,* 92**,** 711-728.

KYRIAKOPOULOS, S. & KONTORAVDI, C. 2013. Analysis of the landscape of biologically-derived pharmaceuticals in Europe: dominant production systems, molecule types on the rise and approval trends. *Eur J Pharm Sci,* 48**,** 428-41.

LAI, P. H., EVERETT, R., WANG, F. F., ARAKAWA, T. & GOLDWASSER, E. 1986. Structural Characterization of Human Erythropoietin. *Journal of Biological Chemistry,* 261**,** 3116-3121.

LAVECCHIO, J. A., DUNNE, A. D. & EDGE, A. S. B. 1995. Enzymatic Removal of Alpha-Galactosyl Epitopes from Porcine Endothelial-Cells Diminishes the Cytotoxic Effect of Natural Antibodies. *Transplantation,* 60**,** 841-847.

LEE, M. S. & LEE, G. M. 2000. Hyperosmotic pressure enhances immunoglobulin transcription rates and secretion rates of KR12H-2 transfectoma. *Biotechnology and Bioengineering,* 68**,** 260-268.

LEIBIGER, H., WUSTNER, D., STIGLER, R. D. & MARX, U. 1999. Variable domain-linked oligosaccharides of a human monoclonal IgG: structure and influence on antigen binding. *Biochemical Journal,* 338**,** 529-538.

LI, G. Y., HU, J. S., WANG, S. W., GEORGOPOULOS, P. G., SCHOENDORF, J. & RABITZ, H. 2006. Random sampling-high dimensional model representation (RS-HDMR) and orthogonality of its different order component functions. *Journal of Physical Chemistry A,* 110**,** 2474-2485.

LI, G. Y. & RABITZ, H. 2006. Ratio control variate method for efficiently determining high-dimensional model representations. *Journal of Computational Chemistry,* 27**,** 1112-1118.

LI, G. Y., WANG, S. W. & RABITZ, H. 2002. Practical approaches to construct RS-HDMR component functions. *Journal of Physical Chemistry A,* 106**,** 8721-8733.

LIS, H. & SHARON, N. 1998. Lectins: Carbohydrate-specific proteins that mediate cellular recognition. *Chemical Reviews,* 98**,** 637-674.

LIU, A. H., LIU, F., LI, Z., GU, J. X. & CHEN, H. L. 1998. Alterations in glycosyltransferases during myeloid and monocytoid differentiation of HL-60 cells. *Cell Biology International,* 22**,** 545-550.

LIU, C. K., SCHMIED, R., SCHER, W. & WAXMAN, S. 1981. Alterations in Glycosyltransferase Levels in Mouse Erythroleukemia-Cells during Erythrodifferentiation and Cell-Growth. *Cancer Research,* 41**,** 790-794.

LIU, C. K., SCHMIED, R., SCHREIBER, C., ROSEN, A., QIAN, G. X. & WAXMAN, S. 1983. Glycosyltransferase Alterations Are Cell Type Related When Human Promyelocytic Leukemia (Hl-60) Cells Are Treated with Various Inducers of Differentiation. *Experimental Hematology,* 11**,** 738-746.

LIU, J., WANG, J., FAN, L., CHEN, X., HU, D., DENG, X., FAI POON, H., WANG, H., LIU, X. & TAN, W. S. 2015. Galactose supplementation enhance sialylation of recombinant Fc-fusion protein in CHO cell: an insight into the role of galactosylation in sialylation. *World J Microbiol Biotechnol,* 31**,** 1147-56.

LJUNGGREN, J. & HAGGSTROM, L. 1994. Catabolic Control of Hybridoma Cells by Glucose and Glutamine Limited Fed-Batch Cultures. *Biotechnology and Bioengineering,* 44**,** 808-818.

LODISH, H. F., HILTON, D. J., KLINGMULLER, U., WATOWICH, S. S. & WU, H. 1995. The erythropoietin receptor: Biogenesis, dimerization, and intracellular signal transduction. *Cold Spring Harbor Symposia on Quantitative Biology,* 60**,** 93-104.

LOSEV, E., REINKE, C. A., JELLEN, J., STRONGIN, D. E., BEVIS, B. J. & GLICK, B. S. 2006. Golgi maturation visualized in living yeast. *Nature,* 441**,** 1002-1006.

MANTZARIS, N. V., DAOUTIDIS, P. & SRIENC, F. 2001. Numerical solution of multi-variable cell population balance models: I. Finite difference methods. *Computers & Chemical Engineering,* 25**,** 1411-1440.

MARKHAM, A. & BRYSON, H. M. 1995. Epoetin Alfa - a Review of Its Pharmacodynamic and Pharmacokinetic Properties and Therapeutic Use in Nonrenal Applications. *Drugs,* 49**,** 232-254.

MATSUDA, Y., SHIMURA, K., SHIRAKI, H. & NAKAGAWA, H. 1980. Purification and Properties of Adenylosuccinate Synthetase from Yoshida Sarcoma Ascites Tumor-Cells. *Biochimica Et Biophysica Acta,* 616**,** 340-350.

MATSUMIYA, S., YAMAGUCHI, Y., SAITO, J., NAGANO, M., SASAKAWA, H., OTAKI, S., SATOH, M., SHITARA, K. & KATO, K. 2007. Structural comparison of fucosylated and nonfucosylated Fc fragments of human immunoglobulin G1. *Journal of Molecular Biology,* 368**,** 767-779.

MATSUURA-TOKITA, K., TAKEUCHI, M., ICHIHARA, A., MIKURIYA, K. & NAKANO, A. 2006. Live imaging of yeast Golgi cisternal maturation. *Nature,* 441**,** 1007-1010.

MCDONALD, A. G., HAYES, J. M., BEZAK, T., GLUCHOWSKA, S. A., COSGRAVE, E. F. J., STRUWE, W. B., STROOP, C. J. M., KOK, H., VAN DE LAAR, T., RUDD, P. M., TIPTON, K. F. & DAVEY, G. P. 2014. Galactosyltransferase 4 is a major control point for glycan branching in N-linked glycosylation. *Journal of Cell Science,* 127**,** 5014-5026.

MEEZAN, E., WU, H. C., BLACK, P. H. & ROBBINS, P. W. 1969. Comparative studies on carbohydrate-containing membrane components of normal and virus-transformed mouse fibroblasts. Separation of glycoproteins and glycopeptides by sephadex chromatography. *Biochemistry,* 8**,** 2518-2524.

MERKLER, D. J. 1994. C-Terminal Amidated Peptides - Production by the in-Vitro Enzymatic Amidation of Glycine-Extended Peptides and the Importance of the Amide to Bioactivity. *Enzyme and Microbial Technology,* 16**,** 450-456.

MILLA, M. E., CLAIRMONT, C. A. & HIRSCHBERG, C. B. 1992. Reconstitution into Proteoliposomes and Partial-Purification of the Golgi-Apparatus Membrane Udp-Galactose, Udp-Xylose, and Udp-Glucuronic Acid Transport Activities. *Journal of Biological Chemistry,* 267**,** 103-107.

MISAIZU, T., MATSUKI, S., STRICKLAND, T. W., TAKEUCHI, M., KOBATA, A. & TAKASAKI, S. 1995. Role of Antennary Structure of N-Linked Sugar Chains in Renal Handling of Recombinant-Human-Erythropoietin. *Blood,* 86**,** 4097-4104.

MOLINARI, M. & HELENIUS, A. 2000. Chaperone selection during glycoprotein translocation into the endoplasmic reticulum. *Science,* 288**,** 331-333.

MONICA, T. J., ANDERSEN, D. C. & GOOCHEE, C. F. 1997. A mathematical model of sialylation of N-linked oligosaccharides in the trans-Golgi network. *Glycobiology,* 7**,** 515-521.

NAKANO, M., HIGO, D., ARAI, E., NAKAGAWA, T., KAKEHI, K., TANIGUCHI, N. & KONDO, A. 2009. Capillary electrophoresis-electrospray ionization mass spectrometry for rapid and sensitive N-glycan analysis of glycoproteins as 9-fluorenylmethyl derivatives. *Glycobiology,* 19**,** 135-143.

NARHI, L. O., ARAKAWA, T., AOKI, K. H., ELMORE, R., ROHDE, M. F., BOONE, T. & STRICKLAND, T. W. 1991. The Effect of Carbohydrate on the Structure and Stability of Erythropoietin. *Journal of Biological Chemistry,* 266**,** 23022-23026.

NELSON, A. L., DHIMOLEA, E. & REICHERT, J. M. 2010. Development trends for human monoclonal antibody therapeutics. *Nature Reviews Drug Discovery,* 9**,** 767-774.

NELSON, A. L. & REICHERT, J. M. 2009. Development trends for therapeutic antibody fragments. *Nature Biotechnology,* 27**,** 331-337.

NISHIMURA, I., UCHIDA, M., INOHANA, Y., SETOH, K., DABA, K., NISHIMURA, S. & YAMAGUCHI, H. 1998. Oxidative refolding of bovine pancreatic RNases A and B promoted by Asn-glycans. *Journal of Biochemistry,* 123**,** 516-520.

NOLAN, R. P. & LEE, K. 2011. Dynamic model of CHO cell metabolism. *Metabolic Engineering,* 13**,** 108-124.

OHADI, K., AGHAMOHSENI, H., GÄDKE, J., MOO-YOUNG, M., LEGGE, R. L., SCHARER, J. M. & BUDMAN, H. M. 2013. Novel Dynamic Model to Predict the Glycosylation Pattern of Monoclonal Antibodies from Extracellular Cell Culture Conditions. *12th IFAC Symposium on Computer Applications in Biotechnology.* Mumbai, India: The International Federation of Automatic Control.

OLDEN, K., PARENT, J. B. & WHITE, S. L. 1982. Carbohydrate Moieties of Glycoproteins - a Re-Evaluation of Their Function. *Biochimica Et Biophysica Acta,* 650**,** 209-232.

OPDENAKKER, G., DILLEN, C., FITEN, P., MARTENS, E., VAN AELST, I., VAN DEN STEEN, P. E., NELISSEN, I., STARCKX, S., DESCAMPS, F. J., HU, J. L., PICCARD, H., VAN DAMME, J., WORMALD, M. R., RUDD, P. M. & DWEK, R. A. 2006. Remnant epitopes, autoimmunity and glycosylation. *Biochimica Et Biophysica Acta-General Subjects,* 1760**,** 610-615.

OZTURK, S. S. & PALSSON, B. O. 1991. Growth, Metabolic, and Antibody-Production Kinetics of Hybridoma Cell-Culture .1. Analysis of Data from Controlled Batch Reactors. *Biotechnology Progress,* 7**,** 471-480.

PACIS, E., YU, M., AUTSEN, J., BAYER, R. & LI, F. 2011. Effects of Cell Culture Conditions on Antibody N-linked Glycosylation-What Affects High Mannose 5 Glycoform. *Biotechnology and Bioengineering,* 108**,** 2348-2358.

PAREKH, R. B., DWEK, R. A., SUTTON, B. J., FERNANDES, D. L., LEUNG, A., STANWORTH, D., RADEMACHER, T. W., MIZUOCHI, T., TANIGUCHI, T., MATSUTA, K., TAKEUCHI, F., NAGANO, Y., MIYAMOTO, T. & KOBATA, A. 1985. Association of Rheumatoid-Arthritis and Primary Osteo-Arthritis with Changes in the Glycosylation Pattern of Total Serum Igg. *Nature,* 316**,** 452-457.

PETRESCU, A. J., MILAC, A. L., PETRESCU, S. M., DWEK, R. A. & WORMALD, M. R. 2004. Statistical analysis of the protein environment of N-glycosylation sites: implications for occupancy, structure, and folding. *Glycobiology,* 14**,** 103-114.

PORTNER, R. & SCHAFER, T. 1996. Modelling hybridoma cell growth and metabolism a comparison of selected models and data. *Journal of Biotechnology,* 49**,** 119-135.

QIAN, J., LIU, T., YANG, L., DAUS, A., CROWLEY, R. & ZHOU, Q. W. 2007. Structural characterization of N-linked oligosaccharides on monoclonal antibody cetuximab by the combination of orthogonal matrix-assisted laser desorption/ionization hybrid quadrupole-quadrupole time-of-flight tandem mass spectrometry and sequential enzymatic digestion. *Analytical Biochemistry,* 364**,** 8-18.

RABOUILLE, C., HUI, N., HUNTE, F., KIECKBUSCH, R., BERGER, E. G., WARREN, G. & NILSSON, T. 1995. Mapping the Distribution of Golgi Enzymes Involved in the Construction of Complex Oligosaccharides. *Journal of Cell Science,* 108**,** 1617-1627.

RAJU, T. S. 2008. Terminal sugars of Fc glycans influence antibody effector functions of IgGs. *Current Opinion in Immunology,* 20**,** 471-478.

RAJU, T. S., BRIGGS, J. B., CHAMOW, S. M., WINKLER, M. E. & JONES, A. J. S. 2001. Glycoengineering of therapeutic glycoproteins: In vitro galactosylation and

sialylation of glycoproteins with terminal N-acetylglucosamine and galactose residues. *Biochemistry,* 40**,** 8868-8876.

RATHORE, A. S., BRANNING, R. & CECCHINI, D. 2007. Design space for biotech products. *Biopharm International,* 20**,** 36-+.

RATHORE, A. S. & WINKLE, H. 2009. Quality by design for biopharmaceuticals. *Nat Biotechnol,* 27**,** 26-34.

REICHERT, E. D. J. M. 2012. World Bispecific Antibody Summit, September 27–28, 2011, Boston, MA. *In:* BIOSCIENCE, L. (ed.) *World Bispecific Antibody Summit.* Boston, MA: mAbs.

REKHERT, J. M. & WENGER, J. B. 2008. Development trends for new cancer therapeutics and vaccines. *Drug Discovery Today,* 13**,** 30-37.

RESTELLI, V. & BUTLER, M. 2002. The effect of cell culture parameters on protein glycosylation. *Glycosylation,* 3**,** 61-92.

RIJCKEN, W. R. P., OVERDIJK, B., VANDENEIJNDEN, D. H. & FERWERDA, W. 1995. The Effect of Increasing Nucleotide Sugar Concentrations on the Incorporation of Sugars into Glycoconjugates in Rat Hepatocytes. *Biochemical Journal,* 305**,** 865-870.

ROGERS, S. & SEGAL, S. 1991. Modulation of Rat-Tissue Galactose-1-Phosphate Uridyltransferase by Uridine and Uridine Triphosphate. *Pediatric Research,* 30**,** 222-226.

RUDD, P. M., WORMALD, M. R., STANFIELD, R. L., HUANG, M. D., MATTSSON, N., SPEIR, J. A., DIGENNARO, J. A., FETROW, J. S., DWEK, R. A. & WILSON, I. A. 1999. Roles for glycosylation of cell surface receptors involved in cellular immune recognition. *Journal of Molecular Biology,* 293**,** 351-366.

RUNKEL, L., MEIER, W., PEPINSKY, R. B., KARPUSAS, M., WHITTY, A., KIMBALL, K., BRICKELMAIER, M., MULDOWNEY, C., JONES, W. & GOELZ, S. E. 1998. Structural and functional differences between glycosylated and non-glycosylated forms of human interferon-beta (IFN-beta). *Pharmaceutical Research,* 15**,** 641-649.

RUSH, J. S., PANNEERSELVAM, K., WAECHTER, C. J. & FREEZE, H. H. 2000. Mannose supplementation corrects GDP-mannose deficiency in cultured fibroblasts from some patients with Congenital Disorders of Glycosylation (CDG). *Glycobiology,* 10**,** 829-835.

SANAI, Y., YAMASAKI, M. & NAGAI, Y. 1988. Monoclonal-Antibody Directed to a Hanganutziu-Deicher Active Ganglioside, Gm2 (Neugc). *Biochimica Et Biophysica Acta,* 958**,** 368-374.

SASAKI, H., OCHI, N., DELL, A. & FUKUDA, M. 1988. Site-Specific Glycosylation of Human Recombinant Erythropoietin - Analysis of Glycopeptides or Peptides at Each Glycosylation Site by Fast Atom Bombardment Mass-Spectrometry. *Biochemistry,* 27**,** 8618-8626.

SCALLON, B. J., TAM, S. H., MCCARTHY, S. G., CAL, A. N. & RAJU, T. S. 2007. Higher levels of sialylated Fc glycans in immunoglobulin G molecules can adversely impact functionality. *Molecular Immunology,* 44**,** 1524-1534.

SCHACHTER, H. 1986. BIOSYNTHETIC CONTROLS THAT DETERMINE THE BRANCHING AND MICROHETEROGENEITY OF PROTEIN-BOUND OLIGOSACCHARIDES. *Biochemistry and Cell Biology-Biochimie Et Biologie Cellulaire,* 64**,** 163-181.

SCHELLEKENS, H. 2004a. Biosimilar therapeutic agents: issues with bioequivalence and immunogenicity. *European Journal of Clinical Investigation,* 34**,** 797-799.

SCHELLEKENS, H. 2004b. How similar do 'biosimilars' need to be? *Nature Biotechnology,* 22**,** 1357-1359.

SCHELLEKENS, H. 2009. Biosimilar therapeutics-what do we need to consider? *NDT Plus,* 2**,** i27-i36.

SCHIESTL, M., STANGLER, T., TORELLA, C., CEPELNJIK, T., TOLL, H. & GRAU, R. 2011. Acceptable changes in quality attributes of glycosylated biopharmaceuticals. Nature.

SEN, G. C. & LENGYEL, P. 1992. The Interferon System - a Birds-Eye-View of Its Biochemistry. *Journal of Biological Chemistry,* 267**,** 5017-5020.

SEO, J. S., MIN, B. S., KIM, Y. J., CHO, J. M., BAEK, E., CHO, M. S. & LEE, G. M. 2014. Effect of glucose feeding on the glycosylation quality of antibody produced by a human cell line, F2N78, in fed-batch culture. *Applied Microbiology and Biotechnology,* 98**,** 3509-3515.

SHELIKOFF, M., SINSKEY, A. J. & STEPHANOPOULOS, G. 1996. A modeling framework for the study of protein glycosylation. *Biotechnology and Bioengineering,* 50**,** 73-90.

SHIELDS, R. L., LAI, J., KECK, R., O'CONNELL, L. Y., HONG, K., MENG, Y. G., WEIKERT, S. H. A. & PRESTA, L. G. 2002. Lack of fucose on human IgG1 N-linked oligosaccharide improves binding to human Fc gamma RIII and antibody-dependent cellular toxicity. *Journal of Biological Chemistry,* 277**,** 26733-26740.

SHINKAWA, T., NAKAMURA, K., YAMANE, N., SHOJI-HOSAKA, E., KANDA, Y., SAKURADA, M., UCHIDA, K., ANAZAWA, H., SATOH, M., YAMASAKI, M.,

HANAI, N. & SHITARA, K. 2003. The absence of fucose but not the presence of galactose or bisecting N-acetylglucosamine of human IgG1 complex-type oligosaccharides shows the critical role of enhancing antibody-dependent cellular cytotoxicity. *Journal of Biological Chemistry,* 278**,** 3466-3473.

SIDOLI, F. R., ASPREY, S. P. & MANTALARIS, A. 2006. A coupled single cell-population-balance model for mammalian cell cultures. *Industrial & Engineering Chemistry Research,* 45**,** 5801-5811.

SIDOLI, F. R., MANTALARIS, A. & ASPREY, S. P. 2004. Modelling of mammalian cells and cell culture processes. *Cytotechnology,* 44**,** 27-46.

SOBOL, I. M. 2001. Global sensitivity indices for nonlinear mathematical models and their Monte Carlo estimates. *Mathematics and Computers in Simulation,* 55**,** 271-280.

SOLA, R. J. & GRIEBENOW, K. 2009. Effects of Glycosylation on the Stability of Protein Pharmaceuticals. *Journal of Pharmaceutical Sciences,* 98**,** 1223-1245.

SOU, S. N., SELLICK, C., LEE, K., MASON, A., KYRIAKOPOULOS, S., POLIZZI, K. M. & KONTORAVDI, C. 2015a. How Does Mild Hypothermia Affect Monoclonal Antibody Glycosylation? *Biotechnology and Bioengineering,* 112**,** 1165-1176.

SOU, S. N., SELLICK, C. A., LEE, K., MASON, A., KYRIAKOPOULOS, S., POLIZZI, K. M. & KONTORAVDI, C. 2015b. How Does Mild Hypothermia Affect MonoclonalAntibody Glycosylation? *Biotechnology and Bioengineering,* 112.

SPELLMAN, M. W. 1990. Carbohydrate Characterization of Recombinant Glycoproteins of Pharmaceutical Interest. *Analytical Chemistry,* 62**,** 1714-1722.

SPIVAK, J. L. & HOGANS, B. B. 1989. The Invivo Metabolism of Recombinant Human Erythropoietin in the Rat. *Blood,* 73**,** 90-99.

SPRINGER, M. S., STANHOPE, M. J., MADSEN, O. & DE JONG, W. W. 2004. Molecules consolidate the placental mammal tree. *Trends in Ecology & Evolution,* 19**,** 430-438.

STANLEY, P. 1984. Glycosylation Mutants of Animal-Cells. *Annual Review of Genetics,* 18**,** 525-552.

STANLEY, P. 2010. *Functional Glycomics* [Online]. Consortium for Functional Glycomics. [Accessed June 2015 2015].

STORRING, P. L. 1992. Assaying Glycoprotein Hormones - the Influence of Glycosylation on Immunoreactivity. *Trends in Biotechnology,* 10**,** 427-432.

STREBHARDT, K. & ULLRICH, A. 2008. Paul Ehrlich's magic bullet concept: 100 years of progress. *Nature Reviews Cancer,* 8**,** 473-480.

TACHIBANA, H., KIM, J. Y. & SHIRAHATA, S. 1997. Building high affinity human antibodies by altering the glycosylation on the light chain variable region in N-acetylglucosamine-supplemented hybridoma cultures. *Cytotechnology,* 23**,** 151-159.

TAKAGI, M., HAYASHI, H. & YOSHIDA, T. 2000. The effect of osmolarity on metabolism and morphology in adhesion and suspension chinese hamster ovary cells producing tissue plasminogen activator. *Cytotechnology,* 32**,** 171-179.

TAKAHASHI, N., ISHII, I., ISHIHARA, H., MORI, M., TEJIMA, S., JEFFERIS, R., ENDO, S. & ARATA, Y. 1987. Comparative Structural Study of the N-Linked Oligosaccharides of Human Normal and Pathological Immunoglobulin-G. *Biochemistry,* 26**,** 1137-1144.

TAKEUCHI, M., TAKASAKI, S., MIYAZAKI, H., KATO, T., HOSHI, S., KOCHIBE, N. & KOBATA, A. 1988. Comparative-Study of the Asparagine-Linked Sugar Chains of Human Erythropoietins Purified from Urine and the Culture-Medium of Recombinant Chinese-Hamster Ovary Cells. *Journal of Biological Chemistry,* 263**,** 3657-3663.

TAKUMA, S., HIRASHIMA, C. & PIRET, J. M. 2007. Dependence on glucose limitation of the pCO(2) influences on CHO cell growth, metabolism and IgG production. *Biotechnology and Bioengineering,* 97**,** 1479-1488.

TANIGUCHI, T., GUARENTE, L., ROBERTS, T. M., KIMELMAN, D., DOUHAN, J. & PTASHNE, M. 1980. Expression of the Human Fibroblast Interferon Gene in Escherichia-Coli. *Proceedings of the National Academy of Sciences of the United States of America-Biological Sciences,* 77**,** 5230-5233.

TOYODA, T., ARAKAWA, T. & YAMAGUCHI, H. 2002. N-glycans stabilize human erythropoietin through hydrophobic interactions with the hydrophobic protein surface: Studies by surface plasmon resonance analysis. *Journal of Biochemistry,* 131**,** 511-515.

TURNER, G. A. 1992. N-Glycosylation of Serum-Proteins in Disease and Its Investigation Using Lectins. *Clinica Chimica Acta,* 208**,** 149-171.

UMANA, P. & BAILEY, J. E. 1997. A mathematical model of N-linked glycoform biosynthesis. *Biotechnology and Bioengineering,* 55**,** 890-908.

UMANA, P., JEAN-MAIRET, J. & BAILEY, J. E. 1999. Tetracycline-regulated overexpression of glycosyltransferases in Chinese hamster ovary cells. *Biotechnology and Bioengineering,* 65**,** 542-549.

VALLEY, U., NIMTZ, M., CONRADT, H. S. & WAGNER, R. 1999. Incorporation of ammonium into intracellular UDP-activated N-acetylhexosamines and into carbohydrate structures in glycoproteins. *Biotechnology and Bioengineering,* 64**,** 401-417.

VAN DEN STEEN, P., RUDD, P. M., DWEK, R. A. & OPDENAKKER, G. 1998. Concepts and principles of O-linked glycosylation. *Critical Reviews in Biochemistry and Molecular Biology,* 33**,** 151-208.

VENTER, J. C., ADAMS, M. D., MYERS, E. W., LI, P. W., MURAL, R. J., SUTTON, G. G., SMITH, H. O., YANDELL, M., EVANS, C. A., HOLT, R. A., GOCAYNE, J. D., AMANATIDES, P., BALLEW, R. M., HUSON, D. H., WORTMAN, J. R., ZHANG, Q., KODIRA, C. D., ZHENG, X. Q. H., CHEN, L., SKUPSKI, M., SUBRAMANIAN, G., THOMAS, P. D., ZHANG, J. H., MIKLOS, G. L. G., NELSON, C., BRODER, S., CLARK, A. G., NADEAU, C., MCKUSICK, V. A., ZINDER, N., LEVINE, A. J., ROBERTS, R. J., SIMON, M., SLAYMAN, C., HUNKAPILLER, M., BOLANOS, R., DELCHER, A., DEW, I., FASULO, D., FLANIGAN, M., FLOREA, L., HALPERN, A., HANNENHALLI, S., KRAVITZ, S., LEVY, S., MOBARRY, C., REINERT, K., REMINGTON, K., ABU-THREIDEH, J., BEASLEY, E., BIDDICK, K., BONAZZI, V., BRANDON, R., CARGILL, M., CHANDRAMOULISWARAN, I., CHARLAB, R., CHATURVEDI, K., DENG, Z. M., DI FRANCESCO, V., DUNN, P., EILBECK, K., EVANGELISTA, C., GABRIELIAN, A. E., GAN, W., GE, W. M., GONG, F. C., GU, Z. P., GUAN, P., HEIMAN, T. J., HIGGINS, M. E., JI, R. R., KE, Z. X., KETCHUM, K. A., LAI, Z. W., LEI, Y. D., LI, Z. Y., LI, J. Y., LIANG, Y., LIN, X. Y., LU, F., MERKULOV, G. V., MILSHINA, N., MOORE, H. M., NAIK, A. K., NARAYAN, V. A., NEELAM, B., NUSSKERN, D., RUSCH, D. B., SALZBERG, S., SHAO, W., SHUE, B. X., SUN, J. T., WANG, Z. Y., WANG, A. H., WANG, X., WANG, J., WEI, M. H., WIDES, R., XIAO, C. L., YAN, C. H., et al. 2001. The sequence of the human genome. *Science,* 291**,** 1304-+.

WALSH, G. 2010. Biopharmaceutical benchmarks 2010. *Nature Biotechnology,* 28**,** 917-924.

WALSH, G. & JEFFERIS, R. 2006. Post-translational modifications in the context of therapeutic proteins. *Nature Biotechnology,* 24**,** 1241-1252.

WASLEY, L. C., TIMONY, G., MURTHA, P., STOUDEMIRE, J., DORNER, A. J., CARO, J., KRIEGER, M. & KAUFMAN, R. J. 1991. The Importance of N-Linked and O-Linked Oligosaccharides for the Biosynthesis and Invitro and Invivo Biologic Activities of Erythropoietin. *Blood,* 77**,** 2624-2632.

WEIKERT, S., PAPAC, D., BRIGGS, J., COWFER, D., TOM, S., GAWLITZEK, M., LOFGREN, J., MEHTA, S., CHISHOLM, V., MODI, N., EPPLER, S., CARROLL, K., CHAMOW, S., PEERS, D., BERMAN, P. & KRUMMEN, L. 1999. Engineering Chinese hamster ovary cells to maximize sialic acid content of recombinant glycoproteins. *Nature Biotechnology,* 17**,** 1116-1121.

WINEARLS, C. G., PIPPARD, M. J., DOWNING, M. R., OLIVER, D. O., REID, C. & COTES, P. M. 1986. Effect of Human Erythropoietin Derived from Recombinant-DNA on the Anemia of Patients Maintained by Chronic-Hemodialysis. *Lancet,* 2**,** 1175-1178.

WITSELL, D. L., CASEY, C. E. & NEVILLE, M. C. 1990. Divalent-Cation Activation of Galactosyltransferase in Native Mammary Golgi Vesicles. *Journal of Biological Chemistry,* 265**,** 15731-15737.

WONG, D. C. F., WONG, N. S. C., GOH, J. S. Y., MAY, L. M. & YAP, M. G. S. 2010a. Profiling of N-Glycosylation Gene Expression in CHO Cell Fed-Batch Cultures. *Biotechnology and Bioengineering,* 107**,** 516-528.

WONG, N. S. C., WATI, L., NISSOM, P. M., FENG, H. T., LEE, M. M. & YAP, M. G. S. 2010b. An Investigation of Intracellular Glycosylation Activities in CHO Cells: Effects of Nucleotide Sugar Precursor Feeding. *Biotechnology and Bioengineering,* 107**,** 321-336.

WONG, N. S. C., YAP, M. G. S. & WANG, D. I. C. 2006. Enhancing recombinant glycoprotein sialylation through CMP-sialic acid transporter over expression in chinese hamster ovary cells. *Biotechnology and Bioengineering,* 93**,** 1005-1016.

WORMALD, M. R. & DWEK, R. A. 1999. Glycoproteins: glycan presentation and protein-fold stability. *Structure with Folding & Design,* 7**,** R155-R160.

WRIGHT, A. & MORRISON, S. L. 1998. Effect of C2-associated carbohydrate structure on Ig effector function: Studies with chimeric mouse-human IgG1 antibodies in glycosylation mutants of Chinese hamster ovary cells. *Journal of Immunology,* 160**,** 3393-3402.

WRIGHT, A., SATO, Y., OKADA, T., CHANG, K. H., ENDO, T. & MORRISON, S. L. 2000. In vivo trafficking and catabolism of IgG1 antibodies with Fc associated carbohydrates of differing structure. *Glycobiology,* 10**,** 1347-1355.

WRIGHT, A., TAO, M. H., KABAT, E. A. & MORRISON, S. L. 1991. Antibody Variable Region Glycosylation - Position Effects on Antigen-Binding and Carbohydrate Structure. *Embo Journal,* 10**,** 2717-2723.

XIE, L. Z., NYBERG, G., GU, X. J., LI, H. Y., MOLLBORN, F. & WANG, D. I. C. 1997. Gamma-interferon production and quality in stoichiometric fed-batch cultures of Chinese hamster ovary (CHO) cells under serum-free conditions. *Biotechnology and Bioengineering,* 56**,** 577-582.

XIE, L. Z. & WANG, D. I. C. 1994. Stoichiometric Analysis of Animal-Cell Growth and Its Application in Medium Design. *Biotechnology and Bioengineering,* 43**,** 1164-1174.

XU, X., NAGARAJAN, H., LEWIS, N. E., PAN, S. K., CAI, Z. M., LIU, X., CHEN, W. B., XIE, M., WANG, W. L., HAMMOND, S., ANDERSEN, M. R., NEFF, N., PASSARELLI, B., KOH, W., FAN, H. C., WANG, J. B., GUI, Y. T., LEE, K. H., BETENBAUGH, M. J., QUAKE, S. R., FAMILI, I., PALSSON, B. O. & WANG, J. 2011. The genomic sequence of the Chinese hamster ovary (CHO)-K1 cell line. *Nature Biotechnology,* 29**,** 735-U131.

YANG, M. & BUTLER, M. 2000. Effect of ammonia on the glycosylation of human recombinant erythropoietin in culture. *Biotechnology Progress,* 16**,** 751-759.

YOSHIOKA, S., SUNWADA, G. H., ISHIDA, N. & KAWAKITA, M. 1997. Expression of the human UDP-galactose transporter in the Golgi membranes of murine Had-1 cells that lack the endogenous transporter. *Journal of Biochemistry,* 122**,** 691-695.

YOUINGS, A., CHANG, S. C., DWEK, R. A. & SCRAGG, I. G. 1996. Site-specific glycosylation of human immunoglobulin G is altered in four rheumatoid arthritis patients. *Biochemical Journal,* 314**,** 621-630.

YU, M., BROWN, D., REED, C., CHUNG, S., LUTMAN, J., STEFANICH, E., WONG, A., STEPHAN, J. P. & BAYER, R. 2012. Production, characterization and pharmacokinetic properties of antibodies with N-linked Mannose-5 glycans. *Mabs,* 4**,** 475-487.

ZALEVSKY, J., CHAMBERLAIN, A. K., HORTON, H. M., KARKI, S., LEUNG, I. W., SPROULE, T. J., LAZAR, G. A., ROOPENIAN, D. C. & DESJARLAIS, J. R. 2010. Enhanced antibody half-life improves in vivo activity. *Nat Biotechnol,* 28**,** 157-9.

ZHAO, W., CHEN, T. L. L., VERTEL, B. M. & COLLEY, K. J. 2006. The CMP-sialic acid transporter is localized in the medial-trans Golgi and possesses two specific endoplasmic reticulum export motifs in its carboxyl-terminal cytoplasmic tail. *Journal of Biological Chemistry,* 281**,** 31106-31118.

ZOU, G. Z., OCHIAI, H., HUANG, W., YANG, Q., LI, C. S. & WANG, L. X. 2011. Chemoenzymatic Synthesis and Fc gamma Receptor Binding of Homogeneous Glycoforms of Antibody Fc Domain. Presence of a Bisecting Sugar Moiety Enhances the Affinity of Fc to Fc gamma IIIa Receptor. *Journal of the American Chemical Society,* 133**,** 18975-18991.

ZUNIGA, M. M., KUCHERENKO, S. & SHAH, N. 2013. Metamodelling with independent and dependent inputs. *Computer Physics Communications,* 184**,** 1570-1580.

Appendix

Appendix A – NSD mechanisms

Table A.1 Summary of all reaction mechanisms of the NSD model

EC number and enzyme name	Reaction	Reaction mechanism
2.7.1.1 - Hexokinase	r1a	Ordered bi-bi mechanism
2.7.1.2 - Glucokinase	r1c	Ordered mnemonical bi-bi
5.3.1.9 - Glucose-6-phosphate isomerase	r2a	Push-pull mechanism (Michaelis-Menten)
2.6.1.16 - glutamine-fructose-6-phosphate transaminase	r3a	Ordered bi-bi mechanism
3.5.99.6 - glucosamine-6-phosphate deaminase	r3b	Ordered bi-bi mechanism
2.3.1.4 - glucosamine-phosphate N-acetyltransferase	r4a	Ping pong bi-bi mechanism
3.5.1.25 - N-acetylglucosamine-6-phosphate deacetylase	r4b	Michaelis-Menten
5.4.2.3 - phosphoacetylglucosamine mutase	r5a	Ping-Pong bi-bi mechanism
2.7.7.23 - UDP-N-acetylglucosamine diphsophorylase	r6a	Ping-Pong bi-bi mechanism
5.1.3.2 - UDP-glucose 4-epimerase	r7b	Single substrate Michaelis-Menten mechanism
2.7.1.59 - N-acetylglucosamine kinase	r8a	Random order (assumed)
2.7.1.1 - Hexokinase	r10a	Ordered bi-bi mechanism
2.7.1.1 - Hexokinase	r11a	Ordered bi-bi mechanism
2.7.1.52 - Fucokinase	r12a	Random order bi-bi (assumed)
2.7.7.30 - fucose-1-phosphate guanylyltransferase	r13a	Ping-Pong bi-bi mechanism (assumed)
1.1.1.271 - GDP-L-fucose synthase	r14a	Ping-Pong bi-bi mechanism
4.2.1.47 - GDP-mannose 4,6-dehydratase	r15a	Random order bi-bi (assumed)
2.7.7.13 - mannose-1-phosphate guanylyltransferase	r16a	Ping-Pong bi-bi mechanism (assumed to be the same as for r6a and r14a)
2.7.1.1 - Hexokinase	r18a	Ordered bi-bi mechanism
2.7.1.2 - Glucokinase	r18b	Ordered bi-bi mechanism
5.3.1.8 - Mannose-6-phosphate isomerase	19a	Single substrate Michaelis-Menten kinetics (assumed)

2.7.1.6 - galactokinase	r20a	Ordered bi-bi mechanism
2.7.7.9 - UTP-glucose-1-phosphate uridylyltransferase	r21a	Ordered bi-bi mechanism
5.1.3.2 - UDP-glucose 4-epimerase	r22a	Single substrate Michaelis-Menten mechanism
2.7.7.12 - UDP-glucose-hexose-1-phosphate uridylyltransferase	r23a	Bi-bi double displacement reaction (following ping pong kinetics)
5.4.2.8 - phosphomannomutase	r26a	Ping-Pong bi-bi mechanism
5.4.2.2 - phosphoglucomutase	r26b	Single substrate Michaelis-Menten mechanism
5.4.2.3 - phosphoacetylglucosamine mutase	r26c	Ping-Pong bi-bi mechanism
2.7.7.9 - UTP-glucose-1-phosphate uridylyltransferase	r27a	Ordered bi-bi mechanism
1.1.1.22 - UDP-glucose 6-dehydrogenase	r28a	Rate constant 110.7 nmol/min/mg
5.1.3.14 - UDP-N-acetylglucosamine 2-epimerase	r29a	Single substrate Michaelis-Menten kinetics (ordered two step mechanism)
2.7.1.59 - N-acetylglucosamine kinase	r30a	Random order bi-bi (assumed)
2.7.1.60 - N-acylmannosamine kinase	r30b	Random order bi-bi (assumed)
2.5.1.57 - N-acylneuraminate-9-phosphate synthase	r31a	Random order bi-bi (assumed)
3.1.3.29 - N-acylneuraminate-9-phosphatase	r32a	Single substrate Michaelis-Menten kinetics
2.7.7.43 - N-acylneuraminate cytidylyltransferase	r33a	Random order bi-bi (assumed)
1.14.18.2 - N-acetylneuraminate monooxygenase	r34a	Single substrate Michaelis-Menten kinetics
4.1.3.3 - N-acetylneuraminate lyase	r37a	Single substrate Michaelis-Menten kinetics
5.1.3.8 - N-Acylglucosamine 2-epimerase	r38a	Single substrate Michaelis-Menten kinetics
2.7.7.23 - UDP-N-acetylglucosamine diphsophorylase	r39a	Ping-Pong bi-bi mechanism
2.7.1.157 - N-acetylgalactosamine kinase	r40a	Ordered bi-bi mechanism

Appendix B – Numerical GSA outputs

Table A.2 Numerical GSA outputs of all parameter inputs against UDP-GlcNAc and UDP-GalNAc outputs at culture times 20h, 40h, 60h, 80h and 120h. Red fields indicate a significant impact on species concentration

	7 - UDP-GlcNAc					8 - UDP-GalNAc				
	20h	40h	60h	80h	120h	20h	40h	60h	80h	120h
E13a	0.0005	0.0006	0.0006	0.0004	0.0003	0.0005	0.0006	0.0006	0.0004	0.0004
E14a	0.0003	0.0005	0.0015	0.0016	0.0014	0.0003	0.0006	0.0015	0.0016	0.0015
E15a	0.0002	0.0002	0.0004	0.0005	0.0004	0.0002	0.0003	0.0005	0.0005	0.0005
E16a	0.0025	0.0022	0.0019	0.0013	0.0008	0.0027	0.0025	0.0023	0.002	0.0014
E17a	0.0007	0.0009	0.0015	0.0014	0.0011	0.0008	0.001	0.0016	0.0016	0.0015
E19a	0.0067	0.0064	0.0051	0.0034	0.0019	0.0071	0.0067	0.0053	0.0037	0.0021
E1a	0.0004	0.0004	0.0004	0.0031	0.0092	0.0004	0.0005	0.0005	0.0033	0.0096
E1c	0.6351	0.6947	0.7847	0.8562	0.9311	0.6093	0.6709	0.766	0.8336	0.9184
E20a	0.0011	0.0014	0.0027	0.0024	0.0017	0.0043	0.004	0.0042	0.0035	0.002
E21a	0.0005	0.0006	0.0005	0.0005	0.0007	0.0012	0.0011	0.0009	0.0009	0.0009
E22a	0.0026	0.0025	0.0019	0.0011	0.0006	0.0025	0.0024	0.002	0.0014	0.001
E23a	0.0008	0.0008	0.0008	0.0009	0.0009	0.0008	0.0008	0.0008	0.0009	0.0009
E26b	0.0008	0.0007	0.0005	0.0003	0.0003	0.001	0.0009	0.0007	0.0005	0.0004
E28a	0.0016	0.0016	0.0014	0.0013	0.0039	0.0015	0.0015	0.0013	0.0013	0.0037
E29a	0.0023	0.0021	0.0014	0.0007	0.0005	0.0022	0.002	0.0014	0.0007	0.0005
E2a	0.001	0.001	0.0008	0.0006	0.0005	0.0011	0.0012	0.001	0.0008	0.0007
E31a	0.0003	0.0005	0.0004	0.0009	0.0017	0.0004	0.0005	0.0004	0.0007	0.0015
E32a	0.0007	0.0006	0.0005	0.0004	0.0003	0.004	0.0033	0.0023	0.0023	0.001
E33a	0.0009	0.0009	0.0007	0.0004	0.0004	0.0009	0.0009	0.0007	0.0005	0.0005
E34a	0.0005	0.0005	0.0005	0.0004	0.0005	0.0005	0.0005	0.0006	0.0005	0.0007
E37a	0.0007	0.0012	0.0027	0.0028	0.0031	0.0009	0.0014	0.0031	0.0036	0.004
E38a	0.0102	0.0097	0.0081	0.0067	0.0044	0.0096	0.0093	0.0078	0.0063	0.0041
E3a	0.4596	0.3992	0.2821	0.1712	0.0845	0.4399	0.3845	0.274	0.1652	0.082
E3b	0.0003	0.0003	0.0004	0.0005	0.0006	0.0003	0.0004	0.0005	0.0007	0.0009
E40a	0.0034	0.0036	0.0034	0.0023	0.0014	0.004	0.0041	0.0037	0.0026	0.0017
E4a	0.0012	0.0014	0.002	0.0025	0.0025	0.0016	0.0018	0.0024	0.0029	0.0029
E4b	0.0028	0.0031	0.0031	0.0021	0.0016	0.0027	0.003	0.003	0.002	0.0017
E5a	0.0002	0.0003	0.0004	0.0007	0.002	0.0003	0.0003	0.0004	0.0007	0.002
E6a	0.0095	0.009	0.0074	0.0061	0.0041	0.009	0.0087	0.0073	0.006	0.0044
E8a	0.0006	0.0014	0.0014	0.0026	0.0031	0.001	0.0017	0.0016	0.0027	0.0033
n29a_CMPNeu5Ac	0.0041	0.0035	0.0022	0.0014	0.005	0.004	0.0035	0.0022	0.0016	0.0051
Km7b_UDPGlcNAc	0.0107	0.0095	0.0076	0.0037	0.0021	0.0671	0.0588	0.0466	0.0542	0.0421
k17aF	0.0006	0.0014	0.0043	0.0065	0.0093	0.0008	0.0015	0.0043	0.0066	0.0093
k19aF	0.0051	0.0049	0.0041	0.0032	0.0027	0.0051	0.005	0.0042	0.0033	0.0028
k21aB	0.0118	0.0097	0.006	0.0036	0.0014	0.0115	0.0095	0.0059	0.0034	0.0013
k21aF	0.0003	0.0003	0.0003	0.0003	0.0004	0.0004	0.0004	0.0004	0.0004	0.0005
k22aB	0.0022	0.0027	0.0034	0.0034	0.003	0.0022	0.0026	0.0033	0.0033	0.0029
k26aF	0.0009	0.0009	0.0006	0.0007	0.0034	0.0019	0.0017	0.0012	0.0012	0.0036
k27aF	0.0007	0.0007	0.0006	0.0005	0.0007	0.0041	0.0035	0.0025	0.0026	0.0015
Ki15a_GDPFuc	0.0026	0.0028	0.0025	0.0021	0.0017	0.0025	0.0027	0.0025	0.0021	0.0017
Ki29a_CMPNeu5Ac	0.0006	0.0007	0.0009	0.0009	0.0008	0.0008	0.0009	0.001	0.001	0.0009
Ki_SA_Tra_UDPGlcNAc	0.0008	0.0009	0.0009	0.0008	0.0009	0.0009	0.001	0.001	0.001	0.001
Km17a_Man6P	0.0012	0.0022	0.0061	0.0087	0.0092	0.0016	0.0025	0.0061	0.0085	0.0088
Km19a_Fru6P	0.0002	0.0003	0.0004	0.0004	0.0004	0.0004	0.0005	0.0007	0.0008	0.0009
Km22a_UDPGlc	0.0105	0.0085	0.0052	0.0031	0.001	0.0103	0.0085	0.0052	0.003	0.001
Km26a_Glc6P	0.0018	0.0018	0.0013	0.0015	0.0029	0.0052	0.0047	0.0034	0.0035	0.0042

Table A.3 Numerical GSA outputs of all parameter inputs against GDP-Fuc and GDP-Man outputs at culture times 20h, 40h, 60h, 80h and 120h. Red fields indicate a significant impact on species concentration

	14 - GDP-Fuc					16 - GDP-Man				
	20h	40h	60h	80h	120h	20h	40h	60h	80h	120h
E13a	0.0001	0.0001	0.0001	0.0001	0.0001	0.0015	0.0013	0.0013	0.0018	0.002
E14a	0.0002	0.0001	0.0001	0.0001	0.0001	0.0012	0.001	0.001	0.0013	0.0012
E15a	0.7847	0.7765	0.7843	0.8193	0.8161	0.0008	0.001	0.0009	0.0006	0.0009
E16a	0.0001	0.0001	0.0001	0.0001	0.0002	0.0047	0.0044	0.0042	0.0064	0.0067
E17a	0.0002	0.0002	0.0001	0	0	0.0139	0.0116	0.0053	0.0013	0.0006
E19a	0.0452	0.0597	0.0524	0.0105	0.0015	0.3389	0.3783	0.3639	0.1267	0.0147
E1a	0.0004	0.0004	0.0004	0.0002	0.0002	0.0026	0.0029	0.0028	0.003	0.0028
E1c	0.0166	0.0069	0.001	0.0017	0.004	0.1246	0.0602	0.0449	0.3244	0.5034
E20a	0.0003	0.0002	0.0002	0.0001	0	0.0019	0.0017	0.0018	0.0016	0.0016
E21a	0.0002	0.0002	0.0001	0.0001	0.0001	0.0029	0.0029	0.003	0.0027	0.003
E22a	0.0001	0.0001	0.0001	0.0001	0.0001	0.0005	0.0005	0.0005	0.0006	0.0009
E23a	0.0001	0.0001	0.0001	0	0	0.0011	0.0011	0.0011	0.0011	0.001
E26b	0.0002	0.0002	0.0002	0.0001	0.0001	0.0025	0.0027	0.0027	0.0026	0.0026
E28a	0.0003	0.0003	0.0003	0.0001	0.0001	0.0011	0.001	0.001	0.0009	0.0041
E29a	0.0002	0.0002	0.0002	0.0002	0.0005	0.0092	0.0084	0.0086	0.0112	0.0118
E2a	0.0001	0.0001	0.0001	0.0001	0.0001	0.0013	0.0013	0.0013	0.0012	0.0012
E31a	0.0013	0.0013	0.0013	0.0014	0.0014	0.0031	0.0031	0.0029	0.003	0.0027
E32a	0.0003	0.0003	0.0003	0.0002	0.0002	0.0052	0.0055	0.0055	0.0047	0.0037
E33a	0.0002	0.0001	0.0001	0.0001	0.0001	0.001	0.0008	0.0007	0.0012	0.0019
E34a	0.0009	0.0009	0.0009	0.0009	0.0009	0.001	0.001	0.001	0.0011	0.0011
E37a	0.0002	0.0002	0.0002	0.0001	0.0002	0.0017	0.0016	0.0016	0.0018	0.002
E38a	0.0002	0.0002	0.0002	0.0001	0.0001	0.002	0.0016	0.0015	0.0026	0.0027
E3a	0.0004	0.0003	0.0002	0.0002	0.0002	0.0025	0.0023	0.0021	0.0044	0.0025
E3b	0.0005	0.0005	0.0005	0.0003	0.0003	0.0042	0.0047	0.0047	0.003	0.0021
E40a	0.0008	0.0008	0.0008	0.0003	0.0003	0.0088	0.0092	0.0095	0.0073	0.005
E4a	0.0002	0.0002	0.0001	0.0001	0.0002	0.0041	0.0035	0.0033	0.0057	0.0056
E4b	0.0012	0.0013	0.0013	0.0011	0.0011	0.0023	0.0027	0.0027	0.0013	0.0016
E5a	0.0003	0.0002	0.0002	0.0002	0.0002	0.0012	0.001	0.0009	0.001	0.0017
E6a	0.0004	0.0002	0.0002	0.0002	0.0002	0.0032	0.0025	0.0023	0.0042	0.0044
E8a	0.0002	0.0002	0.0001	0.0001	0.0001	0.001	0.0011	0.001	0.003	0.001
n29a_CMPNeu5Ac	0.0001	0.0001	0.0001	0.0001	0.0005	0.0089	0.0084	0.009	0.0112	0.016
Km7b_UDPGlcNAc	0.0092	0.0092	0.0093	0.0095	0.0094	0.0032	0.0032	0.0032	0.0027	0.0022
k17aF	0.0008	0.0008	0.0009	0.0014	0.005	0.1266	0.1223	0.1233	0.1503	0.1472
k19aF	0.0096	0.0116	0.0108	0.0047	0.0057	0.2148	0.2286	0.2244	0.1702	0.1232
k21aB	0.0007	0.0007	0.0006	0.0006	0.0007	0.001	0.0008	0.0007	0.0019	0.0021
k21aF	0.0001	0.0001	0.0001	0.0001	0.0001	0.0018	0.0019	0.0017	0.0018	0.0018
k22aB	0.0011	0.0014	0.0013	0.0006	0.0005	0.0118	0.0127	0.0128	0.0087	0.0058
k26aF	0.0005	0.0005	0.0005	0.0002	0.0003	0.0087	0.0089	0.0092	0.0096	0.011
k27aF	0.0006	0.0005	0.0005	0.0006	0.0006	0.0017	0.0018	0.0018	0.0014	0.0018
Ki15a_GDPFuc	0.1676	0.1663	0.1699	0.1807	0.1815	0.0019	0.0017	0.0015	0.0017	0.0015
Ki29a_CMPNeu5Ac	0.009	0.009	0.0091	0.0096	0.0096	0.0026	0.0028	0.0028	0.0026	0.0021
Ki_SA_Tra_UDPGlcNAc	0.0002	0.0003	0.0002	0.0001	0.0002	0.003	0.0031	0.0031	0.0034	0.0034
Km17a_Man6P	0.0006	0.0007	0.0007	0.0006	0.0031	0.1104	0.1067	0.1062	0.1272	0.1213
Km19a_Fru6P	0.0074	0.0094	0.009	0.0035	0.0047	0.2409	0.2601	0.2585	0.1918	0.1378
Km22a_UDPGlc	0.0008	0.0008	0.0008	0.0007	0.0009	0.0073	0.0071	0.0071	0.0078	0.007
Km26a_Glc6P	0.0005	0.0007	0.0007	0.0002	0.0001	0.0049	0.0051	0.0053	0.0036	0.0034

Table A.4 Numerical GSA outputs of all parameter inputs against UDP-Gal and UDP-Glc outputs at culture times 20h, 40h, 60h, 80h and 120h. Red fields indicate a significant impact on species concentration

	22 - UDP-Gal					24 - UDP-Glc				
	20h	40h	60h	80h	120h	20h	40h	60h	80h	120h
E13a	0.0021	0.0022	0.0019	0.0017	0.0024	0.0021	0.0021	0.0017	0.0014	0.0018
E14a	0.0029	0.0025	0.0022	0.0024	0.0027	0.0027	0.0023	0.0018	0.0023	0.0038
E15a	0.0054	0.0058	0.0067	0.0086	0.0044	0.0033	0.0036	0.004	0.0047	0.0035
E16a	0.0029	0.0028	0.0025	0.0023	0.0038	0.0034	0.003	0.0026	0.0023	0.0028
E17a	0.2241	0.2219	0.2104	0.1074	0.0071	0.1961	0.1968	0.2054	0.1019	0.0056
E19a	0.044	0.0338	0.0308	0.0199	0.0038	0.051	0.0383	0.0293	0.0132	0.0026
E1a	0.0027	0.0026	0.0025	0.0033	0.0045	0.0043	0.0037	0.0028	0.0022	0.0029
E1c	0.0475	0.0349	0.0132	0.0662	0.4803	0.0281	0.0189	0.0222	0.1889	0.5501
E20a	0.0037	0.0034	0.0028	0.0021	0.0029	0.0034	0.0029	0.0023	0.0028	0.0048
E21a	0.0039	0.0046	0.0057	0.0102	0.0229	0.0093	0.0086	0.0064	0.0063	0.0097
E22a	0.0035	0.0037	0.0038	0.0034	0.003	0.0032	0.0035	0.0031	0.0023	0.0029
E23a	0.0142	0.017	0.0258	0.0478	0.0601	0.0082	0.0103	0.0168	0.0265	0.0248
E26b	0.013	0.015	0.0194	0.028	0.0171	0.0091	0.0104	0.0141	0.0199	0.0123
E28a	0.0044	0.0044	0.0043	0.0031	0.0046	0.0033	0.0033	0.0033	0.0024	0.0044
E29a	0.0034	0.0035	0.0043	0.0061	0.0052	0.004	0.0038	0.0038	0.0049	0.004
E2a	0.0047	0.0043	0.0037	0.0031	0.0036	0.0069	0.0063	0.0043	0.0025	0.0031
E31a	0.0055	0.0058	0.0058	0.0052	0.0038	0.0039	0.004	0.0036	0.0038	0.0052
E32a	0.0047	0.0051	0.0058	0.0063	0.0045	0.0049	0.0051	0.0057	0.0057	0.0043
E33a	0.0066	0.0062	0.005	0.003	0.0026	0.0041	0.004	0.0031	0.0023	0.0024
E34a	0.0091	0.0097	0.0108	0.0099	0.0046	0.0062	0.0069	0.0081	0.007	0.0037
E37a	0.0027	0.0028	0.003	0.0029	0.0027	0.003	0.0028	0.0031	0.0035	0.0032
E38a	0.0051	0.0053	0.0055	0.0058	0.0057	0.0038	0.004	0.0045	0.0051	0.005
E3a	0.0086	0.0097	0.0126	0.0132	0.0045	0.0044	0.0047	0.0055	0.0063	0.0033
E3b	0.0103	0.0104	0.0102	0.0092	0.0036	0.0108	0.0111	0.0121	0.0127	0.0071
E40a	0.0077	0.0076	0.0073	0.0068	0.0031	0.0099	0.0101	0.011	0.0112	0.0044
E4a	0.0031	0.0032	0.003	0.0039	0.0039	0.0039	0.0038	0.0031	0.0039	0.0039
E4b	0.0028	0.003	0.0034	0.0033	0.0022	0.0032	0.0033	0.0034	0.0028	0.002
E5a	0.0051	0.0055	0.0062	0.0081	0.0041	0.0027	0.0027	0.0032	0.0041	0.0034
E6a	0.0033	0.0034	0.0034	0.0033	0.004	0.0031	0.0031	0.0029	0.0037	0.0043
E8a	0.0031	0.0031	0.0031	0.0039	0.0032	0.0028	0.0027	0.0025	0.0036	0.003
n29a_CMPNeu5Ac	0.0023	0.0025	0.0029	0.0046	0.0078	0.0032	0.0031	0.003	0.004	0.0076
Km7b_UDPGlcNAc	0.0077	0.0074	0.0067	0.0058	0.0061	0.0061	0.0063	0.0073	0.0101	0.01
k17aF	0.0173	0.0189	0.0281	0.0608	0.0593	0.0127	0.0145	0.0221	0.0433	0.046
k19aF	0.0336	0.0258	0.015	0.0116	0.0087	0.0337	0.0292	0.0193	0.0089	0.007
k21aB	0.1104	0.1207	0.1407	0.1686	0.0839	0.0298	0.0384	0.0564	0.0799	0.0567
k21aF	0.0066	0.0069	0.007	0.0068	0.0043	0.0048	0.0046	0.0036	0.0028	0.0027
k22aB	0.1855	0.1883	0.1897	0.1663	0.034	0.4078	0.3808	0.3549	0.3038	0.1319
k26aF	0.121	0.1265	0.1329	0.1279	0.0775	0.0902	0.094	0.1071	0.0987	0.0585
k27aF	0.0903	0.1001	0.1164	0.1447	0.0935	0.054	0.0621	0.0801	0.109	0.0932
Ki15a_GDPFuc	0.0025	0.0025	0.0022	0.0026	0.0043	0.0025	0.0025	0.0022	0.0029	0.004
Ki29a_CMPNeu5Ac	0.0044	0.0046	0.0048	0.0063	0.0046	0.0032	0.0036	0.0041	0.0058	0.005
Ki_SA_Tra_UDPGlcNAc	0.0024	0.0024	0.0027	0.0035	0.0031	0.002	0.002	0.002	0.0026	0.0025
Km17a_Man6P	0.0167	0.0155	0.012	0.008	0.0115	0.0147	0.0137	0.0116	0.0084	0.01
Km19a_Fru6P	0.043	0.0389	0.0289	0.0234	0.013	0.0375	0.0348	0.0287	0.0181	0.0094
Km22a_UDPGlc	0.0148	0.018	0.0244	0.0304	0.0118	0.0083	0.0111	0.0196	0.0296	0.022
Km26a_Glc6P	0.15	0.1541	0.1587	0.15	0.0815	0.125	0.1276	0.1292	0.1125	0.0687

Table A.5 Numerical GSA outputs of all parameter inputs against CMP-Neu5Ac outputs at culture times 20h, 40h, 60h, 80h and 120h. Red fields indicate a significant impact on species concentration.

	30 - CMP-Neu5AC				
	20h	40h	60h	80h	120h
E13a	0.0005	0.0005	0.0006	0.0007	0.0012
E14a	0.0018	0.0018	0.0019	0.0021	0.0022
E15a	0.0022	0.0022	0.0024	0.0025	0.0025
E16a	0.0121	0.0124	0.0133	0.0142	0.014
E17a	0.0006	0.0006	0.0006	0.0006	0.0006
E19a	0.0013	0.0013	0.0011	0.001	0.0019
E1a	0.0003	0.0003	0.0004	0.0004	0.0006
E1c	0.0042	0.0046	0.0051	0.0028	0.0024
E20a	0.0004	0.0004	0.0005	0.0006	0.001
E21a	0.0006	0.0006	0.0006	0.0006	0.0011
E22a	0.002	0.002	0.0021	0.0021	0.0021
E23a	0.0007	0.0007	0.0008	0.0011	0.0014
E26b	0.0002	0.0002	0.0003	0.0004	0.0007
E28a	0.0002	0.0002	0.0002	0.0003	0.0005
E29a	0.3609	0.3462	0.2968	0.2241	0.1694
E2a	0.0004	0.0004	0.0004	0.0005	0.0009
E31a	0.002	0.0021	0.0022	0.0025	0.0026
E32a	0.0017	0.0017	0.0016	0.0016	0.0017
E33a	0.0009	0.0008	0.0008	0.0017	0.0204
E34a	0.0118	0.0121	0.0126	0.0128	0.0122
E37a	0.0011	0.0011	0.0011	0.0018	0.015
E38a	0.0061	0.0063	0.007	0.0119	0.0363
E3a	0.0029	0.0027	0.0021	0.0012	0.0015
E3b	0.0014	0.0013	0.0014	0.0014	0.0014
E40a	0.0007	0.0007	0.0007	0.0007	0.0008
E4a	0.0002	0.0002	0.0002	0.0002	0.0005
E4b	0.001	0.001	0.0011	0.0012	0.0014
E5a	0.0023	0.0023	0.0025	0.0026	0.0026
E6a	0.0003	0.0003	0.0003	0.0004	0.001
E8a	0.0057	0.006	0.0072	0.0139	0.0365
n29a_CMPNeu5Ac	0.6985	0.7166	0.7752	0.855	0.8606
Km7b_UDPGlcNAc	0.0023	0.0023	0.002	0.0016	0.0014
k17aF	0.0354	0.0347	0.0322	0.0286	0.0241
k19aF	0.0008	0.0008	0.0008	0.0008	0.0015
k21aB	0.0009	0.0009	0.0008	0.0009	0.0009
k21aF	0.001	0.001	0.0009	0.0009	0.0015
k22aB	0.002	0.0021	0.0024	0.0027	0.0029
k26aF	0.0015	0.0015	0.0016	0.0018	0.0019
k27aF	0.0081	0.0078	0.0068	0.0053	0.0043
Ki15a_GDPFuc	0.002	0.0019	0.0016	0.0012	0.0015
Ki29a_CMPNeu5Ac	0.0724	0.0696	0.0605	0.046	0.0339
Ki_SA_Tra_UDPGlcNAc	0.0024	0.0024	0.0023	0.0022	0.0027
Km17a_Man6P	0.0008	0.0008	0.0007	0.0007	0.0009
Km19a_Fru6P	0.0061	0.0058	0.0048	0.0035	0.0027
Km22a_UDPGlc	0.0027	0.0027	0.0026	0.0025	0.0025
Km26a_Glc6P	0.0013	0.0013	0.0015	0.0017	0.0017

Appendix C – Estimated parameters Chapter 3

Table A.6 Estimated NSD model parameter values in chapter 3

Parameter name	Parameter value
E15a	2.5400E-05
E8a	0.0000E+00
E26b	0.0000E+00
E19a	6.4400E-06
E21a	6.8586E-06
Eglyc	7.0800E-05
Ki15a_GDPFuc	2.1200E-04
E29a	1.3313E-03
E1c	1.5096E-03
E1a	1.8477E-03
Km17a_Man6P	2.5300E-03
E23a	3.7138E-03
E12a	3.9000E-03
E32a	3.9000E-03
E14a	3.9000E-03
E16a	3.9000E-03
E20a	3.9000E-03
E2a	3.9000E-03
E37a	3.9000E-03
E3b	3.9000E-03
E40a	3.9000E-03
E4a	3.9000E-03
E4b	3.9000E-03
E17a	3.9532E-03
E22a	1.0000E-02
E3a	1.4167E-02
E38a	3.5128E-02
E13a	3.9000E-02
E31a	3.9000E-02
E33a	3.9000E-02
E5a	3.9000E-02
E6a	3.9000E-02
Km26a_Glc6P	9.3842E-02
Km22a_UDPGlc	2.0697E-01
Km7b_UDPGlcNAc	8.2129E-01
Gln_coef	1.0000E+00
n29a_CMPNeu5Ac	4.2000E+00
Ki_SA_Tra_UDPGlcNAc	6.8885E+00
Km19a_Fru6P	1.9700E+01
k5aB	6.0000E+02
Ki34a_CMPNeu5Gc	1.0000E+03
k26aF	2.0972E+03
k6aB	2.3900E+04
k17aF	7.0928E+04
k22aB	1.6151E+05
Ki29a_CMPNeu5Ac	5.2433E+05
k21aB	4.2900E+06
k21aF	6.1200E+06
k19aF	1.5900E+07
k27aF	1.1200E+08

Table A.7 Estimated cell dynamics model parameter values in chapter 3

Parameter name	Parameter value
k_T_gln	3.3800E-06
Kd_Glc_ext	1.0051E-01
Kd_Gln_ext	1.1872E-02
Km_Glc_ext	2.6700E+00
Km_Gln_ext	1.2000E+00
mu_d_max_glc	3.9300E-01
mu_d_max_gln	6.2053E-02
mu_g_max	6.6745E-02
Y_ext_glc	9.1600E+07
Y_ext_gln	5.6400E+08
Y_mAb_mu	0.0000E+00
Y_mAb_Xv	1.1400E-09
Glc_in	0.0000E+00
Gln_in	0.0000E+00
F_in	0.0000E+00
F_out	0.0000E+00

Table A.8 Estimated N-linked antibody constant region glycan parameters in chapter 3

Parameter name	Parameter value
KdiFucTA	0.0000E+00
KdiFucTB	0.0000E+00
KdiGalTa1A	1.0709E+02
KdiGalTa1B	7.2051E+00
KdiGalTa2A	3.4573E+01
KdiGntII	7.7067E+01

Table A.9 Estimated nucleotide model parameter values in chapter 3

Parameter name	Parameter value
Kdf_10_Gln	2.6356E+00
Kdf_11_Glc	2.1296E+00
Kdf_11_Gln	1.3425E+00
Kdf_12_ATP	1.1302E+01
Kdf_13_ADP	3.9892E-04
Kdf_13_Glc	4.7469E+00
Kdf_14_ADP	2.5000E+01
Kdf_15_AMP	1.1312E+01
Kdf_15_Glc	2.3025E+00
Kdf_8_Glc	1.2067E+00
Kdf_8_Gln	2.4832E+00
Kdf_9_Gln	2.1804E+00
Kdf_9_UTP	5.0374E-03
Kdout_ATP	1.0000E-03
Kdout_CTP	1.0000E-03
Kdout_GTP	1.0000E-03
Kdout_UTP	1.0000E-03
kf_10	7.6621E+00
kf_11	6.7500E+00
kf_12	3.2344E+00
kf_13	2.1454E-01
kf_14	1.1649E+02
kf_15	8.6900E+01
kf_8	7.9486E+00
kf_9	1.3393E+00

Appendix D – Estimated Parameter Chapter 5

Table A.10 Estimated parameters of the cell culture dynamics model in chapter 5

Parameter	Final Value	95% Interval	Conf. t-value	95% Standard Deviation
Glc_feed	205.093	9.9	21	5
k_T_asn	3.74E-12	3.10E-13	12	1.60E-13
k_T_glc	6.18E-13	2.10E-13	3	1.00E-13
k_T_glu	2.32E-13	4.00E-13	0.57	2.00E-13
k_T_gua	1.16E-10	1.90E-11	6.2	9.60E-12
k_T_lac	5.47E-13	1.30E-13	4.3	6.40E-14
Kd_amm	36.1187	2.50E+02	0.15	1.30E+02
Kd_asn	0.067008	0.75	0.089	0.38
Kd_dmso	1000			
Kd_man	1000			
KI_amm	1.04339	4.5	0.23	2.3
KI_dmso	10000			
KI_gal	97.695	2.50E+07	3.90E-06	1.30E+07
KI_lac	1000			
KI_man	10000			
Km_amm_gln	0.388317	0.51	0.76	0.26
Km_asn	108.534	7.40E+02	0.15	3.80E+02
Km_glc	0.0001	19	5.20E-06	9.7
Km_gln	0.064644	0.74	0.088	0.37
Km_gua	0.0268	0.0092	2.9	0.0047
Km_lac	1.58295	1.7	0.94	0.86
Km_man	1000			
mu_d_max_PostGua	0.046373	0.27	0.17	0.14
mu_d_max_PreGua	0.040837	0.26	0.16	0.13
mu_g_max_PostGua	0.201601	0.054	3.7	0.027
mu_g_max_PreGua	1			
Y_mAb_mu_PostGua	1.86E-16	6.90E-07	2.70E-10	3.50E-07
Y_mAb_mu_PreGua	1.55E-08	4.80E-09	3.2	2.50E-09
Y_mAb_Xv_PostGua	8.33E-10	1.90E-09	0.45	9.40E-10
Y_mAb_Xv_PreGua	3.75E-10	9.40E-11	4	4.80E-11
Y_X_asn	1.00E+17	1.10E+24	8.80E-08	5.80E+23
Y_X_glc	1.93E+08	3.10E+07	6.1	1.60E+07
Y_X_gln	1.00E+12	1.40E+14	0.0073	6.90E+13
Y_X_glu	4.80E+09	2.50E+09	1.9	1.30E+09
Y_X_lac	6.07E+09	7.20E+09	0.84	3.70E+09
Y_X_man	1.00E+12	2.80E+17	3.60E-06	1.40E+17

Table A.11 Estimated parameters of the nucleotide synthesis model in chapter 5

Parameter	Final Value	95% Interval	Conf. t-value	95% Standard Deviation
KI1_adp	1000			
KI1_amp	1000			
KI1_atp	1000			
KI1_gtp	0.0001	0.06	0.0017	0.03
KI1b_gtp	1.25623	0.73	1.7	0.37
KI3_atp	1000			
KI3_gtp	1000			
KI4a_ctp	0.0001			
KI4a_gtp	194.11	7.70E+06	2.50E-05	3.90E+06
KI4a_utp	1000			
KI5_ctp	0.001983	1.5	0.0014	0.73
Km1_asn	1000	3.60E+04	0.028	1.80E+04
Km1_atp	347.327	3.60E+04	0.0097	1.80E+04
Km1_gln	0.0001			
Km1_gtp	0.0001			
Km2_adp	2.7161	1.70E+04	0.00016	8.80E+03
Km2_amp	1.09475	2.20E+04	5.00E-05	1.10E+04
Km2_atp	1000			
Km3_adp	0.0001	0.0061	0.016	0.0031
Km3_atp	0.358309	0.2	1.8	0.1
Km3_gfl	31.3291	5.2	6.1	2.6
Km4a_asn	1000	1.20E+05	0.0083	6.00E+04
Km4a_atp	1000			
Km4a_glu	0.0001	1.9	5.30E-05	0.94
Km5_atp	0.01	1.3	0.0077	0.65
Km5_glu	0.0001			
Km5_utp	1.00E+07			
Km6_gua	0.906077	1.4	0.64	0.72
n5_ctp	0.277091	0.76	0.37	0.38
n5_utp	1.68886	0.37	4.6	0.19
v_max_1a	129235	7.80E+07	0.0016	4.00E+07
v_max_1b	6.44E+07	3.70E+10	0.0017	1.90E+10
v_max_2b	8862			
v_max_2f	2.54E+06	3.60E+10	7.10E-05	1.80E+10
v_max_3b	0.711928			
v_max_3f	1.07357	0.051	21	0.026
v_max_4a	1.96E+07	2.30E+09	0.0084	1.20E+09
v_max_5	5.59E+08	4.10E+11	0.0014	2.10E+11
v_max_6	1	1.2	0.87	0.59

Table A.12 Estimated parameters of the NSD synthesis model in chapter 5

Parameter	Final Value	95% Interval	Conf. t-value	95% Standard Deviation
E15a	1			
E17a	2.59E-05	1.40E-05	1.8	7.20E-06
E19a	0.020955	0.011	1.8	0.0058
E1a	0			
E1c	0.003772	0.0015	2.5	0.00078
E23a	1.62E-05	8.90E-05	0.18	4.50E-05
E29a	2.33E-02	0.53	0.044	0.27
E38a	1.00E-01			
E3a	5.10E-04	2.30E-05	22	1.20E-05
E5a	1.00E-01	0.055	1.8	0.028
E6a	1.00E-01	2.10E+02	0.00049	1.00E+02
E8a	0.00E+00			
Eglyc	3.79E-05	2.80E-06	14	1.40E-06
Gln_coef	1.00E+02			
k17aF	9.85E+03	5.40E+03	1.8	2.70E+03
k19aF	311.857	1.30E+02	2.4	67
k21aB	2.99E+07	1.70E+08	0.17	8.70E+07
k22aB	652041	5.60E+04	12	2.90E+04
k26aF	4.30E+08			
k27aF	515750	2.70E+06	0.19	1.40E+06
Ki15a_GDPFuc	2.39E-07	3.20E-07	0.74	1.60E-07
Ki29a_CMPNeu5Ac	20834.1	7.80E+05	0.027	3.90E+05
Ki_SA_Tra_UDPGlcNAc	1.0001			
Km17a_Man6P	0.0001			
Km19a_Fru6P	0.001			
Km26a_Glc6P	0.284659	0.26	1.1	0.13
Km7b_UDPGlcNAc	0.81			
n15a_GDPFuc	2.92207	1.3	2.2	0.68
n15a_GDPMan	3.67974	1.1	3.2	0.58
n29a_CMPNeu5Ac	5			

Appendix E – Estimated parameters Chapter 7

Table A.13 Estimated parameters of the cell culture dynamics model in chapter 7

Parameter	Final Value	95% Interval	Conf. t-value	95% Standard Deviation
Glc_feed	218.312	6	37	3
Gln_feed	0.00E+00			
Glu_feed	9.79E+00	1.40E+00	6.9	7.20E-01
k_d_Gln	1.00E-04			
K_lysis	0.00E+00			
k_T_asn	4.73E-12	6.70E-13	7.1	3.40E-13
k_T_gal	0			
k_T_glc	4.58E-13	6.6E-14	7	3.4E-14
k_T_glu	0			
k_T_lac	3.83E-13	3.7E-14	10	1.9E-14
Kc_gal	291.659	1.40E+02	2.10E+00	7.10E+01
Kd_amm	1000			
Kd_asn	0.078805	0.22	0.35	0.11
Kd_gal	160.342	15	5.30E+00	
Kd_urd	1261.74	4700	0.27	2400
Kd_urd_gal	0.000001	0.072	0.000014	0.037
KI_amm	6.6738	52	0.065	
KI_gal	180.918	1.8	51	
KI_lac	0.71716	0.16	4.3	0.084
KI_urd	522.373	340	1.5	170
Km_amm_gln	3.89E-02	1.40E-01	2.90E-01	6.90E-02
Km_asn	7.03E+00	4.80E+00	1.5	2.50E+00
Km_gal	2.40E+01	5.40E-01	23	
Km_glc	1.00E-02	1.60E+01	0.00062	8.20E+00
Km_gln	1.00E-04	1.40E-01	7.30E-04	7.00E-02
Km_glu	1.00E-04	1.10E+00	0.000094	5.40E-01
Km_lac	9.17E+01	1.70E+02	0.55	8.50E+01
Km_urd	1.00E+03			
KmAb_urd	1.00E+03			
m_gln	4.80E-12	4.70E-13	1.00E+01	2.40E-13
mu_d_max_PreGua	7.39E-02	6.00E+01	0.00062	
mu_g_max_PreGua	9.87E+00	4.40E+02	0.011	
nd_urd	1.33E+00	5.00E-01	2.7	2.50E-01
nI_gal	9.28E-01	5.90E+00	8.00E-02	
nI_urd	2.77E+00	2.70E-01	10	1.40E-01
Y_amm_asn	6.87E-01	1.60E-02	4.30E+01	8.10E-03
Y_lac_gal	1.00E-01			
Y_lac_glc	3.00E+00			
Y_mAb_mu_PreGua	1.09E-08	2.10E-09	5.1	1.10E-09
Y_mAb_urd	1.39E-08	5.60E-09	2.5	2.90E-09
Y_mAb_Xv_PreGua	3.46E-10	4.60E-11	7.50E+00	2.30E-11
Y_X_amm	1.00E+14			
Y_X_asn	1.48E+16	3.80E+22	3.9E-07	1.90E+22
Y_X_gal	1.72E+08	7.00E-01	1.20E+08	
Y_X_glc	1.92E+08	1.20E+07	17	5.90E+06

Y_X_gln	9.52E+21	3.90E+33	2.40E-12	2.00E+33
Y_X_glu	2.16E+11	2.90E+12	0.076	1.50E+12
Y_X_lac	2.23E+09	3.40E+08	6.50E+00	1.70E+08
Y_X_urd	1.57E+07	2.80E+06	5.6	1.40E+06

Table A.14 Estimated parameters of the nucleotide synthesis model in chapter 7

Parameter	Final Value	95% Interval	Conf. t-value	95% Standard Deviation
E15a	KI1_adp	0.00035	0.0001	1
E17a	KI1_amp	4.69E-04	0.0001	1.00E+01
E19a	KI1_atp	1.00E+03	1	1000[*]
E1a	KI1_gtp	1.79E+02	0.01	1.00E+03
E1c	KI1a_urd	2.16E+00	0.001	1.00E+02
E20a	KI1b_gtp	1.18E-04	0.0001	1.00E+01
E21a	KI3_atp	1.00E+03	0.1	1.00E+03
E22a	KI3_gtp	0.025675	0.0001	10
E23a	KI3_utp	0.577747	0.0001	100
E26b	KI4a_ctp	1000	0.001	1000[*]
E29a	KI4a_utp	3.73E-04	1.00E-04	1.00E+02
E38a	KI4b_ctp	733.252	1	1000
E3a	KI4b_utp	249.17	0.0001	1000
E5a	KI5_ctp	2.6E-06	1.00E-08	0.001
E6a	Km1_asn	5.65584	1	1000
E8a	Km1_atp	43.8595	0.01	100
Eglyc	Km1_gln	0.0001	0.0001	10
Gln_coef	Km1_gtp	6.49239	0.001	100
k17aF	Km2_adp	0.055145	0.0001	10
k19aF	Km2_amp	0.07886	0.0001	20
k21aB	Km2_atp	1.00E-02	1.00E-02	1.00E+02
k22aB	Km3_adp	1.09E-02	0.0001	2.00E+01
k26aF	Km3_atp	2.07E+00	0.01	1.00E+02
k27aB	Km3_gfl	7.81E+00	0.01	1.00E+03
k27aF	Km4a_asn	1.07E+02	1.00E+00	1.00E+03
Ki15a_GDPFuc	Km4a_atp	1.00E-04	0.0001[*]	0.0001[*]
Ki23a_ATP	Km4a_glu	1.00E-04	0.0001[*]	0.0001[*]
Ki23a_UTP	Km4b_atp	5.16E+00	0.001	1.00E+03
Ki29a_CMPNeu5Ac	Km4b_urd	1.00E+03	0.0001	1000[*]
Ki3a_UDPGlcNAc	Km5_atp	1.00E+03	1.00E+00	1000[*]
Ki_SA_Tra_UDPGlcNAc	Km5_glu	1.00E-04	0.0001[*]	0.0001[*]
Km17a_Man6P	Km5_utp	4.76E+08	100	1.00E+10
Km19a_Fru6P	Km6_gua	2.06E-01	0.0001	2.00E+01
Km22a_UDPGlc	n4b_urd	1.04E+00	2.00E-01	5.00E+00
Km26a_Glc6P	n4b_utp	4.11E+00	0.2	5.00E+00
Km6a_UTP	n5_ctp	8.25E+00	2.00E+00	1.00E+01
Km7b_UDPGlcNAc	n5_utp	5.00E+00	0.25	5[*]
n15a_GDPFuc	v_max_1a	2.49E+06	1.00E+04	1.00E+08
n15a_GDPMan	v_max_1b	1.34E+08	10000	1.00E+09
n23a_UTP	v_max_2b	3.08E+03	3081.6[*]	3081.6[*]
n29a_CMPNeu5Ac	v_max_2f	1.03E+04	1.00E+04	1.00E+08
n6a_UTP	v_max_3b	1.00E+01	10[*]	10[*]
n15a_GDPFuc	v_max_3f	8.84E+00	1.00E-01	1.00E+02
n15a_GDPMan	v_max_4a	4.06E+04	10000	1.00E+06
n23a_UTP	v_max_4b	1.00E+03	1000	1.00E+07

n29a_CMPNeu5Ac	v_max_5	6.15E+10	1.00E+08	1.00E+12
n6a_UTP	v_max_6	4.66E-01	0.46585[*]	0.46585[*]

Table A.15 Estimated parameters of the NSD synthesis model in chapter 7

Parameter	Final Value	95% Interval	Conf. t-value	95% Standard Deviation
E15a	1			
E17a	1.04E-04	1.50E-05	6.9	7.80E-06
E19a	1.00E+01			
E1a	1.00E-07			
E1c	6.36E-04	1.40E-05	46	7.00E-06
E20a	2.11E-03	7.40E-05	28	3.80E-05
E21a	6.98008	1.20E+04	0.00058	6.10E+03
E22a	0.007989	0.00037	21	0.00019
E23a	89.8386	150000	0.00058	78000
E26b	1E-07	0.000017	0.0057	8.9E-06
E29a	0.03243			
E38a	10			
E3a	3.3E-05	1.7E-06	20	8.6E-07
E5a	1.02817	0.31	3.30E+00	0.16
E6a	0.000177	0.000039	4.6	0.00002
E8a	0.000292	0.00023	1.3	0.00012
Eglyc	0.0079	0.0013	6.1	0.00066
Gln_coef	10			
k17aF	9850.2			
k19aF	311.86			
k21aB	1.16E+05	1.10E+06	1.10E-01	5.60E+05
k22aB	9.83E+02	3.40E+01	29	1.70E+01
k26aF	4.06E+04	8.90E+04	0.46	4.50E+04
k27aB	3.31E+04	3.10E+05	0.11	1.60E+05
k27aF	5.77E+04	5.40E+05	1.10E-01	2.80E+05
Ki15a_GDPFuc	2.39E-07			
Ki23a_ATP	1.00E+02			
Ki23a_UTP	1.00E+02			
Ki29a_CMPNeu5Ac	1.24E+02			
Ki3a_UDPGlcNAc	1.00E+05			
Ki_SA_Tra_UDPGlcNAc	1.00E+00			
Km17a_Man6P	1.00E-04			
Km19a_Fru6P	1.00E-03			
Km22a_UDPGlc	1.00E-03			
Km26a_Glc6P	1.00E-03			
Km6a_UTP	1.09E+01	1.70E+00	6.50E+00	8.60E-01
Km7b_UDPGlcNAc	7.04E-01	2.90E-02	25	1.50E-02
n15a_GDPFuc	2.92E+00			
n15a_GDPMan	3.68E+00			
n23a_UTP	5.00E-01	1.40E+01	0.037	6.90E+00
n29a_CMPNeu5Ac	3.04E+00			
n6a_UTP	4.30E-01	7.90E-02	5.40E+00	

Table A.16 Estimated parameters of the glycan model in chapter 7

Parameter	Final Value	95% Interval	Conf. t-value	95% Standard Deviation
FucT_A	4.87342	590	0.0083	290
GalT_A	5.05E+00	9.50E+00	0.53	4.80E+00
GnTI_A	8.29E-01	4.30E+01	0.019	2.20E+01
GnTI_B	1.43E-01	9.00E+00	0.016	4.50E+00
KdiFucTA	7.47E+00	1.10E+04	0.00069	5.40E+03
KdiFucTB	2.03E+03	2.40E+05	0.0083	1.20E+05
KdiGalTa1A	1293.02	2.80E+03	0.47	1.40E+03
KdiGalTa1B	2232.56	4700	0.48	2300
KdiGalTa2A	2000.3	4700	0.43	2300
KdiGalTa2B	1392.07	2900	0.48	1500
KdiGntI	32.2344	1.50E+03	2.20E-02	7.40E+02
KdiGntII	2.69058	3500	0.00077	1700
KdkGalTa1A	17.3253	30	0.58	15
KdKGalTa1B	26.621	31	8.70E-01	15
KdkGalTa2A	238.663	280	0.84	140
KdkGalTa2B	1000			
ManI_A	23.6808	2900000	8.1E-06	1500000
ManI_B	159.11	1.5E+09	1.1E-07	7.4E+08